THE HONG KONG POLYTECHNIC UNIVERSITY

INSTITUTE OF TEXTILES AND CLOTHING

MULTI-SCALE STUDY OF TEXTILE COMPOSITES UNDER LARGE DEFORMATION FOR ENERGY ABSORPTION

Peggie, Sin-wan LAM

A Thesis Submitted in Partial Fulfillment of the Requirements

for the Degree of Doctor of Philosophy

March 2004

CERTIFICATE OF ORIGINALITY

I hereby declare that this thesis is my own work and that, to the best of my knowledge and belief, it reproduces no material previously published or written, nor material that has been accepted for the award of any other degree or diploma, except where due acknowledgment has been made in the text.

Peggie, Sin-wan LAM

March, 2004

By Grace of God

To My Family
for Their Loves, Support and
Understanding

ABSTRACT

This thesis presents a systematic study, in multi-scales, of mechanical properties of newly developed thermoplastic cellular textile composites for energy absorption purposes. This research aims to create a scientific basis for such composite materials with a high specific energy absorption capacity, and to better understand the material system, the fibre architecture and the fabrication techniques for particular applications. The study covers five related aspects: (1) composite fabrication techniques, (2) performance of cellular composites with various material systems under quasi-static compression and impact conditions, (3) deformation mechanism of the cellular structure, (4) in-plane deformation and mechanisms under tensile loading in both macro- and micro-scales, and (5) determination (by employing Raman microscopy) of fibre strain distribution in composites.

Material systems in this study include co-knitting polyester (polyethylene terephthalate, or PET) and polypropylene (PP) continuous filament yarns to be melted as matrix, laminating PET non-woven fabrics and PP matrix films, laminating high performance fibres, ultra-high molecular weight polyethylene (UHMWPE), as knitted fabrics and low-density polyethylene (LDPE) matrix films. The fabrication processes of thermoplastic textile composites, including the corresponding grid-dome with flat-top cellular structure, are described.

The energy-absorption behaviours of these cellular composites are examined under quasi-static compression and impacts. The effects of fibre material, fibre volume fractions and fibre architecture on the energy absorption capacity, are investigated. Cell recovery after impact is also studied. The equivalent cell wall thickness is shown to be a dominant factor governing the energy absorption capacity of the cellular structure made from the same material. Both the composites with knitted and non-woven fabric reinforcements exhibit a high specific energy absorption capacity. In particular, the non-woven composite achieves a higher level of energy absorption than that of the knitted composites. In addition, the non-woven cellular textile composite is able to retain the same level of energy absorption capacity under multiple impacts. This can be attributed to material properties of the composites such as its tensile and shear properties. By further varying the fibre volume fraction in the non-woven composite, different fracture modes are observed and different levels energy absorption capacity are obtained.

Previous studies by others concentrated on the deformation mechanisms of cellular composites with anisotropic knitted reinforcement. The present study is concerned with isotropic materials. The major deformation mode of flat-topped cellular samples made of PET/PP non-woven composites and pure PP polymer is identified as the internal convolution of the conical cell wall during plastic collapse of the cell. Theoretical analysis for the large deformation is carried out to predict the energy-absorption capacity of non-woven cellular composites and pure PP. Good agreement has been found between the predicted and the experimental results, implying that the model can provide a basis for the effective design of similar material systems.

Previous studies demonstrated that the membrane deformation of knitted cellular composites dominates the contribution of energy absorption when the cell collapse is large. Hence, in-plane deformation of the knitted composites is investigated in this study. Tensile properties of the composites are related with the knitting directions and individual components. The deformation mechanisms of the flat composites are identified during tensile loading by in-situ SEM observation. Effects of fabric structure, fibre volume fraction, pre-stretching directions and levels of the knitted fabrics prior to composite fabrication and plasma treatment on fibre surface are studied.

Raman microscopy is employed to determine the fibre strain distribution in a single loop in the knitted composites, made from ultra-high molecular weight polyethylene (UHMWPE) fibres embedded in low density polyethylene (LDPE) matrix. The fibre itself acts as a sensor embedded in the composite and therefore Raman microscopy can be used to follow the Raman band shift of the single fibre due to the applied strain. It has been found that the fibre strains of the deformed loop are very low even when the composite is under large effective strains. Theoretical analysis is concentrated on the fibre strain on single knitted loop during the large deformation. This phenomenon can be explained in terms of the shape change of the fabric loop and fibre sliding, fibre orientation to the stretching direction, and probably the fibre stress relaxation during the loop mapping process.

In summary, the fabrication aspects and the performance of cellular textile composites with various material systems have been investigated in detail. The deformation mechanisms of the isotropic non-woven cellular composite material have been identified and a prediction model has been proposed to provide fundamental information on composite design. The in-plane deformation mechanisms of the composites that contribute to the energy absorption have been studied in multi-scales. The study of non-woven composites provides an alternative material selection to achieve further substantial saving on material cost and fabrication time. More importantly, the outcome of this thesis may contribute significantly to development of high energy absorbing cellular textile composites with great potential in making protection devices, such as sport helmets, car crashing elements or other light weight devices where high specific energy absorption capacity is of great concern.

LIST OF AUTHOR'S PUBLICATIONS

Refereed Journal Publications

1. Lam S.W., Xue P., Tao X.M., and Yu T.X.
   "Fabrication and Performance of Cellular Textile Composites Reinforced by Non-woven Fabric for Energy Absorption"
   Composites A.: Applied Science and Manufacturing, submitted.

2. Lam S.W., Tao X.M., and Yu T.X.
   "Study of Fibre Strain Distribution in UHMWPE /LDPE Knitted Composites under Large Deformation by Raman Microscopy"
   Composites Science and Technology, submitted.

3. Lam S.W., Tao X.M., and Yu T.X.
   "Cellular Textile Composites with Non-woven Fabric Reinforcement"
   Textile Research Journal, submitted.

4. Xue P., Lam S.W., Wong Y.W., Tao X.M., and Yu T.X.
   "Development and Application of Cellular Textile Composites"
   Research Journal of Textiles and Apparel, submitted.

5. Lam S.W., Tao X.M., and Yu T.X.
   "Comparison of Different Thermoplastic Cellular Textile Composites on their Energy Absorption Capacity"
   Composites Science and Technology, in press.

6. Lam S.W., Xue P., Tao X.M., and Yu T.X.
   "Multi-scale Study of Tensile Properties and Large Deformation Mechanisms of Polyethylene Terephthalate/Polypropylene Knitted Composites"
   Composites Science and Technology, 63(10), 2003, P.1337-1348.

7. Lam SW, Tao X.M. and Yu T.X.
   "Polymeric Cellular Textiles Composites for Energy Absorption"
   Research Journal of Textiles and Apparel, 6(2), 2002, P.1-8.

Patent Application

Lam S.W., Tao X.M., and Yu T.X.
"Three-Dimensional Textile Structure and Manufacture and Use Thereof"
US Patent, pending.

Book Chapter

Lam S.W., Tao X.M., Xue P. and Yu T.X.
"Tensile Properties of Thermoplastic Weft Knitted Composites"
Key Engineering Materials, Editors: Yu T.X., Sun Q.P., Kim J.K.,
Trans Tech Publications, Switzerland, Vols.: 177-180, 2000, P.339-344.

Professional Journal

Lam S.W., Tao X.M., and Yu T.X.
"Tensile Behaviour of Thermoplastic Weft-Knit Composites"
Textile-Asia, 2002; 33(5): 28-31.

Conference Publications

1. Lam S.W., Tao X.M., and Yu T.X.
   "Non-woven Fabric Reinforced Cellular Textile Composites with Improved Energy Absorption Capacity"
   The 4th Asian-Australasian Conference on Composite Materials Composites Technologies for 2020, Sydney, Australia, 6-9th July 2004.

2. Xue P., Tao X.M, Yu T.X., Wong Y.W. and Lam S.W.
   "Laminated Cellular Textile Composites Used for Energy Absorption"
   13th International Conference on Textile Coating and Laminating, Charlotte, USA, November 18-19, 2003.

3. Lam S.W., Tao X.M., and Yu T.X.
   "Energy Absorption of Thermoplastic Cellular Textile Composites"
   Proc. of 5th International Conference, Texsci 2003, TEXTILE SCIENCE 2003, Liberec, Czech Republic, 16-18th July 2003, P. 139.

4. Lam S.W., Tao X.M. and Yu T.X.
"Fabrication and Mechanical Characterization of Weft Knitted UHMW Polyethylene Fabric / Low Density Polyethylene Matrix Composites"
Proc. of World Textile Conference 2nd AUTEX Conference: Textile Engineering at the Dawn of A New Millennium: An Exciting Challenge, Brugge, Belgium, 1-3 July 2001, P. 287-297.

5. Lam S.W., Tao X.M. and Yu T.X.
"Macro- and Micro-scale Study of Tensile Behaviour of Thermoplastic Weft Knitted Textile Composites"
Proc. of The 6th Asian Textile Conference, Hong Kong, 22-24th August, 2001, P.219.

6. Lam S.W., Tao X.M. and Yu T.X.
"Micromechanical Deformation on Single Poly(ethylene Terephthalate) /Polypropylene Matrix Model Composites"
Proc. of The 6th Asian Textile Conference, Hong Kong, 22-24th August, 2001, P.107.

7. Lam S.W., Xue P., Tao X.M., and Yu T.X.
"Multi-scale Study of Tensile Properties and Large Deformation Mechanisms of Polyethylene Terephthalate/Polypropylene Knitted Composites"
Proc. of The International Conference of Materials for Advanced Technologies, Singapore, 1-6 July, 2001.

8. Lam S.W., Tao X.M. and Yu T.X.
"Micromechanical Deformation of Single Poly(ethylene Terephthalate) Fibre/Polypropylene Matrix Model Composites"
Proc. of The Thirteenth International Conference on Composite Materials, Beijing, 25-29th June, 2001, P.436.

9. Lam S.W., Tao X.M., Yu T.X. and Yang X.
"Micromechanic Properties of Single Poly(ethylene Terephthalate) Fibre/Polypropylene Matrix Model Composites"
Proc. of Hong Kong Society of Theoretical and Applied Mechanics, 17th March 2001, HKSTAM Annual Meeting.

ACKNOWLEDGEMENTS

This research study has been financially support by the Research Grant Council of The Hong Kong Polytechnic University [Project code: GV-984], which is gratefully acknowledged. I am also grateful for the award of the Research Studentship and Tuition Scholarship offered by The Hong Kong Polytechnic University.

I would like to express my sincere gratitude to my chief supervisor, Professor Xiao-ming Tao, who brought me to this interesting and promising research field. I am grateful for her patient guidance and continuing encouragement in training me to conduct scientific research. Her enthusiasm in scientific pursuits and indefatigable dedication to research study have inspired me. Her support of my participation in international conferences, academic activities and hall life are especially appreciated.

I would also like to express my special thanks to my supervisor, Professor Tong-xi Yu, Department of Mechanical Engineering, The Hong Kong University of Science and Technology, for his continuing guidance and cares about my research progress. I appreciate for his constructive discussions and critical comments on my project.

My heartfelt appreciation goes to Dr. Pu Xue who is my teacher and friend as well. She has contributed many important ideas in the modeling part of the cellular composite study. I would also like to thank Professor Xu-gang Yang at Dong Hua University, Shanghai, China, for his sharing of many experiences on Raman measurement and valuable suggestions in the analysis of results.

I am indebted to the staff and technicians in the Institute of Textiles and Clothing, for creating a pleasant environment for our research students. Research facilities and technical supports in our department are gratefully acknowledged. Thanks are given to our technicians in the Physical Testing Laboratory, and the Knitting Workshop, for their kind assistance for my experimental work.

More thanks go to Dr. Buo-run Shi of the optical laboratory, Materials Characterization and Preparation Facility (MCPF), HKUST, Mr. Alex Fok and Mr. TinYan Leung (Dept. of Mechanical Engineering, HKUST), Ms. Meileng Liu and Mr. Leo Lee (Advanced Engineering Materials Facility (AEMF) in HKUST), for their friendly help and technical support.

I am indebted to my colleagues who have given me many helpful suggestions on the project, in particular to Mr. Jiang-ming Yu and Dr. Dong-xiao Yang. My special thanks go to Wayne Wong for his continuing love and support. I am also thankful to many friends, Burley Wang, Debbie Jiang, Joyce Chan, Winnie Lo, Michelle Wong, Ivan Lam, Wilson Wong, Kaman Cheng, Derry Law, Aping Zhang, Joanne Yip, Vicky Man, Bonny Kwan, Gloria Leung, Michelle Lee, Franky Mak, Rise Choi, Ah-Pun Chan, MeiMei Lau, Cherry Lo, Hai-hui Ruan, Shi-lun Ruan, Zi-yang Gao and Bo Zhu, for their continuing help and happiness brought all the time.

TABLE OF CONTENTS

LIST OF FIGURES

LIST OF TABLES

NOTATIONS

Symbol	Definition
C	Courses per cm in knit fabric
D	Diameter of the die punch
D_I, D_o	Cell diameters at the hinge of cell wall and cell bottom referred to Fig. 3.9
E_c	Composite modulus
E_f	Young's modulus of fibres
E_m	Matrix modulus
F	Tensile load
G	Shear modulus
H_i	Loop height of a unit cell geometry referred to Fig. 6.19
H	Length of specimen
L	Cell height referred to Fig. 3.9
M_p	Fully plastic bending moment per unit length of cell wall
P	Axial load applied on a flat topped grid dome cell
$\overline{P}$	Mean axial post-buckling load
S_{ys}	Shear yield stress of thin sheet specimen
S_{ms}	Maximum shear strength of thin sheet specimen
T	Mean thickness of the composite and pure matrix specimen
T	Fibre tension
V_f	Fibre volume in cellular textile composite
V_m	Matrix volume in cellular textile composite
V_T	Total volume of cellular textile composite
V_v	Void volume in cellular textile composite
W	Wales per cm in knit fabric
W_m	Plastic dissipation due to the membrane deformation
W_b	Plastic dissipation due to the bending the plastic hinge lines
W	Total energy dissipation of a flat-topped grid dome cell
W_i	Width of loop a unit cell geometry referred to Fig. 6.19
W	Width of specimen referred to Fig. 6.19
Y	Hoop stress in the extended composite referred to Fig. 3.9

Symbol	Definition
a	Length of a fibre bundle in a unit cell
d	Diameter of a cell top
d	Distance between wales referred to Fig. 4.7
e_1, e_2	Mean strain in extending the segment between hinge lines referred to Fig. 3.9
h	Loop height referred to Fig. 4.7
l	Distance between loop leg referred to Fig. 4.7
l	Length of a fibre loop
n	No. of fibre bundle
r	Radius measured from the inner line of the loop head to the centre O located in the matrix
t	Projected yarn thickness in a unit cell referred to Fig. 6.19
t	Nominal cell wall thickness
t_e	Equivalent cell wall thickness
v	Shape change ratio of a unit cell of knitted loop
x	Length of fibre leg in a unit cell
w	Loop width referred to Fig. 4.7
x_1, x_2	the length variables on the cell wall as a flat topped grid dome cell forming internal convolution, referring to Fig. 3.9
ϕ	Semi-apical angle of the conical shell
θ, β	Angles referred to Fig. 3.9
ε	Effective composite strain
ε_f	Fibre strain
γ	Shear yield strain
Δv	Raman wavenumbers shift
Δ	Composite displacement

CHAPTER 1
INTRODUCTION

1.1 Background: Textile Composites for Energy Absorption

When advanced applications need a combination of properties that no single material can provide, composites become one of the choices. Composites can be defined as a combination of dissimilar materials to perform a task that neither of the constituent materials can perform alone. Generally, a composite is made of at least two components: reinforcement and matrix. In textile composites, textile reinforcements can be formed by integrating fibres or yarns into fabrics by weaving, knitting and braiding etc. Textile preforms can be in various shapes or forms. Well established textile techniques allow near-net-shape preform manufacturing and also reduce cost considerably. The preforms can be consolidated by various conversion processes, such as resin transfer molding or hot pressing. Matrix materials can be thermoplastic or thermoset polymer, ceramic or metal. Depending on the product design for specific application, consolidation of the textile material with matrix material can produce three-dimensional textile composites.

In recent years, development of three-dimensional textile composites for energy absorption application has received increasing attention from researchers due to the design flexibility of the composite structures, their high specific strength and stiffness with a large amount of reduction in weight as well as low fabrication cost as compared with metals. In many engineering problems, the main concern in selecting

materials is their energy-absorption capacity rather than their elastic moduli or ultimate strength. The energy-absorbing devices, as described by Johnson & Reid (1977) and Yu (1986), should utilize the in-elastic deformation as their major energy-absorption mechanism; the force required for their deformation should be almost constant with a long deformation stroke under a stable mode. They should be light-weight, and possess high specific energy-absorption capacity (i.e. energy-absorption capacity per unit weight). Therefore, these requirements for the structural components are different from those designed for high load or strain bearing.

Typical examples can be found in the devices for crashworthiness of vehicles in collision accidents. Bumpers and other crushing elements in chassis and doors should be designed to obtain high specific energy absorption capacity while keeping the peak force (and thus the deceleration) below the threshold above which a collision will cause damage or injury. When a collision happens, the kinetic energy of the vehicle can be completely dissipated by these crushing elements on reducing the damage to the occupants in the vehicle to a minimum. Similar principles are applied to other energy absorbing devices, such as road barriers, auxiliary protective helmets, hard hats used in construction sites, protective packaging of fragile goods, etc. These energy-absorbing devices should undergo a non-reversible deformation, and thus they are usually one-shot items. After the plastic deformation, they are discarded and replaced. The mode of deformation should be stable under various impact conditions and not adversely affected by dirt, corrosion or other environmental factors.

Manufacturing the textile composites should be fast, easy and at reasonable cost, the

component size and shape capability are also of paramount importance. Traditionally, a variety of materials such as metal, plastic and wood in cellular structures (thin-wall tubes, honeycomb, conical frusta and foams etc.) have been used for making energy absorption devices. Textile composites can be fabricated into cellular structures as new members of the material family for high energy-absorption purposes.

The term "cellular textile composites" used in this study comes from the concept of cellular solids (Gibson and Ashby, 1997), which comprises an assembly of cells that are interconnected by a network of solid edges and faces of cells. The members of the cellular solid family include a large variety of natural and artificial materials such as wood, coral, bone, honeycombs, foams and so on. These cellular solids contain a large amount of space and normally have a low relative density. Due to their excellent capacity for energy absorption and thermal insulation, cellular solids have been used for cushioning, packaging, insulation of heat and sound as well as light-weight structural components (Hua and Yu, 1991). Similarly, textile material is an assembly of fibres with certain orientations, which can be fabricated to give low-density cellular structures. The structural parameters of fibre assemblies can be engineered for particular applications such as energy absorption. Due to the design versatility of textile structures and three-dimensional shapes, textile materials can be designed specifically to absorb large amounts of energy with light weight and flexibility, such as in protective helmets, bullet proof panels, crash barriers, etc.

1.2 Introduction to the Study of Cellular Textile Composites

1.2.1 Historical Development of the Composites

Starting from early 1997, Tao and Yu (1997) conducted a systematic study on the specific energy absorption capacity of cellular textile composites. Various cellular textile composites with five configurations, as shown in Fig. 1.1, were fabricated and tested under quasi-static compression and impact conditions. The study identified that textile composites with a suitable cell geometry which could undergo large plastic deformation (bending or/and membrane stretching) to achieve high levels of energy absorpion capacity. Those having large elastic deformation or brittle fracture during deformation are not suitable for this kind of application. It was found that a grid-domed cellular structure has the highest specific energy absorbing capacity among all the five configurations, which is also greater than that of polyester foams of identical density.

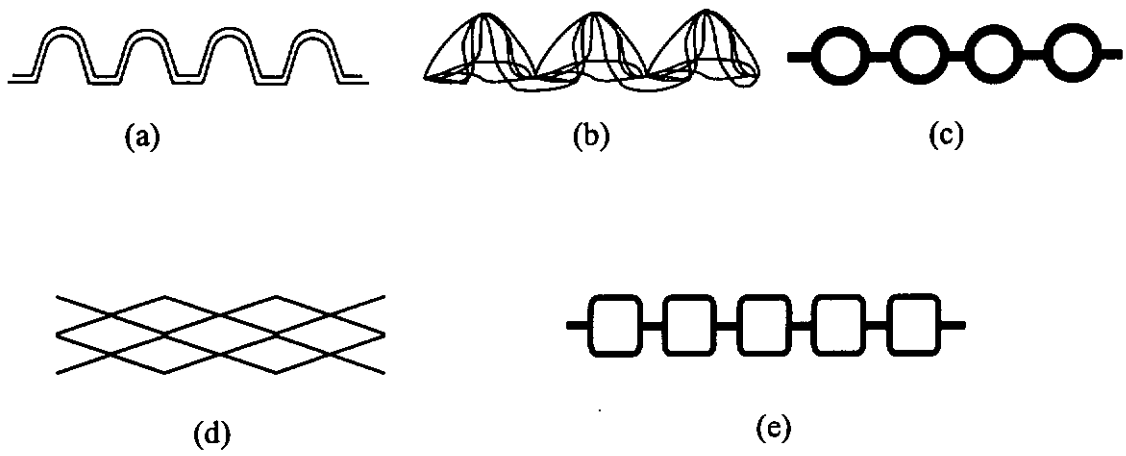

Figure 1.1 Schematic diagrams showing different configurations of cellular textile composites. (a) Spherical topped with tapered wall grid domed structure molded from knitted fabrics (b) Spunbond non-woven structure (c) Circular-tube shaped knitted composite (d) Multi-layer woven structure (e) Square-tube shaped knitted composite

In their subsequent work, a thorough characterization and optimization of grid-domed cellular textile composites reinforced with knitted fabrics were carried out. The large deformation processes (Yu et al., 2000) of hemispherical topped grid-domed composites involve three-stages: (1) local inversion of hemispherical dome cell, (2) global plastic collapse of the truncated spherical cap and then (3) large plastic deformation of a truncated conical shell, as illustrated in Fig. 1.2. Elastic and rigid plastic models for the individual deformation stages (Yu et al., 2000) have good agreement with the experimental data. These models also show that in the first two stages of deformation, there is an elastic or elasto-plastic snap of the spherical cap of the hemi-spherical dome, which leads to comparatively lower energy dissipation.

It is also found that by further improving the hemi-spherical top configuration to a flat topped one, it would effectively minimize the elastic deformation and facilitate the plastic deformation leading to higher energy absorption capacity (Xue et al., 2000). The modified flat-topped grid-domed cellular composites is shown in Fig.1.3.

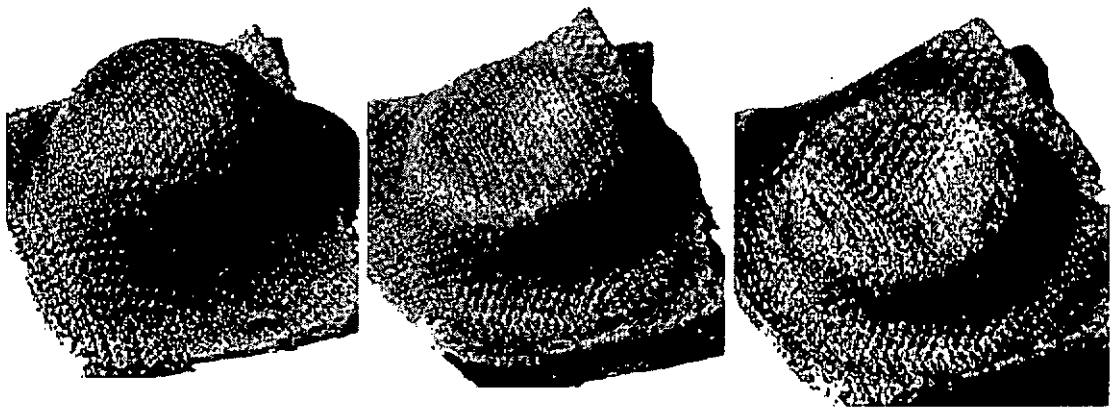

(a) (b) (c)

Figure 1.2 Images of a hemispherical topped dome cut from the cellular composite developed at early stage (Yu et al., 2000), (a) the undeformed configuration; (b) an axisymmetric deformation of the dome at small deflection; and (c) a 3-fold deformation pattern of the dome at larger deflection

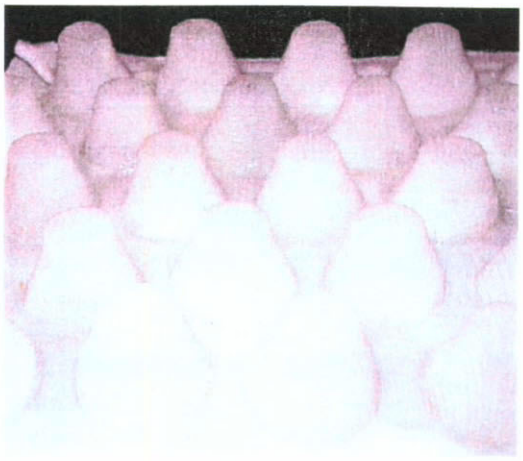

Figure 1.3 Flat-topped grid-domed cellular composites (Xue et al., 2000b)

Table 1.1 compares the energy-absorption capacity of composites with hemi-spherical tops and flat-topped configurations under quasi-static compression and impact tests. The samples contained the same number of domes in a panel area of 100x100 mm^2 having a weight of approximately 10.5 g, with a dome height of 13.8 mm and resin add-on of 155-162 % (Xue et al., 2000). The flat-topped cells exhibit a much higher energy-absorption capacity than the hemi-spherical ones under both quasi-static compression and impacts. The flat-topped cells deform in a stable mode with a low peak force and under a long stroke during the large deformation process.

Table 1.1 Comparison of energy-absorbing capacity for hemispherical topped and flat-topped cell configurations (Xue et al., 2000)

E_0, impact energy; V_0, impact velocity	Configurations	Energy absorption up to 4mm displacement		Energy absorption up to 8mm displacement	
		J	J/g	J	J/g
Quasi-static test, 5mm/min.	Hemispherical topped	0.50	0.29	2.27	1.34
	Flat-topped	1.33	0.60	5.00	2.27
E_0=23J, V_0=3.47m/s	Hemispherical topped	3.42	0.45	16.11	2.15
	Flat-topped	11.39	1.08	23.74	2.26
E_0=45 ± 2%J, V_0=4.8m/s	Hemispherical topped	4.10	0.54	16.46	2.19
	Flat-topped	11.02	0.96	28.00	2.43

Other geometrical parameters of the cells that have significant effects on energy absorption were also investigated (Xue et al., 2000). When the diameter of the cell-bottom remains constant, a varying diameter of the cell-top or the semi-apical angle of the truncated conical shell would have a significant effect on the energy-absorption capacity of the composites. The effective area of the cell or the cell wall area dominates the energy-absorption capacity of grid-domed cells. As long as the effective area remains constant, varying the cell size has little effect on the energy absorption capacity of the composites. With the same cell size, increasing the cell density can obtain a higher energy-absorbing capacity, but also increases the pre-extension of fabrics during the molding process.

By observing the collapse of cells with a flat-topped configuration under axial compression, the deformation mechanism was identified having the elastic buckling followed by a plastic collapse of the truncated conical wall. A theoretical model

including both the elastic and plastic deformation of a cell was developed to predict the load-displacement and energy absorbing characteristics. In the rigid perfect plastic analysis, the total energy dissipation (W) during large plastic deformation including bending (W_b) of the plastic hinge lines and membrane deformation (W_m) is written in the following expression:

$$W = W_b + W_m = \int_0^{\Delta} P d\Delta$$

The total energy absorption dissipation is equal to the external work done by the axial compressive force (P) with a vertical displacement (Δ) of the cells during the deformation process. Figure 1.4 illustrates the rigid-plastic deformation model of a flat-topped conical cell having a horizontal circumferential hinge line under axial compression. This membrane deformation of the cell will dominate the energy absorption at large deformation, accounting for over 80 % of energy absorbed when the vertical displacement of the cell-top reaches half of the cell height. The model also enables to predict the large deformation behaviour of the grid-domed cell including the strain distribution and possible failures. Based on the previous experimental studies and theoretical analysis, the finite element simulation was performed (Bao). The effects of the geometrical parameters, such as wall thickness, cell height and anisotropy of composite, etc. on energy absorption capacity were discussed.

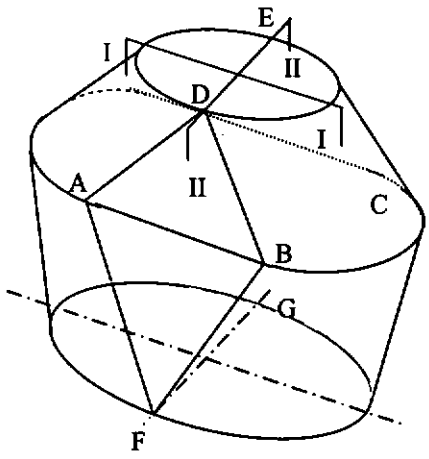

Figure 1.4 Sketch of the rigid-plastic deformation model of a flat topped grid-domed cell having a horizontal circumferential hinge line

The mechanism of energy absorption by large membrane stretching and bending deformation of the cellular textile composites are different from the rigid composites, such as the composite I-beam (Hamada, 1997), carbon fibre/epoxy tube, carbon knitted /epoxy tube (Ramakrishna and Hull, 1995) and braided composite square tube (Chiu et al., 1995), which are designed to absorb high impact energy by localized matrix cracking, fibre/matrix debonding and further fracture in the crush zone. Further examination of the deformation mechanism of the knitted cellular composites in microscopic level has been conducted by in-situ quasi-static compression loading of a composite cell inside scanning electron microscope (SEM). The damages, including the localized matrix crack initiation, propagation, and debonding of fibre/matrix, have also been observed in the buckling region, as shown in Fig. 1.5. However, these kinds of deformation have minimal effects on the energy absorption as long as the composite structures hold their integrity.

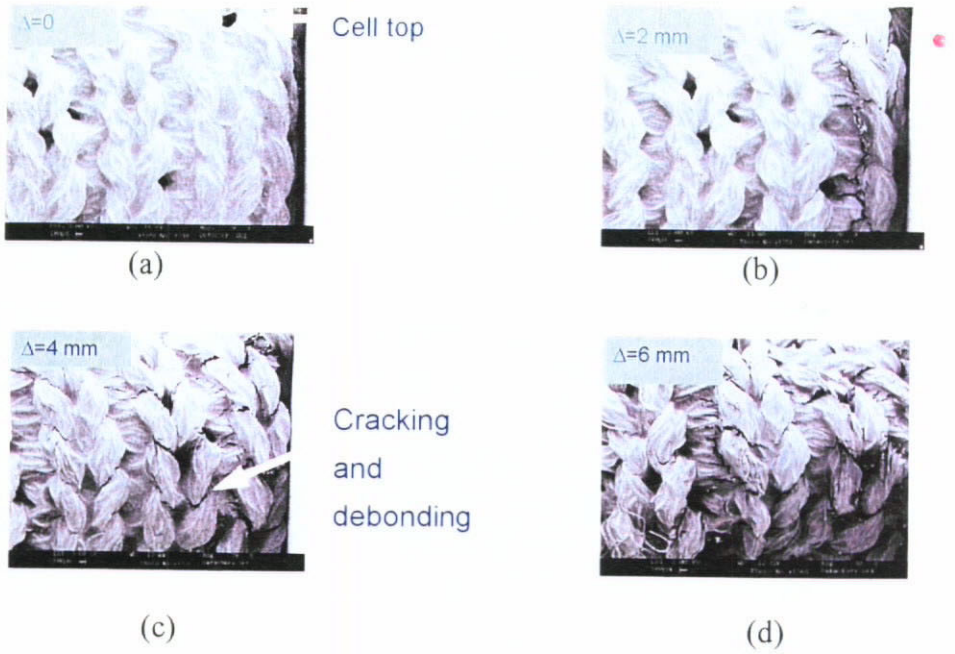

Figure 1.5 Deformation mechanism of the thermoset flat-topped cellular composite being observed in the buckling region (Xue, 2000a)

In order to study the failure mode of the knitted textile composites, the tensile loading of flat knitted composites was conducted and the deformation mechanism was observed under microscope, as shown in Fig. 1.6 (Xue et al., 2002). The crack propagation in matrix, the change of the loop shape and the straining of fibres before fracture can be identified in the cases with the three loading directions. In particular, the size of holes approaches a constant with the tensile loading while the growing speed of hole in wale loops increases progressively and this is quantitatively described.

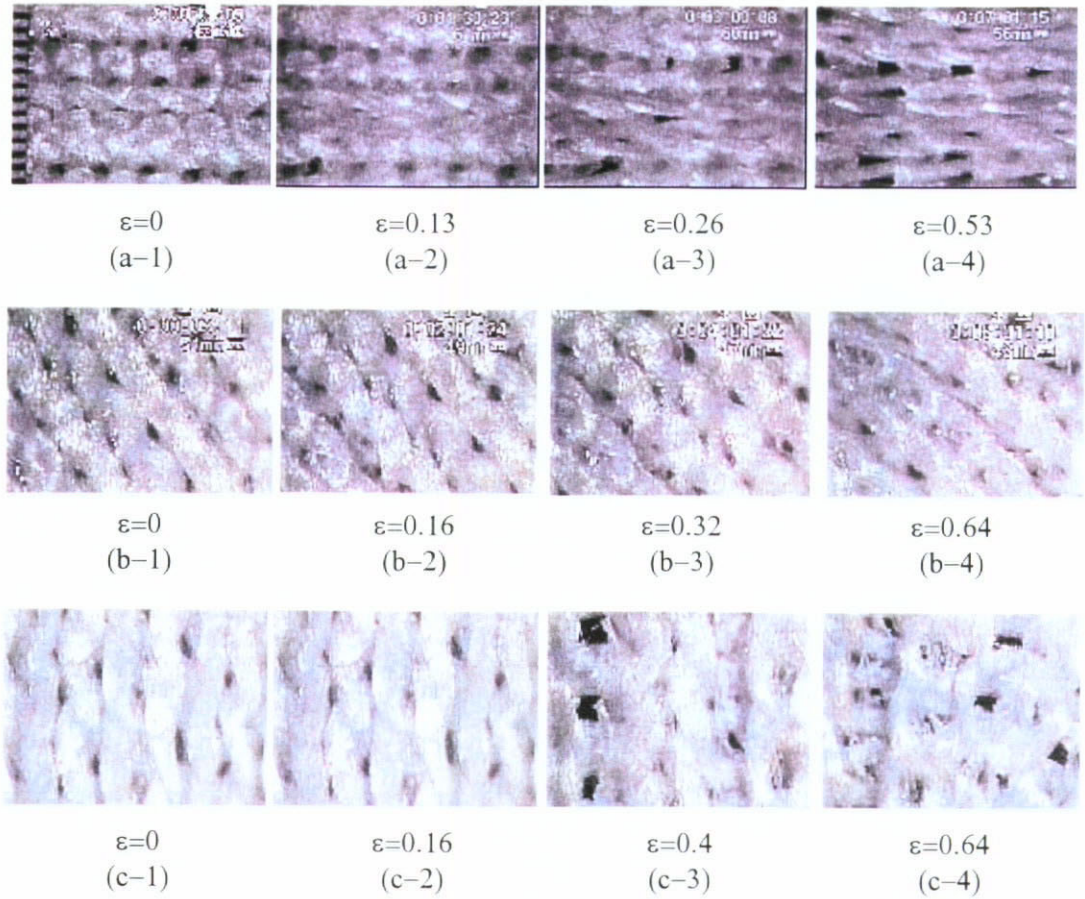

Figure 1.6 The deformation process of PET/PP knitted composites under tension along (a) the wale direction, (b) the diagonal direction; and (c) the course direction (Xue et al., 2002)

1.2.2 Fabrication of the Composites

There are various types of well established textile processing and composite manufacturing techniques (Mazumdar, 2002). Many published papers have demonstrated (Tung and Jayaraman, 1991; Araujo, 1996; Hansson, 1998; Svensson, 1998; Kamiya et al., 2000) the versatility of textile processing on three-dimensional composite design. These are good guidance for the design and fabrication of the grid-dome shaped cellular textile composites. Considering the formability of textile

preforms into cellular structural panels, however, filament winding, 3D weaving or braiding would not be appropriate choices. Other considerations for material selection of the cellular composites should focus on promoting the plastic collapse of the projected cells to obtain a high specific energy absorption capacity. Highly rigid and brittle fibres such as glass, carbon or ceramic fibres embedded in brittle matrices/resins for high performance application would not be suitable for the large deformation application. Feasible ways for fabricating polymeric cellular textile composites were studied and are summarized in Fig. 1.7.

1.2.2.1 Material System

The selection of fibres and matrix/resin has a key effect on the properties/performance of the final composite products. Based on the application requirements of a high energy absorbing material, the fibres should be sufficiently strong but ductile. Conventional fibres such as, fully drawn polyester and nylon, possess a certain strength and extensibility, pliability (forming knitting loops) and lightness. They may have a great potential to be used for energy absorption purpose. The mechanical properties of these fibres compared with some high performance fibres are listed in Table 1.2 (Morton and Hearle, 1993). In addition, conventional fibres can be texturized as crimped, deformed or stapled yarns for enhancing preform formability during composite molding and achieving a better matrix impregnation. Other minor considerations when selecting the fibre material, including the level of moisture absorption of the polymer fibres (e.g. nylon fibres can absorb moisture up to 4 %), would affect the properties and dimensional stability of the composites while the fibre/matrix compatibility (inappropriate adhesion of fibre/matrix interface) would strongly affect the failure mode of the composites.

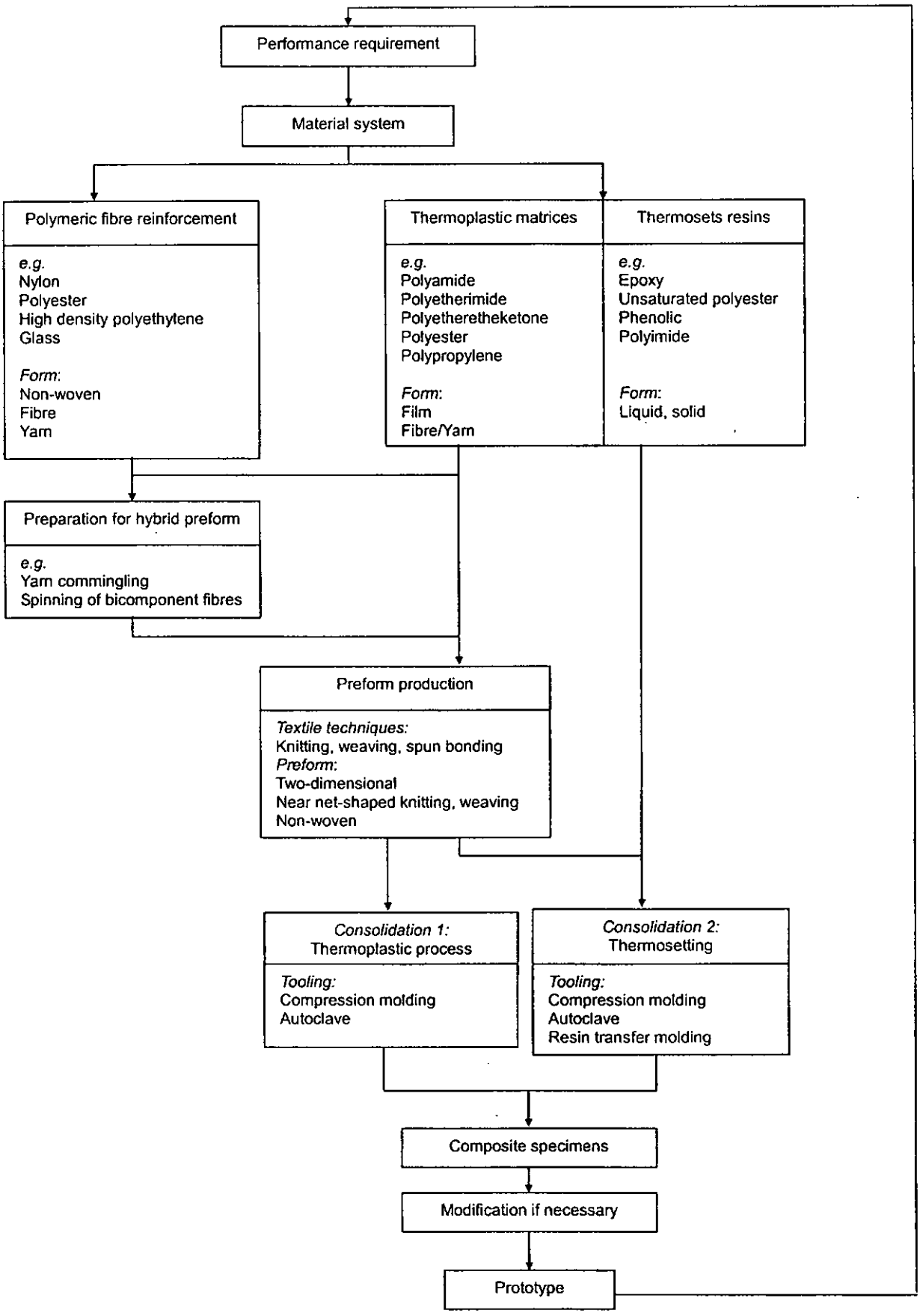

Figure 1.7 Alternative routes of fabricating polymeric cellular textile composites

Table 1.2 Mechanical properties of textile fibres for composite reinforcement (Morton and Hearle, 1993)

Properties	Fibre Type						
	High performance fibres				Conventional textile fibres		
	Polyethylene (High density) Dyneema SK75	Aramid Kevlar 49	S-Glass	Carbon (High-strain) Hysil Grafil	Polyester	Nylon Nylon 6,6 high-density	Polypropylene (Ulstron)
Density (g cm^{-3})	0.97	1.44	2.49	1.8	1.36-1.38	1.14	0.90
Tenacity (N/Tex)	3.5	2.1	1.8	2.1	0.47	0.66	0.65
Initial modulus (N/Tex)	113	80	35	128	10.6	4.4	7.1
Elongation at break (%)	3.6	2.9	5.4	1.7	18	16	17
Tensile strength (GPa)	3.4	3.0	4.6	3.7	-	-	-
Tensile modulus (GPa)	110	115	87.0	230	-	-	-

Both thermoplastic and thermoset polymeric matrices/resins can be used in the composite system. Typical thermoplastic matrices include polyamides, polyester, polyethylene, polypropylene, and polystyrene. Their properties are listed in Table 1.3. Other than considering the material compatibility of the fibre/matrix interface, the matrix system in the polymeric composite should provide optimized toughness so as to facilitate the large plastic deformation. Thermoplastic matrices are usually tougher than thermoset resins, but the former require much higher temperatures and pressures during processing. In contrast, thermoset resins provide easy processing and better fibre impregnation when the liquid resin is used at room temperature. Sometimes the viscosity of thermosets may be reduced to some extent at elevated temperatures for better fibre wetting and impregnation. Examples of thermoset resins are epoxies, phenolics, unsaturated polyester, vinylester, cyanate esters, and polyimides. Unsaturated polyester and epoxies are the most widely used. If flammability should be considered, phenolic resins can be used (Disselbeck and Stahl, 1986). Generally composites made from unsaturated polyester resins have low strength, poor impact performance and high shrinkage during the curing process, while epoxies provide

better performance on chemical and solvent resistance, flexibility, strength and hardness, creep and fatigue resistance and fibre adhesion, depending on the manufacturing conditions. Improvement in resin toughness can be achieved by adding an elastomeric modifier of liquid polymer, such as carboxyl-terminated butadiene acrylonitrile (CTBN). Although the thermoset composite processing is more mature than those for thermoplastics, thermoplastic matrices offer more advantages than thermoset resins in terms of composite properties and performance (Lou, 1991) (Table 1.4).

Table 1.3 The most commonly used thermoplastic matrix polymers and some of their properties

Property	Polypropylene	Nylon 6.6	Polycarbonate	PET
Density (g cm^{-3})	0.9	1.14	1.06-1.2	1.21
Young Modulus (GPa)	1.0-1.4	1.4-2.8	2.2-2.4	2.7
Poisson's ratio	0.3	0.3	0.3	0.3
Tensile yield strength (MPa)	25-38	60-75	45-70	62
Thermal conductivity ($Wm^{-1}{}^{o}C$)	0.2	0.2	0.2	0.2
Coefficient of thermal expansion ($10^{-6}{}^{o}C^{-1}$)	110	90	70	65
Melting Point (°C)	175	264	-	254-259

Table 1.4 Comparison on general thermoset and thermoplastic composites (Lou, 1991)

Material Properties	Thermosets	Thermoplastics
Quality Assurance	Fair	Good
Shelf Life	Poor	Excellent
Toughness	Fair	Excellent
Solvent Resistance	Good	Good
Creep Resistance	Good	Fair
Composite Processing	Slow	Fast
Cost Reduction	Fair	Good
Heat Bondable	Poor	Good

1.2.2.2 Preform Preparation

Reinforcing fibres can be in different forms, including knitted, or woven fibre networks, and non-woven spunbond fabric into cellular shapes. Ko (1997) has suggested that fibre orientations and volume fractions in composites are the key engineering parameters for the formability, matrix impregnation and performance of textile composites.

Epstein (1991) demonstrated near-net-shape structures with knitted or woven T-pipe junction, cone, flanged pipe and domes to produce complex shaped components, and Ramakrishna et al. (2000) described many fully fashioned technologies of knitting for engineering composites. For textile processing, the use of knitted fabrics for composite reinforcement was highly recommended by Kim (1999a) due to the good conformability of fabric without excessive extending the fibre loops. This conformability means that layers of knitted fabric can be stretched to cover the complete component/device surface without the need to cut and overlap sections. In constrast, woven fabrics are comparatively less flexible than knitted fabrics in terms of yarn movement, and the stretching of woven fabrics exert a stretching force directly on the axial fibres or yarns. Therefore, the mechanical shaping of flat knitted fabrics would be more effective and economical to form the cellular structures.

A knitted fabrics can be formed through a row of closely spaced needles on the needle bed which pull loops of yarn through previously formed knit loops. The conversion of yarn into loops can be done either in a horizontal direction (weft knitting) or in a vertical direction (warp knitting).

In weft knitting, there is the feeding of yarn coming into the knitting machine horizontally and this yarn forms a row of knitted loops across the width of the fabric. The weft knitted machines include flat bar machines, circular machines, and staight bar fully fashioned machines. In warp knitting, there are multiple yarns being fed into the machine in the direction of fabric production, and each yarn forms a line of knitted loops vertically in the fabric direction. Usually the warp knitted fabrics can be produced in Tricot and Raschel machines (Gohl, 1988; Spencer, 2001).

Due to the fact that a weft knitted fabric is comparatively more extensible and drapeable than a warp knitted fabric, weft knitted fabrics were selected as reinforcing preforms in this study. Changing the knit architecture can vary the properties of knitted fabric itself quite significantly. The fabric characteristics, such as fabric extensibility, areal weight, thickness, surface texture, etc, can be controlled quite closely. This allows knitted fabric to be tailor-made to suit the particular component being produced. For the fabrication of the knitted textile composites, the weft knitted fabrics, including plain, rib 1x1 and interlocking, are selected. Other complex knitted fabric structures, that may complicate the analysis on the mechanical properties of knitted composites, are out of scope in this study.

Usually, weft knitted fabrics display anisotropic properties. Fabric pre-stretching before composite fabrication has proved an effective method for tailoring the mechanical properties of knitted composites. A number of researchers have improved the strength of knitted composites by pre-extending the knitted fabrics uni-axially or bi-axially. Ramakrishna et al. (1999) reported that the pre-extension of polyester knitted reinforced fabric with polyurethane elastomer composite improved the tensile

strength and stiffness in the pre-extension direction. In addition, Wilde and Ziegmann (1997) reported the composite stiffness becoming more isotropic with the pre-stretching applied prior to the consolidation. This pre-stretching on knitted fabrics can be applied multi-axially without causing fabric folds.

Although knitted fabrics are still not widely accepted in composite industry due to their relatively poor strength and modulus compared to other fibre architectures, such as woven preforms or braided tubes (Verpoest et al., 1997), the mechanical properties of such knitted textile composites may have a profound improvement on mechanical properties (e.g. stiffness, energy absorption) with proper fibre orientation (Chou et al., 1992; Verpoest and Dendauw, 1992; Verpoest and Dendauw, 1993; Wu et al., 1995) and fibre volume fraction (Ko and Du, 1997). The excellent conformability of knits is also an important feature for fabricating relatively non-structural components of complex shape with acceptable mechanical properties. (Ramakrishna et al., 1995; Verpoest et al., 1997; Xue et al., 2002; Lam et al., 2003).

An attempt in the present study is to investigate the possibility of the replacement of knitted fabrics with a commerical available non-woven fabric made of staple filaments entangled in bulk layer (Gioello, 1982; Corbman, 1983), which are usually used in the washable filling of clothing, bedding and furniture. It may be formed either by bonding or interlocking of fibres or both, accomplished by mechanical, chemical, thermal, or solvent means, and a combination thereof. More specifically this kind of non-woven fabric may be formed by needle punching a web of fibres – already formed by cards, garnets or air-laying – which is passing through a machine equipped with groups of specially designed needles (Albrecht et al., 2003). The

needle loom consists of a pad with closely spaced needles, which are forced in the web of fibres to reorient and become entangled to form a cross-laid non-woven fabric at the delivery. The bulk form non-wovens may have a thickness ranging from 0.05 - 8.0 cm or more, without increase in weight. The primarily advantage brought by the non-woven fabric over the knitted fabrics is the elimination of yarn spinning and conversion of yarn into fabric. The production cost of non-woven is much lower than the knits. The fabric is soft and provides good conformability by compression molding into three-dimensional cellular structure. Although the non-woven fabrics generally lack tensile strength, which is usually weaker than in knits, the cross-laid fibre orientation in non-woven fabric may be preferred for the compression through thickness and allows better matrix penetration during the molding process. The cell wall thickness of the molded panel may be kept more uniform than those knitted composites due to high conformability of the bulk form non-woven fabric structure.

1.2.2.3 Consolidation/Curing to Cellular Structure

Generally, two main steps are involved in the processing cycle of the composites: the impregnation of textile reinforcing structure with resin/matrix and consolidation of the shaped polymer fibre network. During consolidation, hardening of the resin/matrix takes place, and bonding is formed between the resin/matrix and fibres in the reinforcement structure. A range of fabrication processes for either thermoplastic or thermoset systems have been demonstrated (Hoechst, 1991; Klecka, 1992; Leclerc, 1993) for molding the textile preforms.

For the thermoplastic material processing, the form of prepreg can be achieved in several ways: co-knitting, co-weaving, forming hybrid yarn during spinning, or film stacking. The co-knitting or co-weaving of two types of fibres can be processed into prepreg so that the fibre and matrix content can be controlled. Another method of combining the reinforcing fibres and the thermoplastic matrix is to produce bicomponent fibres containing two different polymers, in side-by-side or concentric core-sheath arrangement, during the fibre spinning process; or to commingle filament yarns of both reinforcing fibres and thermoplastic matrix fibres as a type of texturing. This pre-mixing reinforcing fibres/matrix fibres can improve the impregnation quality during melting of the thermoplastic matrix, which then spread more evenly between the reinforcing fibres. A further simple method of prepreg preparation is the film stacking process. The thermoplastic film is laminated with the reinforced preforms and consolidated under heat and pressure to fully impregnate the fibres. This process is clean and solvent-free, but requires proper care for the production of a void-free prepreg.

Disselbeck (1994) commented that compression molding seems to be the most feasible technique for fast fabrication of textile composites. He demonstrated a deep-drawable hybrid textile preform being placed into an open mold. The mold is then closed where heat and pressure are applied for a sufficient time until the structure is formed and cured. He suggested that knitted preform is preferred for the deep-drawing process by compression molding.

Compression molding of textile prepreg allows the fabrication of intermediate complexity, such as the grid-domed cellular structure. Other advantages of

compression molding include low production cost, little material waste, good control of fibre-to-matrix volume ratio and void content. As the compression molding technique involves only heat and pressure for molding fabric reinforcement with matrix in a closed mold cavity, it allows a shorter cycle time for the whole pressing process than with thermoset cellular composites, and a one-step process can be achieved as long as the prepregs are put into the mold. High productivity can be achieved and thus, the technique would be economical for the mechanical forming of the shape. However, compression molding of the fibre network may limit the fibre impregnation for some textile structures. Mosleh et al (1998) reported that there was poor impregnation of resin diffusion into the high density fibre arrangement in woven structures where the fibres were compressed together during the consolidation.

For thermoset grid-domed cellular composites, consolidation can be achieved in a one-step or two-step process with or without application of heat and/or pressure for faster polymerization. Zarandi and Youssef (1990) demonstrated a fabrication process, as shown in Fig. 1.8, of conical projected cellular textile composites. A stretchable light-weight fabric is impregnated with resin and the amount of impregnation is controlled by squeeze-off rollers. The impregnated preforms is then cured inside a closed-mold under pressure and a composite panel with conical projections is made. After being cut into the desired size and shape, several panels can be laminated with interface panels made of plastic, metal, foam, paper or fabric. The molded panels can be assembled to reach the desired thickness of the multilayered panel structure to obtain a desired energy absorption level. For the preparation of thermoset resin coated textile composites at a laboratory-scale, the

knitted fabrics can be deformed in a grid-domed mold at elevated temperatures in an autoclave or a hot press machine. Then the heat-shaped preforms were rigidized by coating polyester resin and cured at room ambient condition. The thermoset resins can be in liquid or powder form to be coated onto the fabric before curing. The time for resin curing is long, which normallys take one to several days for resin curing at ambient temperature, unless at elevated temperatures for shortening to about 1 hour. Alternatively, faster curing of the liquid resins can also be achieved by mixing them with other initiators or accelerators. However, more time is consumed for mixing the resin with other activators, diluting solutions or toughening agents before curing, and ventilation is another concern because of gas release during the curing process of these resin mixture.

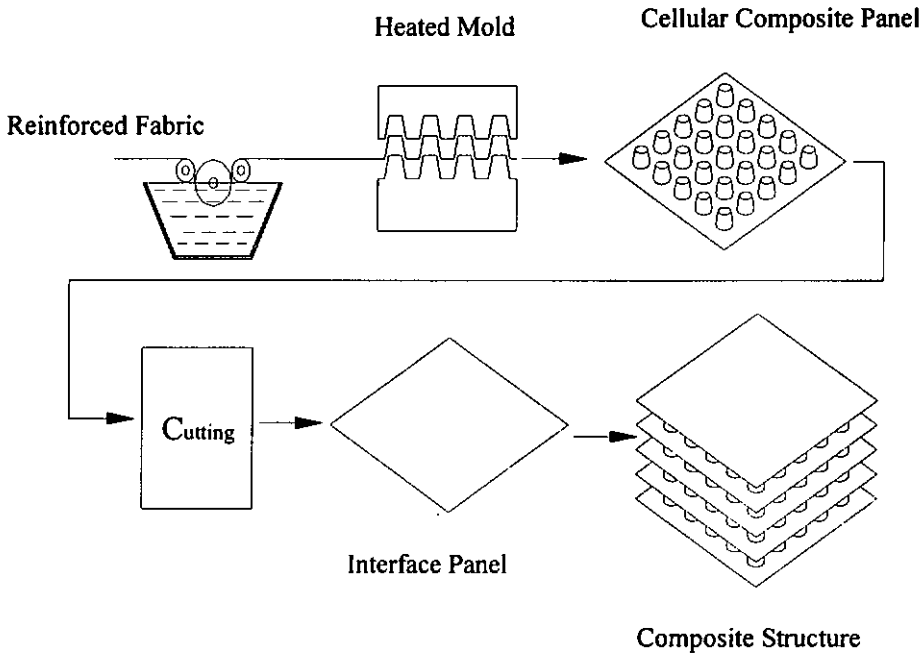

Figure 1.8 Schematic representation of fabrication of conical projected textile composites for energy absorption (re-printed diagram) (Zarandi and Youssef, 1990)

Another thermoset process used for fabricating and manufacturing of the three-dimensional composite components with thermoset materials is illustrated by resin transfer molding (RTM). In this process, a liquid resin is transferred from a reservoir into a three-dimensional closed heated mold. Layers of fabric preforms are placed inside the mold prior to resin injection. The liquid resin is then injected into the mold by pressure and/ or vacuum to wet the preforms and resin curing takes place due to the temperature of the resin and the mold. It has been demonstrated the feasibility of fabricating a three-dimensional glass-fibre fabric reinforced composite by RTM (Gelin et al., 1996). The advantage of this resin injection process is that it allows complex shapes to be made in a single step operation. In addition, the closed mold system of RTM, that enclose the preform, can allow excellent surface finishes and close dimensional tolerances can be obtained if high quality of tooling materials are used. Since the reinforcement is placed in the mold prior to resin injection, improved preform technology is the key issue for developing this fabrication technique to large scale production. It is an ideal technology for the fabrication of high strength/high rigidity parts in medium series production. The RTM process allows the fabrication of the fabric-reinforced composite components in small to very large molding (e.g. car body structure and boat hulls).

Injection molding, also a closed mold process, is common not only in the thermoplastic industry but also in the thermoset industry. This process allows either a thermoplastic or a thermoset system to be injected under high pressure into a closed three-dimensional cavity, which is held at low or high temperature, respectively (Akovali, 2001). It also allows the injection of short fibres with length typically ranging from 1 to 5 mm. A typical injection molding machine that facilitates the

processing of a predetermined amount of thermoplastic matrix to be forced into heated mold cavity, is illustrated in the schematic diagram in Fig. 1.9. The pellets of thermoplastic matrix flow from a funnel-shaped feed hopper into a heated compression cylinder. Most injection molding machines have a reciprocating screw-type barrel that transports pellets through heating stages before the material is injected. The cylinder will be heated up to melt the solid pellets into a viscous liquid that can be forced through the connecting nozzle, sprue, and runners to the gates that lead into the mold cavities. The plunger forces a controlled quantity of material through the injection molded nozzle into the closed mold. The viscous liquid with short fibres injected in the closed mold will form a part of the desired shape. The mold is tightly clamped against injection pressure and is cooled down. After the molded part cools, the mold halves are opened at the mold parting plane, and the parts are ejected by a knockout system.

The injection molding process allows the production of complex shapes in one shot, ranging from only 30 to 60 seconds for the processing time. It also allows net-shape or near-net-shape parts with a much better surface finish, part repeatability and a tight dimensional control ($\pm$ 0.002 inch). It is a high-volume manufacturing process and allows very low labour costs.

Although injection molding is the process of choice for the production of most thermoplastic parts, the process suffers from the following limitations for fabricating fibre reinforced composites:

(1) Usually the fibre types used are the carbon, glass fibres or other stiff fibres with very short fibre length. The attempt to use longer (such as over 5 mm) ductile

fibres may block the injecting nozzles.

(2) The flow of matrix through the nozzles may lead to more pronounced fibre orientation and anisotropic properties than those being processed by compression molding.

(3) This process is not suitable for the fabrication of low-volume parts because of high equipment and tooling costs, such as for the mold part. Thus, changes in the design are not frequently allowed.

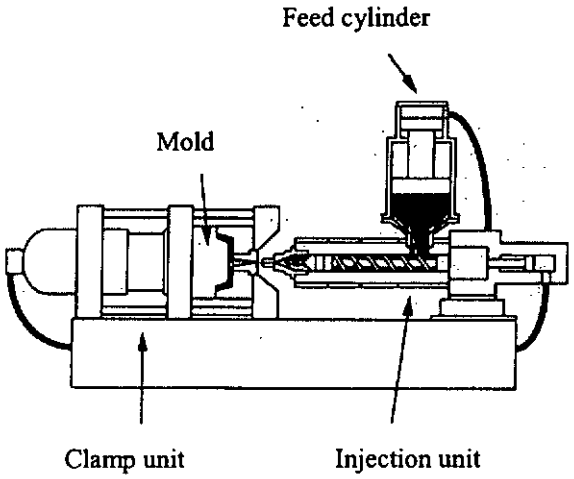

Figure 1.9 Injection molding machine for processing bulk molding materials

1.2.3 Potential Applications

Textile fibre networks with cellular geometry have found many potential applications, such as, for heat insulating textile material (Roysancour, 1965), protective packaging for delicate items, crash helmets, vehicular interior components, medical casts and orthopedic devices (Kim et al., 1999b), bullet-proof vests (Droste, 1986), mattresses or shoe midsoles for athletics shoes (Fig. 1.10) (Kim et al., 1999c), seat cushions in

automobile seats, etc. The cellular structure of these product designs is primarily not for energy dissipation but for providing semi-rigid support and padding. It is because the cells are usually resilient and flexible to recover their original shape after slight compression. It has been illustrated by Romano et al. (2001) that the three-dimensional network can be used as a part of the mattress or cushion layer in an automobile seat cushion in order to improve the pressure distribution capabilities. As the cellular structure is fabricated by projections from the textile fabric structures made of monofilaments or multifilaments, the porous nature of the cellular structure allows good ventilation or breathability to skin. It can be used as an infant mattress to prevent suffocation.

In contrast, the cellular composites designed for energy absorption purposes should be suitably stiff and collapse plastically during energy absorption. Zarandi et al. (1990) reported the adoption of a grid-domed cellular panel from knitted textile preforms to be mounted on a vehicle door as shown in Fig. 1.11. The axial collapse of a grid-domed cellular panel, originally made from foam or honeycomb materials, is able to avoid yielding laterally upon imposition of a force rebound. Several layers of these composite panels with various arrangements, as shown in Fig. 1.12 (a) and (b), were suggested to monitor the energy absorption capacity during its axial collapse of domes. A similar safety protection application of the light-in-weight feature of cellular textile composite materials has been demonstrated for high-energy absorption capacity in cycling helmets (Tao et al., 2003). The emphasis placed on their applications is related to energy absorption at medium and low velocities. Other factors governing the material properties that should be considered are the perspiration and comfort. As the textile fabric structures allow retaining a plurality of

fabric pores in the resulting composites, this type of composite liner allows a certain amount of ventilation.

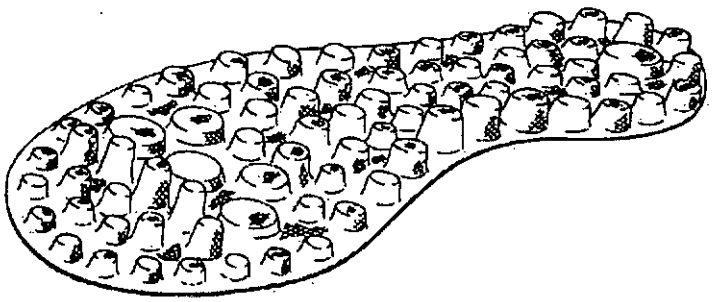

Figure 1.10 Schematic three-dimensional fibre network as light-weight and breathable layer, which provides support and cushioning effect in athletics shoes (Kim et al., 1999c)

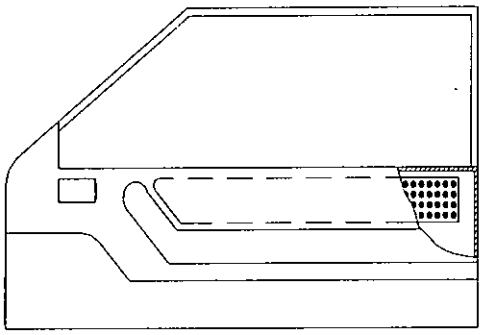

Figure 1.11 Side view of a vehicle door having parts broken away and in section to show the cellular structure for energy absorbing in the arm rest position mounted on the door inner panel (re-printed diagram) (Zarandi and Youssef, 1990)

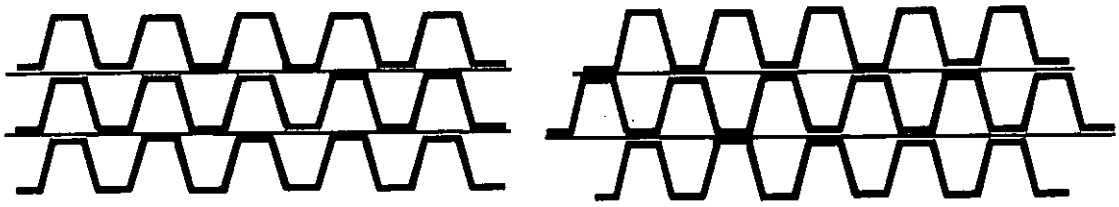

(a) (b)

Figure 1.12 Schematic cross-sections of two proposed arrangements of flat-topped cellular composite panel as an energy absorbing device in arm rest of vehicle door inner panel

1.2.4 Characterization of the Composites

Characterizing the structure and properties of fibres, polymer matrix and composites provides information of the composite performance and its serviceability. The mechanical behaviour of textile composites can be studied in the following scales:

- Macro-scale: larger than 10^{-3} m
- Meso-scale: in the range of $10^{-3} - 10^{-5}$ m
- Micro-scale: in the range of $10^{-5} - 10^{-7}$ m

Macro-scale study of the mechanical properties of a cellular composite may be an assessment of the effective behaviour of a composite material, including unidirectional tensile stress-strain behaviour, compression, shearing, flexural strength, and dynamic impact response. While in the meso-scale or micro-scale study, deformation and damage mechanisms of the composite materials can be examined by observation under optical microscopy or in-situ scanning electron microscopy (SEM).

The determination of the state of stress/strain in structural materials during service has been one of the key issues. Micro-scale study of the stress or strain state of the

reinforcing fibres in the composite may help to guide the material design and manufacture. However, only a few instrumental techniques have been identified as suitable candidates for measuring the fibre stress/strain inside textile composite materials. These are optical or electrical techniques. Comparison of their principles and working criteria regarding to the stress/strain measurement, as illustrated in Table 1.5 (Du et al., 1998; Tao et al., 2000; Zhang and Tao, 2001), are highlighted as follows:

The Fibre Bragg grating sensor (Du et al., 1998) is one kind of fibre optical sensor (FOS), that can be integrated in textile composites. Usually a change in the grating period or refractive index results in a change in the reflected wavelength. Strain variation in a composite structure can be determined through the expansion or contraction of the grating period and through the strain-optical effect. As for conductive textiles being applied as stress/strain sensors, the variation of fabric stress/strain can be determined through the change of resistivity in the clamped region of the conducting fibres/fabric in the circuit. Different from the optical fibre sensor (which requires the FBG sensor to be embedded in the composite structure and connected at the other end to the light source and spectrum analyzer) or the conducting polymeric fibres as electrical resistance 'strain gauge' (which requires the specimen being clamped in the formed electrical circuit), micro-Raman, which is an optical technique, does not require a physical connection with the specimen.

Although both FBG sensor technique and conducting fibres/fabric allow localized stress/strain measurement, Raman microscopy has a highly selective probing area and a spatial resolution of maximum 1 μm with a very low power density. Thus, this

method may appear as an interesting technique to determine the local fibre stress or strain inside composite materials at the microscopic level, provided that the composite matrix is transparent.

Conductive fibre, or yarns or coating embedded in matrix or resin, may affect the conductivity of the composite. FBGs needed to be embedded in the composite structures. In contrast, by using the Raman technique, the reinforced fibres themselves, can be used as strain sensors in the composite materials that they actually reinforce. This phenomenon is due to the macroscopic deformation of the fibre leading to a direct stretching of the covalent bonds along the polymer backbones resulting from a change in the vibrational force constants of the molecular vibrations. Usually, the positions of the Raman bands shift to lower wavenumbers by stretching a single fibre in air on a suitable mechanical tester operating at a low strain-rate. The effect is particularly apparent in crystalline materials for which an applied macroscopic stress can be transferred directly to the atomic bonds. Most reinforcing fibres are crystalline materials and thus have been found to exhibit this effect. The difference between the Raman wavenumbers obtained at each of the strain levels and that of the free-standing fibre represents the Raman band shift. The magnitude of the Raman wavenumber shift can be related to the external stress or strain, thus making stress/strain measurements possible.

Similar to the fibre material used in FBG or conductive polymers or other conductive fibres, many high performance polymeric fibres, such as substituted polydiacetylene (Galiotis et al., 1985; Zwagg et al., 1987; Young et al., 1991), poly(p-phenylene benzobisthiazole), PBT (Day et al., 1987; Young et al., 1990), and carbon, which

have been successfully studied using the Raman technique, are brittle and cannot undergo large deformation as in textile structure. Usually they are highly crystalline materials, which lead to a brittle feature and exhibit significant fibre strain sensitivity. In particular, it has been demonstrated that aramids or UHMWPE fibres, exhibiting strong Raman signals, are flexible to be integrated as a knitted structure in composites. The strain detected by Raman shifts can be used in single fibre pull out testing, and detecting crack bridging. Another important issue regarding composite micromechanics is the distribution of fibre stresses/strains, such as the residual stress/strain raised from composite fabrication, or the embedded fibre stress/strain raised during an external loading of a composite part. An illustration of strain mapping of composites under tensile loading has been given by Young et al. (1996) showing that the periodic distribution of fibre strain being mapped along a plied yarn in both plain weave and four-harness satin weave aramid/epoxy textile composite subjected to different levels of strain in the horizontal direction, as shown in Figs. 1.13 and 1.14. With a motorized x-y stage motion attached to the Raman microprobe, the stress/strain distribution on two-dimensional composites can be further mapped. A measurement of fibre stress concentration around a hole (Fig. 1.15) was conducted in a uni-directional aramid/epoxy composite subjected to an axial strain.

Having compared various instrumental techniques for stress or strain measurements in textile composites, especially for detecting the distributive fibre strains in knitted reinforcement, Raman microscopy is ideal for assessing interfacial strength and for mapping fibre stress/strains in a composite panel when subjecting an external mechanical loading.

Table 1.5 Potential usage of sensors in polymeric fibre-reinforced composites for stress/strain measurement (Du et al., 1998; Tao et al., 2000; Zhang and Tao, 2001)

Technique	Fibre Bragg Grating	Conductivity		Micro-Raman
Principle	Bragg Wavelength shift with local strain	Change of resistance with strain		Wavenumber shift with fibre strain
Detector source	Laser	Ohmmeter		Laser
Detecting system attachment on sample	✓	✓	✓	×
Detecting area	Global/Local/ Distributive Length of grating: 2 mm – 20 mm	Global only		Global/Local/ distributive Probing area: ~1-2μm
Material	Single mode optical fibre	Conductive fibre/yarn	Conductive coating	Polymeric fibre
Examples	Silica-based fibres Polymeric fibres (e.g. PMMA)	Organza Stainless-steel Copper Metal coated fibres Polymeric fibres (e.g. doped PBZT, PPTA)	In powder form	Aramid UHMWPE
Strain range	~1% (silica based) ~4-6% (polymeric fibres)		-	3-4%
Fibre flexibility	× (silica based)	✓	-	✓
Sample preparation	Complex	Moderate		Easy and fast

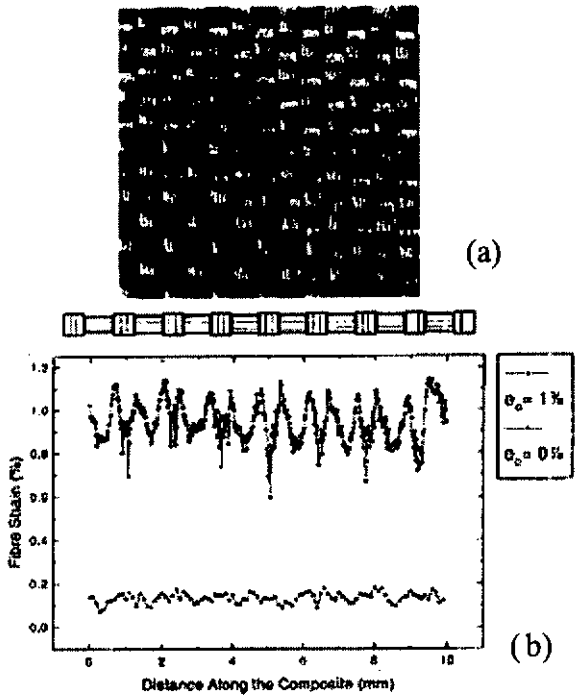

Figure 1.13 (a) Optical micrograph of the Kevlar/epoxy plain weave composite, and (b) the measured of variation of axial fibre strain with distance along the center of the repeat pattern, at two levels of composite strain in the horizontal direction (Young, 1996)

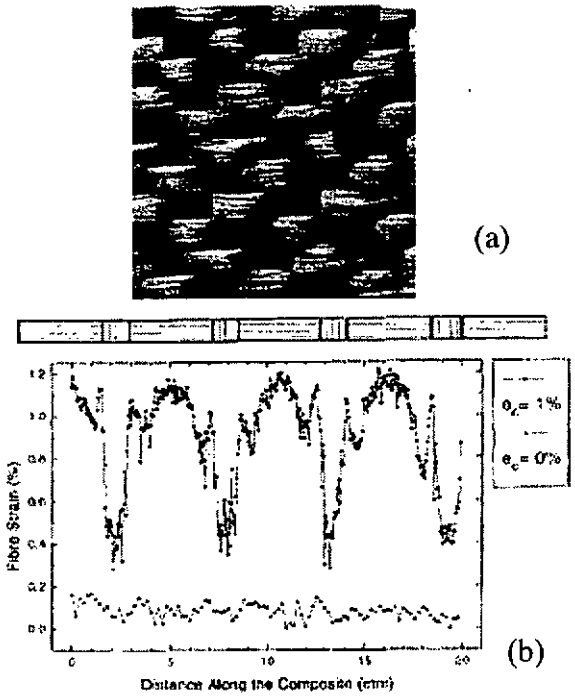

Figure 1.14 (a) Optical micrograph of the Kevlar/epoxy four-harness stain weave composite, and (b) the measured variation of axial fibre strain with distance along the center of the repeat pattern, at two levels of composite strain in the horizontal direction (Young, 1996)

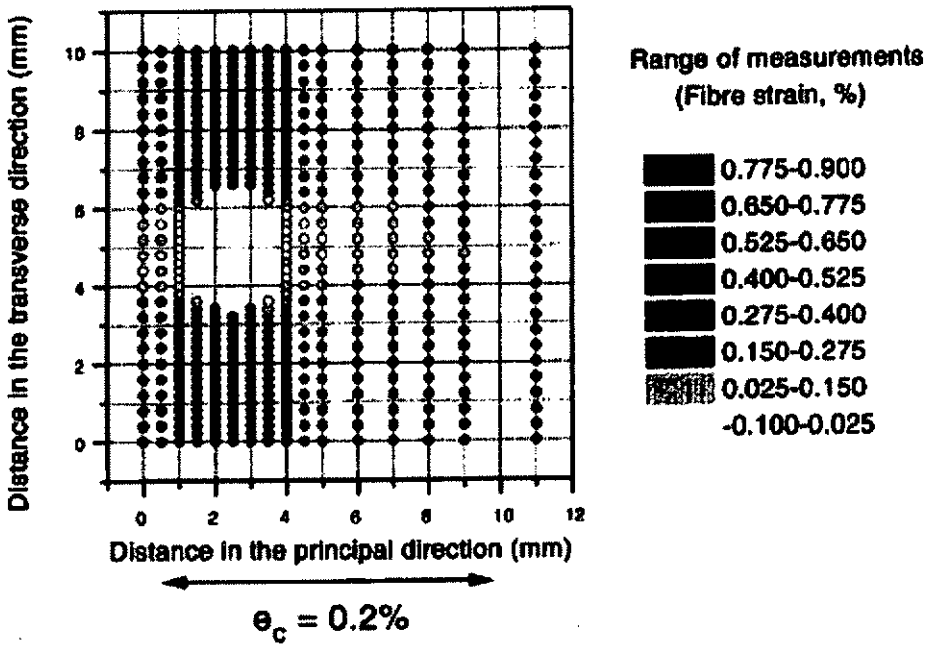

Figure 1.15 Axial fibre strain distribution for a Kevlar 49/epoxy unidirectional composite containing a 3-mm diameter hole subjected to an axial strain of 0.2% in the direction indicated (Young, 1996)

1.2.5 Theoretical Study of the Knitted Composites

Theoretical analysis of a reinforced structure is usually done to generate their mechanical behaviours, such as:

- to predict the stiffness and strength of the composite material
- to assess the overall stress/strain distribution within a structural component
- to simulate the structural deformation

Due to the anisotropic properties and the ability of knitted fabric to develop a high degree of deformability by its loop structure, theoretical study of the deformation behaviour of knitted fabric reinforcement would help to understand the contribution of large deformation to the energy absorption of cellular composites.

There are generally two approaches for modeling the performance of knitted composites: (1) Numerical method such as Finite Element Modeling (FEM) and (2) Micromechanical analysis. All of the models that have been developed for knitted composites start by first describing the representative volume element (RVE) or a repeat unit of the knitted architecture. Currently most of the work has focused on plain knitted structures, while determination of RVE of other knit architectures is often time consuming and difficult to measure.

An FEM model to predict the deformation and mechanical properties of a plain knitted fabric structure was demonstrated by Araujo et al. (2003). The simulation of tensile deformation of plain knitted fabric is achieved by simplifying the knitted loops as a 2D hexagonal structure constructed by non-linear truss elements. It is a simple approach for predicting the load-extension behaviour of a knitted fabric when it is under tension in one, two or multi directions. Further it may also be used to simulate the plain knitted fabric being deformed on a spherical surface, which assesses the deformability of the fabric during composite molding.

Another approach by micromechanical analysis is considered as the easier and more practical means of modeling knitted composites. The mechanical properties of knitted composites depend on three criteria: properties of constituent materials, fibre volume fraction and knit loop architecture, of which the last is the most critical. Leaf and Glaskin (1955) developed an analytical model to describe the geometry of a plain weft knitted fabric using three geometric parameters, i.e. fibre yarn diameter, d(cm), number of wales per unit length, w(loops/cm), and number of courses per unit length, c(loops/cm). This model has been extensively used by Ramakrishna and

Huang et al. (1997) in their studies for the prediction of the stiffness and strength behaviours of plain weft knitted fabric composites.

A basic unit cell of the plain knitted loop shown in Fig. 1.16(a) can be divided into four identical sub-cells. A three-dimensional representation of a sub-cell is shown in Fig. 1.16(b).

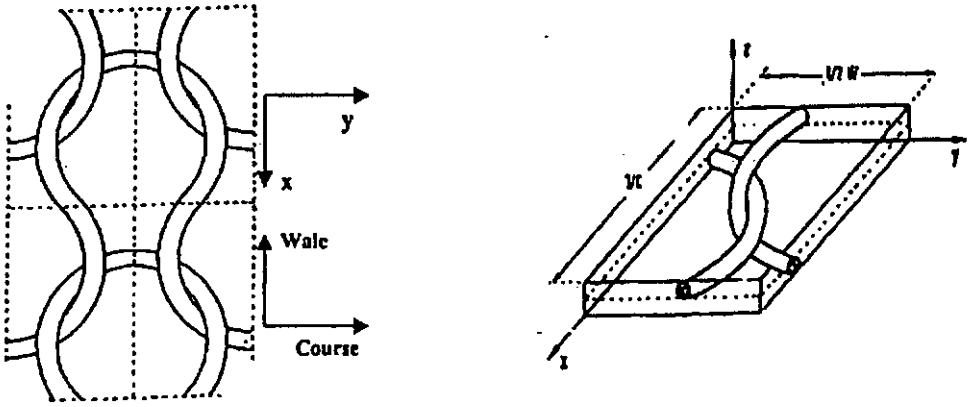

(a) (b)

Figure 1.16 Schematic diagrams of (a) unit cell and (b) RVE of the composites

This sub-cell, which contains two yarns crossing over each other, is taken as the RVE of the composites, as shown in Fig. 1.16(b). For micromechanical analysis purposes, each yarn is assumed to consist of a number of infinitesimal segments, and it is important to know the orientation of each yarn segment in the RVE. The coordinates of a point on the first yarn in the unit cell are determined from (Leaf, 1955; Ramakrishna, 1997) :

$$x = ad(1-\cos\theta)$$
$$y = ad\sin\theta$$
$$z = \frac{hd}{2}\left(1-\cos\left(\pi\frac{\theta}{\phi}\right)\right) \qquad (1)$$

where h is a constant representing the maximum height hd of the central axis above the plane of the fabric. The parameters a, h and φ in Equations (1) are determined from the following formulae:

$$a = \frac{1}{4wd\sin\varphi}$$

$$\varphi = \pi + \sin^{-1}\left(\frac{C^2 d}{\left[C^2 + W^2(1-C^2d^2)^2\right]^{1/2}}\right) - \tan^{-1}\left(\frac{C}{W(1-C^2d^2)}\right)$$

$$h = \left[\sin\left(\pi\frac{\psi}{\varphi}\right)\sin\left(\pi\frac{\phi}{\varphi}\right)\right]^{-1}$$

$$\psi = \sin^{-1}\left(\frac{2a}{2a-1}\sin\varphi\right)$$

$$\phi = \cos^{-1}\left(\frac{2a-1}{2a}\right)$$

Having described the RVE, a simple approach to theoretically estimate the stiffness of a plain weft knitted fabric reinforced composite was reported by Rudd et al.(1990). It is known as Krenchel's model, which uses a combination of the rule of mixtures and a reinforcement efficiency to describe the elastic modulus.

$$E_c = \eta V_f E_f + V_m E_m \qquad (2)$$

$$\eta = \frac{1}{L}\int_0^L \cos^4(\alpha)dL \approx \frac{1}{L}\sum_{i=1}^{M} L_i\cos^4(\alpha_i) \qquad (3)$$

where E_f and E_m are Young's moduli of the fibre and matrix, respectively. V_f and V_m ($=1-V_f$) are the volume fractions of the fibre and matrix in the composites. E_c is Young's moduli of the composites in the loading direction. L is the total length of the yarns in the RVE, and α_i is the inclined angle of a considered yarn segment L_i with the loading direction, and M is the total number of yarn segments. However, the predicted value of the Young's modulus in the wale direction is generally lower than experimental values and the one-dimensional approach limits its ability to predict the full set of elastic constants.

One of the micromechanics models, called the Bridging Model developed by Huang (1999), has the capability to model the stress-strain behaviour of the composite up to failure. It is worth highlighting a planar elasto-plastic response (Huang and Ramakrishna, 2000) derived from the model which can be used to describe the stress states in the constituents in the knitted textile composites when the composite is subjected to a planner load only.

Another related theory derived from the model is called the plastic hardening theory, which is used to describe the plastic behaviour of both the fibres and matrix, assuming that the fibres used undergo isotropic hardening only during a plastic deformation. The general Prandtl-Reuss theory is applied to do this (Adams, 1974).

The modeling approach highlighted above has demonstrated a promising ability for the prediction of the mechanical performance of knitted composites. It may lead to an easy approach for our micromechanics study of knitted composite material undergoing large plastic deformation.

1.3 Brief Summary and Purpose of the Study

1.3.1 A Brief Summary

It has been demonstrated that the grid-domes projected from knitted fabric as cellular textile composites are an effective structure to obtain a high specific energy absorption capacity. Thoughtful experimental and analytical investigations of the deformation mechanism on the cellular composite have shown that membrane deformation and bending along the plastic hinges on cells dominate the contribution of energy absorption when the cells collapse. Material characterization of the

composites has been conducted in multiple scales. Raman microscopy has been demonstrated to be effective in determining the fibre stress/ strain or interfacial shear strength (*IFSS*) profile in experiments including single fibre pull out in model composites, and crack bridging in unidirectional composite or woven composite structure. However, mapping of fibre strain on a knitted loop during composite deformation has not been done so far.

Various fabrication routes for cellular textile composites have been investigated. The curing time of thermoset cellular textile composites in the previous study is long. Alternatively faster curing the liquid resins can be achieved by mixing the liquid resins with other initiators or accelerators. Ventilation is another concern because of gas release during the curing process of these resin mixture. An addition of expensive toughening agents in the epoxy resins is also necessary in order to tailor the material properties. In contrast, the thermoplastic method involves heat and pressure for molding the fabric reinforcement with the solid matrix in a closed mold cavity, taking shorter processing time than the thermosets. Therefore, our further investigation in the present study will focus on fabricating a cellular textile composite with thermoplastic matrix in a simple, cost-effective and clean processing, as well as leading to better performance than have previous composite materials.

Weft knitted fabrics as composite reinforcement exhibit good mechanical performance and excellent conformability into three-dimensional shapes without folds. In the previous study, weft knitted nylon fabric has also proven itself a promising candidate for shaping into grid-domed cellular form and for achieving a high energy absorption capacity. However, a further consideration is the use of an

inexpensive, light, and highly compressible non-woven fabric as reinforcement that have high conformability as good as the weft knitted fabrics, skipping the yarn spinning and textile processing such as knitting, would also bring about further reduction in the material and production costs.

Previous studies have identified the optimized geometrical dimensions of the grid-domed cellular structure which are used in the present study. Furthermore, the mechanism of energy absorption for the isotropic non-woven reinforced composites should be studied.

Potential uses for this cellular textile composite structure in energy absorbing components or devices include door members for automobiles or safety helmets. Other potential applications include semi-rigid supports in shoe liners, padding or cushions.

1.3.2 Objectives

This thesis presents a systematic multi-scale study of the mechanical behaviours of thermoplastic cellular textile composites for high specific energy absorption capacity, with the following objectives:

1. To fabricate thermoplastic cellular textile composites from knitted and non-woven fabrics by compression
2. To characterize the energy-absorption behaviour of the cellular composites reinforced by knitted and non-woven fabric reinforcements under quasi-static

compression and dynamic impact conditions, in which various material factors, such as fibre selection, fibre volume fractions and fibre architecture, are studied;

3. To characterize the mechanical properties, mechanisms of energy absorption and predict theoretically energy-absorption capacity of the cellular composites with isotropic non-woven fabric reinforcement;
4. To measure the tensile properties of knitted composites fabricated from various knitted structures and identify the deformation mechanisms of knitted textile composite in micro-scale by tensile loading with in-situ SEM observation;
5. To investigate the micromechanics of in-plane knitted textile composite, including fibre strain distribution, interfacial strength and propagation of deformation with the applied loading of unidirectional single short PET fibre embedded in PP matrix dog-bone shaped model composites by means of Raman microscopy;
6. To further measure the strain distribution in a single fibre loop by Raman mapping and theoretically predict the fibre strain in the knitted loop with the knitted composite under stretching at different levels and compared with the experimental results.

1.4 Thesis Outline

The thesis consists of seven chapters.

Chapter 1 provides a general introduction to the concept of cellular textile composites. The chapter begins with a description of the development of the composite material, the manufacturing process, further determination of the micromechanics of the material and micro-mechanical models that can be potentially used to analyse theoretically the mechanical properties of knitted composites. The

current and potential applications of cellular textile composites are also given. Relevant disciplinary areas that cover related knowledge have led to identify the knowledge gaps, hence to determine the objectives of the research project.

Three-dimensional cellular textile composites are investigated in Chapters 2 and 3, respectively. The energy absorption capacity of various cellular composites with different fabric reinforcements are compared in Chapter 2. The effects of various parameters on energy-absorption capacity and the deformation mechanisms of cellular textile composites are examined. The comparison among the resultant cellular textile composites is presented in terms of energy absorption capacity, formability and cost. This chapter identifies the potential of using non-woven fabric reinforcement to achieve similar or even better performance than the knitted cellular composites. Thus, Chapter 3 extends the study of cellular composites to non-woven fabric reinforcement, in which material properties of the non-woven composites are assessed, observation of deformation mechanism and a model for determining the energy absorption capacity of the isotropic materials are presented.

The in-plane mechanical properties of the knitted composites and pure materials are presented in Chapters 4 to 6. The in-plane tensile behaviour of various material systems, the deformation mechanisms of the knitted composites observed by SEM are investigated chapter 4. The attempt of using conventional fibres such as single PET fibre embedded PP matrix dog-bone shaped composite by means of Raman microscopy is described in Chapter 5. Limitations of the instrucment and the method are discussed. Micro-Raman technique is presented for the study of the UHMWPE/LDPE composite system in Chapter 6. The fibre properties and fibre

strain distribution in embedded UHMWPE fibre loop are examined. A thoretical model of a single fibre loop in knitted textile composites is developed for predicting the fibre strain under different levels of composite stretching.

Chapter 7 summarizes the major findings of the study, proposes the potential application of these cellular composites and discusses the future work in the area of concern.

CHAPTER 2

COMPARISON OF ENERGY ABSORPTION CAPACITY OF COMPOSITES WITH DIFFERENT REINFORCEMENTS

2.1 Introduction

A previous study (Xue et al., 2000) has demonstrated the effectiveness of the flat-topped grid domed cellular composites made from thermoset matrix. However, thermoplastic composites may offer more advantages in cost and performance as reviewed in chapter 1. In this chapter, various thermoplastic composite materials in flat-topped grid dome cellular structure are fabricated and their potential use for energy absorption is examined. Their energy-absorption behaviour and mechanism were compared under quasi-static compression and impact conditions. The effects of fibre volume fraction, fibre type and fibre architecture on the energy absorption capacity are investigated. The cell recovery after impact is also studied. Material performance, formability and fabrication cost are also compared among the thermoplastic composite reinforcement and matrix materials.

2.2 Fabrication of Cellular Composite Samples

2.2.1 Material Systems

The material systems include (1) PET knitted /PP matrix, (2) UHMWPE knitted/LDPE matrix, and (3) highly compressible PET non-woven/PP matrix that were fabricated by compression molding technique, whilst (4) pure LDPE and pure PP were fabricated by injection molding for comparison.

The textile reinforcements include highly stretchable weft knitted fabrics made of either PET or UHMWPE multi-filament yarns and deformable PET non-woven fabrics. There are three basic weft-knitted structures: plain, rib 1x1 and interlock, and one non-woven PET fabric being examined, as illustrated in Fig. 2.1. The conformability of these fabric structures allows themselves to be molded in the grid-domed cellular structure. Material properties of the knitted yarns are listed in Table 2.1 and specifications of the knitted fabric reinforcements are listed in Table 2.2, respectively. When sourcing the PET and UHMWPE multi-filament yarn for producing the fabric specimens, it was difficult to obtain both in similar yarn size, as seen in Table 2.2. It is expected that both of the fibre diameter and yarn size, which relate to the total surface area, may affect the interfacial strength between the fibre/matrix. It is also expected that the fibre diameter may have effect on the impact performance of the composite when the diameter is large. The high stiffness of such fibres would also make it difficult to form the fibre loop shape of the yarn bundle. Although there is some difference in linear density of both PET and UHMWPE multi-filament yarns for knitting the fabrics, the fibre diameters of both yarn bundles being measured under microscope are in same range of 20-30 microns. Therefore, it is expected that the difference in yarn linear density would have minimum effect on the comparison of the energy absorption behaviour of both material systems.

The preparation procedures of the fabric reinforcements are described as follows.

PET/PP Knitted Composites

Two types of continuous filament yarns were used to produce the fabric preforms, i.e. polypropylene (PP) and polyethylene terephthalate (PET). Two types of interlock weft-knitted fabrics were produced from PP and PET filament yarns on V-bed

knitting machines (SHIMASEIKI) with different gauges. The blending ratio was calculated as a ratio of linear density of PP to PET continuous filament yarns in the fabrics.

UHMWPE/LDPE Knitted Composites

Commercial gel-spun ultra-high molecular weight polyethylene (UHMWPE) continuous filament yarn of 88 Tex (Dyneema SK75 supplied by DSM) was used to produce interlock knitted fabrics on the 12 gauge V-bed knitting machine (SHIMASEIKI). A commercial pure LDPE film with a thickness of 0.06 mm was used as a thermoplastic matrix material of the knitted fabric composites. The UHMWPE/PP knitted composites was fabricated by laminating the fabric and the matrix films for compression molding.

PET/PP Non-Woven Composites

A commercial needle-punched PET non-woven fabric of 200g/m^2 and polypropylene films were used as composite reinforcement and matrix, respectively. Each fabric preform in 20 x 20 cm^2 was sandwiched between layers of thermoplastic PP matrix films and then put for compression molding. The number of non-woven fabric layers and PP matrix films for molding the composite depended on the fibre volume fraction required.

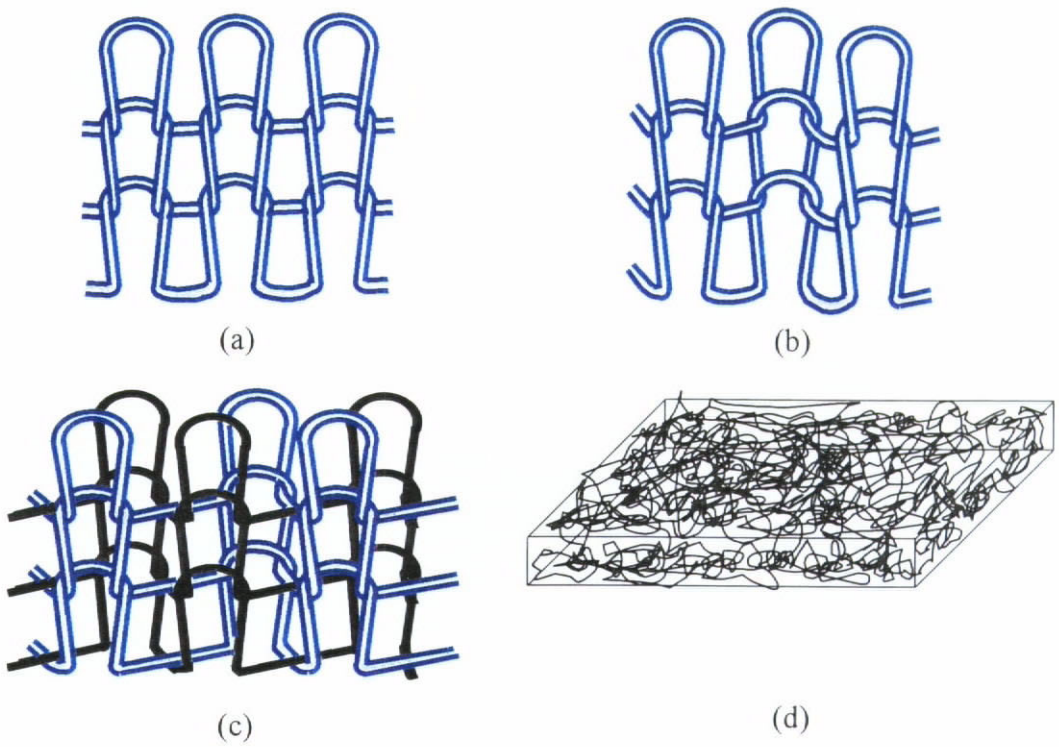

Figure 2.1 Basic weft knit structures, (a) plan, (b) rib 1x1 and (c) interlock 1x1, and (d) a non-woven structure

Table 2.1 Fibre properties for knitting fabric reinforcements

Fibre Type	Testing Method Used	Young's Modulus (GPa)	Tensile Strength (GPa)	Failure Strain (%)
PET	ASTM D3822-96	13.00	0.98	19.00
UHMWPE	ASTM D2256-97	103.64	3.05	5.68

Table 2.2 Specifications of knitted fabrics for composite fabrication

Fabric components	Fabric structure	Machine gage (needles/inch)	Yarn Tex (g/1000m)	Loop density		Loop length (mm)	Tightness factor
				Wales/cm	Courses/cm		
UHMWPE	Plain	12	88	5.1	4.2	8.9	10.5
UHMWPE	Interlock 1x1	12	88	5.6	4.3	9.4	10.0
PET	Interlock 1x1	5	140	4.2	5.0	11.6	10.2
PET	Interlock 1x1	12	140	7.0	6.4	8.0	14.8

2.2.2 Consolidation Process

The cellular textile composites were made in a two-step process by using a compression molding machine (a hydraulic press, Model TMP) as shown in Fig. 2.2. Flat thermoplastic composite panels of various fabric reinforcements in 200mmx200mm were first obtained by compression molding and further molded into three-dimensional composite structure. Figure 2.3 shows a schematic diagram of hot pressing the fabric panel that was sandwiched between two squared steel plates, thickness and dimensions of the resultant composite panel being controlled by a molded frame. The prepreg was first preheated for 10 min. without adding pressure in order to release any moisture in there. The pressure was then raised to approximately 7 MPa at a pressing temperature of 180 °C for the PET/PP composite system or 130 °C for the UHMWPE/LDPE composites. Before further raise to a maximum pressure of 11 MPa, the pressure was abruptly reduced to zero to release air trapped in the fabric panel so as to remove voids from the composite. The samples were then cooled from the pressing temperature to 30 °C in 15 minutes under pressure. The whole pressing process took 38 minutes. Details of the variation of the hot-press parameters in the consolidation process are illustrated in Fig. 2.4.

The prepared flat composite samples were further softened in an oven at a softening temperature, which was below the melting point of the matrix material to produce cellular composite samples. The softened composites were further deformed in a pre-heated grid-domed compression mold, two mold plates containing 25-domes as shown in Fig. 2.5, to form the grid-dome cellular samples by compression molding with a short curing cycle. Schematic diagram in Fig. 2.6 shows the dimensions of a grid-domed cellular structure which possesses optimized geometry in the previous

study (Xue et al., 2000). The fillets were considered on both top and bottom of each cell to reduce high peak load. Dimension details of the cellular mold are shown in *Appendix* 2.1.

The grid-domed cellular samples made of pure PP and LDPE materials were prepared by injection molding. These samples have the same dimension as described in compression-molded samples. Further modification in thickness on the injection mold was made to produce thinner PP samples at 0.8 mm. Table 2.3 lists the specifications for all the produced cellular composite samples and pure cellular materials.

Figure 2.2 A Hydraulic Press Machine (Model TMP)

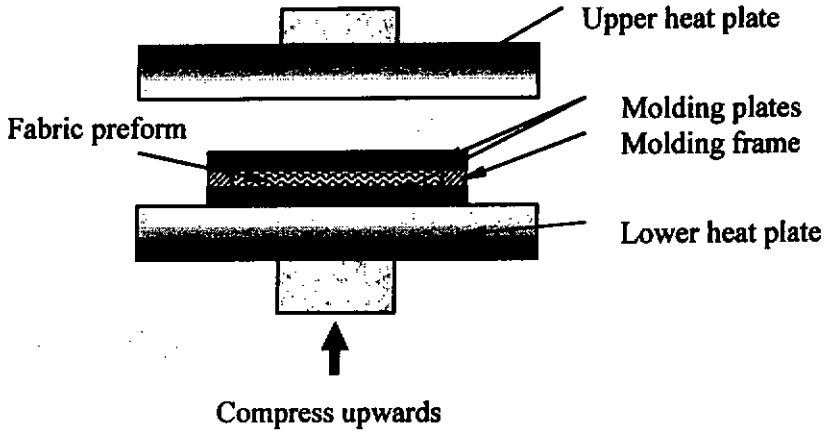

Figure 2.3 Schematic diagram of composite consolidation by a hydraulic press

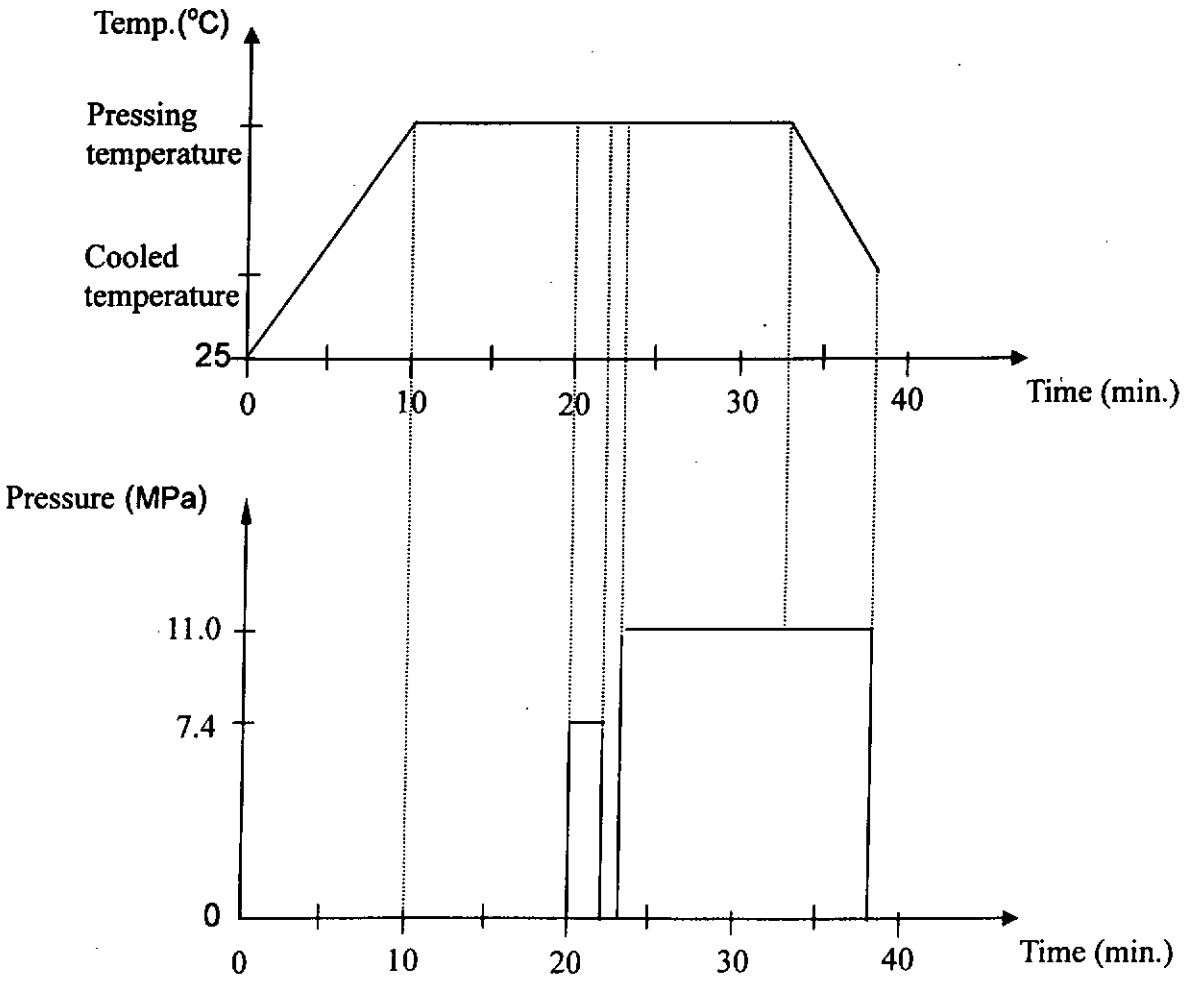

Figure 2.4 Consolidation process of thermoplastic composite fabric preform

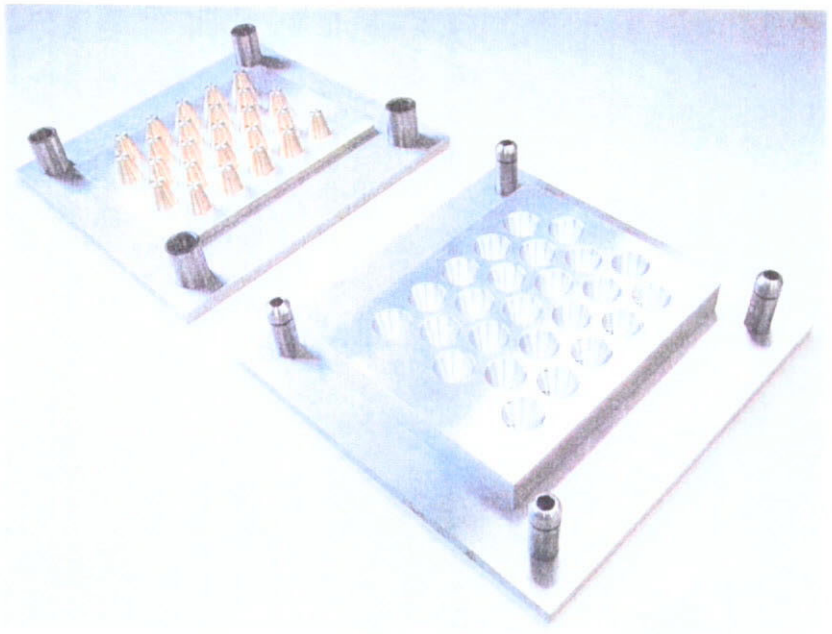

Figure 2.5 The compression mold for molding 25-domes of flat plate of cellular textile composites

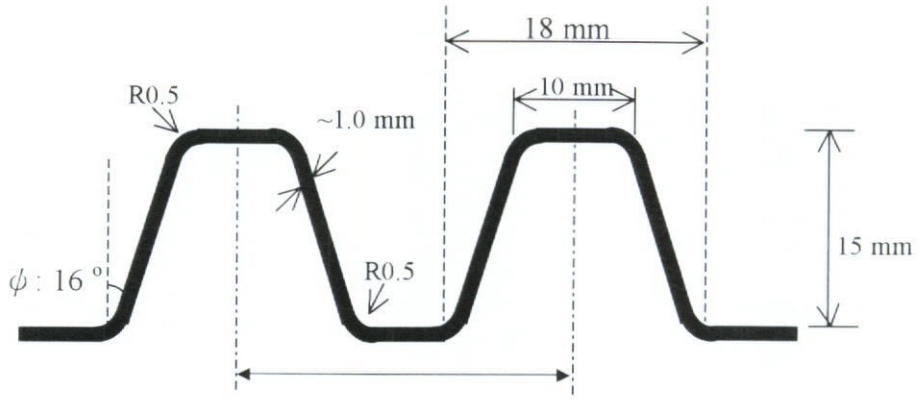

Figure 2.6 Schematic geometry of a grid-domed sample

Table 2.3 Specifications of cellular textile composites

Sample code	Material	Fabric structure	Sample weight in 11 x 11cm^2 (g)	Fibre volume fraction	Measured cell wall thickness (mm)	Equivalent cell wall thickness (mm)
PE12G_Plain	UHMWPE / LDPE	Plain knit	14.28	0.16	0.92	0.76
PE12G_Int	UHMWPE / LDPE	Interlock knit	15.63	0.28	1.02	0.81
PET5G_Int	PET / PP	Interlock knit	22.87	0.38	1.04	0.74
PET12G_Int	PET / PP	Interlock knit	18.27	0.45	1.01	0.94
PETfv1_NW	NWPET / PP	Non-woven	14.76	0.14	1.00	--
PETfv2_NW	NWPET / PP	Non-woven	16.26	0.24	1.00	--
PETfv3_NW	NWPET / PP	Non-woven	17.33	0.38	1.00	--
LDPE	Pure LDPE matrix	--	21.29	0	1.09	--
PP_1.15mm	Pure PP matrix	--	20.87	0	1.15	--
PP_0.8mm	Pure PP matrix	--	18.67	0	0.80	--

2.3 Quasi-static Compression and Impact Tests

The UHMWPE/LDPE knitted, PET/PP knitted and PET/PP non-woven fabric reinforced cellular composites, pure LDPE and PP cellular samples were tested under quasi-static compression and impact conditions. Specimens each containing four conical cells were used for quasi-static compression test and specimens with twenty domes were tested under impact conditions. All specimens were weighted before tests. The quasi-static compression tests were carried out on a Universal Material Tester with a constant loading speed of 5 mm/min. The impact tests were conducted on a GRC8250 *Dynatup* Drop Weight Impact Tester in Structural Dynamics Laboratory in The HKUST, as shown in Fig. 2.7. The mass of a drop weight was either 3.85 kg or 6.61 kg including a plate striker of 120mmx20mmx12mm, which was normal to the plane of the samples, whilst various impact velocities (3.5 m/s, 4.7 m/s, 6.0 m/s) were used by adjusting the height of the drop weight and the air pressure of the pneumatic assistance. Specimens were put on the supporting base of the testers and were compressed or impacted by a flat steel plate.

Figure 2.7 The *Dynatup* Drop Weight Impact Tester

2.4 Energy Absorption Capacity of Grid-Domed Cellular Textile Composites

2.4.1 Effect of Cell Wall Thickness

Typical load-displacement curves of PET/PP and UHMWPE/LDPE composites are shown in Figs. 2.8 (a) and (b). All the samples were compressed down to approximately 70 % of their original cell height. It is observed from the figures that the knitted reinforced composites in both material systems exhibit low levels of energy absorption capacities when compared with those pure materials and non-woven samples. The energy absorption capacities per unit weight of all the cellular samples are also given in Table 2.4.

The results can be interpreted as follows. The total volume of the cellular structure (V_T) in a 20-domes area with a mold cavity with a thickness of 1.0 mm comprises the volumes of fibre (V_f), matrix (V_m) and void (V_v) during forming the cellular structure.

$$V_T = V_f + V_m + V_v \tag{2.1}$$

The fibre and matrix volumes are given during fabrication of the flat panel of knitted composite samples. When the flat knitted composite panel is deformed into a cellular structure, the knitted reinforcement is stretched to form voids across the composite thickness, assuming there is no matrix splitting from the mold cavity. Then, an equivalent cell wall thickness (t_e) of the composites having a volume in the molded cellular structure that is occupied by the fibre and matrix only, can be estimated as follows.

$$t_e = \frac{V_T - V_v}{V_T} t \tag{2.2}$$

where t is the nominal thickness of the cell wall.

Thus, the equivalent cell wall thickness of the knitted composites produced by a mold with 1.0 mm thick was always less than t=1.0mm. During fabricating the non-woven composites, the cell wall thickness of 1.0 mm was achieved by adding excessive matrix films during laminating the non-woven fabric in order to impregnate into the fibre mat and fully occupy the mold, while excessive matrix would split out the compression mold. Pure material was fabricated by injection molding and the cell wall thickness was kept more uniform. Although both pure materials were produced from the same injection mold, their little difference in wall thickness was mainly due to different polymer shrinkage during cooling. Both the measured and the equivalent cell wall thickness of the cellular composite samples can be referred to Table 2.4.

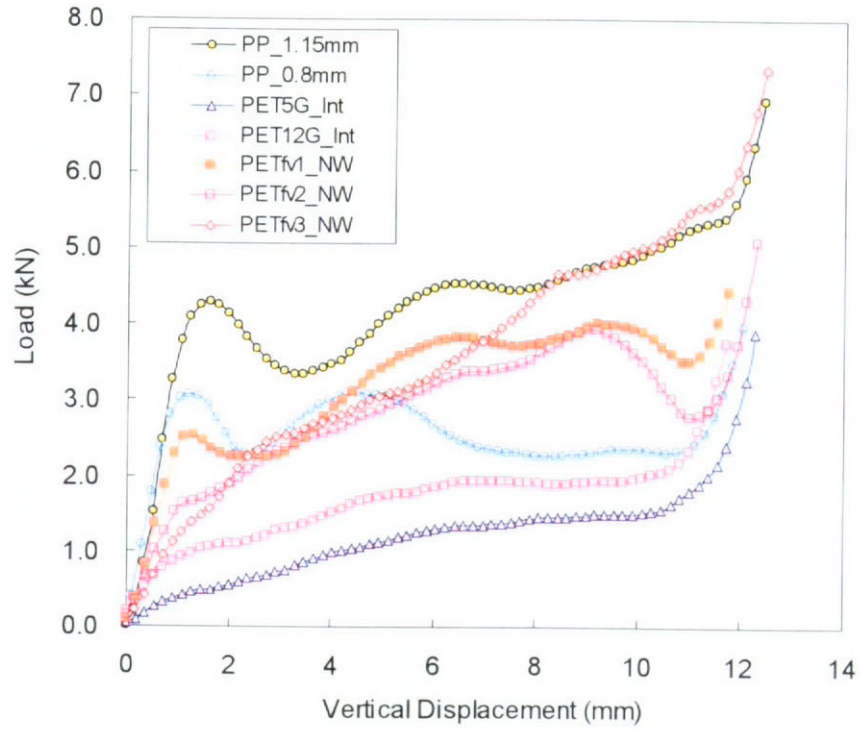

(a)

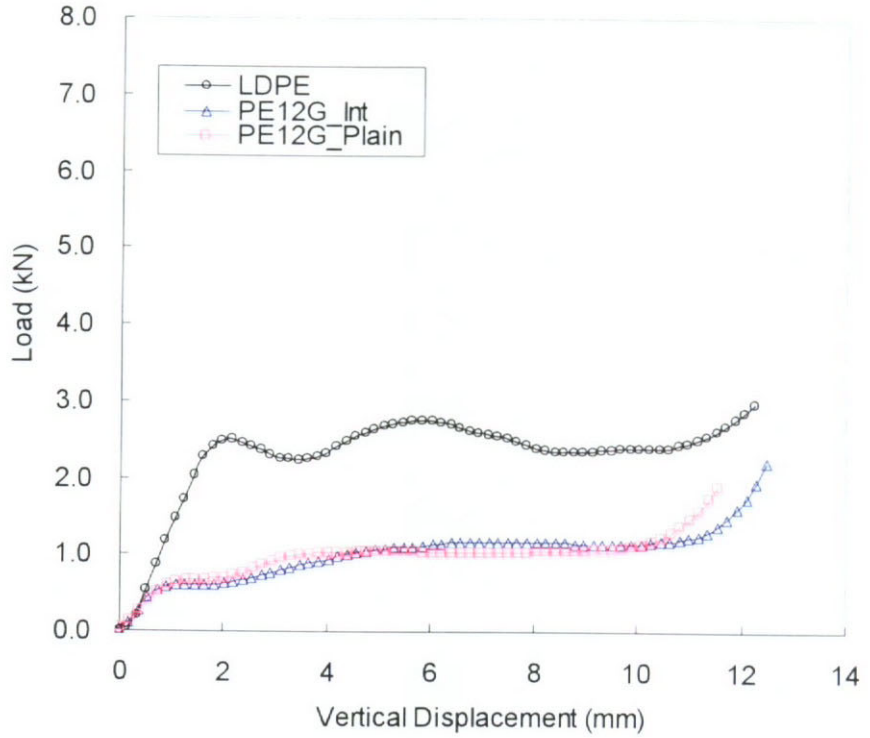

(b)

Figure 2.8 Load-displacement curves of the grid-domed cellular samples under quasi-static compression of 5mm/min. (a) PET/PP material system, (b) UHMWPE/LDPE material system

The effect of the equivalent thickness on the energy absorption capacity is evident by comparing pure PP samples of different thickness, i.e. 1.15 mm and 0.8 mm, under compression. With a reduction in the cell wall thickness of the pure PP by approximately 0.4 mm, the load level is lower and the energy absorption capacity is reduced by approximately 34 %. The equivalent thickness of the knitted composites ranged from 0.76 to 0.94 mm is lower than those of the non-woven and pure materials (ranged from 1.0 to 1.2 mm). Thus, those having larger equivalent thickness lead to a higher peak load and result in a higher specific energy absorption capacity.

For the knitted composites, the equivalent thickness governs the energy absorption capacity due to the presence of large amount of voids inside the fibre loops. In the case of fabricating the non-woven PET/PP composite, the composite thickness was controlled at 1.0 mm. The total volume is composed of the volume of matrix and fibre mat, assuming void volume is negligible. With increasing the fibre volume in the non-woven PET samples, the energy absorption capacity reduces by approximately 30 % at 38 % fibre volume.

Table 2.4 Energy absorption capacity of the grid-domed composites and matrix materials under quasi-static compression at a loading speed of 5 mm/min.

Sample code	Weight of four domes	Energy absorption up to 4 mm displacement		Energy absorption up to 8 mm displacement	
	g	J	J/g	J	J/g
PE12G_Plain	3.26	1.76	0.55	5.65	1.75
PE12G_Int	2.97	1.74	0.59	5.61	1.89
PET5G_Int	3.28	1.62	0.49	6.20	1.88
PET12G_Int	4.41	3.42	0.78	10.49	2.38
PETfv1_NW	2.91	6.62	2.27	20.18	6.93
PETfv2_NW	2.77	5.51	1.99	17.39	6.28
PETfv3_NW	2.98	4.30	1.44	16.47	5.51
LDPE	3.82	7.32	1.92	17.96	4.70
PP_1.15mm	4.12	13.99	3.40	32.31	7.85
PP_0.8mm	3.97	10.07	2.54	21.15	5.33

2.4.2 Effect of Impact Energy

Taking the UHMWPE/LDPE interlock knitted composite as an example, the effect of the impact energy on the energy absorption capacity of knitted composites has been demonstrated under various impact conditions, including (1) impact velocity of 3.5 m/s with impact mass 3.85 kg (impact energy = 24.0 J), (2) 4.76 m/s with 3.85 kg (impact energy = 44.0 J), and (3) 6.0 m/s with 6.61 kg (impact energy = 119.0 J). Figure 2.9 shows the load-displacement curves of the composites under various impact energies. The energies absorbed by the knitted cellular composites at these input energies are 16.0 J, 43.4 J, and 110.0 J, respectively. The photos taken for the deformed cells in Fig. 2.10 show that there is little collapse of the cell wall at low impact energy (24 J), while the cells exhibited a large deformation and consequently cells close at high impact energy, as evident by a sharp rise of the peak load on the curve. Thus, the cell deformation of the knitted composites is monitored by the

amount of impact energy.

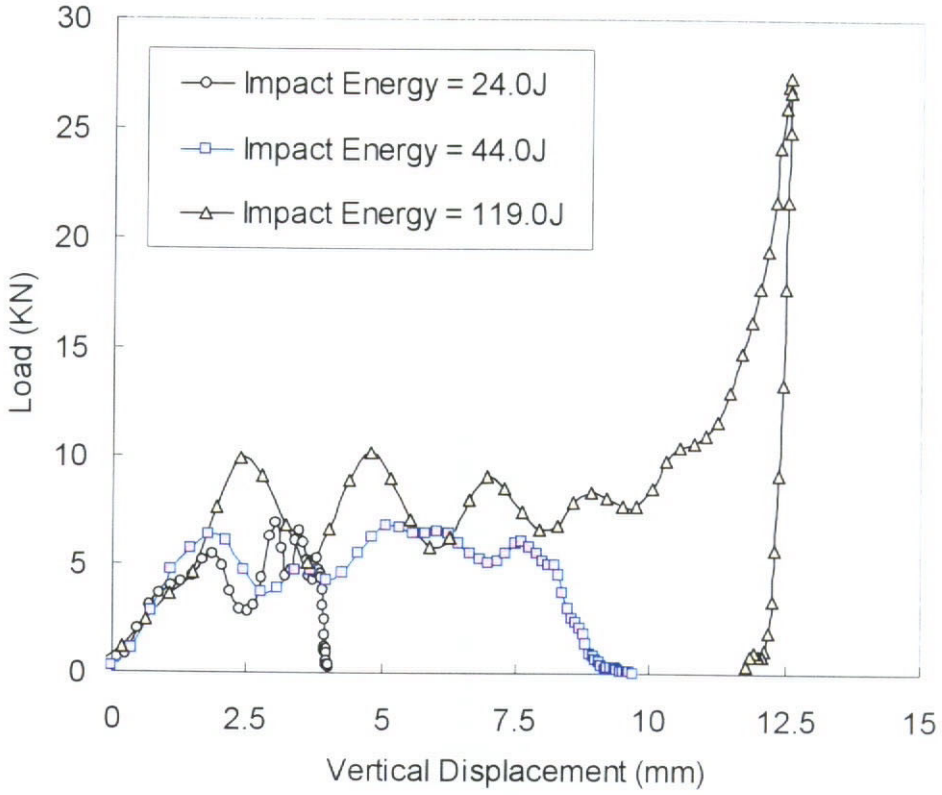

Figure 2.9 Load-displacement curves of UHMWPE/LDPE interlock knitted composites under impact with various impact energies

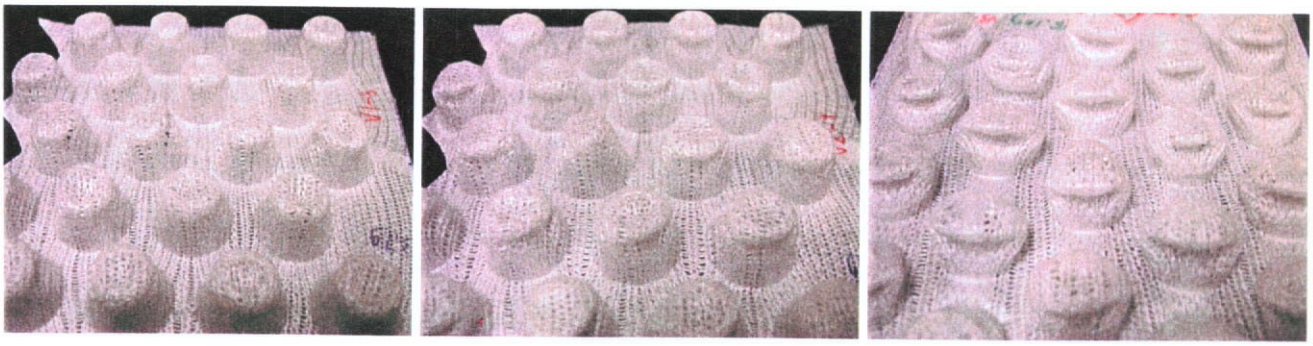

(a) (b) (c)

Figure 2.10 The deformed cells of the UHMWPE/LDPE interlock knitted composites under impacts with various impact energies (a) 23.6 J, (b) 39.0 J and (c) 119.0 J

2.4.3 Effect of Fibre Volume Fraction

Figures 2.11 and 2.12 depict typical load-displacement curves of the two composite systems with different fibre volume fractions under the same impact condition (impact velocity of 6.0 m/s with impact mass of 6.61 kg). As the pure PP (with two wall thickness) or LDPE materials are rigid and brittle, they exhibit a high peak load with limited deformation. However, those composites with knitted reinforcement show much lower peak loads and the cells collapse with a long stroke. Voids present in the composites reduce the stiffness and enhance the large deformation of the cellular composites.

The equivalent thickness as described in section 2.4.1 is found to play an important role on energy absorption. As shown in Table 2.3, the equivalent thickness of interlock PET/PP composites with looser machine gauge (PET5G_Int) is 0.74 mm whist those with the finer gage (PET12G_Int) is 0.94 mm. Thicker cell wall deform less than the thinner one even their fibre volume fractions are similar. In the case of UHMWPE/LDPE composites, although the plain knitted composites (PE12G_Plain) consist almost half of the fibre volume fraction of the interlock knitted samples (PE12G_Int), the equivalent thickness of both composites is similar and results in similar dynamic performance.

Thus, the production of knitted composites with a desired energy absorption level can be obtained even when a fibre volume fraction of 16% is selected with optimized composite thickness during fabrication.

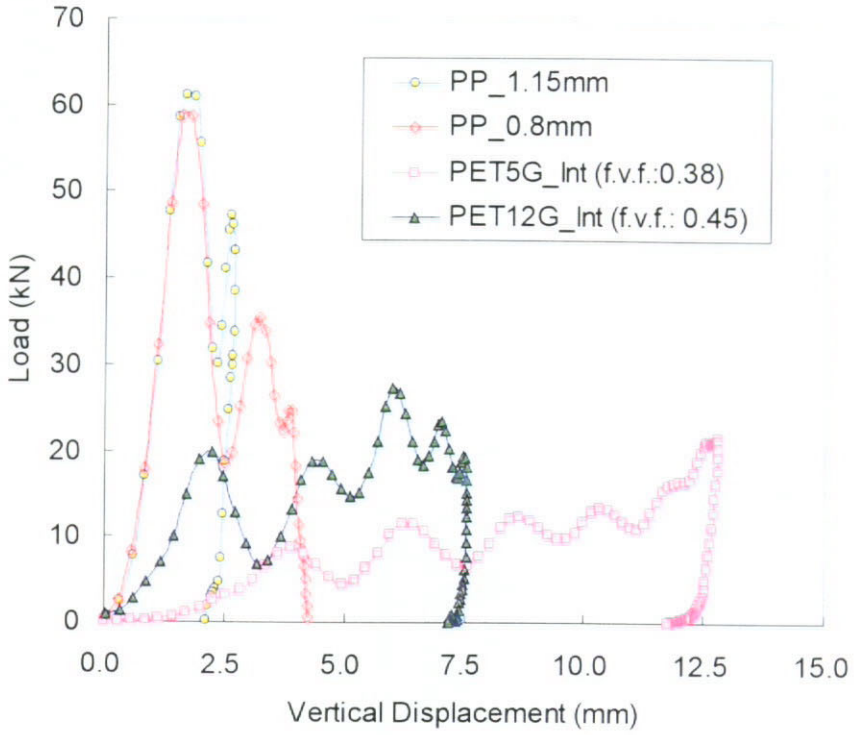

Figure 2.11 Load-displacement curves of PET/PP knitted composites with different fibre volume fractions under impact

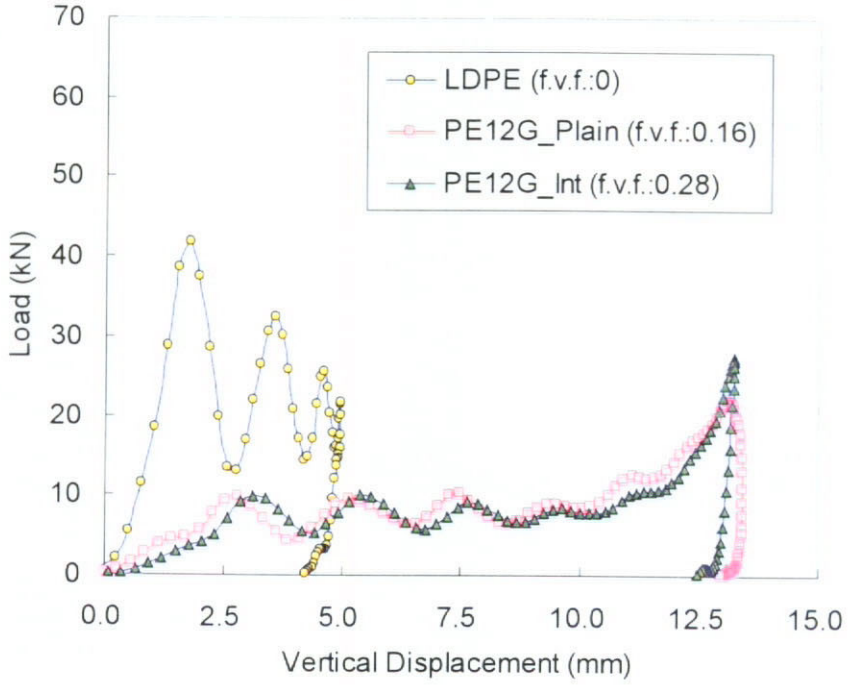

Figure 2.12 Load-displacement curves of UHMWPE/LDPE knitted composites with different fibre volume fractions under impact

2.4.4 Effect of Fibre Type

The effect of fibre types on the energy absorption capacity of the cellular composites was studied. High performance UHMWPE continuous filament yarns and fully drawn PET continuous filament yarns were used to fabricate the knitted preforms. The UHMWPE fibres have a much higher fibre axial stiffness and fibre strength than the PET fibres as shown in Table 2.1. Figure 2.13 depicts the load-displacement curves of the knitted fabric reinforced cellular composites made of PET/PP and UHMWPE/LDPE systems under impact (impact velocity of 6.0 m/s with impact mass of 6.61 kg). A PET knitted composite (samples of PET12G_Int) with thicker cell wall (t_e = 0.94 mm) exhibits only half collapse of the cells. With the similar wall thickness, both of the PET fabric reinforced composites (PET/PP_5G samples) and the UHMWPE/LDPE composites, (t_e ranged 0.73 to 0.81 mm) display similar load level and stroke under the same impact condition in which all the domes are fully collapsed. The cells deform in diamond shape in such a way similar to the knitted composites in the previous studies (Xue et al., 2001). Only when the fibres are flexible to bend into knitted loops, the orientation of reinforcing loops plays a more predominant role on governing the cell deformation than the material properties of the fibre itself. Although the UHMWPE fibres display a much higher axial stiffness and fibre strength than the PET fibres, the industrial graded fully drawn PET yarns may perform as good as the high performance UHMWPE fibres when the fibres are oriented in the knitted fibre loops.

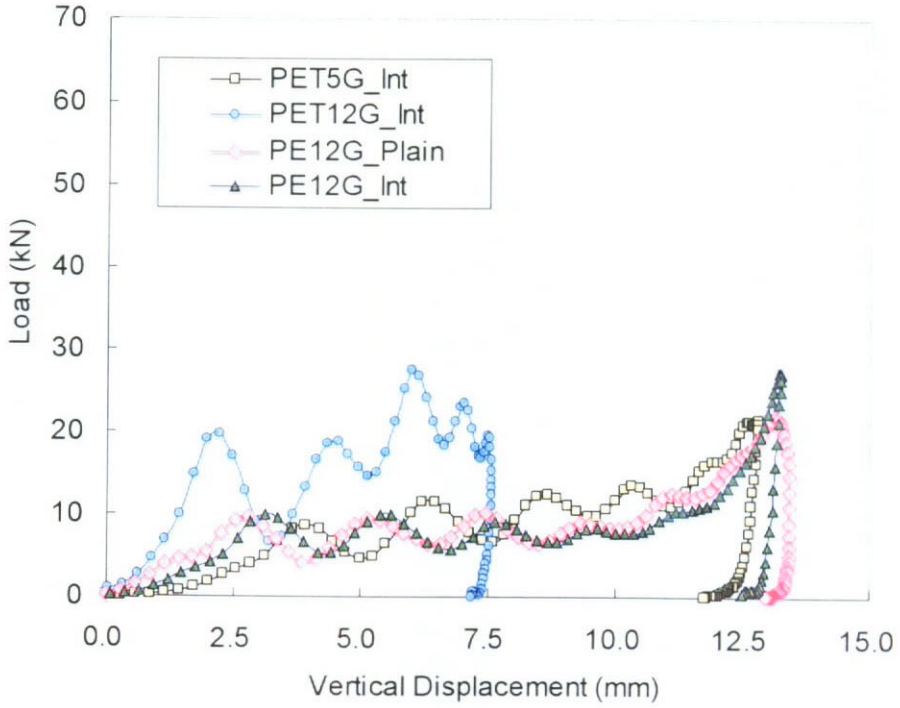

Figure 2.13 Load-displacement curves of the grid-dome cellular samples under impact of a flat striker of 6.61kg with 6.0m/s impact velocity

2.4.5 Effect of Fibre Architecture

Figures 2.14 and 2.15 compare the load-displacement and energy-displacement curves of the pure PP, PET non-woven/PP composites and PET knitted/PP composites. Both of these composites are composed of the same fibre volume fraction, although they have different wall thickness. The pure PP exhibits a high peak load and a brittle failure. The deformation of the non-woven composite samples and the knitted composites (PET12G_Int) with similar wall thickness stop at a half of their original height at which all the impact energy is absorbed. While the knitted composite (PET5G_Int) with thinner wall deformed with closure of cells under the same impact energy. It is believed that if the cell wall thickness of the non-woven samples is further reduced, the cells would have a much larger deformation with lower peak load leading to an improved performance. On the other hand, the deformation mode of the non-woven composites, a ring pattern on the cell wall, is different from those of the knitted composites, which will be discussed in the next chapter.

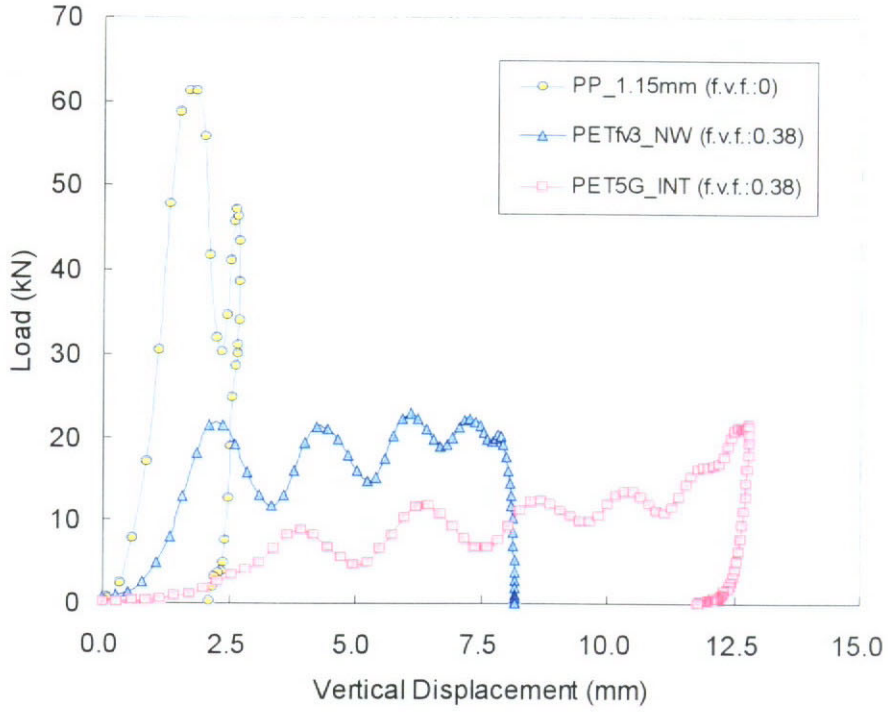

Figure 2.14 Load-displacement curves of the grid-domed cellular samples under impact

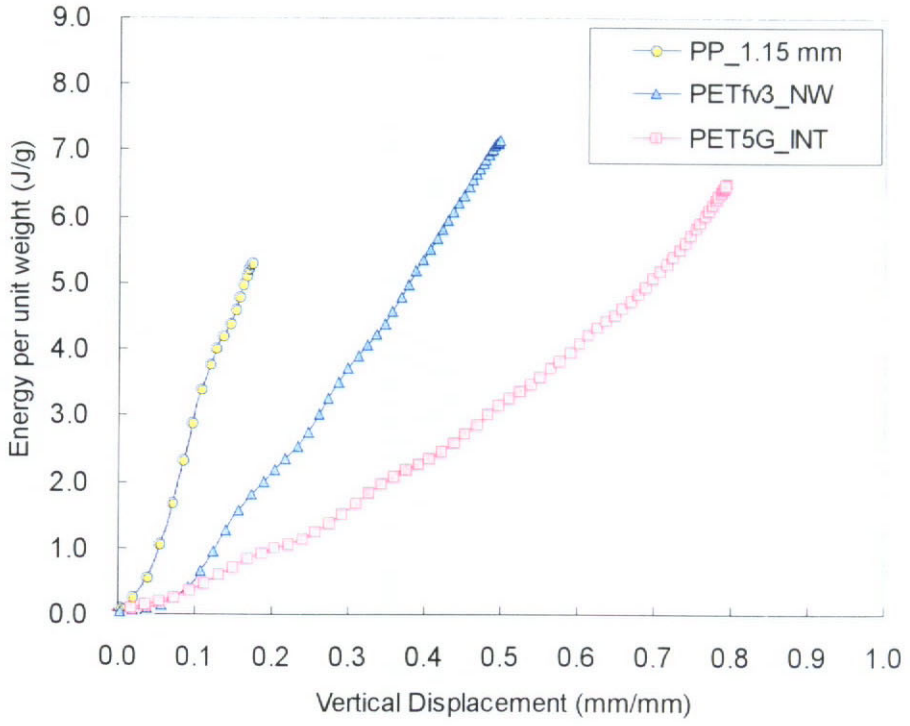

Figure 2.15 Energy-displacement curves of the grid-domed cellular samples under impact

2.4.6 Recovery of Cells after Impact

The visco-elastic property of the grid-dome samples was investigated by measuring the height of the cells before and after an impact of velocity 6.0 m/s with a drop mass of 6.61 kg. The height of a cell was measured at 0 min., 10 min., 30 min., 45 min., and 1 hour after impact. Final recovery of the cells among samples with different material systems is listed in Table 2.5. The UHMWPE/LDPE knitted and PET/PP knitted cellular composites show the highest cell recovery (7 – 16 %) among the samples except the knitted cellular composites with finer gage (PET12G_Int). The pure LDPE also exhibits a certain degree of recovery (4 %) after impact, while the pure PP samples with two cell wall thicknesses (0.8mm and 1.15mm, respectively) and the PET/PP non-woven (fibre volume fraction = 0.14) samples are brittle and fractured at the cell tops after impact. With the increase of fibre volume fraction in the non-woven cellular samples (fibre volume fraction = 0.38), the degree of recovery increases to approximately 2 % which is still much lower than those knitted composites with the same fibre volume (PET5G_Int).

Table 2.5 Recovery of cellular samples after impact

Sample Code	Original Height (mm)	0 min.	10 min.	20 min.	30 min.	45 min.	60 min.	Final Recovery (%)	Recovery Rate (mm/min.)
PE12G_Plain	15.00	11.40	11.99	12.11	12.13	12.23	12.28	7.72	0.015
PE12G_Int	14.75	7.69	8.36	8.55	8.74	8.88	8.95	16.38	0.021
PET5G_Int	14.67	9.93	10.27	10.43	10.53	10.60	10.81	8.86	0.015
PET12G_Int	14.82	12.34	12.38	12.46	12.53	12.56	12.55	1.70	0.004
PETfv1_NW	14.78	12.42	12.46	12.48	12.48	12.48	12.48	0.48	0.001
PETfv2_NW	14.73	12.22	12.41	12.49	12.49	12.48	12.49	2.18	0.004
PETfv3_NW	14.87	12.80	12.97	13.02	13.06	13.07	13.07	2.11	0.004
LDPE	15.26	13.27	13.52	13.66	13.89	13.80	13.80	4.02	0.008
PP_1.15mm	15.42	14.53	14.48	14.52	14.51	14.52	14.55	0.14	0.000
PP_0.8mm	15.35	14.99	15.03	15.04	15.04	15.04	15.05	0.36	0.001

2.5 Comparison of Energy Absorption Capacity, Formability and Cost among the Developed Cellular Textile Composites

We have so far investigated the effect of material properties and fabric reinforcement on the performance on energy absorption capacity of cellular composites. In this section, we will compare the performance, ease of fabrication and costing of these systems. Table 2.6 summarizes the processing issue and the performance of the four material systems.

Injection molding of pure polymer cellular structure is a fast and easy process of fabrication, the molded parts are also uniform on the wall thickness and perfect on the surface. However, the pure PP or LDPE cells all exhibit a high peak load with

brittle fracture, the sharp broken edges may result in injure for the subject to be protected.

Knitted composites made from either thermoplastic or thermoset systems have been studied thoroughly. Due to the flexibility of the fabrics, they can be used to fabricate the composites in three dimensional shapes, and designed to absorb high energy absorption by controlling the cell wall thickness for its fully collapse of the cells. Considering the material compatibility of fibres and matrix in the thermoplastic systems, polyester fabric/ PP matrix system and the UHMWPE/LDPE systems were selected to represent the conventional and high performance fibre systems in composite fabrication. Among all the fibre types studied, UHMWPE is more expensive than the conventional textile fibres or the industrial grade PET fibres. As long as the filament yarns have sufficient strength and ductility to be bent into knitted loops, as shown the performance by the PET yarns being constructed as knitted reinforcement, the fabricated cellular composites perform as good as those with the high performance fibre reinforcements. Thus, the UHMWPE fibres are not necessary for this particular application from the economic points of view.

Non-woven fabric may be an alternative choice for reducing fibre/yarn cost and the intermediate textile processing. In addition, the performance of non-woven composite can be superior to the knitted one as discussed in section 2.4.5. The potential of using non-woven fabric reinforcement in composites will be further explored in Chapter 3.

Table 2.6 Evaluation of the material systems on composite performance, formability and cost

Cellular Composite Components	Pure polymeric matrix	PET knitted/ PP matrix	UHMWPE knitted/ LDPE matrix	Non-woven PET/PP matrix
Processing Type	Thermoplastic			
Fabrication Method	Injection molding	- Compression molding - Resin injection molding		
Performance on EAC under Dynamic Environment	Too brittle, high peak load	- Good, subjected to cell wall thickness		
Manufacturing Concern	- Easy - Fast process	- One-step process for co-knitted pregreg - Two-step for film stacking - Clean process		
Fibre Cost	Nil	Mediate	High	Low
Fabric Cost	Nil	High	High	Low
Priority of Use	4	2	3	1

2.6 Concluding Remarks

Various thermoplastic cellular textile composites with knitted and non-woven fabrics and pure polymer cellular samples have been fabricated. The energy absorption behaviour and deformation mechanisms of these were studied experimentally under both quasi-static and impact conditions.

It is revealed that the equivalent cell wall thickness is a predominant factor on governing the energy absorption capacity of the cellular structure. Under quasi-static compression, the cellular samples with thicker cell walls, including pure LDPE or PP materials and non-woven reinforced cellular samples, exhibit a higher level of specific energy absorption capacity through the collapse of cells than those knitted composites with thinner equivalent cell wall. The cellular composites have little

recovery after impact while pure PP and LDPE even exhibit brittle fracture.

As long as the fibre material is sufficient strong, ductile and flexible to be bent to form knitted loops, UHMWPE fibres or industrial grade fully drawn PET fibres can perform similarly as composite reinforcement. The effect of fibre volume fraction on the energy absorption capacity of knitted composites is not as significant as the equivalent thicknesses due to the presence of large amount of void content. By keeping a constant wall thickness, increase in fibre volume fraction in non-woven cellular samples leads to a reduction of the high peak load and allowed a prolonged stroke. The deformation of the cellular composites is monitored by the amount of impact energy. The deformation mode of the non-woven composites has been found to be different from those of knitted reinforcement. Non-woven composites perform similarly or even higher energy absorption levels compared with that of the knitted composites, which may bring in more advantages on ease of fabrication and cost reduction.

CHAPTER 3

PERFORMANCE OF NON-WOVEN FABRIC REINFORCED CELLULAR TEXTILE COMPOSITES ON ENERGY ABSORPTION

3.1 Introduction

In Chapter 2, we have characterized the cellular textile composites with different reinforcements, including PET/PP knitted, UHMWPE/LDPE knitted and PET/PP non-wovens. We have found that the non-woven cellular composites have a high potential as energy absorbing components due to its ease of fabrication and comparable energy absorption levels to the knitted composites.

Some of other studies have demonstrated that short fibre mat reinforced spherical shells and conical frusta (Gupta and Easwara, 1999; Gupta and Velmurugan, 2002) utilized the brittle fracture of the fibre and matrix. These fibre-reinforced composite materials usually have high specific strength and high stiffness; and they utilize the brittle fracture during a progressive crushing as the deformation mode. In contrast, we expect the non-woven composite cells deformed plastically on the cell wall.

In the present study, the cellular textile composites made of non-woven polyester (PET) fabric with different fibre volumes and polypropylene (PP) matrix are fabricated, in an attempt to yield similar or even higher energy absorption levels compared with the knitted cellular composites. The material properties are characterized to interpret the performance of the cellular composites under dynamic response. The energy absorption capacity of the composites is also evaluated under

multiple impacts. The deformation mechanisms of the non-woven composites and pure material are examined and a theoretical analysis is proposed to predict the energy-absorption capacity of the cellular material.

3.2 Experimental

3.2.1 Sample Preparation

Bulk form PET non-woven fabric of 200 g/m^2 and polypropylene films were used for fabricating flat and cellular composite panels. Flat sheets of composites of approximately 1.0 mm thick were fabricated by compression molding. Layers of fabric preforms were sandwiched between layers of thermoplastic PP matrix films and then put for compression molding. The prepreg in the compression platen were first preheated at a pressing temperature for 10 minutes to remove moisture inside and melt the matrix. Then, they were pressed at 180 °C under 10 MPa for 15 minutes, followed by cooling from the pressing temperature to 30 °C in 15 minutes under pressure. The flat composite samples were prepared for the tensile and punch shear tests. Some of the other flat composite samples were further processed in the same procedures as described in section 2.2.2 to produce cellular composite samples. Pure PP material in flat sheet form and cellular structure were also produced by injection molding as control experiment. Details of the non-woven composite samples with three fibre volume fractions and the pure PP material are listed in Table 2.3 in Chapter 2.

3.2.2 Simple Tensile Test

Tensile test of flat non-woven composites with three fibre volumes and pure PP material was performed using a MTS Universal Testing Machine with a load cell of 5KN capacity. Flat composite specimens were cut into narrow strips with dimensions of 20 mm x 150 mm and approximately 1 mm thick. The gauge length was set 80 mm and each specimen was elongated at a crosshead speed of 5 mm/min.

3.2.3 Punch-Type Shear Test

A punch-type shear testing on flat non-woven composites and pure PP panels was performed to examine the shear properties of the materials following ASTM standard D732. A specially designed fixture with a punch and die tool was manufactured according to the standard (dimensions as shown in *Appendix* 3.1) and the fixture with the specimen placed inside is mounted on MTS Universal Testing Machine, as shown in Fig. 3.1. The shear test setup is shown in Fig. 3.2. The test specimens were cut in a 50 x 50 mm^2 from the molded flat non-woven composite sheets and pure PP panels. A hole was drilled centrally on the specimens in order to locate a guide pin on the punch. The thicknesses around the drilled hole of the specimens were measured before test. The specimen was then placed over the pin of the punch and fastened tightly by means of washers and nuts. The tool jig was assembled and the bolts were tightened so that the specimen was sheared by the close-fitting punch at the punch edge. The tests were conducted at a crosshead speed of 1.25 mm/min with a punch diameter of 25 mm. The shearing properties of the non-woven composites were compared of different fibre volume fractions. Five specimens were tested on each composite or pure PP samples. Usually, the shear stress at yield indicates the pure shear strength of the composite material, while the maximum shear strength is

closely related to the tensile strength. The shear yield stress (S_{ys}) and maximum shear strength (S_{ms}) are given by the expression as follows:

$$S_{ys,\,ms} = \frac{F_{ys,ms}}{\pi DT}$$

where $F_{ys,ms}$ is the force at yield and at break, respectively, D is the diameter of the punch and T is the mean thickness of the specimen.

Figure 3.1 A punch-type shear testing device mount on the Universal Testing Machine

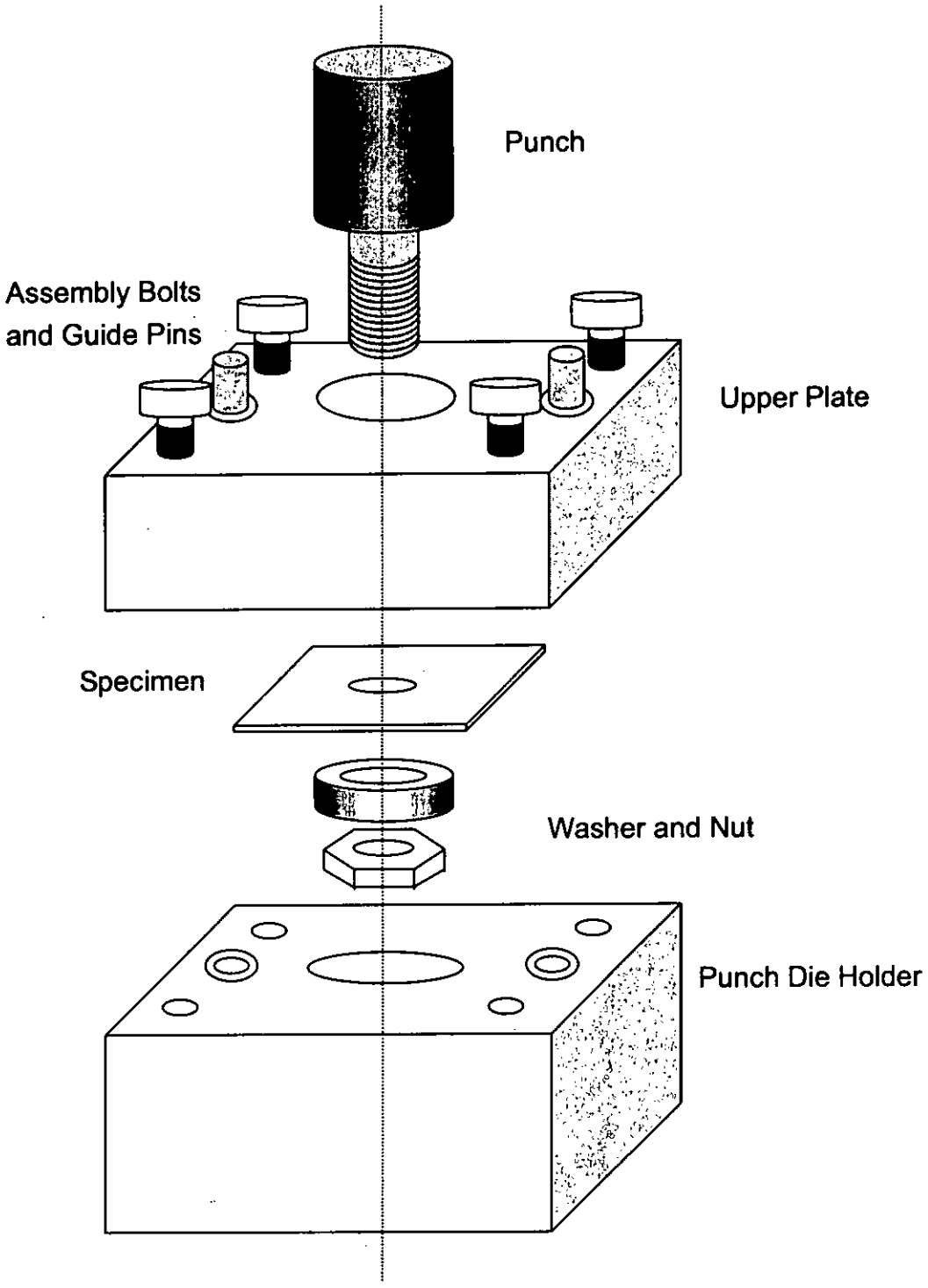

Figure 3.2 Schematic diagram of the punch-type shear testing device

3.2.4 Impact Tests on Cellular Composites

Impact tests on the PET/PP non-woven cellular composites and pure PP cellular samples were performed on a Dynatup Drop Weight Impact Tester (Model GRC8250). Each specimen with 20 domes was tested under a single impact and multiple impacts. All specimens were weighted before tests. The specimen was put on the supporting base of the testers and impacted by a flat steel plate. The mass of a drop weight (6.61 kg) included a plate striker of 120mmx120mmx12mm, which was normal to the plane of the samples. The impact velocity was set at 6.0 m/s by adjusting the height of the drop weight and the air pressure of the pneumatic assist.

3.3 Mechanical Properties of Flat Composite Samples

Table 3.1 lists the specifications and material properties of the flat samples. Pure PP sample is the most brittle, while all the PET/PP composites with non-woven fabric reinforcement are more ductile. Figure 3.3 depicts the tensile curves of the non-woven composites with the three fibre volume fractions and the pure PP. Pure PP breaks at 4 % while most of the non-woven composites at 32 – 35 %. With an increase in fibre volume fraction of the non-woven reinforcement, the yield stress of the composites reduces. All the three non-woven composites with different fibre volume fractions have similar tensile strength and extensibility. Thus, the non-woven reinforcement reduces the stiffness of the composite material with the increase in fibre volume fraction. Similar to the knitted reinforcement, the non-woven reinforcement enhance the material ductility during impact.

Table 3.1 Specifications and properties of thermoplastic flat composite samples

Sample code	PP	FV1	FV2	FV3
Material	Pure PP	PET / PP	PET / PP	PET / PP
Thickness (mm) [s.d.]	0.94 [0.03]	0.92 [0.03]	0.94 [0.02]	1.08 [0.04]
Fibre volume fraction	0.00	0.14	0.24	0.38
Sample weight in 11x 11cm^2 (g)	20.87	14.76	16.26	17.33
Young's modulus (MPa) [s.d.]	1443.0 [60.5]	1420.3 [73.6]	1337.8 [22.2]	1131.1 [180.5]
Tensile strength (MPa) [s.d.]	27.41 [2.1]	31.80 [1.1]	32.10[1.0]	32.30 [0.7]
Strain at break (mm/mm) [s.d.]	0.047 [0.0]	0.348 [0.0]	0.353 [0.0]	0.321 [0.0]
Shear yield stress S_{ys} (MPa) [s.d.]	20.12 [0.66]	15.77 [0.80]	14.64 [0.24]	11.04 [0.24]
Shear yield strain γ[s.d.]	1.441 [0.17]	0.910 [0.06]	0.765 [0.02]	0.670 [0.03]
Shear modulus G (MPa) [s.d.]	21.24 [1.84]	19.98 [1.37]	19.80 [1.64]	15.85 [1.59]
Max. shear stress S_{ms} (MPa) [s.d.]	26.49 [0.76]	40.63 [2.04]	48.79 [1.25]	58.86 [3.26]

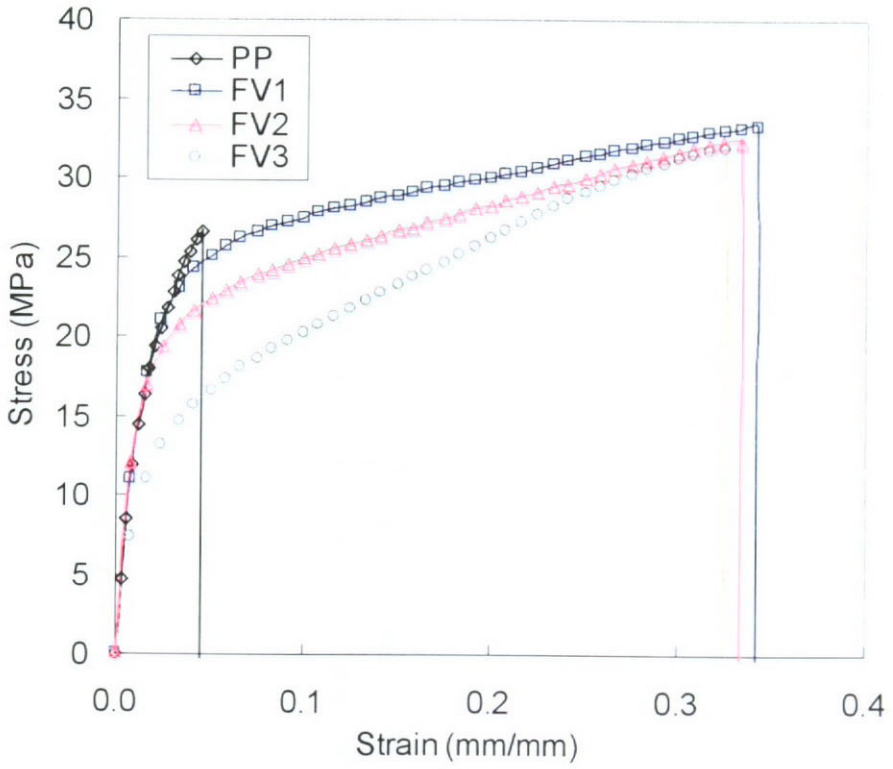

Figure 3.3 Tensile stress-strain curves of non-woven composites and pure PP

Figures 3.4 (a) and (b) show the load-displacement curves of the non-woven composites with three different fibre volume fractions and the pure PP under punch-type shearing. Pure PP has a higher shearing stiffness than the three composites. The shear yield strength (S_{ys}) of the composite material decreases with the increase of fibre volume fraction, as listed in Table 3.1. After the initial linear region, there is a sharp rise in the load-displacement curves for composites until the maximum shear strength (S_{ms}) is reached. The maximum shear strength increases with the fibre volume fraction as shown in Fig. 3.4 (a), while there is a constant loading of the pure PP observed in Fig. 3.4 (b). It is found that the values of the maximum shear strength and tensile strength of the pure PP specimen are quite close to each other, as shown in Table 3.1. However, the maximum shear stress becomes much higher in the non-woven fabric composites as compared with the PP samples. As the shearing tested specimens are thin (approximately 1 mm), the non-linear region of the curves after the shearing yield can be regarded as the tensile loading of the non-woven reinforcement while the corresponding region in Fig. 3.4 (b) is a pure stretching of the pure PP.

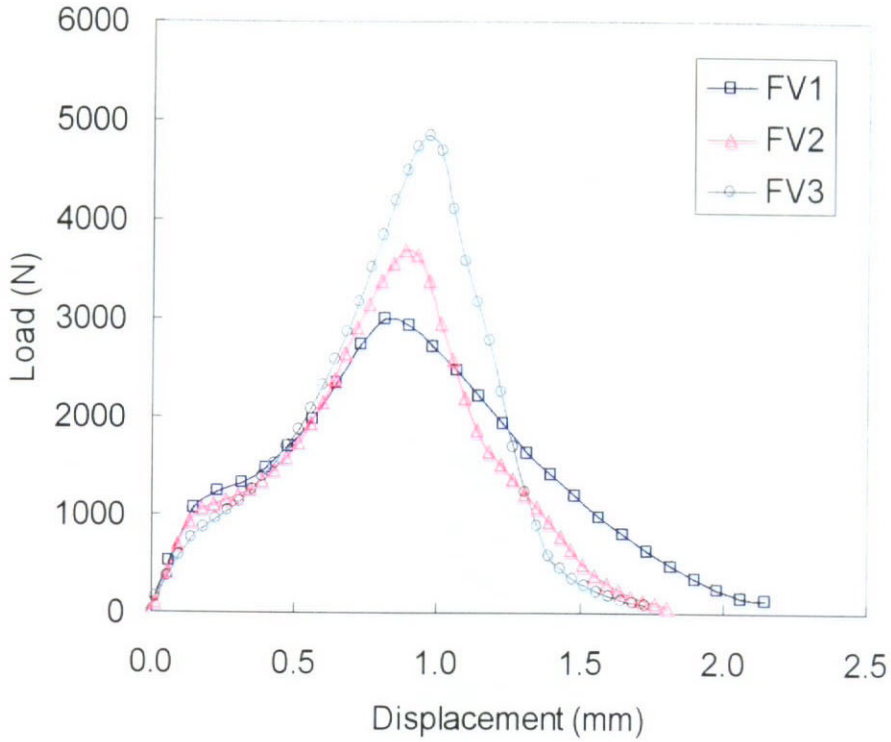

Figure 3.4 (a) Load-displacement curves of non-woven composites with three fibre volume fractions under punch shearing

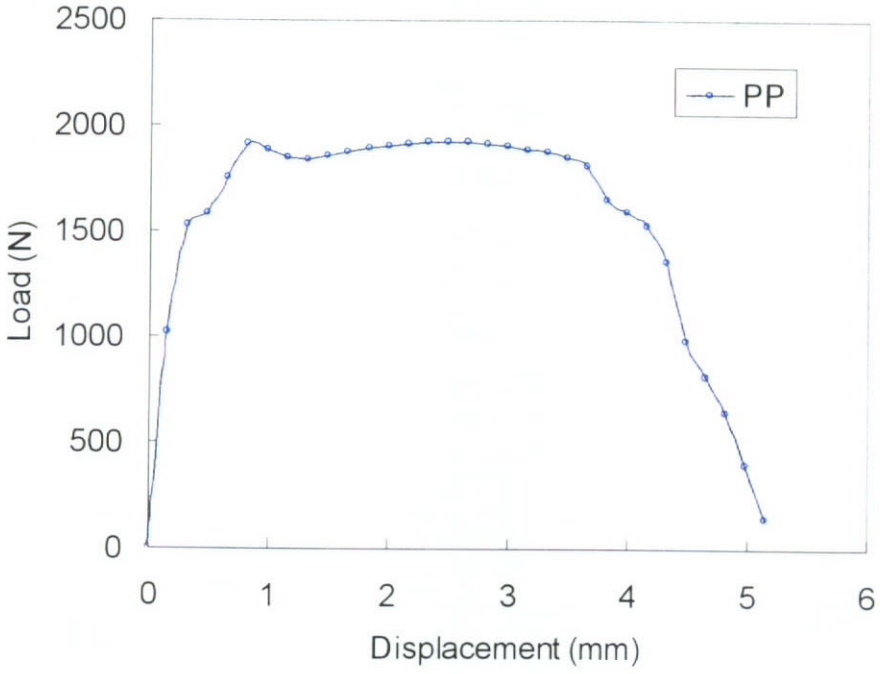

Figure 3.4 (b) Load-displacement curves of pure PP under punch shearing

3.4 Energy Absorption Behaviour of Non-woven Composites

3.4.1 Effect of Fibre Reinforcement on Impact Response

The pure PP cellular specimens exhibit a high level of energy-absorption under axial quasi-static compression because the cells can deform globally as the load increases. However, they show a brittle fracture on the cell tops with limited deflection under impact loading because they are sensitive to the strain rate effect. Figure 3.5 shows the load-displacement curves of PET non-woven fabric reinforced composites and pure PP cellular samples under impact. With a low fibre volume content (fibre volume fraction = 0.14), the non-woven composites perform similarly to those rigid matrix grid-domes with an unsustainable high peak load. As observed in experiments, some of the cell tops of the pure PP even fall out during impact, as shown in Fig. 3.6 (a). Fragments can be found around the cell walls and brittle fracture is observed on the cell tops, as shown in Fig. 3.6 (b). When increasing the fibre volume fraction (ranged from 0.14 to 0.38), the peak load is much reduced and the cell collapse is extended to a half of their height. The fibre network prevents the cell tops from falling out or brittle fracture, as shown in Fig. 3.6 (d). The observed fracture on the cell tops of the pure PP and the composites with low fibre volume fractions can be attributed to the low ductility rather than the shear properties. Increase in fibre volume of the non-woven reinforcement would reduce the brittleness resulted from the matrix material or increase the toughness of the cellular structure. As there is a fillet on the cell top, the impact force from the flat plate striker induces a bending load between the fillet and the flat-topped plate. Pure PP or composite with low fibre volume fraction are brittle so that the fracture around the cell tops or cell walls occur. On the contrary, the ductility of the non-woven reinforcement prevents it from fracture at the bending region, which enhances further collapse of the cell wall.

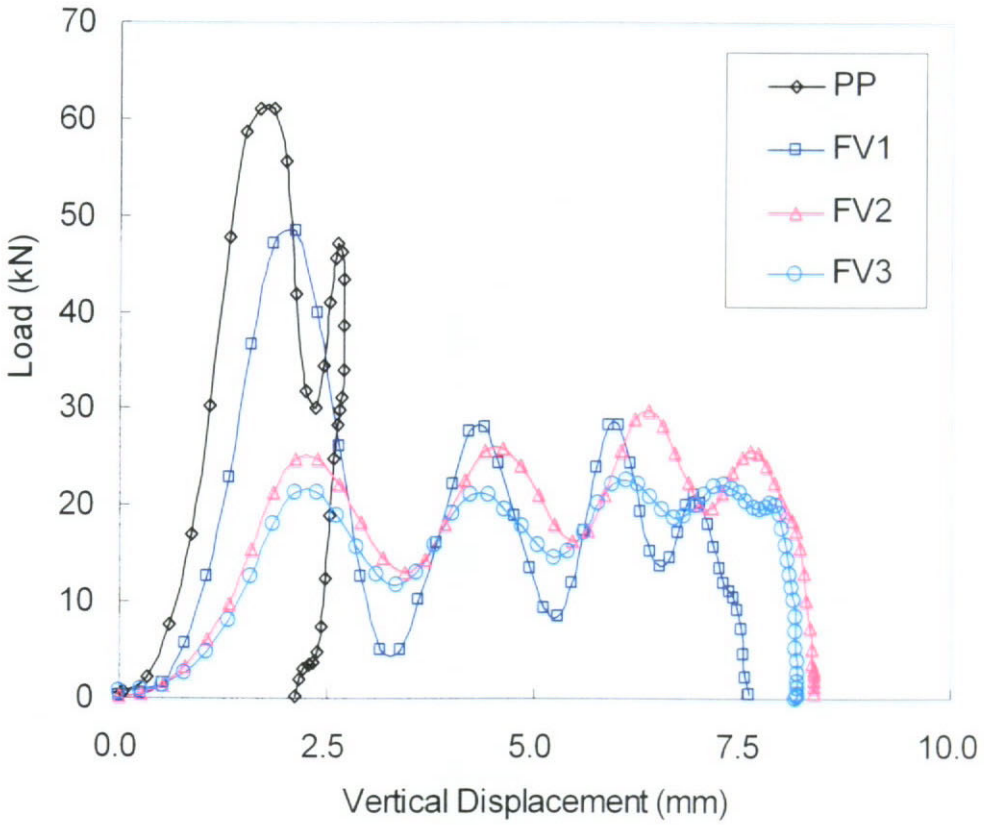

Figure 3.5 Load-displacement curves of the PET/PP non-woven composites with different fibre volume fractions and injection molded PP specimens under impact

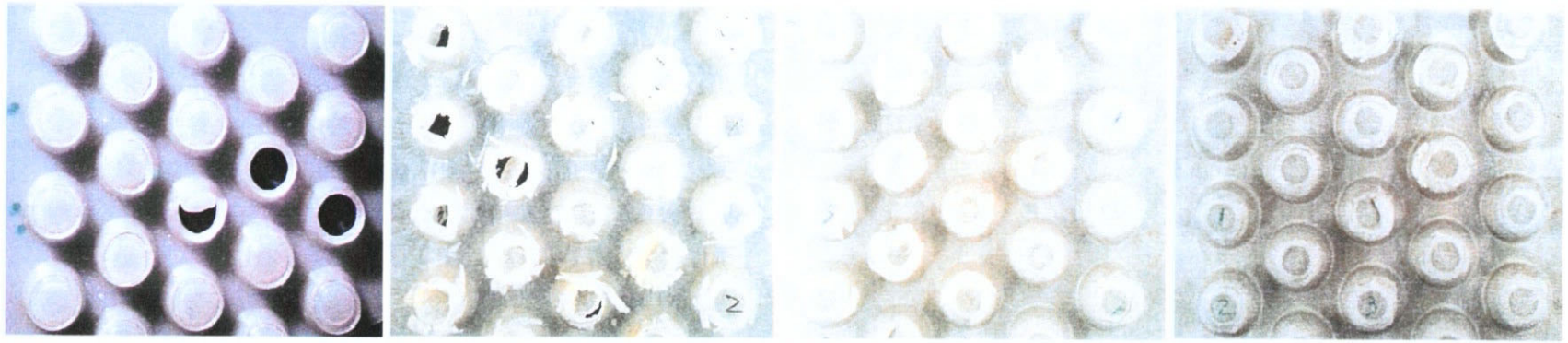

(a) Fibre volume fraction: 0 (b) Fibre volume fraction: 0.14 (c) Fibre volume fraction: 0.24 (d) Fibre volume fraction: 0.38

Figure 3.6 The deformed cell of the nonwoven textile composites with different fibre volume fractions after impact

3.4.2 Cellular Composites under Multiple Impacts

The non-woven composite samples only collapse at a half of their height and a ring formed on the cell wall at a single impact with energy of 120 J. The cell has not reached the stage of cell densification. Hence, a higher impact energy can be applied to reach the full densification of cells. This assumption can be further verified by conducting a multiple impact test. Figures 3.7(a-b) show the load-displacement and the specific energy-displacement curves of the non-woven cellular composites with fibre volume fraction of 0.38 (FV3) under multiple impacts with the same impact conditions as in the previous impact test. The cellular composites were able to sustain multiple impacts and only collapsed on the cell wall until the third impact was applied, which almost reach the upper limit of the load cell on the impact tester. It is believed that if the cell wall thickness of the non-woven samples is further reduced, the cells would have a much larger deformation with a lower peak load applied.

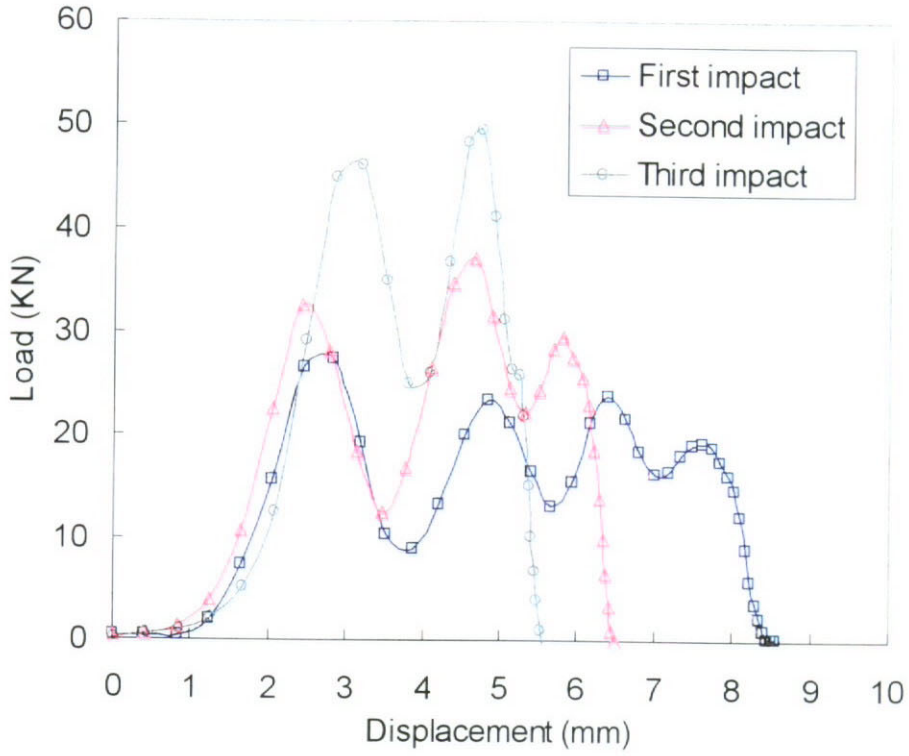

Figure 3.7(a) Load-displacement curves of non-woven composite FV3 under multiple impacts

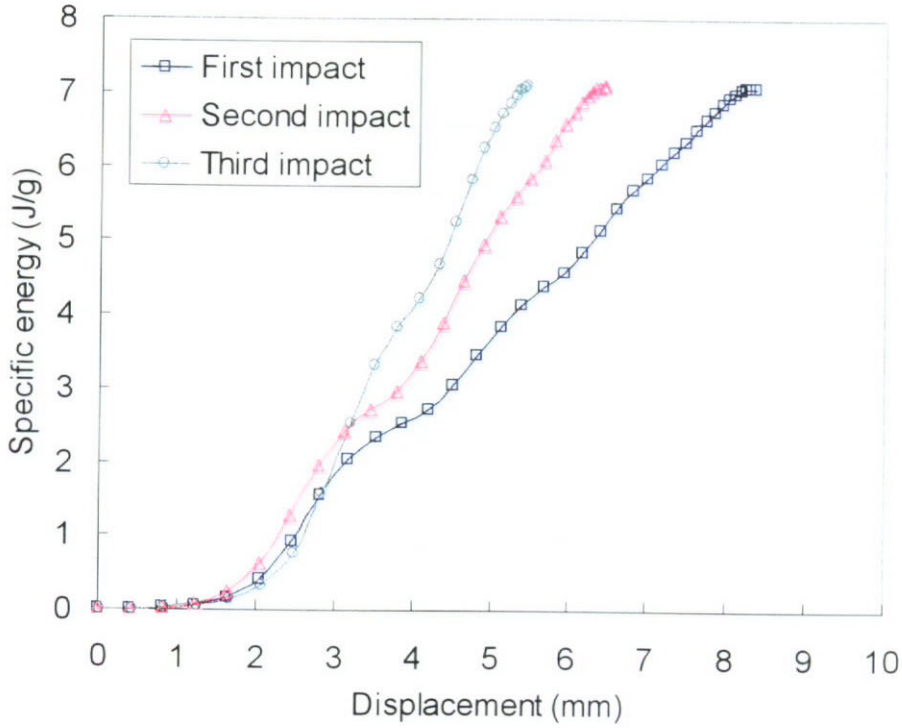

Figure 3.7(b) Specific energy-displacement curves of non-woven composite FV3 under multiple impacts

3.5 Deformation Mode of a Cell

The deformation mechanism of the cellular composites was observed by conducting quasi-static axial compression tests on the MTS Universal Material Tester. A grid-domed cell specimen was put on the supporting base of the Tester and axially compressed by a rigid flat plate moving down with a cross-head speed of 5 mm/min. A mirror and a transparent plate were used to make it possible to observe the deformation process from different directions. A series of photographs were taken during the compression process, whilst the load and displacement curves were recorded by the Tester system. It is observed that for all those isotropic pure PP and non-woven PET/PP cellular samples, a ring formed on the cell walls, which is different from the previous study by Xue et al. (2001) on the knitted composites that deform into a two-lobe diamond pattern.

Figure 3.8 shows a typical deformation process of a single dome of pure PP recorded by a series of photographs taken from the front-view, side-view and top-view. During the deformation process, (1) the flat top bends inwards during the large deformation process; (2) the flat-topped conical shell plastically collapses inwards to form a ring pattern; (3) and eventually circumferential hinge lines can be observed when the loading plate is removed.

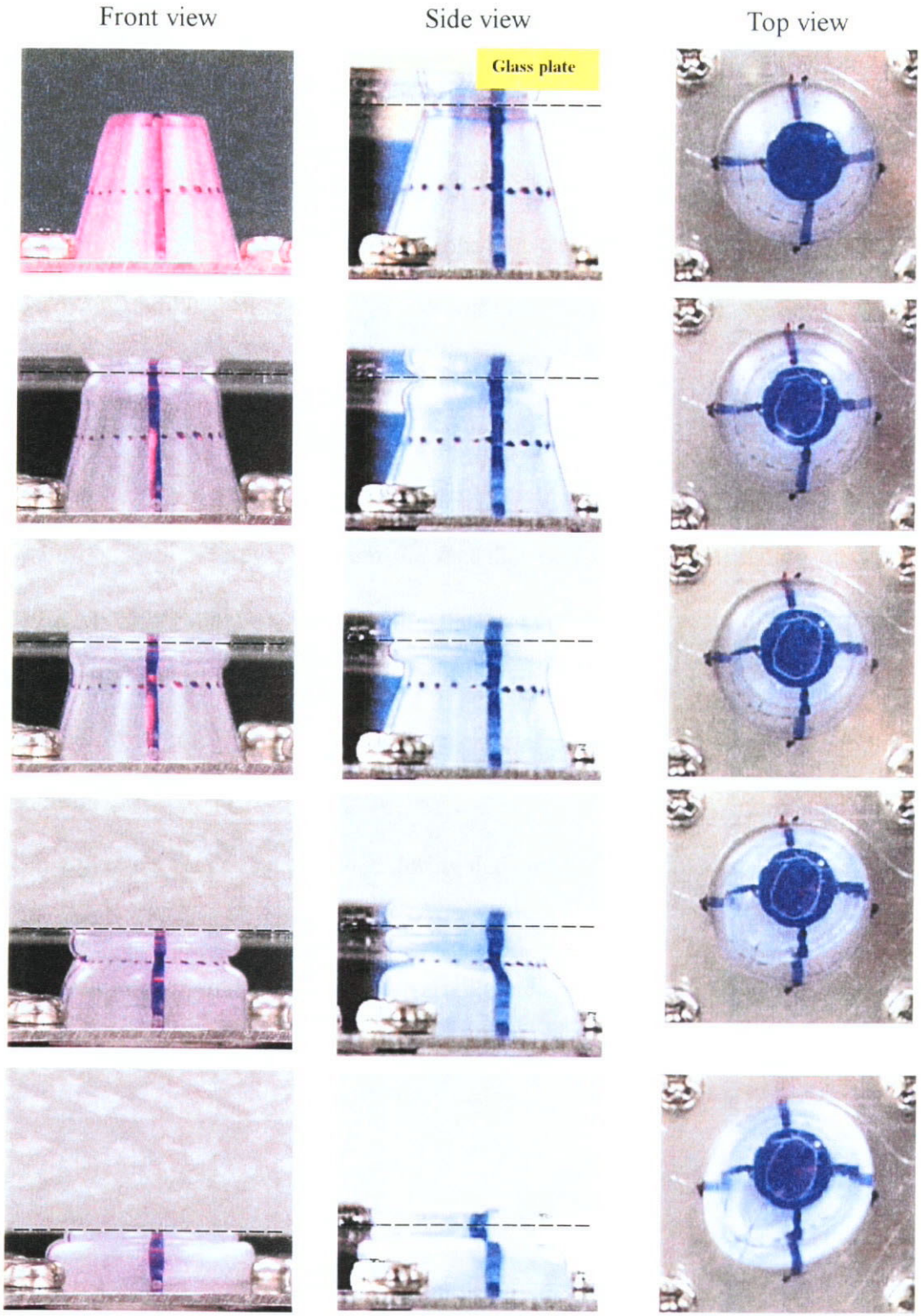

Figure 3.8 Deformation process of a cell made of pure PP material under quasi-static compression at a loading speed of 5 mm/min.

3.6 Prediction of *E.A.C.* of Cellular Structure

3.6.1 Mean Peak Load Prediction of Cellular Structure

Up to now, theoretical treatments have been confined to open-end cylindrical shell during axial compression (Mamalis et al., 1986; Mamalis et al., 1988). In this section, we propose an analytical model to predict the load-displacement curve and energy absorption capacity of the flat-topped close-end conical shell for the pure PP and non-woven samples. Based on the experimental observation in section 3.5, the phenomenon can be further interpreted referring to the analysis for a ring collapsing under compression between two flat plates (Ja and Hodge, 1963; Lu and Yu, in press). The effect of local deformation at the contact points between the ring and the plate is very limited, which is evident from the fact that two typical deformation modes of the ring have the same force-deformation curve. Therefore, the assumptions are made for our model as follows:

1. the cell wall collapses internally with a circular plastic hinge between the top and bottom;
2. the top circle remains unchanged during deformation;
3. the effect of the cell top deformation is negligible;
4. the values of x_1 and x_2, the length variables referring to Fig. 3.9, are the same as those measured from the experiment.

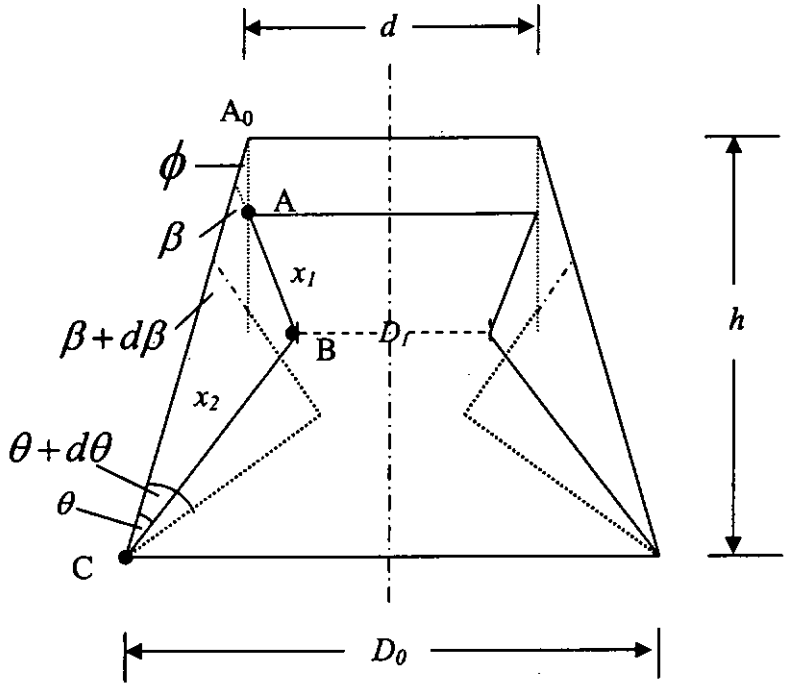

Figure 3.9 Deformation mode of a flat topped grid dome cell forming internal convolution

Let ϕ represent the semi-apical angle of the conical shell. After deformation, sides AB and BC will deviate from the original position with angles β and θ, respectively. The following relations can be obtained:

$$x_2 \sin(\theta+\phi) = (x_1 + x_2)\sin\phi + x_1 \sin(\beta-\phi)$$

$$\theta = -\phi + \sin^{-1}\left[\frac{x_1}{x_2}\sin(\beta-\phi) + \frac{x_1+x_2}{x_2}\sin\phi\right] \tag{3.1}$$

which leads to

$$d\theta = \frac{x_1}{x_2}\frac{\cos(\beta-\phi)}{\cos(\theta+\phi)}d\beta \tag{3.2}$$

The vertical displacement at the cell top is

$$\delta = x_1[\cos\phi - \cos(\beta-\phi)] + x_2[\cos\phi - \cos(\theta+\phi)] \tag{3.3}$$

The increment of load advance of $d\delta$ is given by

$$d\delta = x_1 \cos(\beta - \phi)[\tan(\beta - \phi) + \tan(\theta + \phi)]d\beta \tag{3.4}$$

Then, the external work done by the applied axial load P during the incremental displacement $d\delta$ is

$$\begin{aligned} dW^e &= Pd\delta \\ &= Px_1 \cos(\beta - \phi)[\tan(\beta - \phi) + \tan(\theta + \phi)d\beta \end{aligned} \tag{3.5}$$

The internal plastic dissipation of energy is done by bending along plastic hinge lines and by stretching of material between them. The increment of plastic dissipation for further bending at the circular plastic hinges at points A, B and C of the cell wall as shown in Fig. 3.9, is

$$\begin{aligned} dW_1 &= (dW_1)_A + (dW_1)_B + (dW_1)_C \\ &= \pi d(M_P)d\beta + \pi D_1(M_P)(d\beta + d\theta) + \pi D_0(M_P)d\theta \end{aligned} \tag{3.6}$$

where d is the diameter of the cell top,

$$D_0 = d + 2(x_1 + x_2)\sin\theta \tag{3.7}$$

And

$$D_1 = d - 2x_1 \sin(\beta - \phi)] = d + 2(x_1 + x_2)\sin\phi - 2x_2 \sin(\theta - \phi)$$

$$M_P = \frac{2}{\sqrt{3}}\frac{Yt^2}{4} \tag{3.8}$$

denotes the fully plastic bending moment per unit length of cell wall.

Substituting equations (3.4) and (3.5) into (3.3), and simplifying, we obtain

$$dW_b = 2\pi(M_P)\ \{[d - x_1 \sin(\beta - \phi)]d\beta + [d + 2(x_1 + x_2)\sin\phi - x_2 \sin(\theta + \phi)]d\theta\} \tag{3.9}$$

and

$$W_b = \frac{\pi Yt^2}{\sqrt{3}}\{\int_0^{\frac{\pi}{2}+\phi}[d - x_1\sin(\beta-\phi)]d\beta + \int_0^{\frac{\pi}{2}-\phi}[d + 2(x_1+x_2)\sin\phi - x_2\sin(\theta+\phi)]d\theta$$

$$= \frac{\pi Yt^2}{\sqrt{3}}[\pi d + 2(x_1+x_2)\sin\phi(\frac{\pi}{2}-\phi) - (x_1+x_2)\cos\phi] \tag{3.10}$$

The mean strain in extending the segment between hinge lines A and B, during incremental change dβ, is

$$e_1 = \frac{-x_1\cos(\beta-\phi)}{d - x_1\sin(\beta-\phi)}d\beta \tag{3.11}$$

Also, for segment between hinge lines B and C,

$$e_2 = \frac{-x_2\cos(\theta+\phi)d\theta}{d + 2(x_1+x_2)\sin\phi - x_2\sin(\theta+\phi)} \tag{3.12}$$

By denoting the hoop stress in the extended composite as Y, the increment of plastic dissipation in stretching is,

$$dW_m = Ye_1\pi[d - x_1\sin(\beta-\phi)]x_1t + Ye_2\pi[d + 2(x_1+x_2)\sin\phi - x_2\sin(\theta+\phi)]x_2t \tag{3.13}$$

where the subscript m pertains to the membrane deformation.

substituting (3.9) and (3.10) into equation (3.11) leads to

$$dW_m = \pi Yt[x_1^2\cos(\beta-\phi)d\beta + x_2^2\cos(\theta+\phi)d\theta] \tag{3.14}$$

Integrating it, we have

$$W_m = \pi Ytx_1^{\,2}\left|\sin(\beta-\phi)\right|_0^{\frac{\pi}{2}+\phi} + x_2^{\,2}\left|\sin(\theta+\phi)\right|_0^{\frac{\pi}{2}-\phi}$$

$$= \pi Yt[x_1^{\,2}(1+\sin\phi) + x_2^{\,2}(1-\sin\phi)] \tag{3.15}$$

The total energy dissipation is

$$W = W_b + W_m \tag{3.16}$$

The corresponding mean axial post-buckling load,

$$\bar{P} = \frac{W}{h} = \frac{W_b + W_m}{(x_1 + x_2)\cos\phi} \tag{3.17}$$

$$= \frac{\pi Y t^2}{\sqrt{3}}\left[\frac{\pi d}{(x_1 + x_2)\cos\phi} + 2\tan\phi\left(\frac{\pi}{2} - \phi\right) - 1\right] + \pi Y t\left[\frac{x_1^2(1+\sin\phi) + x_2^2(1-\sin\phi)}{(x_1 + x_2)\cos\phi}\right] \tag{3.18}$$

To verify the theoretical model, two sets of samples, i.e. the pure PP and non-woven PET/PP samples are made possessing the same cell parameters: semi-apical angle=16°, cell height h=15mm, D=10mm, d=18mm. The wall thickness measured for the pure PP cell and non-woven composites is t_{PP}=1.15mm and t_{NW}=1.0mm, respectively. The mean peak load and the energy absorption capacity predicted by the theoretical model are obtained and compared with those obtained from experiments, as summarized in Table 3.2. The theoretically predicted mean buckling load and the corresponding energy absorption capacity of a single cell of the three material systems during axial deformation agree well with those obtained from the experiments. The deviation comes up with 5.5 % for the prediction on the PP samples, but only 2 % on the non-woven PET/PP samples. The difference between the predicted and the experiment results may be attributed to the negligence of the deformation of the cell top, non-uniformity of the non-woven fabric reinforced composites and the measurement errors on the deformed cell.

Table 3.2 Measured and predicted mean peak load and energy absorption capacity for a single cell until collapse

Sample	Mean yield stress (MPa)	Buckling load (KN)			Energy absorption capacity (J/g)	
		Maximum peak load (P_{max})	Mean $\bar{P}$			
			Exp.	Theor.	Exp.	Theor.
PP	33.65	1.310	1.071	1.130	11.29	11.91
FV3	23.38	0.957	0.684	0.670	8.68	8.51

3.6.2 Optimization of Cellular Geometry

Section 3.6.1 shows that the prediction of the mean peak load of the cellular structure depends on the three factors: thickness t, height h and the apical angle ϕ. The optimized cell parameters for fabricating non-woven cellular structures are the ϕ =16°, h=15mm, D=10mm, d=18mm. This cell geometry is optimized to obtain the desired energy absorption capacity for the knitted reinforced cellular composites.

The optimization of the cell geometry can be achieved from experiment. There are three geometrical variables including the thickness, the cell height and the apical angle. A 2^3 factorial design of non-woven composite cellular structure with eight sets of cellular geometry can be done to approximately identify the best combination of the geometrical factors. To design the experiment, each geometrical factor can be selected in a range of maximum and minimum. The optimized cell geometry can be identified through the observation of the value of the mean peak load level of each experimental set. From experimental results, it may observe any other deformation modes being different as the geometry is changed. However, it is not a feasible way to do these experiments even for such eight sets of cell geometry because the

thermoplastic composites are fabricated by compression molding using a designed mold with one specified cell geometry. The tests would be too expensive for extra mold making and time consuming.

An alternative approach to the optimization of geometry to achieve the desired energy absorption capacity of the non-woven composites can be easily done by solving the prediction as derived in section 3.6.1. Analytically we can find the optimized parameters by partial differentiation of the function $\overline{P}$ (Equation 3.18). It is able to find all the relative maximum or minimum of the function and further compare with the boundary.

$$\frac{\partial \overline{P}}{\partial t} = 0 \quad , \quad \frac{\partial \overline{P}}{\partial \phi} = 0 \quad , \quad \frac{\partial \overline{P}}{\partial x_1} = 0 \tag{3.19}$$

Then, the values of thickness t, apical angle ϕ and the x_1 at maximum are found after solving the equations.

As the mean peak loads are predicted by the function $\overline{P}$, they should have the same deformation mode, that is, the internal convolution of the cell wall, each factor should not be set too wide. Thus, the thickness is ranged from 0.9 – 1.2 mm, apical angle from 12° to 20° and the cell height from 10 mm to 20 mm. From the experiment in section 3.5, it is observed that the internal buckling of the non-woven composite cell wall happened on 1/4 of the cell height. Therefore, some assumptions have to be made.

- all of the possible factor combinations will produce the same deformation mode
- the ratio of x_1 to x_2 is 1/4 for all sets of geometrical design

After solving the equation, it is found that the maximum values at the boundary of the factors – cell height and cell wall thickness, and the minimum value at the boundary of the semi-apical angle, give the highest mean peak load and the energy absorption capacity.

3.7 Concluding Remarks

In this chapter, the cellular composites made of PP and non-woven polyester fabric demonstrate their ability for fabricating the complicated structure. PET/PP non-woven composites and pure PP panel have been characterized with regard to their energy absorption behaviour and deformation mechanisms under impact conditions. The fracture of the composites becomes less obvious with increasing fibre volume fraction. Increase in the fibre volume fraction in non-woven composites improves the shear strength and composite toughness under impact. In addition, brittle fracture on the cell tops can be avoided by a high fibre volume fraction, thus allowing the large plastic deformation of cell till its densification. The non-woven composites exhibit high specific energy absorption capacity and retain the same capacity during multiple impacts.

A theoretical model has been presented to predict the mean peak load and energy absorbing capacity of the cell during plastic collapse. The theoretical predictions for pure material or non-woven reinforced composite are all in good agreement with the experimental results. Hence, the model can provide guidance for design of the similar material systems. Only if the deformation mode is consistent, the designed geometrical parameter of the cells can be as large as possible to obtain maximum energy absorption capacity.

CHAPTER 4

TENSILE BEHAVIOUR OF KNITTED COMPOSITES AND THEIR LARGE DEFORMATION MECHANISM

4.1 Introduction

In the earlier investigation (Xue et al., 2001), it has shown that the membrane deformation of the knitted cellular composites dominates the contribution of energy absorption when the cell collapse is large. However, limited publications have been found on the energy absorption behavior during tensile loading of knitted composites. Kelay et al (1997) studied the tensile deformation mechanisms of warp knitted composites, made of glass and polypropylene/polyurethane composites. Ramakrishna et al (1996) investigated the effects of fabrication conditions on mechanical properties of knitted aramid fibre/polypropylene composite laminates. Only recently, Cox and Davis (2001) studied the energy absorption of weft knitted composites under tensile loading in the wale direction. The composite was made from a narrow knitted strip with three wales and epoxies. The textile preform was knitted with Kelvar fibre tows wrapped in shrinkable tubes.

In this chapter, tensile properties of weft knitted composites are examined in terms of the knitting directions and constituent materials. The deformation process of the knitted loops is studied that will help to depict the similar distortion of reinforcing loops in composites during the large deformation. Then, the deformation mechanisms of the flat composites are identified during tensile loading in micro-scale by in-situ SEM observation that leads to the understanding the insight of the loop fibre bundle

and matrix debonding at critical loads along the loading directions. Fractured surfaces of the composites are also observed to reveal the failure mechanism of the composites. Influencing factors include fabric structure, fibre volume fraction, pre-stretching directions and levels of the knitted fabrics prior to composite fabrication and plasma treatment on fibre surface on the mechanical properties of the knitted composites are also studied.

4.2 Experimental

4.2.1 Materials and Composite Fabrication

The material systems in fabricating knitted composites for the characterization include (1) PET knitted/PP matrix and (2) UHMWPE knitted/LDPE matrix, respectively. They are the same type of material that described in section 2.2.1 but there are more fabric structures and fabric factors to be investigated in this chapter.

PET/PP Knitted Composites

Fabric preforms of interlock and rib 1x1 knitted structures were produced by co-knitting PET and PP multi-filament yarns on the 5-gauge V-bed knitting machine (SHIMASEIKI). The fabric details are shown in Table 2.1. *Fabric II* denotes a pure PP fabric, which was used as a comparison. Some of co-knitted interlock *Fabric I* received a plasma treatment prior to compression molding in an attempt to improve the adhesion between fibres and matrix. The treatment was conducted using a Plasma Polymerization System SPP-001 (Showa Co Ltd., Japan) with a radio frequency of 13.6 MHz. These samples were exposed to low temperature oxygen plasma at a pressure of 15 Pa discharge power of 150 W for 10 or 15 minutes.

Table 4.1 Specifications of the fabric preform samples

PET fabrics	I	II	III
Structure	Interlock	Interlock	Rib 1x1
Yarn blending ratio (PP : PET)	1 : 1.4	1 : 0	1 : 1.4
Tightness factor	13.61	14.02	12.12
Thickness (mm)	3.91	4.09	2.85

UHMWPE/LDPE Knitted Composites

Similarly, the UHMWPE continuous filament yarn of 88 Tex was used to produce the fabrics with interlock knitted structures on the 12-gauge flat-bed knitting machine (SHIMASEIKI). Specifications of these fabrics are shown in Table 2.2 in Chapter 2. Laminates of commercial pure LDPE film of 0.06 mm thick was used as a thermoplastic matrix material for the knitted fabric composites. In order to investigate the effect of fabric pre-stretching on the composite properties, a special bi-axial pre-stretching molding frame was designed (in Appendix 4.1) to hold the stretched fabric during consolidation. The fabrics were pre-stretched on the walewise (10 %, 20 %), coursewise (25 %, 45 %) and bi-axial (5% walewise: 25% coursewise) directions, respectively, as the molding frame held the fabric firmly with the extensions in the corresponding directions.

Flat sheet composite panels as described above were fabricated by compression molding with the same procedures and fabrication parameters as described in Section 2.2.2. Specifications of the produced PET/PP composites and UHMWPE/LDPE composites are given in Table 4.2 and Table 4.3, respectively. The measured thicknesses of the flat samples are lower than the nominal ones because of the material shrinkage during cooling.

Table 4.2 Specifications of the composite samples with PET/PP material system

Sample No.	Fabric structure	Blending ratio (PP : PET)	Composites thickness (mm)	Fibre volume fraction	Ave. composites weight in 17x 17 cm^2 (g)	Pre-treatment
*a*1	Interlock	1 : 1.4	1.05	0.34	30.6	Nil
*a*2	Interlock	1 : 1.4	1.01	0.36	30.0	Plasma 10min.
*a*3	Interlock	1 : 1.4	0.98	0.37	30.3	Plasma 15min.
*a*4	Interlock	1 : 0	1.34	0.00	32.7	Nil
*a*5	Rib 1x1	1 : 1.4	1.15	0.19	18.2	Nil

Table 4.3 Specifications of UHMWPE/LDPE knitted composite (Interlock structure) with various pre-stretching conditions

Sample No.	Treatment	Courses per 5cm	Wales per 5cm	Composite thickness (mm)	Fibre volume fraction
*b*1	No stretch	20.0	26.5	0.87	0.40
*b*2	10% wale pre-stretched	18.0	30.5	0.89	0.40
*b*3	20% wale pre-stretched	17.0	32.0	0.90	0.39
*b*4	25% course pre-stretched	22.0	20.0	0.76	0.37
*b*5	45% course pre-stretched	23.0	16.5	0.68	0.36
*b*6	Bi-axial pre-stretched, 5% wale: 25% course	21.5	19.0	0.77	0.35

4.2.2 Tensile Tests on Fabrics, Composites and Pure Matrix

Tensile tests were conducted on the PET knitted fabric (*Fabric I*), composites and sheet of pure matrices. Fabric specimens each for PET and UHMWPE fabrics were cut in 200mm×200mm parallel to the three directions, i.e. walewise, diagonal and coursewise directions. The clamp width was 150 mm and gauge length of 75 mm. The tensile test was carried out on the Instron (Model 4466) Material Testing Machine with a 10KN-load cell at a crosshead speed of 100 mm/min. During the tensile testing, a high speed digital camera (1000 films/sec.) with a digital TDI camera power supply (Model RS4015) was set up, as illustrated in Fig. 4.1, to record the fabric loop distortion. The images were captured at the middle region of the clamped area.

Tensile tests on composite and pure matrix specimens were carried out according to the ASTM standard D3039-93. Specimens were cut into narrow strips of 150mm×20mm. In the case of knitted composites, the strips were cut parallel to the walewise, coursewise or diagonal directions. The composite specimens were tested on the MTS Universal Testing Machine with a maximum 10 KN-load cell at a loading speed of 5 mm/min. The gauge length between the top and bottom grip was set as 80 mm. Five specimens were tested for each composite type or pure materials.

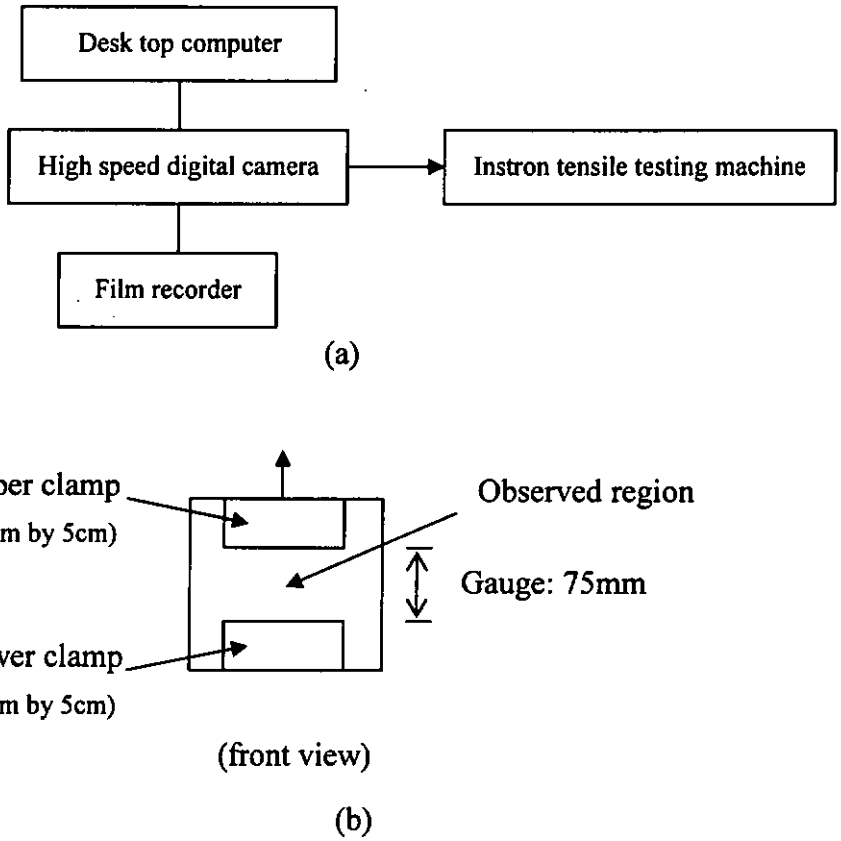

Figure 4.1 (a) Schematic diagram of the experimental setup of knitted fabric tensile testing, (b) Illustration of the fabric sample placement on the tensile machine

4.2.3 In-situ SEM Observation Set-up

Lecia Steroscan 440 Scanning Electron Microscopy was employed to observe the morphological changes of the interlock knitted structure and the fibre/matrix debonding during tensile deformation. PET/PP composite samples were cut in a dimension 12mm×40mm along the wale, course and biaxial directions. Both composite strip ends were glued to two metal plates in the centre of which a hole being inserted with a pin attached to the loading device. Schematic diagram of the tested specimens is illustrated in Fig. 4.2. The loading speed was set as 8 m/s. All

samples were gold coated to avoid surface charging during the in-situ tensile test by SEM.

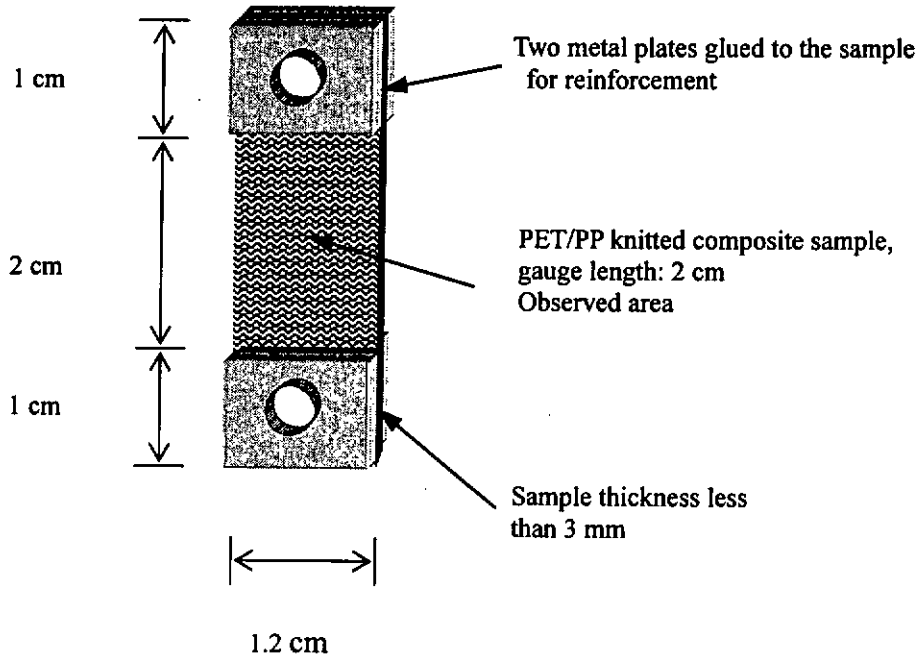

Figure 4.2 Schematic diagram of composite sample prepared for in-situ SEM tensile testing

4.3 Tensile Behaviour of Knitted Composites and their Components

PET/PP Knitted Composites

Figure 4.3 shows the tensile curves of a single PET fibre, the pure PP matrix, the knitted composite (sample *a*1), and the pure PET fabric in the walewise, coursewise and diagonal directions. Both knitted fabric and composite samples exhibit strongly anisotropic non-linear tensile behaviour.

For the composite samples, the tensile strength of the composites in the walewise

direction is the highest among the three loading directions. The material properties of single PET fibre, PP matrix and the composites with three loading directions are summarized in Table 4.4. It is found that initial elastic modulus and yield stress are the largest in the walewise direction, followed by those in the diagonal and coursewise direction, and thus the tensile properties of the composites are orientation-dependent. All the three stress-strain curves undergo a very short elastic deformation stage compared with the long plastic deformation. The slope of the initial linear portion of the stress-strain curves is calculated as the initial elastic modulus. The yield stress is defined as the highest stress prior to the drop in load for the interlock composites. For those rib 1x1 structures (sample *a5*) which exhibit a stress-strain curve with a gradually decreasing slope, the yield stress was identified at a point where the first departure from linearity occurred.

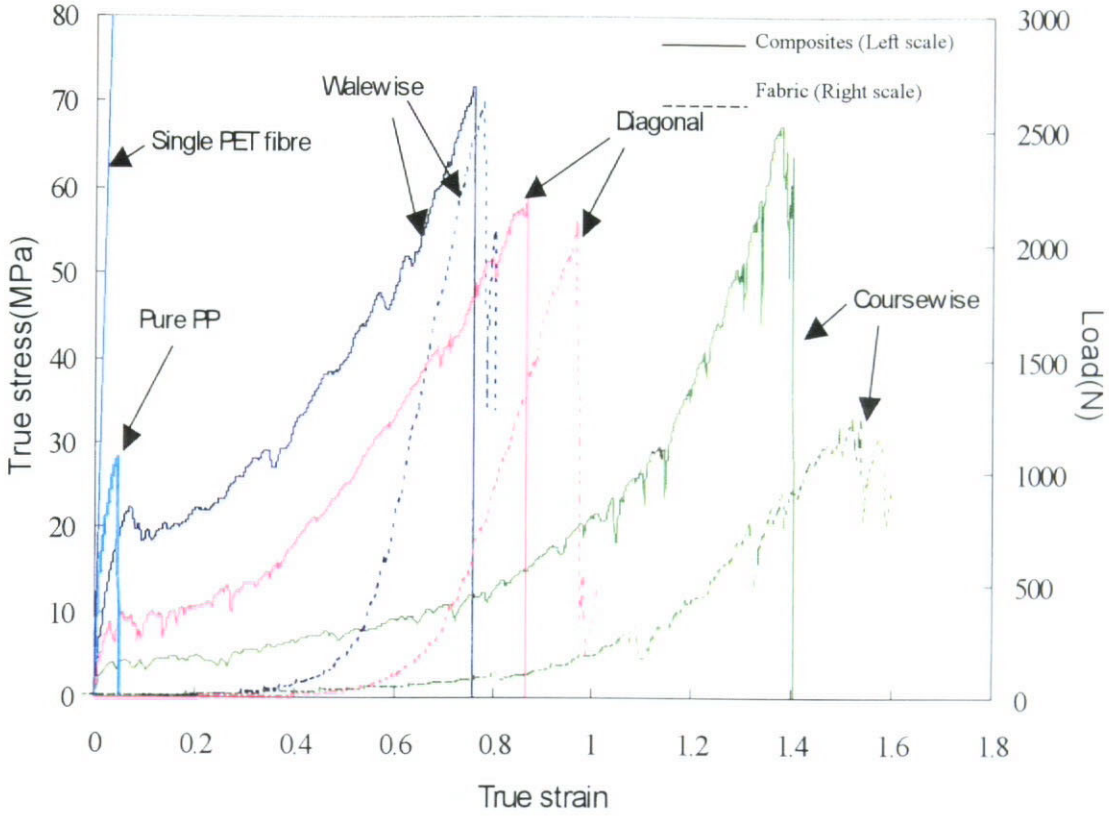

Figure 4.3 Typical tensile behaviours of a single PET fibre, the pure PP matrix, the interlock knitted fabric and the composite (sample *a*1)

The distinctive properties of the composites material from its individual components can be seen from their stress-strain curves as shown in Fig. 4.3. Pure PP has high strength but only reach a maximum strain of 0.04, which is brittle and lack of ductility. Although both fabrics and composites show similar extensibility, the fabric exhibits very low loads until strain hardening is reached. Comparing the fabric and composites, it is clearly observed that matrix has contributed most of the load bearing in the elastic region. On the other hand, the fibre is ductile with a breakage strain of 0.17. The tensile properties of reinforcing fibres are illustrated in Fig. 4.4. With the presence of reinforcing fibres oriented as knitted fabric loops, the composite

material extends up to a maximum strain of 1.4 in the coursewise direction. The fibre and matrix alone can only deform much less than the composites. It is the structural change that contributes most to the large strain of composites. The maximum strain in the coursewise direction of the interlock composite (sample *a*1) is the largest among the three loading directions. The matrix between two interfaced loops is under compression while the other under tension. Even though both of the knitted fabric and composite samples exhibit strongly anisotropic non-linear tensile behaviour, the debonding between fibres and matrix as well as breakage of matrix of the composites have given rise to a constant and relatively much higher stress level in the large plastic deformation, thus results in a high energy absorption level, in contrast with the low and non-linear tensile curve of the pure PET fabric. Thus, the knitted composite materials perform superior energy absorption capacity to their individual components during the large deformation.

Table 4.4 Material properties of single PET fibre, pure PP matrix and PET/PP co-knitted composite (sample *a*1) (values in square brackets are standard deviations)

Materials	Single PET fibre	Pure PP matrix	Composites		
Loading direction	Axial	Isotropic	Wale	Diagonal	Course
Young's modulus (MPa) [STD]	13000.0	1443.0	511.0[0.62]	309.1[0.84]	137.7[0.67]
Yield stress (MPa) [STD]	--	--	22.8[0.90]	7.8[0.72]	4.1[0.17]
Yield strain [STD]	--	--	0.10[0.02]	0.07[0.01]	0.05[0.01]
Maximum stress (MPa) [STD]	975.0	27.4	71.1[0.59]	58.1[1.56]	67.4[1.31]
Maximum strain [STD]	0.047	19.0	0.76[0.06]	0.87[0.11]	1.38[0.05]

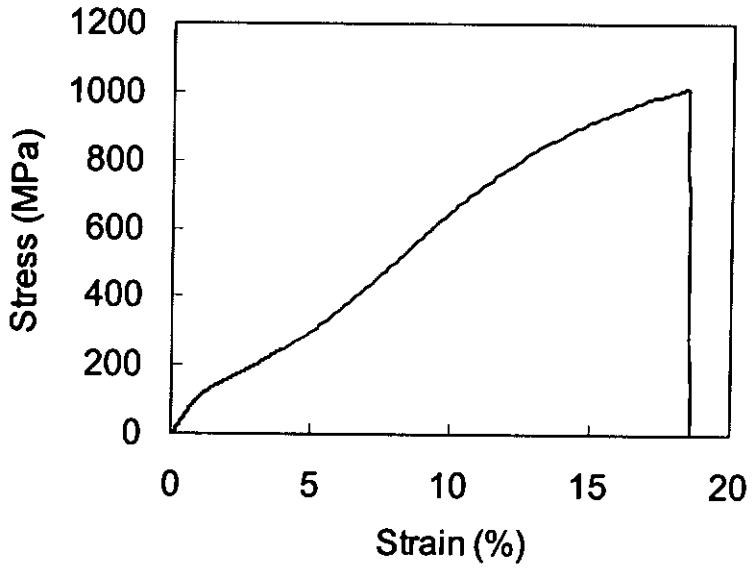

Figure 4.4 Stress-strain curve of a single PET fibre

UHMWPE/LDPE Knitted Composites

The tensile behaviour of the UHMWPE fibre, matrix and composites are shown in Fig. 4.5 and their material properties are compared in Table 4.5. UHMWPE fibre possesses high strength and very low elongation whereas the knitted fabric has non-linear tensile behaviour. Both fabric and composite show anisotropic properties as seen in the walewise and coursewise directions. Composites on walewise direction display higher stiffness and tensile strength than in the coursewise direction while the energy absorption capacity in both directions is similar (~20 MJ/m^3). Matrix takes up most of the load and then the fabric loop is deformed to share the load. LDPE matrix is very ductile with a very large ultimate strain (880 %) and thus exhibits a high-energy absorption level (113 MJ/m^3) than the composites. The large stress concentration leads to the failure of the composite fibre loops at the points where most of the matrix is fractured. Although the matrix is very ductile, the large deformation mechanism is similar to those PET/PP knitted composites.

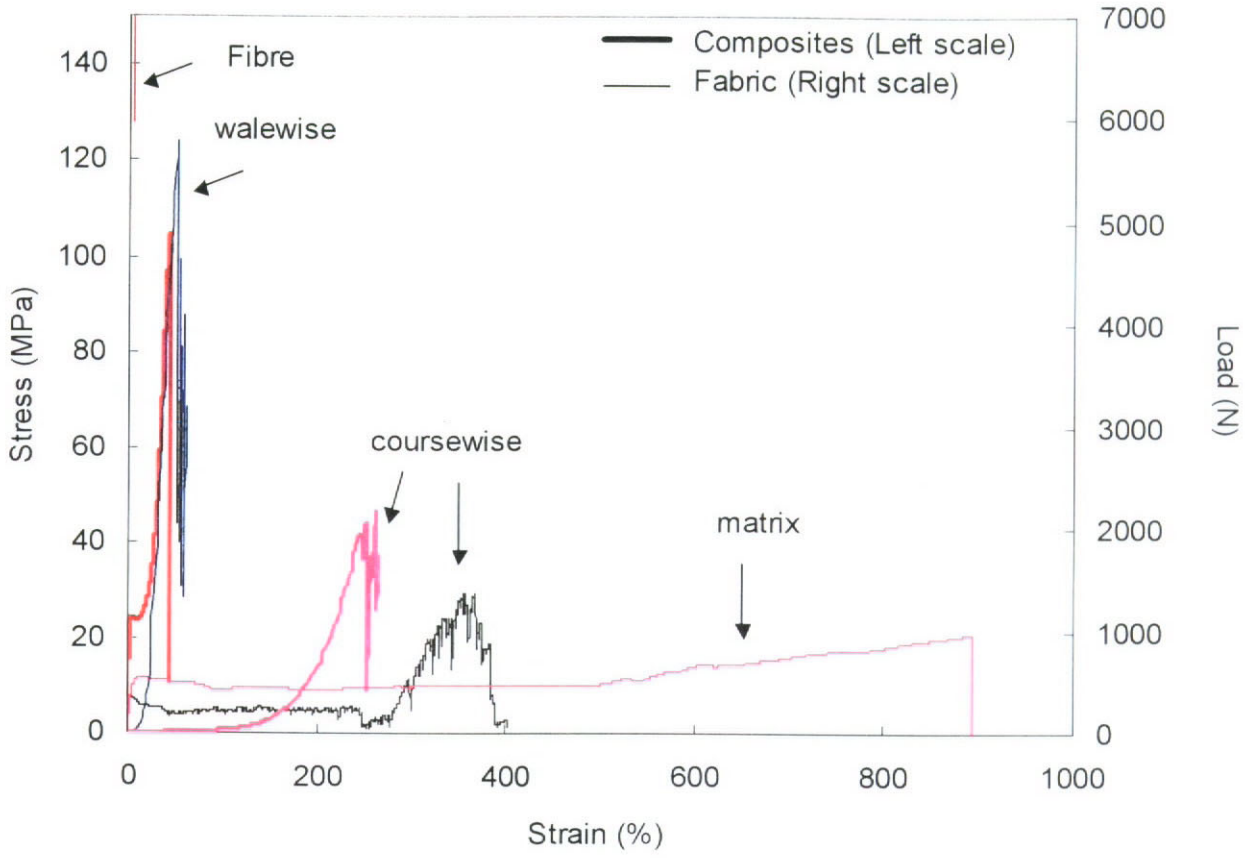

Figure 4.5 Material properties of the knitted composite and its components

Table 4.5 Material properties of the interlock UHMWPE fabric/ LDPE matrix composites

Sample	Young's modulus (MPa) [s.d.]	Yield stress (MPa) [s.d.]	Yield strain (%) [s.d.]	Ultimate stress (MPa) [s.d.]	Ultimate strain (%) [s.d.]	Energy absorption (MJ/m^3) [s.d.]
HMWPE fibre	110000	-	-	3400	3.60	-
DPE matrix	300.99 [31.08]	11.27 [0.44]	9.42 [0.41]	20.21 [1.61]	879.59 [31.29]	113.43 [9.56]
omposite alewise, b1	2271.35 [386.89]	22.71 [2.65]	2.90 [0.24]	104.20 [14.16]	44.24 [3.23]	18.34 [1.42]
oursewise, b1	1060.13 [146.44]	8.46 [0.44]	2.92 [0.29]	30.68 [1.58]	349.81 [8.75]	19.28 [0.07]

4.4 Large Deformation Mechanism of Weft-Knitted PET Fabric

A series of images, as shown in Fig. 4.6, were captured to investigate the loop distortion in the PET interlock fabric subjected to large deformation in the wale, the diagonal and the course directions. The changes in loop dimensions as illustrated in Fig. 4.7 were measured during the tensile tests. Figures 4.8 (a-c) quantitatively describe the amount of changes in loop height (h), loop width (w), distance between loop legs (l) and distance between wales (d), of a knitted loop being extended in the three knitting direction as observed in Fig. 4.6.

As the fabric is extended in the wale direction, as shown in Fig. 4.6 (a), the wale loops are straightened and become thinner. Thus, the matrix in the two interlacing loops in composites is compressed by the legs and that in between the loop is extended. The fibre loops become densely packed and aligned along the loading direction, which contributes to a higher strength and stiffness. For the diagonally extension of the fabric, as shown in Fig. 4.6 (b), all the fibre loops are straightened and thinner as there is sliding of the wale loops with respect to each other as the load increases, thus shifting the angle of wale loops, from approximately 58° to 82° near tensile failure. As a consequence, the wale loops are elongated and straightened. It has been found that there are similar changes in loop shape when the fabric loops are extended in the wale and diagonal direction. Figures 4.8 (a) and (b) show that there is a significant increase in loop height (h), a slightly reduction of loop width (w) and the distance between loop legs (l), but the distance between wales (d) remains unchanged. As shown in Fig. 4.6 (c), the vertical rows of yarn loops are diversely extended outwards to a greater extent which involves a substantial movement of yarns from wale loops and fibre yarns straightened between wales during tensile

loading in the coursewise direction. It is shown in Fig. 4.8(c) that there is an extensive straightening of the fibre loops between wales and the distance (d) is measured to have a significant increase with the fabric strain. However, the loop widths (w), the distance (l) and the loop height (h) have slightly or no significantly dropped with the fabric strain. Thus, a lower fibre density decreases in sharing the load but maximize in extensibility. Due to low levels of friction on the smooth fibre surface, free yarn rotations and sliding of fibre loops occur resulting in a large distortion of the fabric loops. The localized compression and extension of the matrix are presented in all the three knitting directions.

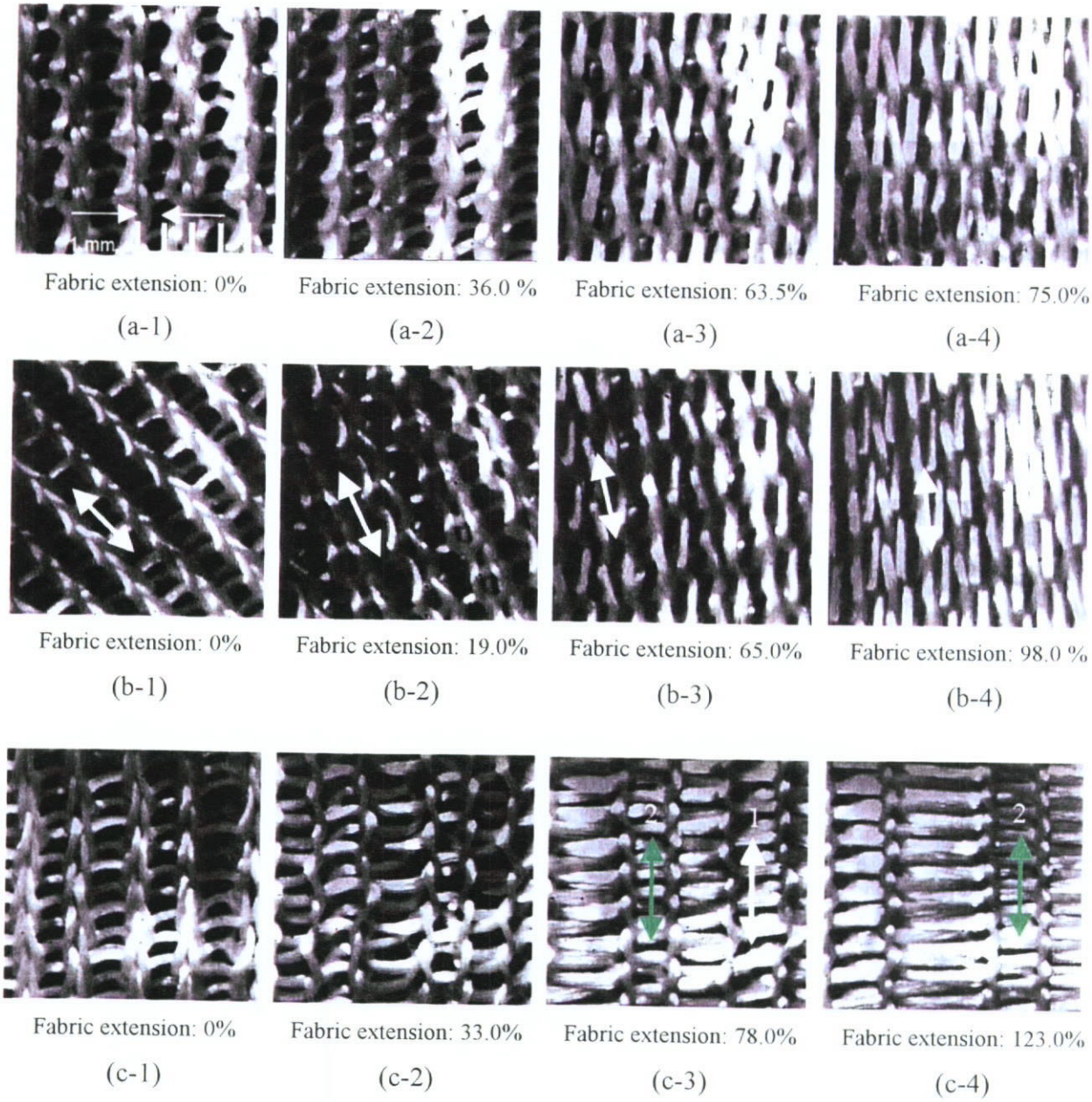

Figure 4.6 The fibre loop deformation of PET knitted fabric under tension (a) along the wale direction, (b) along the diagonal direction; (c) along the course direction. (arrows " ◄► indicating the same wale loops during fabric extension)

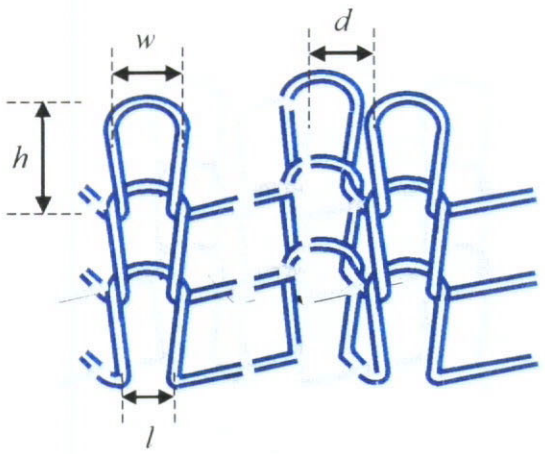

Figure 4.7 Schematic diagram of the dimension measurement on the weft knitted loops during fabric stretching

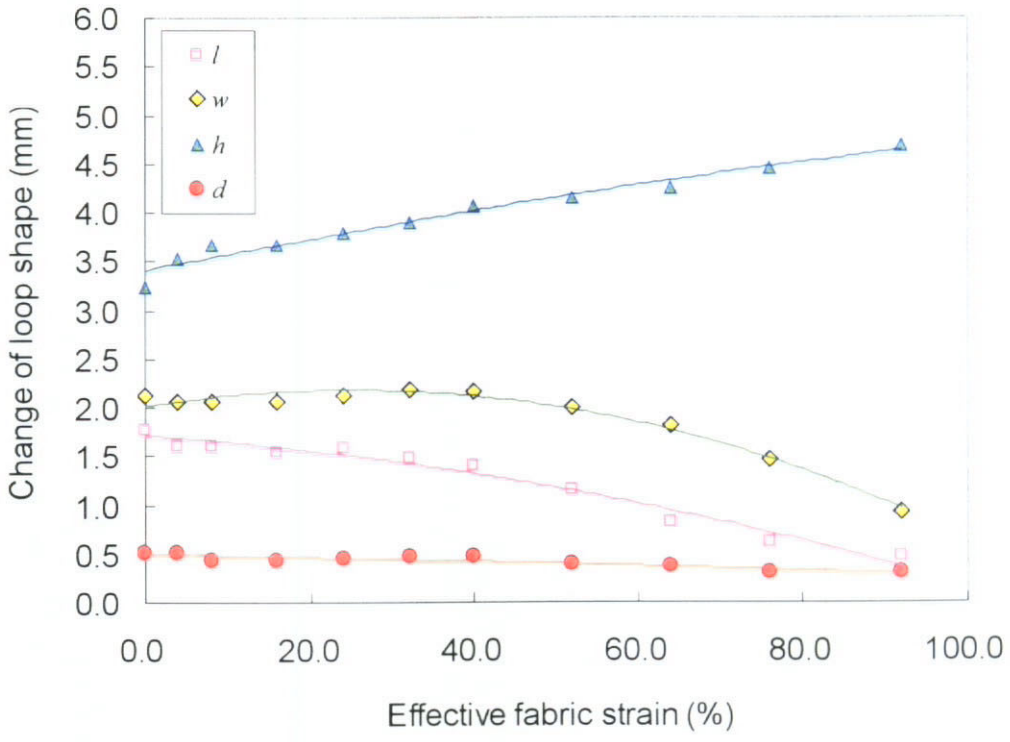

(a)

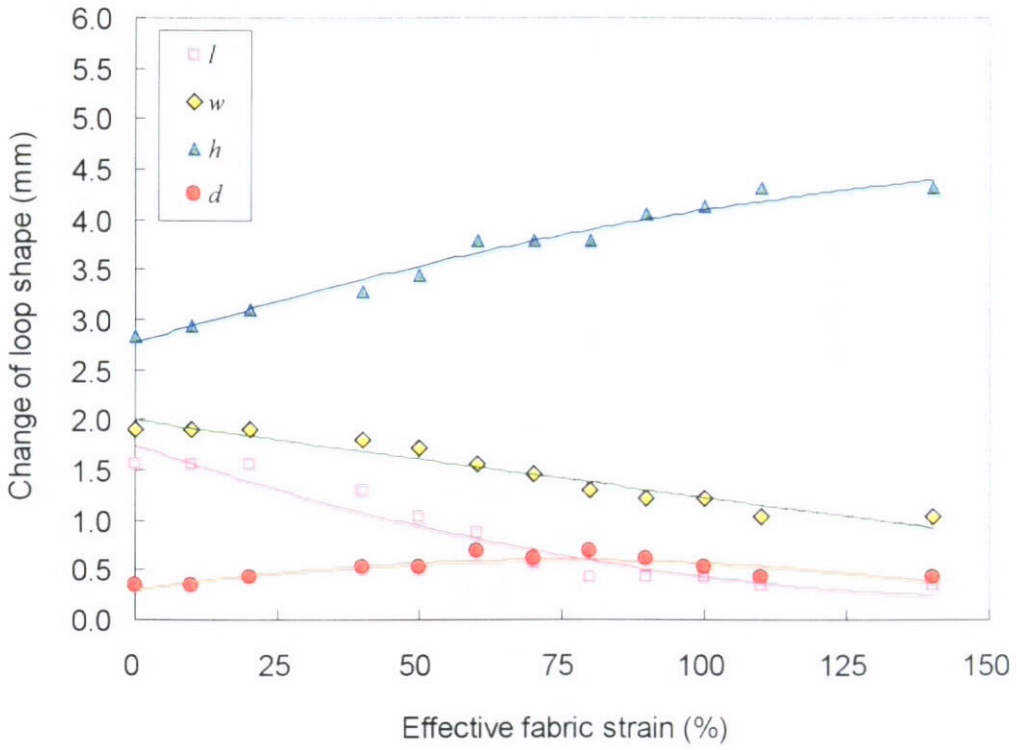

(b)

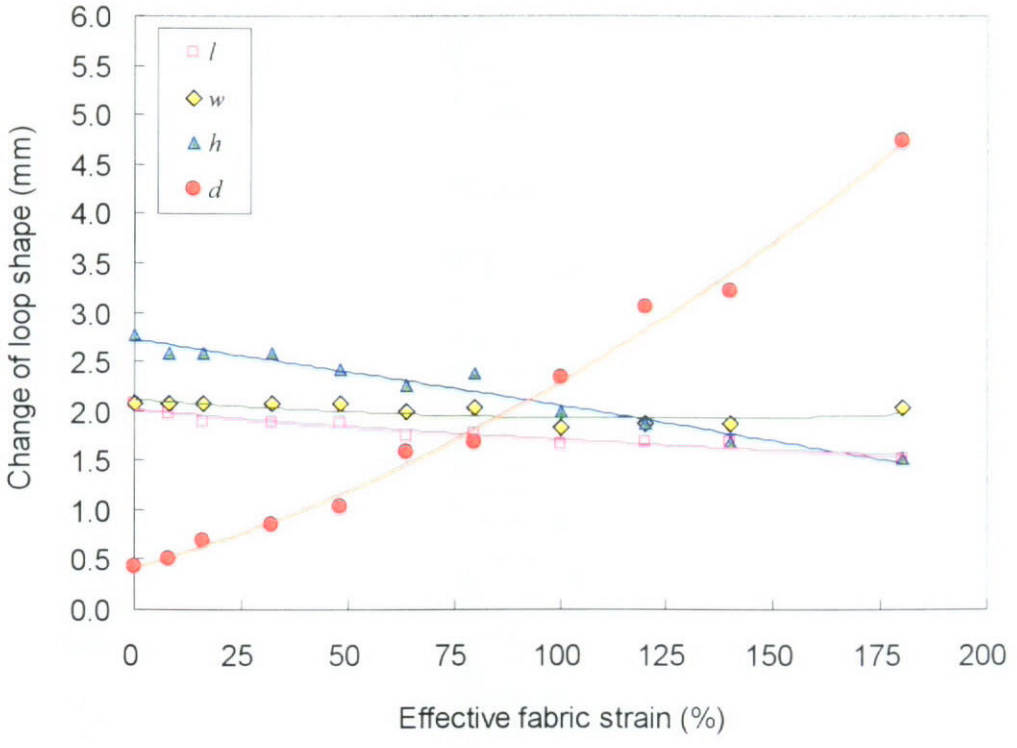

(c)

Figure 4.8 The change in loop dimensions with the applied tensile strain in the (a) wale, (b) diagonal and (c) course directions

4.5 Observation on the Composite Deformation by In-situ SEM

4.5.1 Large Deformation Mechanism of the Composites

The deformation process was monitored by in-situ observation of the deformation of a mounted sample with a Scanning Electron Microscope, as illustrated in Fig. 4.9 (a)-(c). The composite surface, as shown in Fig. 4.9 (a-1), (b-1) and (c-1), is rough and imperfect with small slits. Some fibres are exposed on the composite surface. This imperfect structure with rough surface will facilitate the crack initiation and accommodate the large deformation of the composite structure.

The mechanisms of tensile deformation of the textile composites can be identified as localized stressing of matrix, brittle matrix crack initiation, fibre/matrix debonding in composite material, localized loop distortion along the loading directions and large deformation leading to composite fracture.

Tensile loading of interlock composites in the wale direction is shown in Fig. 4.9 (a). The matrix cracking starts at a true strain of 0.1, as shown in Fig. 4.9 (a-2). As the strain increases to 0.26, the matrix crack spreads along the imperfect contour lines or slits above the fibre loop bundles, as illustrated in Fig. 4.9 (a-3). Then matrix cracks across the wale loops that further develop into a hole. It allows the wale loop being elongated or straightened and the next wale loop repeats the same process, as shown in SEM micrograph, Fig. 4.9 (a-4). The whitening part of the image reveals the brittle matrix falling off from the surface of sample. A similar deformation process is observed when the wale loops are extended in coursewise and diagonal directions, as shown in Figs. 4.9 (b) and 4.9 (c), respectively. Sliding of yarns and tearing of the fibre loops occur at the sample edge when the strain is 0.41 (Fig. 4.9 (c-4)).

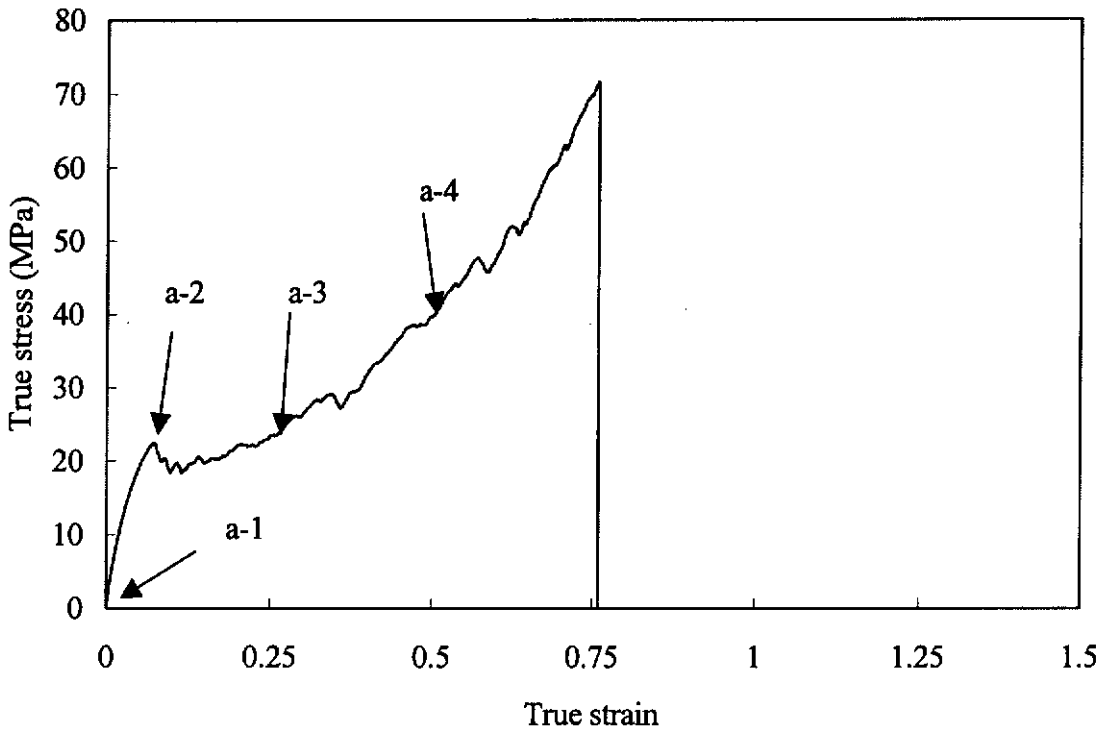

Figure 4.9 (a) Stress-strain curve of interlock textile composite extended in the wale direction

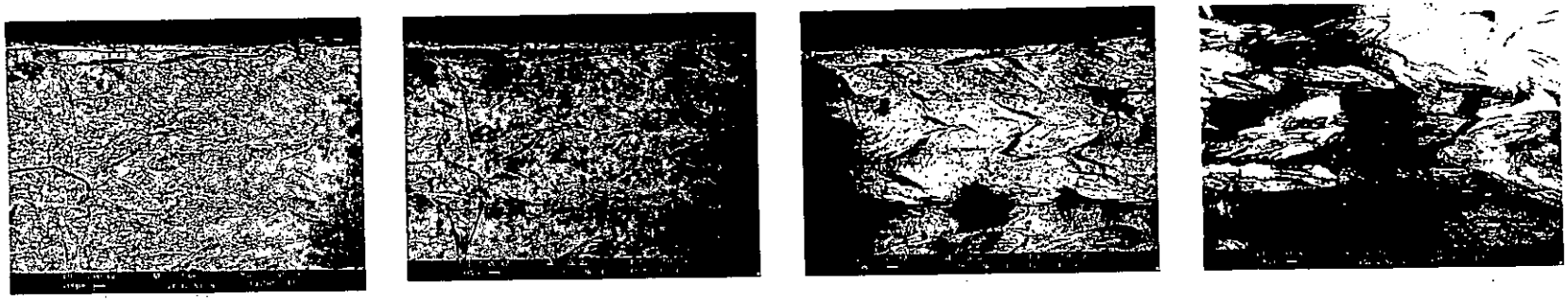

True strain: 0 (a –1)

True strain: 0.10 (a –2)

True strain: 0.26 (a –3)

True strain: 0.41 (a –4)

Figure 4.9 (a –1-4) SEM micrographs at different stages of deformation of interlock knitted composite, tensile loading in the wale direction

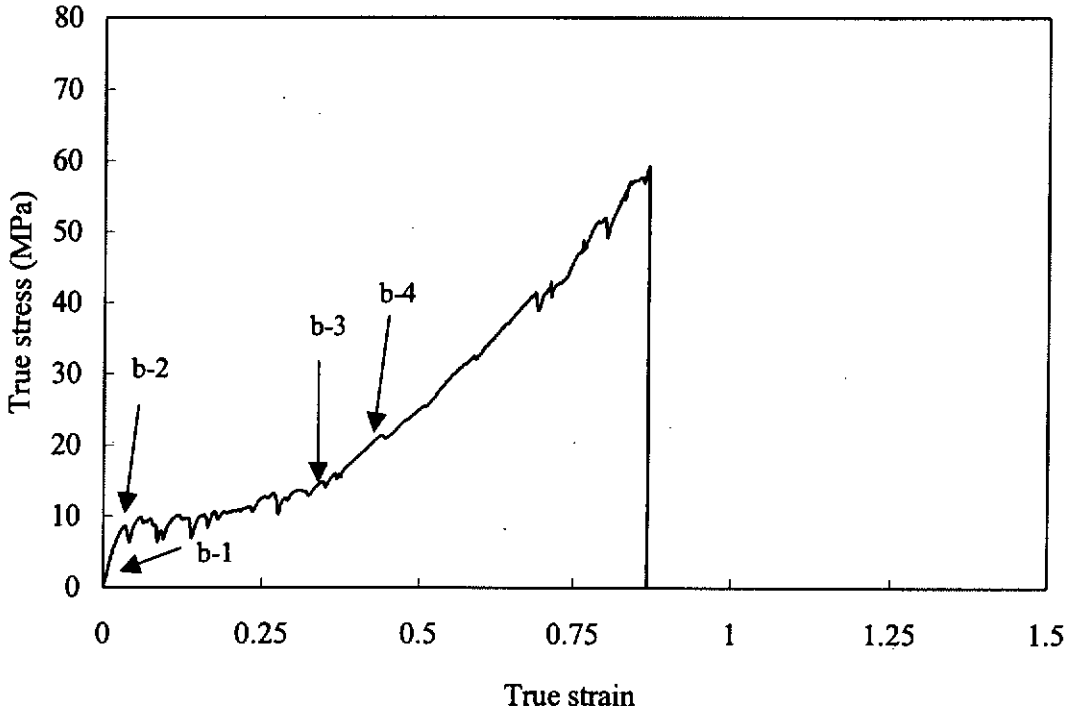

Figure 4.9 (b) Stress-strain curve of interlock textile composite extended in the diagonal direction

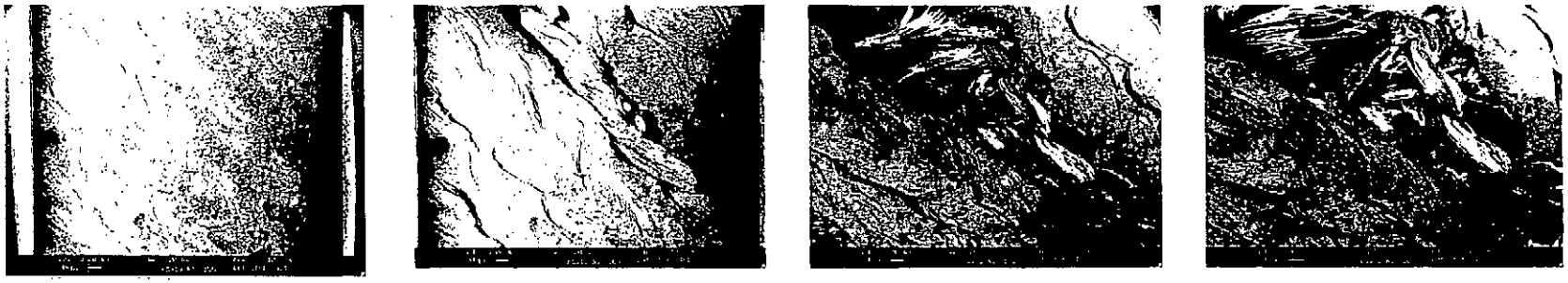

True strain: 0
(b –1)

True strain: 0.07
(b –2)

True strain: 0.34
(b –3)

True strain: 0.41
(b –4)

Figure 4.9 (b–1-4) SEM micrographs at different stages of deformation of interlock knitted composite, tensile loading in the diagonal direction

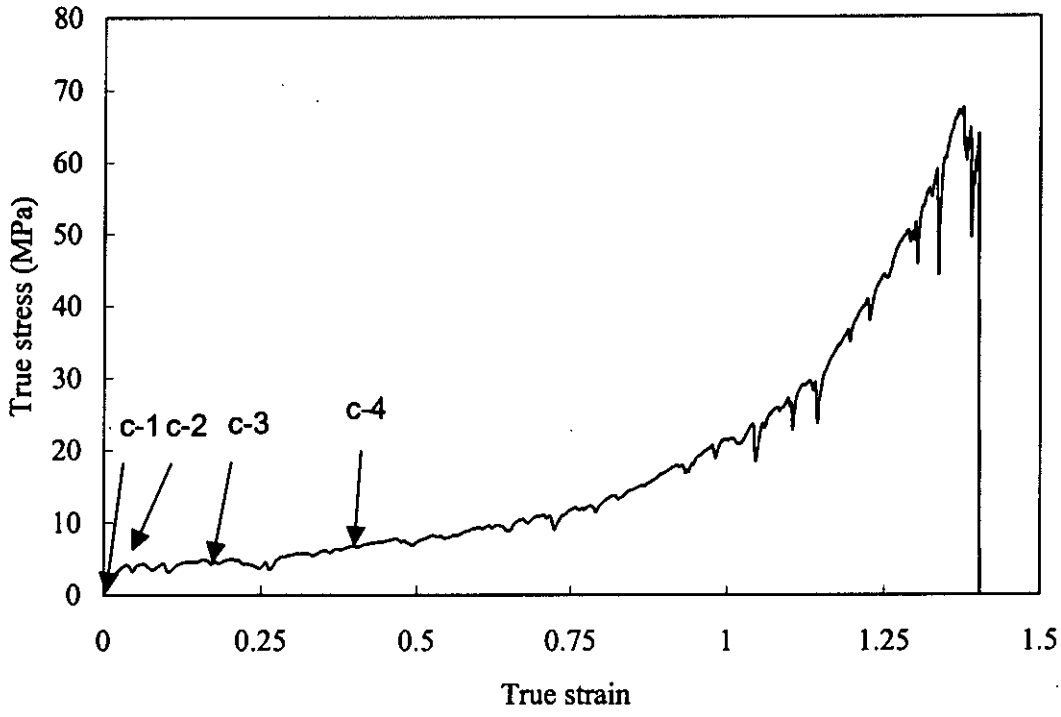

Figure 4.9 (c) Stress-strain curve of interlock textile composite extended in the course direction

True strain: 0 (c –1)

True strain: 0.05 (c –2)

True strain: 0.18 (c –3)

True strain: 0.41 (c –4)

Figure 4.9 (c –1-4) SEM micrographs at different stages of deformation of interlock knitted composite, tensile loading in the course direction

4.5.2 Observation of the Fractured Surface

The further examination of the fractured surface of the knitted composites are demonstrated by observing in the highly stressed region on the composite specimen extended in the wale direction, as shown in Fig. 4.10.

At the fractured surface, micro cracks of matrix have been found that initiate perpendicular to the loading direction. The initiation of matrix cracks across the wale loop can be found where there is the matrix rich region inside the fibre loop, as shown in Fig. 4.11. Further extending the composite will lead to the gradual matrix crack propagation into holes inside the fabric loop, as demonstrated in Fig. 4.9 (a-4). On the other hand, fibre/matrix debonding can be clearly seen on the knitted loop at the interlocking region as shown in Fig. 4.12. The fabric loop contour can be seen more obviously where some fibres are exposed at the fractured surface and its closer view is shown in Fig. 4.13. These matrix cracking and fibre/matrix debonding allow the load transfer to the fabric loop and facilitate the large loop distortion. The straightening of the fibre loops can be seen in Fig. 4.14. The next wale loops in the composite specimen will follow the similar process until the stress/strain hardening of the fabric loop and composite fracture.

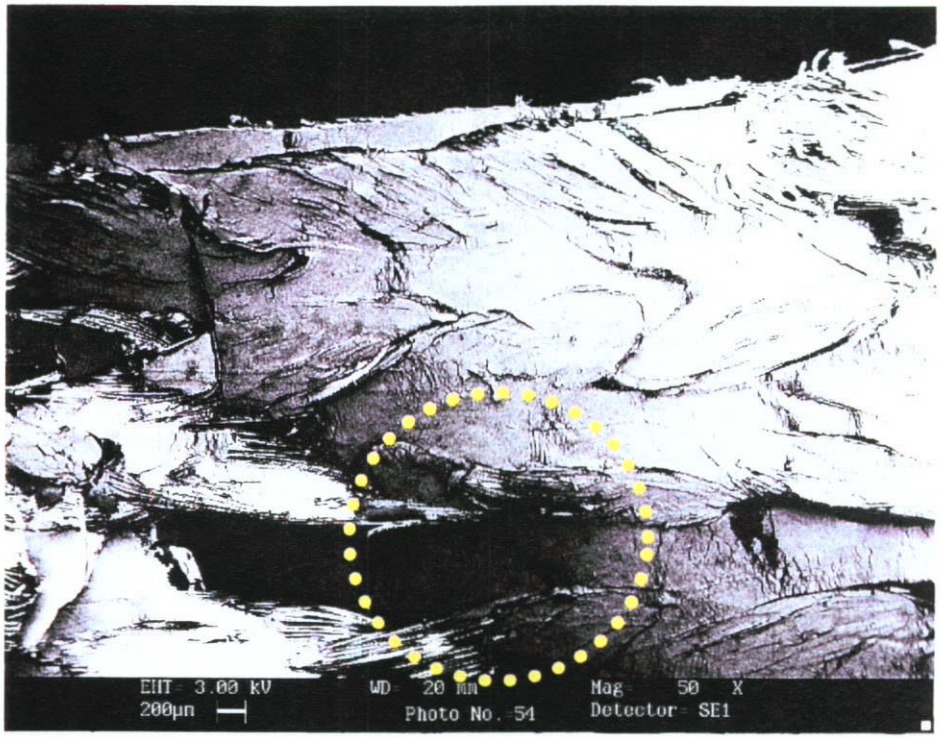

Figure. 4.10 The close up region selected for observing the fractured surface of the knitted composite

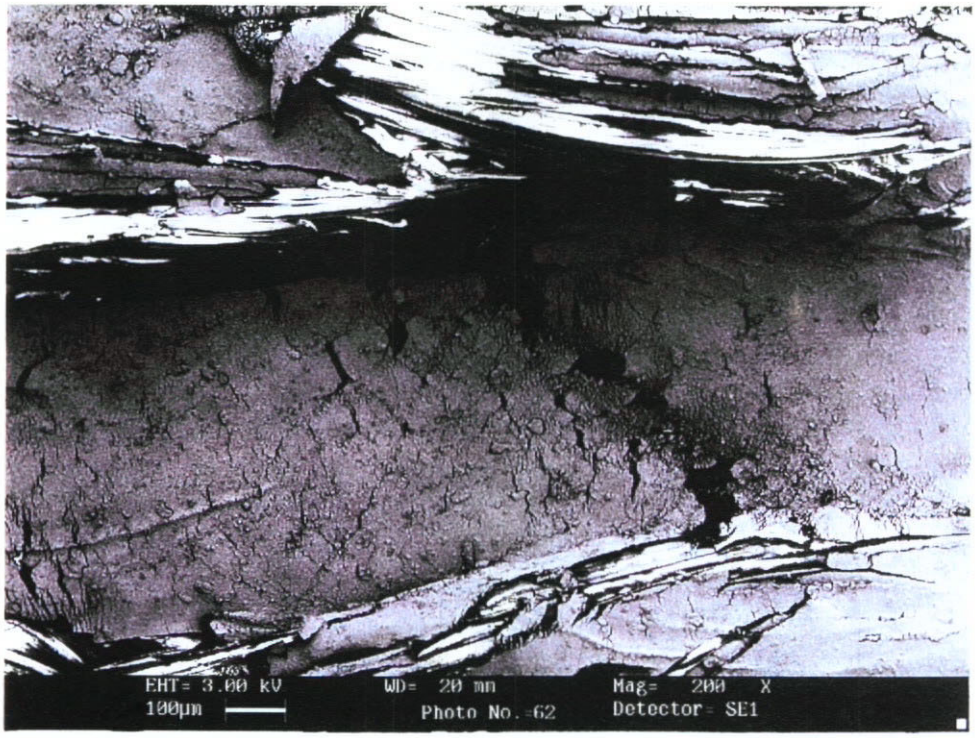

Figure. 4.11 The PP matrix crack across inside the wale loop

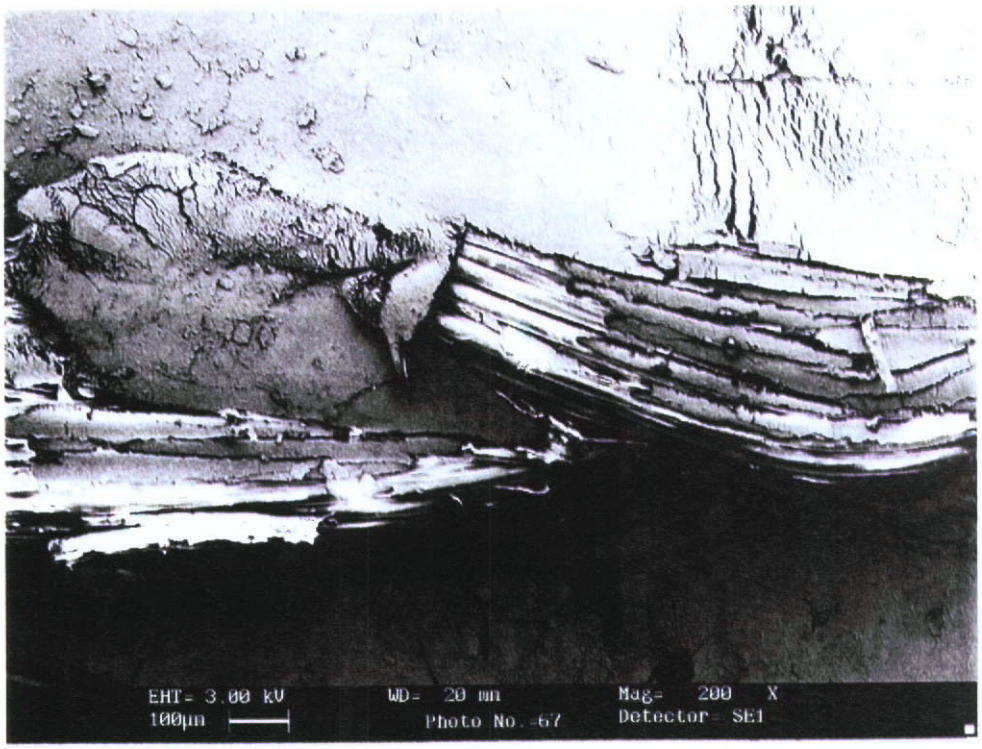

Figure. 4.12 The fractured surface of the composite loop at the interlocking region

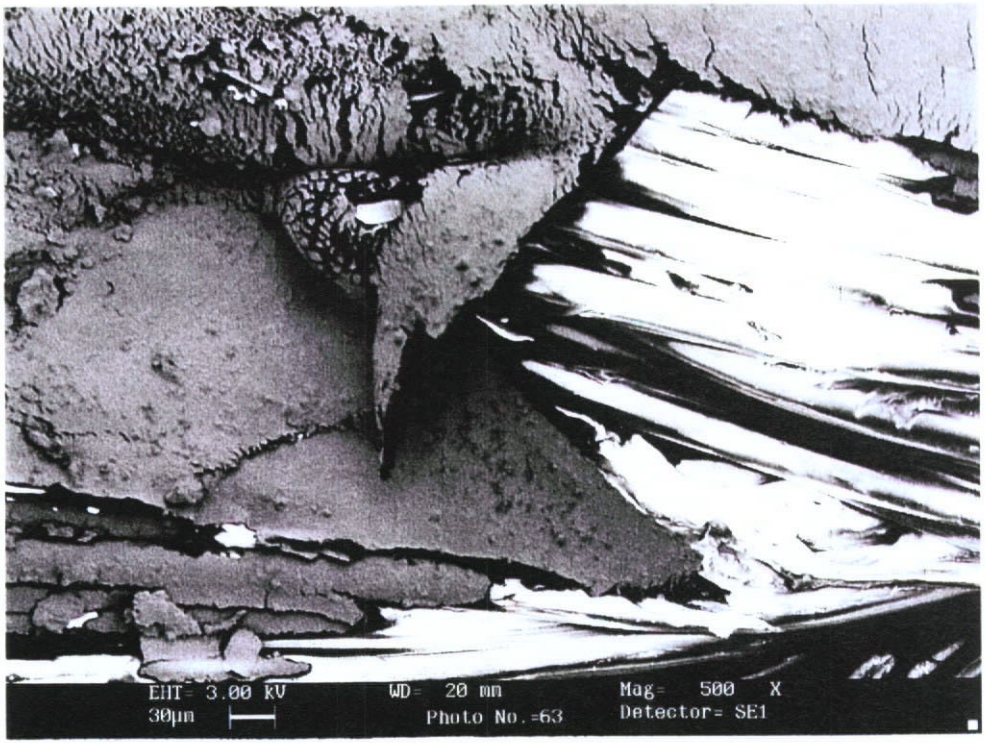

Figure. 4.13 A closed up view of the Fig. 4.12

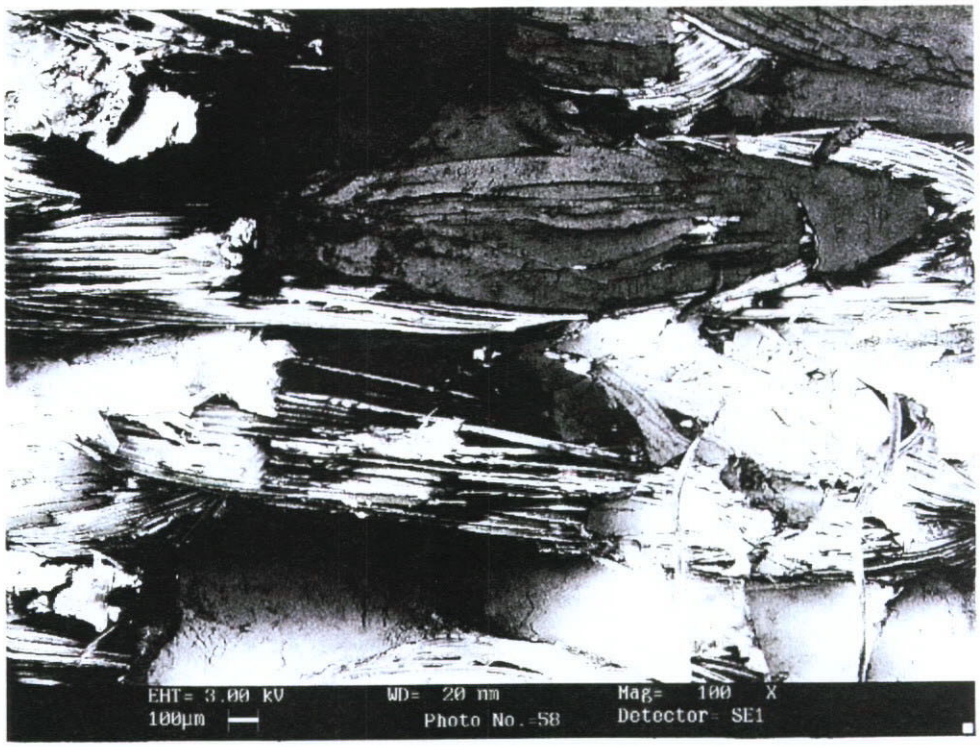

Figure. 4.14 The fibre/matrix debonding, matrix fracture and further straightening of the fabric loop at large strain

4.6 Effects on Tensile Properties of the Textile Composites

4.6.1 Fabric Structure and Fibre Volume Fraction

Figure 4.15 shows the stress-strain curves of interlock (sample *a*1) and rib 1×1 (sample *a*5) knitted composites in the walewise direction, having fibre volume fraction of 0.34 and 0.19, respectively. Their material properties are summarized in Table 4.6.

The interlock composite has a much higher Young's modulus and yield stress than the rib composite. Both composite samples exhibit a large deformation before fracture.

The interlock composite shows approximately three folds of the stress level in the large deformation regime higher than the rib composite. The tensile strength of the interlock structure is almost three times, in both walewise and coursewise, higher than those of rib 1×1 composite. The difference in tensile behaviour of the two knitted structures can be attributed to the fibre volume fraction in the composites. Interlock fabric can be considered as a double-layered rib 1×1 structure. The more reinforced fibres in interlock (sample *a*1) (Vf: 0.34), the higher strength and stiffness they should have when compared with those of rib composite (sample *a*5) (Vf: 0.19). Besides, the thinner rib 1×1 fabric does not fully fill up the molded space that resulted in a higher void content and relatively soft in handle.

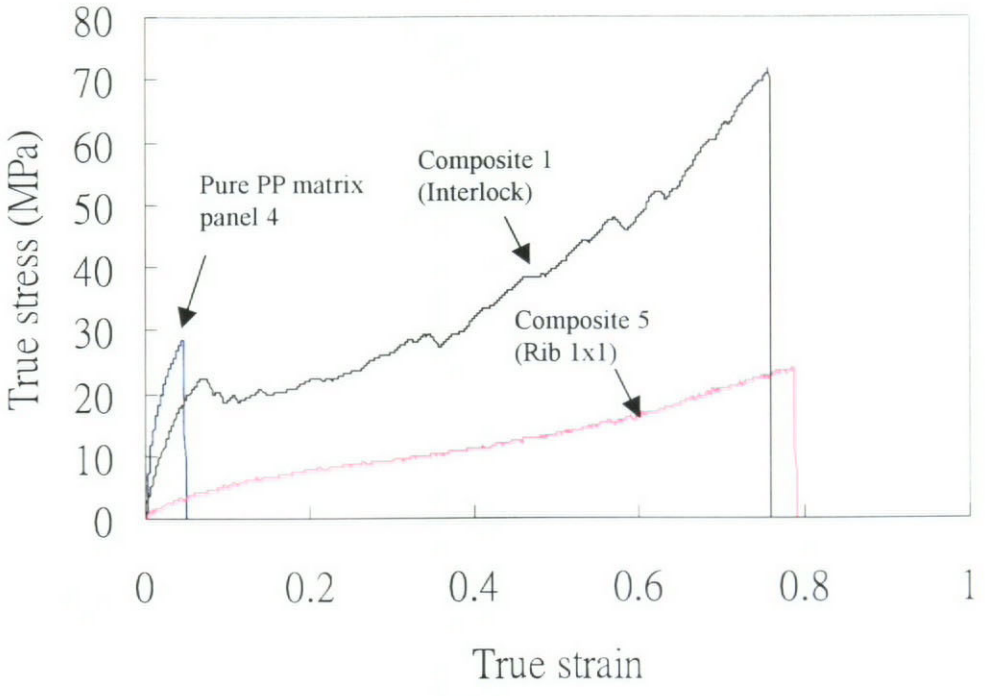

Figure 4.15 Effects of fabric structure and fibre volume fractions

Table 4.6 Comparison of material properties of interlock composite (sample *a*1) and rib 1x1 composite (sample *b*1) (values in square brackets are standard deviations)

Composites			Elastic modulus (MPa) [STD]	Yield stress (MPa) [STD]	Yield Strain [STD]	Ultimate stress (MPa) [STD]	Ultimate strain [STD]
No.	Structure	Knitting direction					
*a*1	Interlock	Wale	511.0[0.62]	22.8[0.90]	0.10[0.02]	71.1[0.59]	0.76[0.06]
*a*5	Rib 1X1	Wale	51.5[0.08]	5.3[0.44]	0.15[0.06]	24.1[0.20]	0.79[0.02]
*a*1	Interlock	Course	137.7[0.67]	4.1[0.17]	0.05[0.01]	67.4[1.31]	1.38[0.05]
*a*5	Rib 1X1	Course	55.8[0.16]	3.6[0.23]	0.12[0.01]	21.9[1.29]	1.23[0.51]

4.6.2 Plasma Treatment on Fibre Surface

The effect of plasma treatment can be identified on the PET knitted composites samples *a*1 to *a*3, being tested along the wale direction. The true stress-strain curves are depicted in Fig. 4.16. The plasma treatment, which brings surface morphological change and increases surface energy, has shown some positive effect on the tensile properties of the composite samples. There is a rise of stress level in the large deformation regime with the increase of plasma treatment time. It is particularly increased by almost 25 % for the 15-min treatment. Figure 4.17 shows the SEM micrographs of surface morphology of PET fibres as received and after the plasma treatment. The as-received PET fibres have a smooth surface as shown in Fig. 4.18 (a); the surface roughness increases with plasma exposure time as shown in Figs. 4.17 (b) and (c). This surface modification on the reinforcing fibres is believed to improve the interfacial adhesion between reinforcing fibres and matrix. The improvement on interface has led to a higher interfacial strength and better load transfer from fibres to matrix.

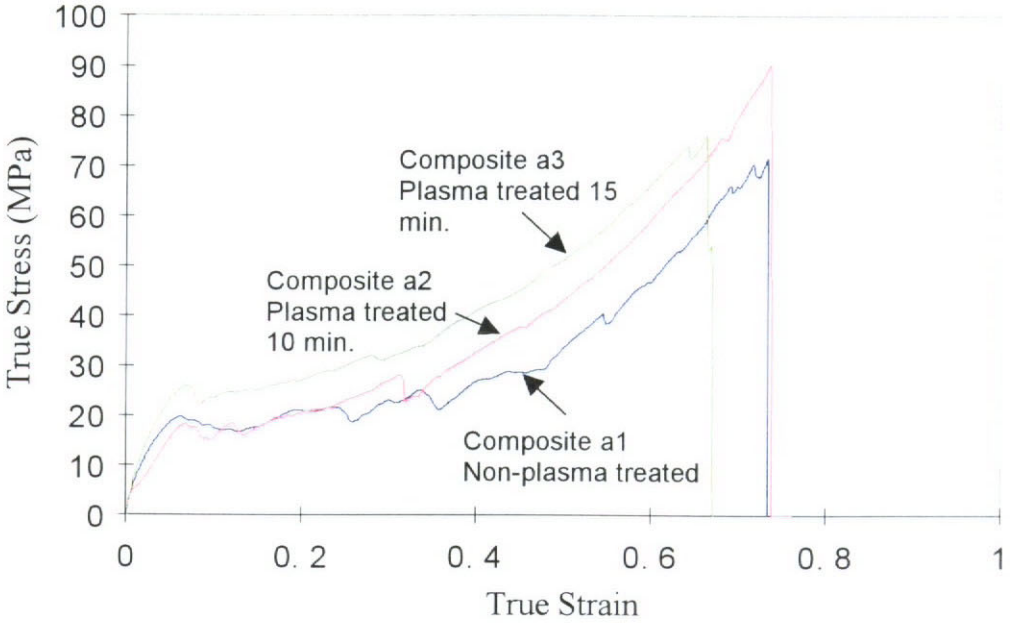

Figure 4.16 Effect of plasma treatment on PET fibres

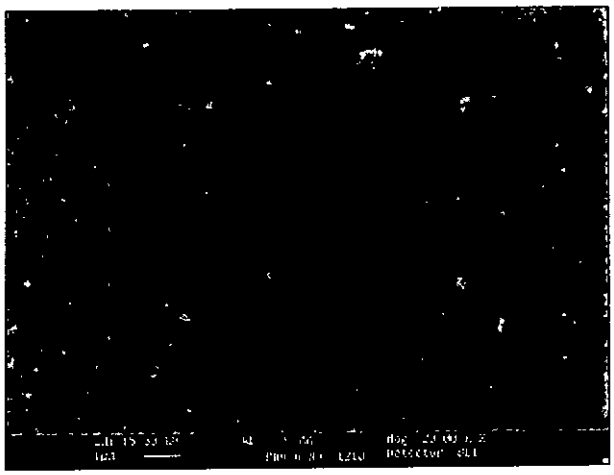

(a)

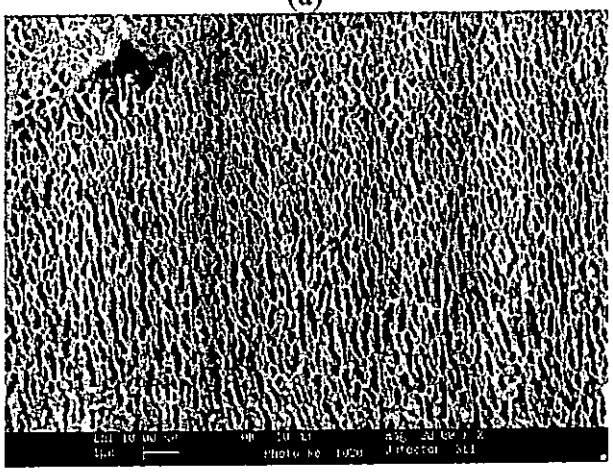

(b)

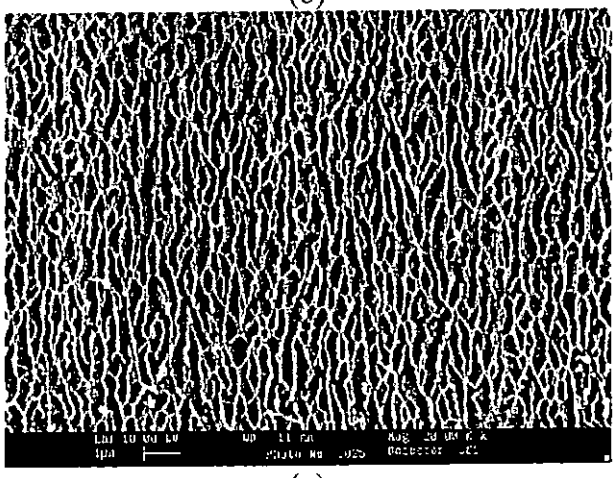

(c)

Figure 4.17 SEM micrographs showing sections and their enlarged views of PET fibre surface morphology (a) non-plasma treated, (b) 10min. treated, and (c) 15 min. treated

4.6.3 Pre-stretching Direction

The effect of composite pre-stretching along three knitting directions are demonstrated in UHMWPE/LDPE composites as shown in Fig. 4.18 (a) for specimens deformed in the wale direction and Fig. 4.18 (b) in the course direction. For the composites with the same pre-stretching and test directions, there are an increase in stress level and a reduction in ultimate strain. When the pre-stretching direction is opposite to the test direction, there is a slight variation stress level and an increase in the ultimate strain. While the bi-axial specimens show a limited increase in the stress level but drop in the ultimate stress in the walewise tested specimens, for the coursewise testing, the bi-axial stretched specimens shows an increase in tensile strength and drop in strain. The mechanical properties of all the composite specimens are given in Table 4.7. All the walewise tested specimens show much stiffer than the coursewise tested specimens. It is interesting to note that the energy absorption level of the 0 % pre-stretched composites is similar in both tested directions. For the walewise tested specimens, all pre-stretched samples display some increase in energy absorption. While for the coursewise tested samples, most pre-stretched samples doubles energy absorption capacity to the 0% pre-stretched samples except the 20 % wale pre-stretched specimens.

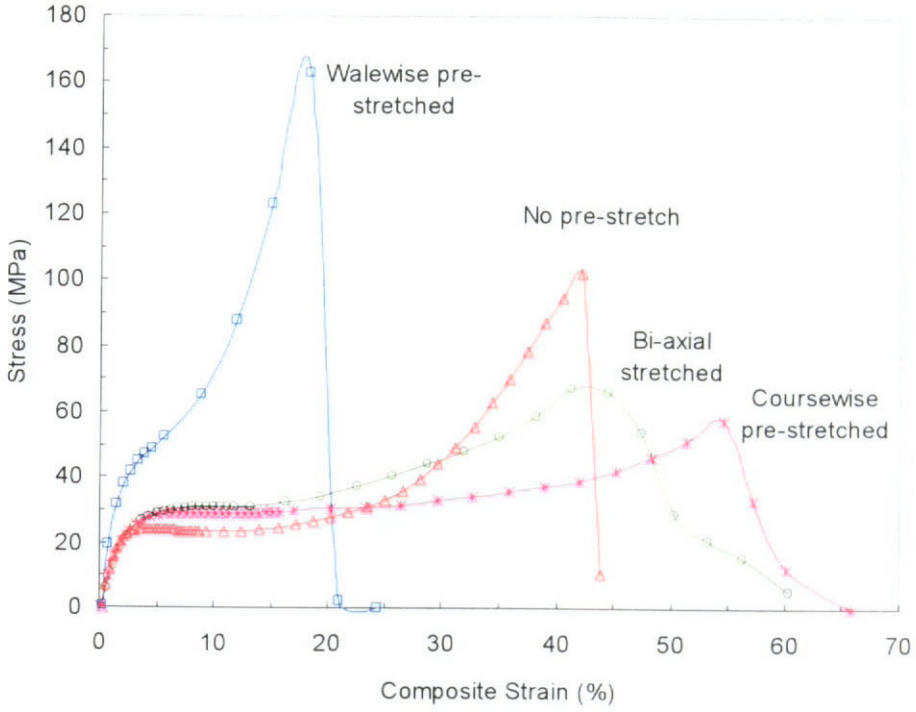

(a)

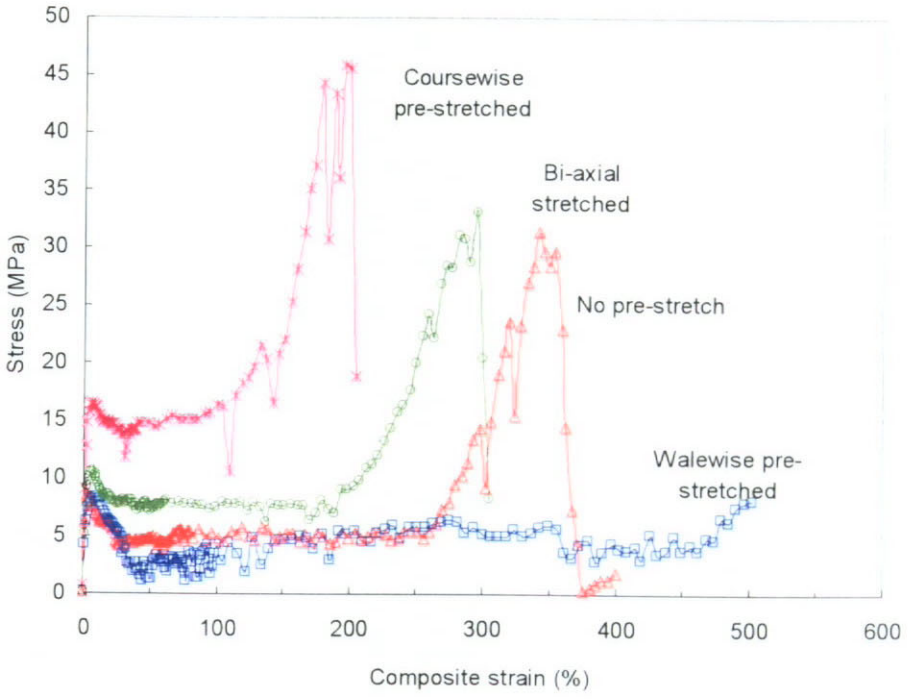

(b)

Figure 4.18 Effects of pre-stretching directions in 20% walewise, 45% coursewise, (5% walewise and 25% coursewise) bi-axial and non pre-stretched on composite mechanical properties (a) deformation in walewise, (b) deformation in coursewise

4.6.4 Pre-stretching Level

Figure 4.19 (a) shows the stress-strain curves of UHMWPE/LDPE composite samples including 0% and 20 % walewise pre-stretched fabric, 10 % and 20 % walewise pre-stretched composites deformed in the wale direction. Figure 4.19 (b) shows the 0% and 50 % coursewise pre-stretched fabric, 25 % and 45 % coursewise pre-stretched composites deformed in the course direction. In Fig. 4.19 (a) and (b), both pre-stretching direction and the testing direction are the same. It is noted that with the increase in pre-stretching level, the stress plateau level generally increases, whereas the failure strain decreases. It may be contributed by the straightening of the fabric loop to the corresponding pre-stretching direction. When examining the effect of walewise pre-stretching on the fabric, most of the fibre loops are straightened and aligned more densely at 20 % pre-stretched state, extending these fibre loops would result in a higher load and the fibre are more stiffer than the non stretched fabric. When the fabric is 50 % pre-stretched in the course direction, only the maximum strain reduces without causing the increase in fabric load. However, composites with 25 % pre-stretched in the coursewise direction leads to a significantly increase in the stress level.

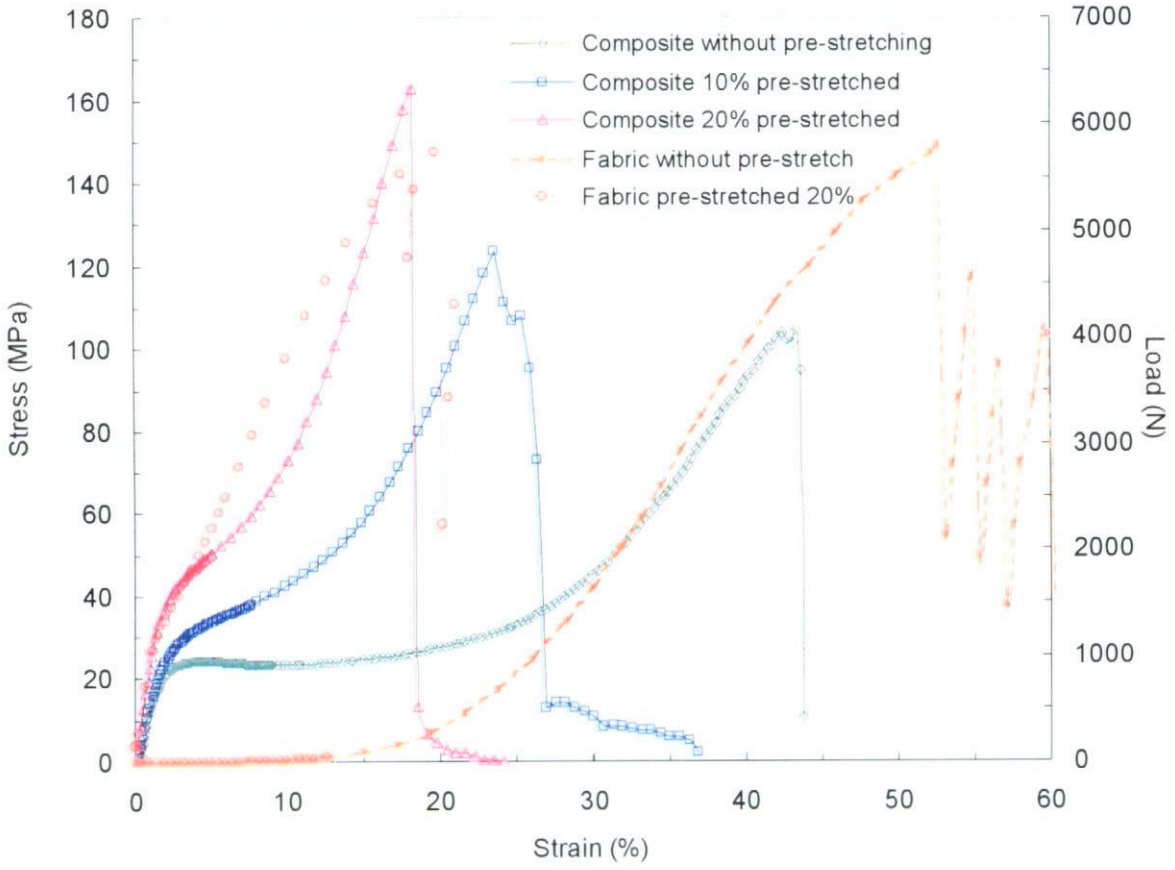
Composite without pre-stretching
Composite 10% pre-stretched
Composite 20% pre-stretched
Fabric without pre-stretch
Fabric pre-stretched 20%
Stress (MPa)
Load (N)
Strain (%)
0
20
40
60
80
100
120
140
160
180
0
1000
2000
3000
4000
5000
6000
7000
0
10
20
30
40
50
60

(a)

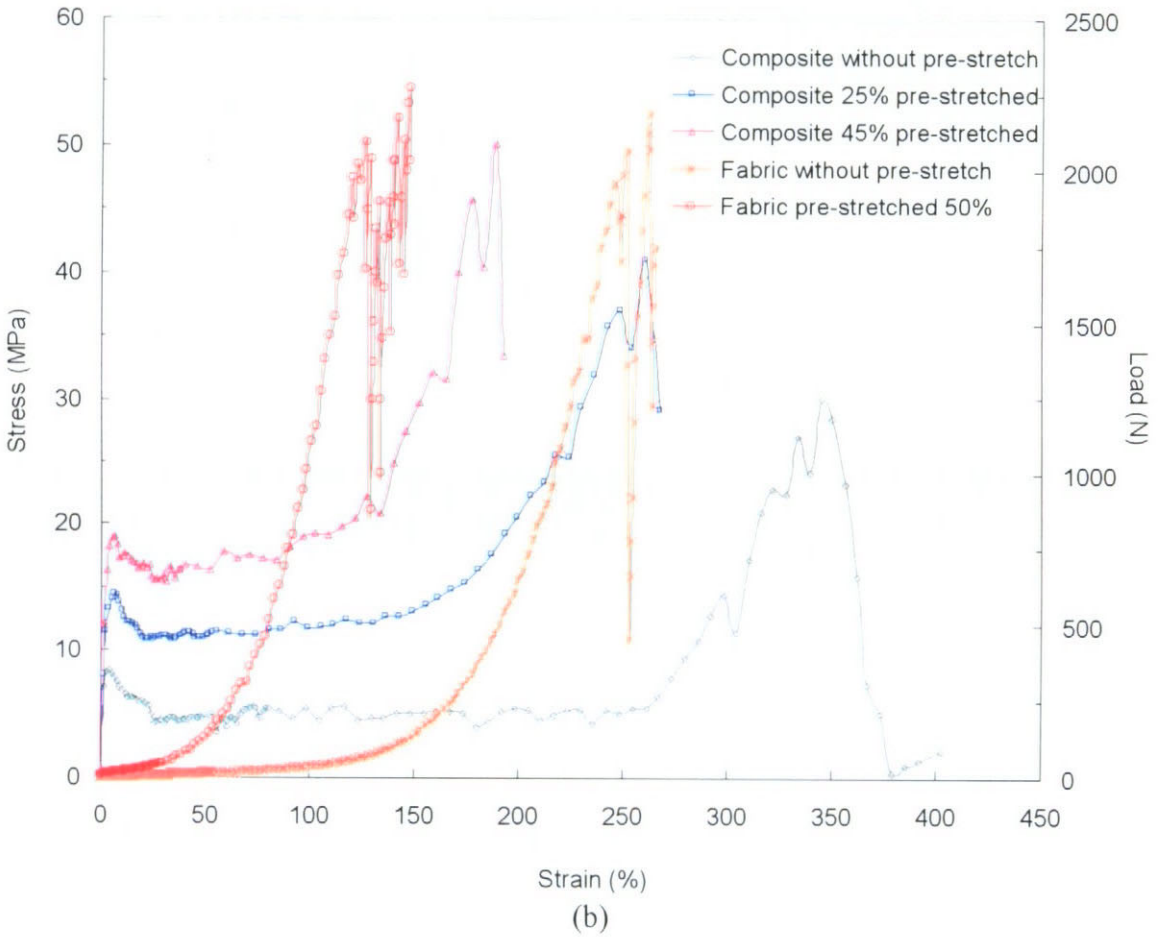

(b)

Figure 4.19 Effect of pre-stretching level on composites and fabric specimens (a) pre-stretched on walewise and deformed on walewise direction, (b) pre-stretched on coursewise and deformed on coursewise direction

Table 4.7 Effects of pre-stretching on material properties of the UHMWPE Interlock knitted fabric/ LDPE matrix composites (values in square brackets are standard deviations)

Sample	pre-stretching	Young's modulus (MPa) [s.d.]	Yield stress (MPa) [s.d.]	Yield strain (%) [s.d.]	Ultimate stress (MPa) [s.d.]	Ultimate strain (%) [s.d.]	Energy absorption (MJ/m^3) [s.d.]
	Deformed walewise						
*b*1	No	2271.35 [386.89]	22.71 [2.65]	2.90 [0.24]	104.20 [14.16]	44.24 [3.23]	18.34 [1.42]
*b*2	10% walewise	1204.77 [263.60]	26.71 [3.12]	2.14 [0.23]	127.45 [8.08]	24.79 [3.08]	16.04 [0.64]
*b*3	20% walewise	2958.05 [562.24]	33.60 [2.36]	1.69 [0.26]	148.71 [16.88]	18.26 [2.47]	15.58 [0.97]
*b*4	25% coursewise	2302.51 [402.84]	28.07 [0.86]	3.98 [0.17]	85.80 [2.34]	50.71 [2.87]	21.96 [0.92]
*b*5	45% course wise	2203.10 [231.12]	28.42 [1.05]	4.48 [0.28]	60.74 [4.97]	54.20 [4.30]	20.97 [1.48]
*b*6	Bi-axially 5% wale: 25% course	1587.08 [250.10]	29.18 [2.00]	4.76 [0.21]	79.77 [12.49]	43.96 [4.00]	20.58 [1.49]
	Deformed coursewise						
*b*1	No pre-stretch	1060.13 [146.44]	8.46 [0.44]	2.92 [0.29]	30.68 [1.58]	349.81 [8.75]	19.28 [0.07]
*b*2	10% walewise	1009.09 [27.63]	10.62 [0.08]	4.57 [0.21]	19.38 [1.14]	485.23 [14.22]	45.24 [1.07]
*b*3	20% walewise	550.76 [36.75]	8.16 [0.41]	7.06 [0.73]	11.34 [2.94]	497.53 [2.43]	24.06 [3.14]
*b*4	25% coursewise	1273.91 [67.75]	14.83 [0.34]	6.65 [0.33]	43.92 [3.49]	257.10 [8.44]	45.72 [4.44]
*b*5	45% coursewise	1767.08 [127.34]	17.15 [1.12]	4.72 [0.69]	52.77 [2.86]	192.70 [6.11]	44.16 [2.11]
*b*6	Bi-axially 5% wale: 25% course	962.94 [58.72]	11.54 [0.60]	5.53 [0.29]	39.75 [3.36]	300.80 [2.50]	43.12 [4.12]

4.7 Concluding Remarks

In this chapter, in-plane mechanical properties of various weft-knitted fabrics and their thermoplastic composites for the two material systems, PET/PP and UHMWPE/LDPE composites, as well as the energy absorption mechanisms were investigated in multi-scales.

The tensile behaviour of both interlock fabric and composites was found strongly nonlinear and anisotropic by the fibre orientations. The interlock structure displays superior tensile properties in the walewise to in the diagonal and coursewise directions. Both matrix and fibres contribution on most of the load sustained in the elastic region, debonding of the fibre/matrix interface, which gives rise to a high and steady stress level, and the large extensibility of reinforcing fibres in large composite deformation have proved a better combination of properties than its individual components.

The SEM micrographs show that the imperfect surface morphology of this kind of composites would facilitate large deformation and deformation mechanism, including matrix crack development, fibre/matrix debonding and loop distortion until composite fracture.

Effects of other fabric parameters on the tensile behaviour of the composites have been summarized as follows. Interlock composite is superior to the rib 1×1 composite since the former contains more reinforcing fibres which leads to a higher tensile strength and stiffness. Increase in the fibre volume fraction of the composite structure produces a positive effect on its mechanical behaviours. Surface

modification by plasma treatments on PET fibre improves the interface adhesion, leading to a smooth load-deformation curve. The effects of pre-stretching directions and levels of knitted fabric on the mechanical properties of the composites have been investigated. When the composite is pre-stretched along the testing direction, both of its stiffness and tensile strength increase but its failure strain reduces. When the pre-stretching direction is perpendicular to the testing direction, the opposite result is expected. When the bi-axial specimens are deformed in the walewise direction, there is a little increase in the stress plateau level but a drop in fracture strength. When the bi-axial specimens are tested in the coursewise direction, their tensile strength is similar to the non-stretched specimens although their failure strain is reduced. For the walewise tested specimens, all pre-stretched samples display some increase in energy absorption. As for the coursewise tested samples, most pre-stretched samples display doubled energy absorption capacity to the non pre-stretched samples.

CHAPTER 5

MICRO-MECHANICAL CHARACTERIZATION OF SINGLE FIBRE MODEL COMPOSITES BY RAMAN MICROSCOPY

5.1 Introduction

In the literature, there has been an increased interest in the application of Raman spectroscopy to characterize the deformation of crystal polymers, fibres and composites. Usually the technique of Raman spectroscopy can be applied in conjunction with an optical microscope ('Raman microscope' or 'Raman microprobe'). Raman microscopy has been demonstrated as a useful tool for micromechanic study of high-performance fibres and composites. The mapping of fibre stress/strain in unidirectional fibre composites using Raman spectra and fluorescence spectra has obtained significant success when analyzing the failure and interfacial behaviour of composites subjected to a load (Young and Yeh, 1994; Andrews et al., 1996). Most of the previous works were concerned with high modulus fibres which normally have high levels of crystallinity. Until recently, conventional fibres have not received much attention. Yeh and Young (1998) reported primary investigation results on the molecular deformation during the mechanical straining of single filaments of a high-tenacity poly(ethylene terephthalate)(PET) technical yarn using Raman spectroscopy, indicating that there is clearly scope to use Raman deformation studies to gain a detailed understanding of the molecular deformation processes in a variety of industrial and textile fibres.

In this chapter, we make an attempt to use the Raman microscopy to measure the strain of fibres embedded in a composite, which is subjected to a load, and subsequently to relate the obtained results with the macroscopic mechanical properties. A short PET fibre embedded in a dog-bone shaped PP matrix 'model composite' was fabricated and studied. Followed by a short review of the principles of Raman technique and the instrumentation used in Raman spectroscopy, the deformation of a single PET fibre, thermal residual strain raised from cooling during composite fabrication and interfacial behaviour of the composites when subjected to loading, are investigated.

5.2 Principles of Raman Scattering

When a beam of electromagnetic radiation impinges on a molecule, it can be transmitted, absorbed or scattered. Raman spectroscopy is concerned with the scattering of radiation by vibrating molecules, which undergoes a change in the wavelength (Raman scattering). This effect was discovered by an Indian scientist Sir C.V. Raman in 1928. It is due to the changing dipole moment or polarization of molecules stimulated by an incident radiation, described in the classical electromagnetic theory. Another way to describe the Raman scattering is the quantum mechanical representation by considering that the radiation as consisting of discrete particles or quanta of energy, known as photons. This quantization of vibrational energy levels is taken into account involving the vibrational quantum of energies and electronic levels.

5.2.1 Classical Electromagnetic Theory (Siesler and Holland, 1980; Koenig, 1999)

When a molecule is introduced into an electric field $\boldsymbol{E}$ of a monochromatic electromagnetic radiation, an electric dipole moment $\boldsymbol{P}$ is induced in the molecule. If α is the polarizability of the molecule, the magnitude of the induced dipole moment $\boldsymbol{P}$ is given in a linear system by:

$$\boldsymbol{P} = \alpha \boldsymbol{E} \tag{5.1}$$

Because the electric field oscillates as it passes through the molecule with the frequency ν_o, it will excite the molecular electron cloud to vibrate and radiate a varying electric field. Thus, the electric field, $\boldsymbol{E}$, can be expressed in terms of its amplitude $\boldsymbol{E_0}$ and a time-dependent term:

$$\boldsymbol{E} = \boldsymbol{E_0} \cos(2\pi\nu_o t) \tag{5.2}$$

Substitution in equation (5.1) gives

$$\boldsymbol{P} = \alpha \boldsymbol{E_0} \cos(2\pi\nu_o t) \tag{5.3}$$

With the exception of isotropic molecules (for example, CCl_4) the molecular polarizability α shows directional properties, and the induced dipole moment **P** is not parallel to the electric field vector **E**. The components of the induced dipole moment **P** are connected via linear vector functions with the components of the electric field

$$\begin{pmatrix} P_x \\ P_y \\ P_z \end{pmatrix} = \begin{pmatrix} \alpha_{xx} & \alpha_{xy} & \alpha_{xz} \\ \alpha_{yx} & \alpha_{yy} & \alpha_{yz} \\ \alpha_{zx} & \alpha_{zy} & \alpha_{zz} \end{pmatrix} \begin{pmatrix} E_x \\ E_y \\ E_z \end{pmatrix} = P = \alpha E \tag{5.4}$$

where the α_{ij} are the components of the tensor α. The component determines the i-th component of the induced dipole moment that is caused by the j-th component of the electric field vector. After expanding α in a power series of the coordinates r,

$$r = r_o \cos(2\pi\nu_{vib} t) \tag{5.5}$$

It gives

$$\alpha = \alpha_o + \left(\frac{\partial \alpha}{\partial x}\right)_{r=r_0} (r - r_0) + \ldots \text{ and } \alpha_0 = \alpha(r_0) \tag{5.6}$$

where r_o is the coordinate of the initial position, taken as the maximum displacement from the equilibrium bond length.

By combing equations (5.3), (5.5) and (5.6), and using a trigonometric identity, it gives the expression of the induced dipole moment:

$$\begin{aligned} P = {} & \alpha_o E_0 \cos 2\pi\nu_0 t + \frac{1}{2}\left(\frac{\partial \alpha}{\partial x}\right)_{r=r_0} E_0 (r - r_0)\cos[2\pi(\nu_0 - \nu_{vib})t] \\ & + \frac{1}{2}\left(\frac{\partial \alpha}{\partial x}\right)_{r=r_0} E_0 (r - r_0)\cos[2\pi(\nu_0 + \nu_{vib})t] \end{aligned} \tag{5.7}$$

From equation (5.7), the induced dipole moment **P** varies with the original incident frequency ν_o, the sum and different frequencies $\nu_o + \nu_{vib}$ and $\nu_o - \nu_{vib}$ which correspond to Rayleigh scattering, Stokes and anti-Stokes Raman scattering, respectively. The latter occurs only if the polarizability changes during a vibration.

5.2.2 Quantum Mechanical Representation

When a material is radiated with an intense monochromatic beam of radiation with frequency ν_{0i}, a certain portion of it is absorbed, even by most transparent samples. The absorption spectrum is called the IR spectrum. The other would be scattered elastically and in-elastically. Most collisions of the incident photons with the sample molecules are elastic, called Rayleigh scattering where radiation is scattered elastically at the same frequency in all directions as the exciting radiation. However, there is a small amount of the radiation is scattered inelastically at a different frequency. In the quantum-mechanical representation, the origin of Raman scattering

lies in inelastic collisions and involves an exchange of energy between the molecules and the incident photons.

Let ν_0 and ν'_0 be the frequencies of the incident and the scattered photons respectively, and E_1 and E_2 be the energies of the molecule before and after it scatters the photon. From the conservation of energy principle,

$$h\nu_0 + E_1 = h\nu'_0 + E_2 \qquad (5.8)$$

where h is the Planck's constant. Equation (5.8) can be rewritten as

$$\Delta E = E_2 - E_1 = -h(\nu'_0 - \nu_0) = -h\Delta\nu$$

The energy difference ΔE is the difference between two molecular energy levels and measurement of the Raman shift $\Delta\nu$ gives the molecular energy level spacing. Thus, by monitoring the inelastically scattered photons we can probe the molecular vibrations (Willard, 1988).

In the quantum-mechanical model, the incident photon elevates the scattering molecule to a quasi-excited state whose height above the initial energy level equals the energy of the exciting radiation, as illustrated in Fig. 5.1. The light scattering process involves a two-photon process. In the first step, some of the incident wavelengths absorbed by the molecule excite the molecules into unstable virtual excited states that have energy levels higher than that of the original state by an increment equivalent to the energy of the exciting photon, depicted as the upward-pointing arrows in Fig. 5.1. This radiation that stimulates the induced oscillating dipoles of sample molecules would lead to the transfer of energy with the

rotation and vibrational modes of the sample molecules. The second step, indicated by the downward-pointing arrows, involves the release of photons with energy higher and lower than the incident light to produce the Stokes and Anti-Stokes lines in the Raman spectrum, respectively.

The Raman spectra usually studied are the Stokes lines because at ordinary temperatures most of the molecules are in the ground state that leads to a greater intensity of the Stokes lines than the anti-Stokes lines, which originate from an excited state with a lower population.

By convention the positions of Raman lines are expressed as wavenumbers, but it is more correctly referred to the wavenumber differences.

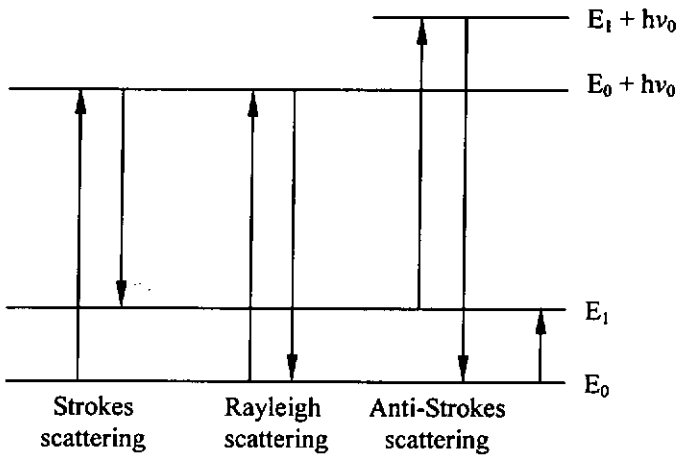

Figure 5.1 The energy levels of the Raman spectroscopic experiment showing the Rayleigh and Raman scattering: Stokes and Anti-Stokes lines

5.3 Instrumentation of Raman microscopy

The schematic diagram of a typical Raman microscope system is shown in Fig. 5.2. The Raman spectroscopic measurement for the polymeric material in this study was conducted using a model of Reinshaw Raman microscope (System 3000) (Fig. 5.3) in the optical laboratory in the Material Characterization and Preparation Facility (MCPF), The HKUST. Generally, a Raman instrument consists of three basic components:

- A signal generator, usually a laser;
- A signal analyser, either a spectrometer or interferometer, and
- A signal detector, either a monochannel or a two-dimensional array.

A Raman microprobe also contains a focusing component, usually provided by a microscope, and a mapping unit such as a computer-controlled micromanipulator. Each of these components plays an important role in the Raman mapping experiment.

A Raman microscope system is employed to obtain Raman spectra of single fibre or composite sample. The system is based on a double monochromator with a charge-coupled device (CCD) camera connected to an optical microscope. Raman spectra are obtained by focusing the laser beam – the 514 nm green line of a 5 mW Argon – on a small spot as small as 2 μm in diameter on the specimen using an objective lens (x50) of the optical microscope attached to the instrument and the scattered light is collected from the focused point. The scattered light is sent on the entrance slit of the optical filter, which can work as a Raman microspectrometer when the detector is a photomultiplier followed by an amplifier and a chart recorder

(monochannel detection) or a Raman micro-spectrograph when the detector is a two-dimensional detector. In this latter case the spectrum is visualized on a monitor (Delhaye and Dhamelincourt, 1975).

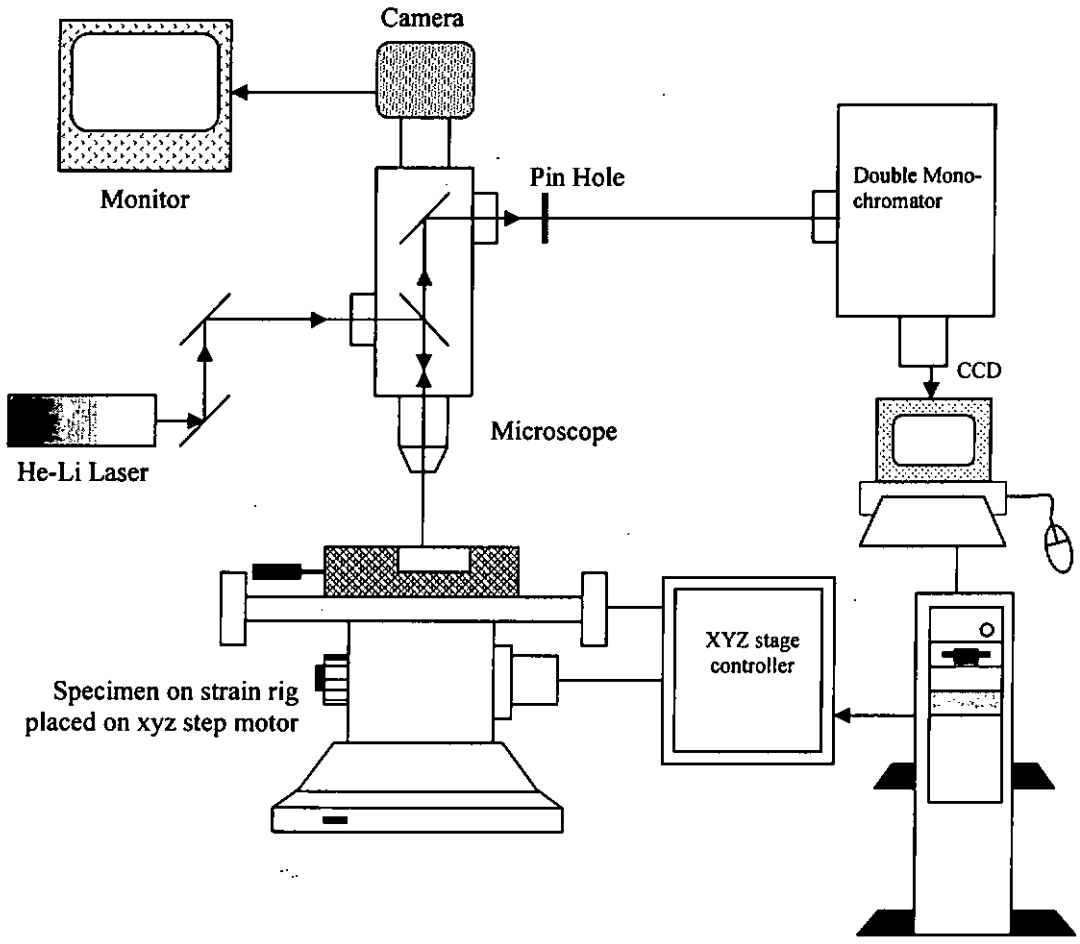

Figure 5.2 Schematic diagram of the Raman microscope system

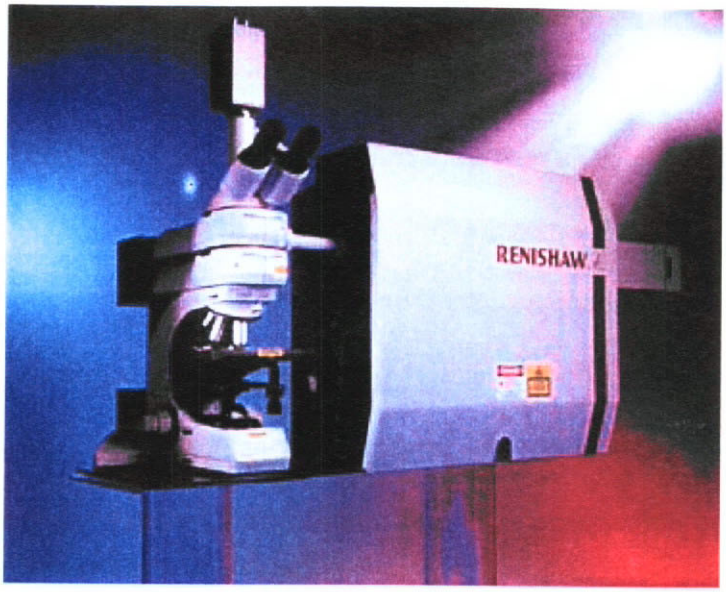

Figure 5.3 *Renishaw* RM 3000 Micro-Raman system

5.4 Sample Preparations and Experimental Details

5.4.1 Tensile Properties of Single PET Fibre

Single filaments of high strength PET yarns used for the micro-mechanics study are the same as those for producing the PET knitted reinforcement in the early chapters. The tensile properties of the single fibres were measured by using an Instron Automated Materials testing system (Model 4466) following the ASTM standard D3822-96. The tensile behaviour of the un-treated PET fibres was examined by conducting simple tensile test on 30 fibres with a gauge length of 25 mm at a loading speed of 2 mm/min., in a similar manner to those for PET fibres obtained by previous workers (Young and Yeh, 1994). The diameters of the fibres were measured using an optical microscope. The average value was 34.5±3.8 μm. The strength, initial modulus and elongation at break are 975±75 MPa, 13.0±2.2 GPa and 19.0±2.9 %, respectively.

5.4.2 Surface Modification of PET Fibre by Plasma Treatment

Some of the straight aligned PET fibres mounted on a square paper frame were subjected to a plasma treatment in an attempt to improve adhesion between the fibres and the matrix. The treatment was conducted in a Plasma Polymerization System SPP-001 (Showa Co Ltd., Japan) and the same treatment conditions were applied as those for the PET fabric as mentioned in Chapter 4.2.1. In this section, the fibres with plasma treatment for 15 minutes and the un-treated PET fibres were used to fabricate the single short-fibre embedded model composites. The observation of the modified fibre surface has already been given in section 4.6.2, in which it is demonstrated that the plasma treatment on the fibres can effectively improve the interfacial properties during a large deformation of the knitted composites. Thus, the effect of plasma treatment on the interfacial behaviour of the single PET fibre is further investigated by the micro-Raman measurement in this chapter.

5.4.3 Fabrication of Single Short-Fibre Model Composite

As the polypropylene matrix is rather brittle, the model composite cannot be simply cut by a punch die on the molded flat plate, and it has to be molded in shape directly by compression molding instead. The PET fibres were cut in a short fibre length of approximately 1.5 mm as longer fibre length may bend during the molding process. Laminates of pure PP films with each having a thickness of 40 μm were cut in specified dimensions for fitting a dog-bone shaped mold. The film laminates were first placed inside the mold, and a single fibre was aligned carefully in the film centre and covered with one film before closing the mold with a metal plate on top. Then the model composites were fabricated using a hot-pressing method at a temperature of 180°C under pressure for 20 minutes. The samples were allowed to cool to room

temperature. The geometry of the single PET fibre embedded in the PP model composite is shown in Fig. 5.4. All of the molded composite specimens were polished for surface smoothness and improving transparency before conducting the Raman microscopic experiment.

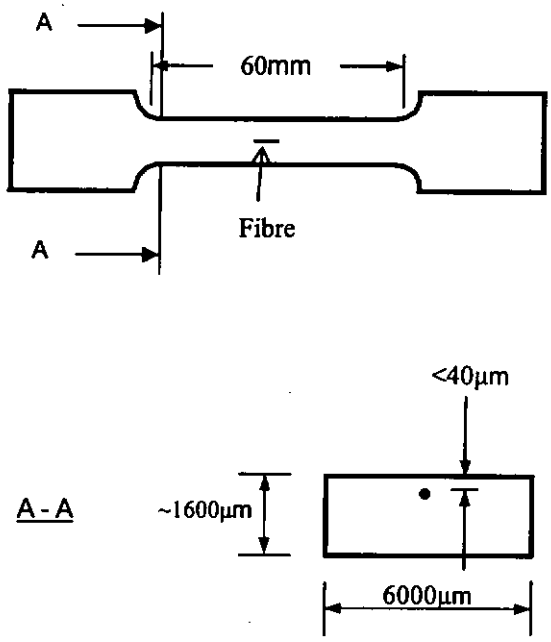

Figure 5.4 Geometry of dog-bone shaped model composites

5.4.4 Raman Microscopy Measurement

Raman spectra of the PET fibres under different conditions were obtained by focusing a 514.5 nm green line of a low-power 5 mW Argon laser to a spot of about 2 μm diameter on the surface of the fibre. Data analysis was conducted by first selecting the spectrum of PET consisting of a single band at 1616 cm^{-1} in the region of 1550-1640 cm^{-1} and subsequent subtracting the background from the spectrum. Then, the data were curve fitted by applying mixed Gaussian and Lorentzian curves to identify the peak positions, intensities and full width at half-maximum of the Raman band.

Raman spectra from a single PET fibre during tensile deformation in air were obtained by using a small stretching rig, as shown in Fig. 5.5, which was fitted directly on the microscope stage. The experimental details were similar to those for the measurement of Raman spectra during the deformation of ceramic fibres (Galiotis et al., 1988). The fibre was strained manually in increments. Raman spectra were taken from the fibre surface after each increment step in strain. A home made tensile rig was made for the deformation of the model composites, as shown in Fig. 5.6, which can hold the stretched composite specimen during the Raman measurement. The Raman spectra were obtained by focusing the laser beam on the fibre surface through the transparent PP matrix either at intervals of about 30 microns along the embedded fibre to measure the point-to-point variation of strain or at the middle region of the embedded fibre at each composite strain increment.

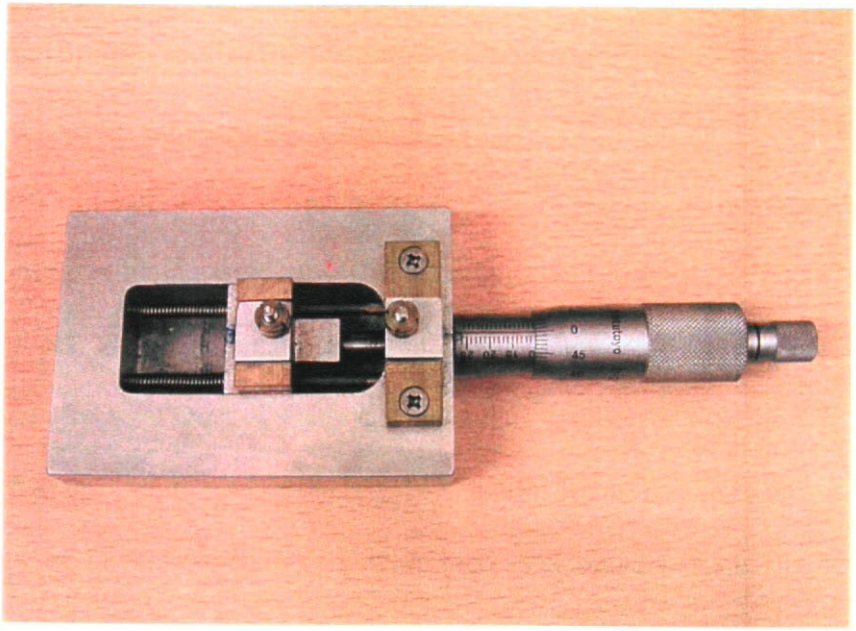

Figure 5.5 A fibre straining rig with micrometer

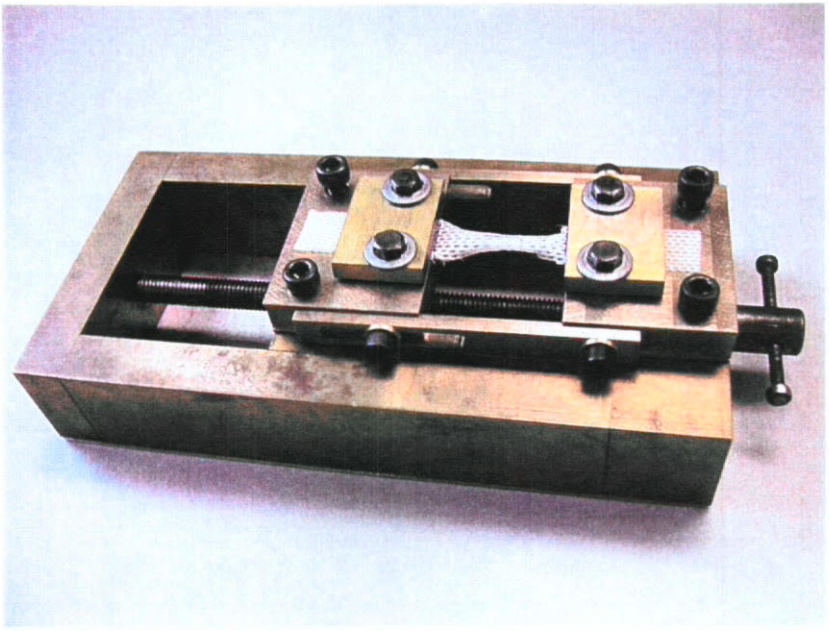

Figure 5.6 Stretching frame for extending composite specimens

5.5 Micro-Mechanics of Single PET Fibre/ PP Matrix Model Composites

5.5.1 Deformation of Single PET Fibre

A Raman spectrum obtained from an individual PET fibre in the region of 800-1850 cm^{-1} is shown in Fig. 5.7. The spectrum consists of several well-defined bands. The 1616 cm^{-1} Raman band assigned to C-C stretching vibration of the phenylene ring in the PET fibres, which is sensitive to the strain in the PET fibres, was selected to investigate in detail. Figure 5.8 shows the Raman spectra for the fibres in the region of 1580-1640 cm^{-1} up to approximately 16% strain. It can be seen that the 1616 cm^{-1} band shifts to lower wavenumbers with increased tensile strain. In addition, the deformation results in the broadening of the Raman band.

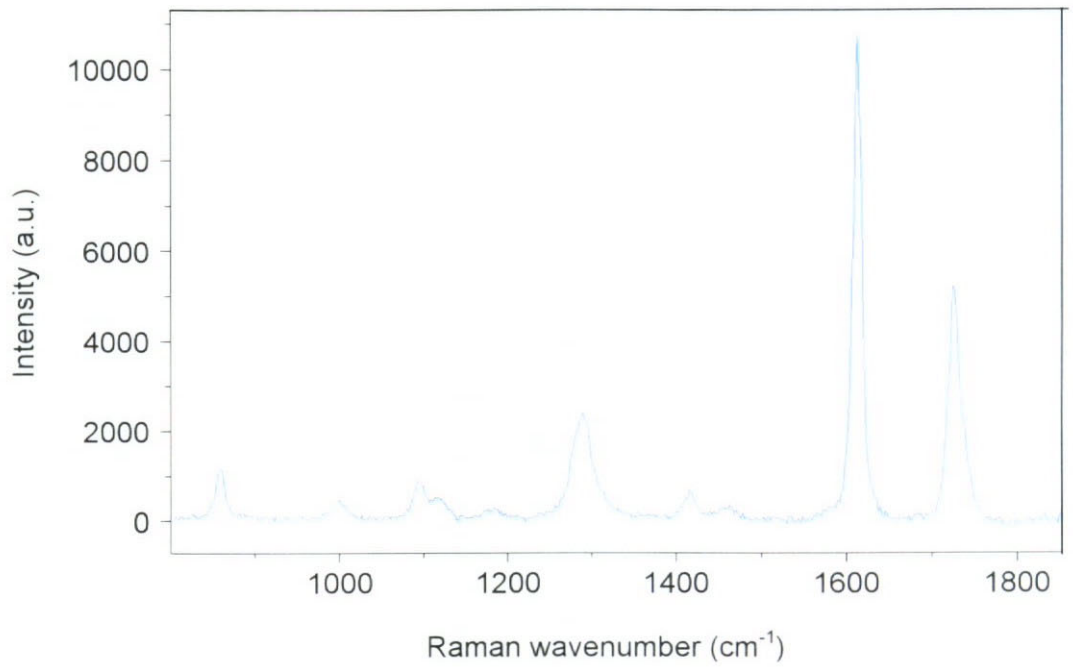

Figure 5.7 Raman spectrum of PET fibre from 800 to 1850 cm^{-1}

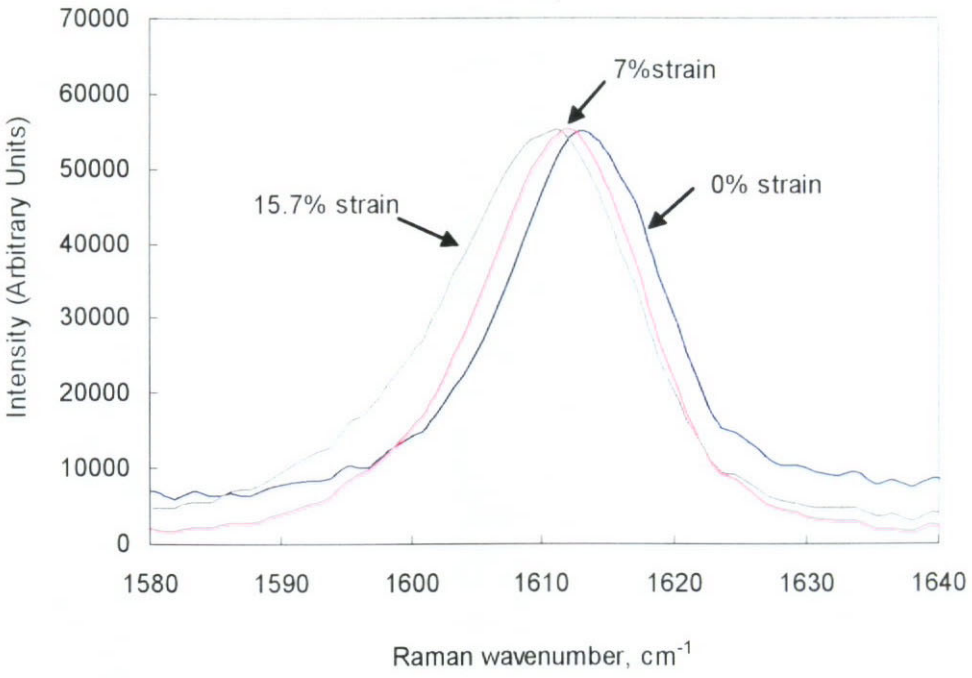

Figure 5.8 Shift and broadening of Raman band at 1616 cm^{-1} with fibre strain for PET fibre in air

The dependence of the shift of 1616 cm^{-1} Raman band upon the applied tensile strain for the PET fibres is shown in Fig. 5.9(a). There is an approximately linear shift in the wavenumber with strain until the fibre failure occurs and the slope of the fitted line for the band is -0.21 cm^{-1}/% strain. The dependence of the broadening of the band with strain is shown in Fig. 5.9(b), indicating an approximately linear relationship between the full width at the half maximum of the band and the strain of the fibre. The fitted line in Fig. 5.9(b) has a slope of 0.23 cm^{-1}/%strain. The solid lines in both figures are results of linear least square fits of the experimental data. It is noted that they are both excellent fits to the measured data with correlation coefficients of 0.998 and 0.994 respectively. The slope in Fig. 5.9(a) has been used as a calibration of the strain sensitivity to determine the residual strain of the fibres and the distribution of fibre strain in the single fibre model composites; and to monitor the failure of the fibre-matrix interface.

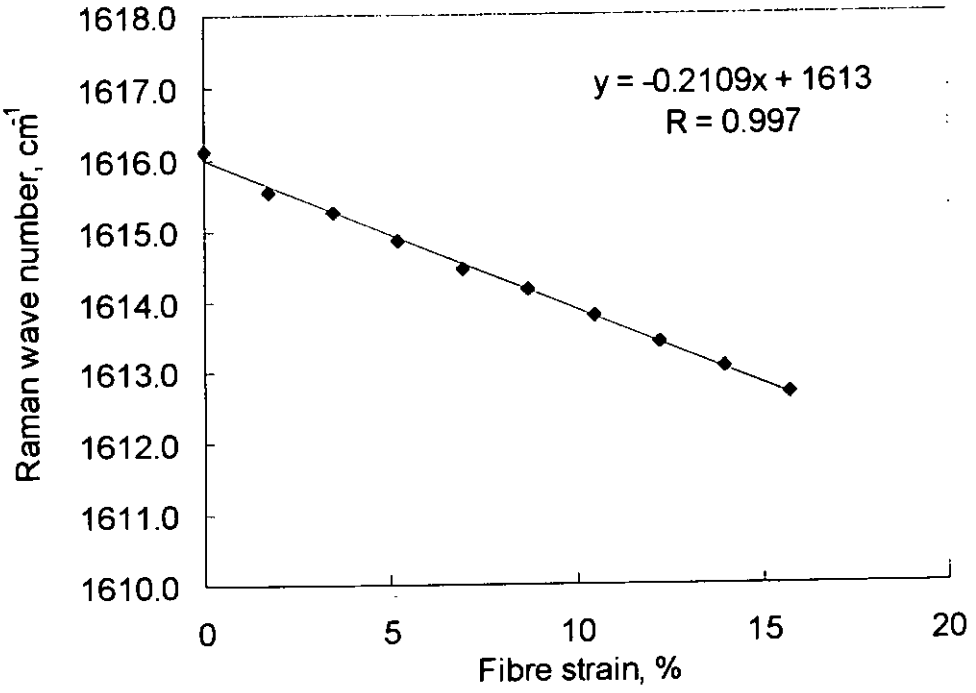

(a)

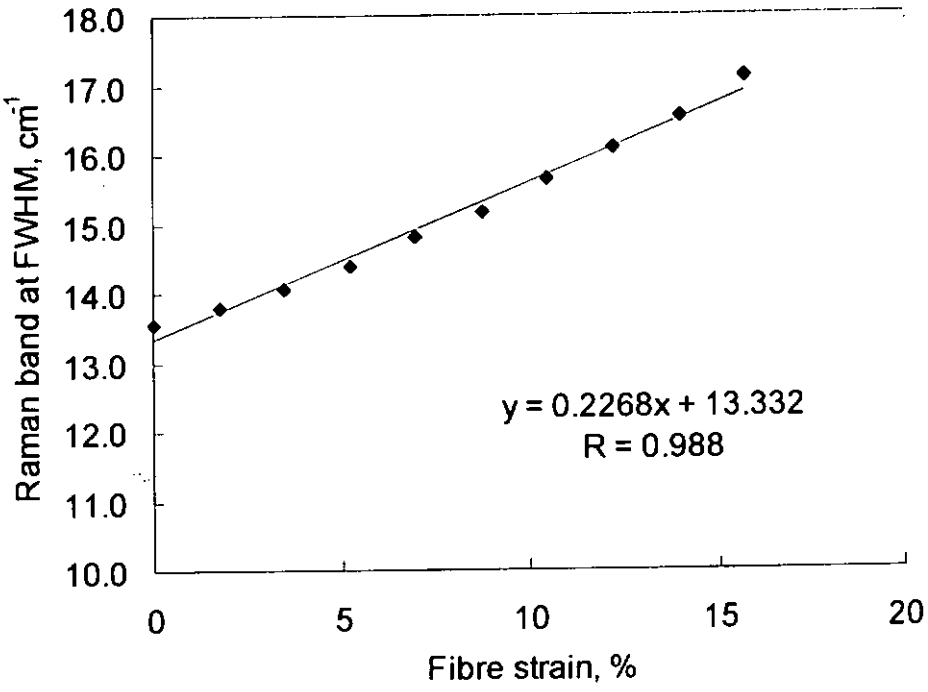

(b)

Figure 5.9 Raman band variations as a function of the applied strain of PET fibre (a) band peak position (b) full width at half maximum

5.5.2 Thermal Residual Strain

The strain mapping along the embedded fibre was carried out to determine the residual strain distribution along the fibre length. The fibre residual strain distribution of a single as-received PET fibre of 1.4 mm in the undeformed model composite is plotted in Fig. 5.10. The values of axial residual strain scattered along the whole fibre length, ranging from -1.5 % to -2.8 % and the average value was about -2.0 %. The negative value implies that the fibre was under axial compression. This resultant fibre compression behaviour is due to the larger thermal shrinkage or a higher expansion coefficient of the PP matrix than that of the PET fibre. On cooling from the fabrication temperature, there is a large volume shrinkage of the matrix from the processing temperature at 177 °C to ambient temperature (approximately 22.5 % (Nairn and Zoller, 1985)). Figure 5.10 also shows that the value of compressive strain is not zero at both fibre ends. This non-zero strain at the fibre ends has been found in every specimen being investigated. This phenomenon differs from those as indicated by Cox shear-lag theory (Delhaye and Dhamelincourt, 1975; Young et al., 1989), which suggests that the strain should fall to zero at the fibre ends. This difference may be due to the fact that the fibres were subjected a triaxial compression raised from the large thermal contraction of the matrix during fabrication of the model composites. The results differ from the prediction based upon the Cox theory where assumptions that no strain at both fibre ends are applied. This assumption is obviously not applicable to the PET fibre which is subjected to compressive strain from the contracting matrix at both fibre ends. Similar results were reported in a study of short embedded ceramic-fibre glass-matrix model composites by Yang and Young, (1995).

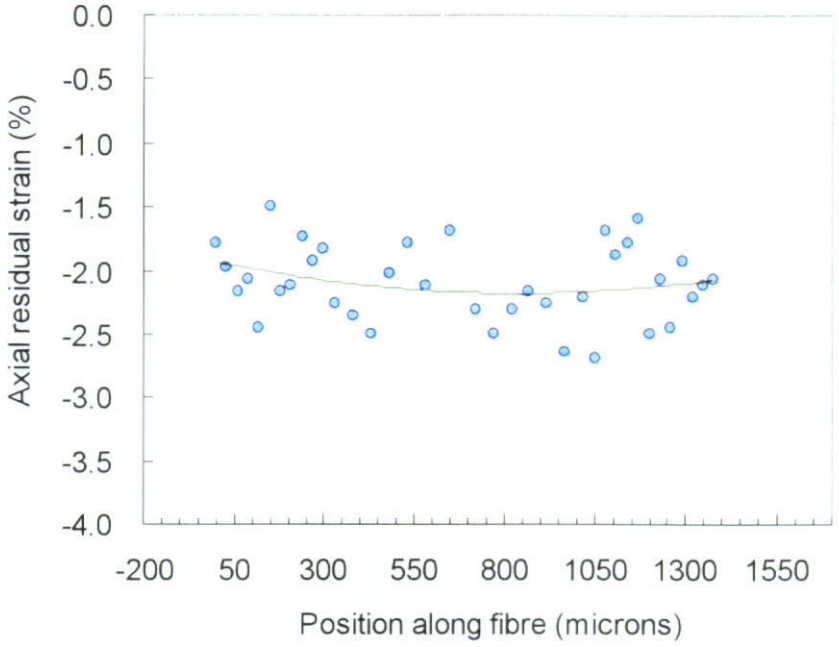

Figure 5.10 Distribution of axial residual strain along the embedded as-received PET axis in the model composites

5.5.3 Interfacial Behaviour

The interfacial behaviour of the model composites can be examined by the axial fibre strain at the middle of the embedded fibre. Figure 5.11 shows (a) the un-treated PET fibre strain and (b) the plasma-treated PET fibre at the middle of fibre as a function of effective composite strain. Both of them show initially a similar linear relationship between the fibre strain and the effective composite strain when the fibre is under compression. However, the fibre strain increment becomes smaller than the composite strain when the fibre is under tension. This difference in fibre and composite strains may be caused by two reasons. The first one is the ratio of Young's moduli of the fibre and matrix being 13GPa/1.4GPa (Lam, 1999), respectively. The soft matrix transfers less strain to the rigid fibre. The second consideration is the de-bonding at the interface. The combination of the two possible reasons makes the

determination the starting of interfacial failure more complicated. For the un-treated PET embedded fibre, the fibre strain does not increase further after 5.1 % applied composite strain until the composite breaks at about 9 % strain. The drop of fibre strain indicates that the massive interfacial failure occurs. For the plasma treated PET embedded fibre, the massive interfacial failure occurred at about 8.2 % followed by the complete composite breakage at approximately 16 %. This occurrence of massive interfacial failure at a relatively higher matrix strain implies that the plasma treatment improves the interfacial adhesion between the fibre and matrix.

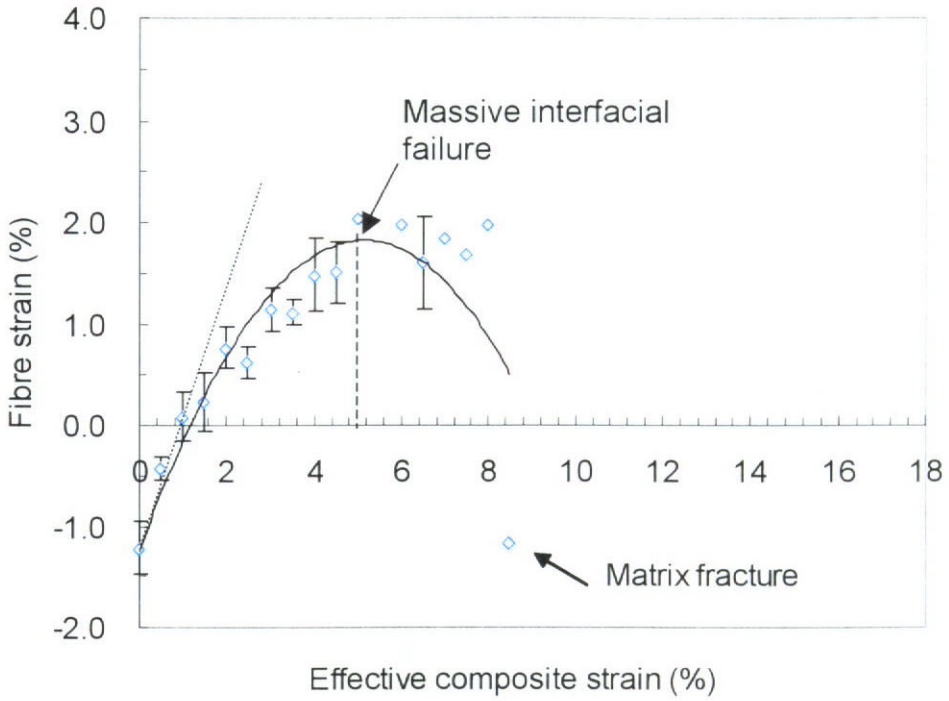

(a)

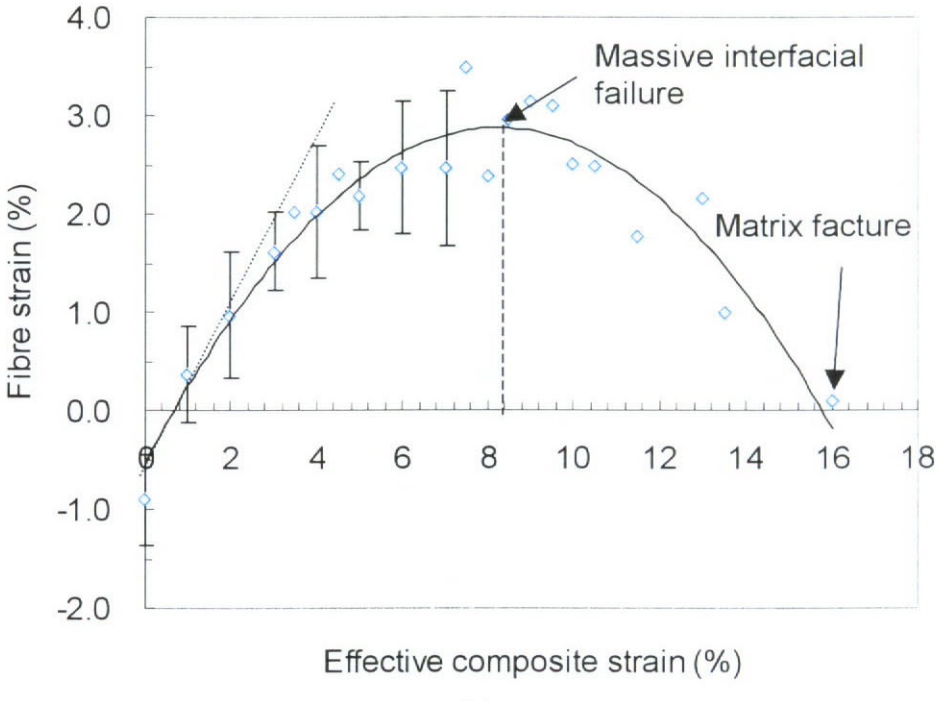

(b)

Figure 5.11 Interfacial behaviour of the model composites. (a) As-received PET fibre in matrix, (b) Plasma-treated PET fibre in matrix

5.6 Limitation of Micro-Raman Technique on Fibre Strain Measurement

Although the Raman measurement is able to detect the residual thermal strain and indicate the interfacial properties by fibre surface treatment on single PET fibre/PP embedded model composites, the strain derived from the sensitivity factor -0.21 cm^{-1}/% strain Raman band shift of the PET fibre is very small.

The active 1616 cm^{-1} main-chain phenyl group stretching vibration and its associated Raman peak are relatively strong in a fully drawn PET fibre and well isolated from other bands. However, the band shift is very small as compared with other high performance fibres, as illustrated in Table 5.1. In the case of Raman mapping on a fibre loop, the fibre strain distributed in a fibre loop under stretching may become more complicated and the spectral resolution is 1 cm^{-1}, which makes the strain related Raman shift difficult to be observed or identified. If the fibre is used for fibre strain measurement of a knitted loop in composite during large deformation, it is not surprising that no obvious shift will be observed.

Generally, high values of modulus of the fibre material usually give larger magnitudes of the shift of the stress/strain sensitive Raman bands. Examples have demonstrated for the aromatic polyamides such as Kelvar and rigid-rod polymer fibres such as poly(p-phenylene benzobisthiazole) (PBT), poly(p-phenylene benzoxazole) (PBO). These fibres have well-defined Raman spectra due to the high degree of molecular orientation and also the possibility of resonance enhancement. Their extraordinary high value of Young's modulus means that during tensile loading the macroscopic deformation of fibre is translated to the direct stressing of the backbone in the molecules. Similar behaviours have been found in gel-spun

polyethylene fibre and other non-polymeric fibres such as carbon, silicon carbide and alumina. Consequently, the study of the deformation process of embedded fibres or composite by micro-Raman may be restricted to the use of high modulus fibres rather than the conventional fibres such as PET.

Table 5.1 Peak frequency, $\Delta\nu$, and strain sensitivity, $S = d\Delta\nu/de$, of the Raman bands of various material (Feast et al., 1993)

Materials	$\Delta\nu$ (cm^{-1})	$d\Delta\nu/de$ (cm^{-1}/%)*
Polydiacetylene		
Single crystals	2080	-20.0
Aramids	1613	-4.4
UHMW-PE	1060	~-5
Rigid rods		
PBT	1477	-12.1
PBO	1280	-7.9
ABPBO	1555	-5.9
Non-polymeric fibre		
Carbon	1580	-14.6
Silicon carbide	1600	-6.6
Alumina-zirconic	460	-5.7
Conventional polymers		
PET	1615	< -1
Polypropylene	808	< -1

* The data quoted are the highest values in the literature.

5.7 Micro-Mechanical Study of UHMWPE Fibre/LDPE Composites by Raman Microscopy

Most of the high rigidity fibres, such as substituted polydiacetylene (Galiotis et al., 1985), and poly(p-phenylene benzobisthiazole), PBT (Day et al., 1987; Young et al., 1990), carbon, are brittle although they exhibit significant fibre strain sensitivity. Alternatively, aramids or the ultra-high molecular weight polyethylene fibres are flexible and displayed a high modulus. Thus, they may be the most appropriate to be made into a knitted structure in composite as the sensing fibres for the strain measurement by using Raman microscopy.

Considering the thermoplastic fabrication process of the composite material by compression molding and the effect of material compatibility on the interfacial properties, UHMWPE fibres and LDPE matrix were chosen in this study for fabricating the knitted composite, though its macro-mechanical properties of both in-plane and three-dimensional cellular form have been characterized in previous chapters. Conventionally polyethylene fibres combined with resins such as epoxies have the problem of interfacial adhesion. Some modification has been reported that plasma treatment (Nardin and Ward, 1987; Chao et al., 1993) on the fibre surface has significant improvement on interfacial strength. By far a better improvement on interfacial adhesion has been achieved by fabricating polyethylene fibre/polyethylene matrix composites in which the constituent materials are of the same nature (Mosleh et al., 1988; Teishev et al., 1993). This homocomposite with good material compatibility facilitated the transcrystalline growth on fibres surface. It has been reported that the composite strength and modulus values lie in between those of carbon/epoxy and aramid/epoxy composite (Marais and Feillard, 1992). In Chapter 6, fibre strain measurement in the UHMWPE knitted/LDPE composites will be

demonstrated, using Raman microscopy.

5.8 Concluding Remarks

The technique of Raman spectroscopy would be a very useful tool for us to investigate the micromechanics of deformation in both the fibres and fibre-reinforced textile composites. Its basic principles and the general set up of the Raman microscopy have been reviewed. Raman microscopic measurements were conducted on single Poly(ethylene terephthalate) fibres in air and embedded in polypropylene matrix model composites. Well defined Raman spectra were obtained from the PET fibres in air and in the PP matrix. The band of 1616cm^{-1} shifts due to tensile strain to low wavenumbers and broadens. Linear relationships have been found between both the wavenumber, the full width at half maximum and the applied axial strain. The strain sensitivity is –0.21cm^{-1}/%. The point-to-point variation of the residual thermal strains along the embedded fibres can be determined in model composites.

It is found that the whole length of the embedded fibre, before composite deformation, was under axial compression strain of –2.0 %, which is caused by different volume shrinkages of the fibre and matrix on cooling from high fabrication temperature. The fibre strain increases linearly with the effective composite strain when the fibre is under compression. The fibre strain increment becomes smaller than the composite strain where interfacial failure possibly happens. Results show that the plasma treatment on PET fibres leads to a delay of the massive occurrence of interfacial failure, implying some improvement on the adhesion between the fibre and matrix.

Although the Raman microscopy is able to indicate the deformation of the conventional fibre and its short fibre model composites, the low sensitivity of the Raman microscopy has limited to high modulus fibres rather than those conventional fibre material. Alternatively UHMWPE fibre/LDPE material system is suggested to obtain significant strain sensitivity for the embedded fibre strain measurement in knitted composites by the Raman microscopy, which will be presented in chapter 6.

CHAPTER 6

FIBRE STRAIN MAPPING OF WEFT-KNITTED TEXTILE COMPOSITES BY RAMAN MICROSCOPY

6.1 Introduction

In Chapter 4, it has been demonstrated that knitted loops in both fabric and composite exhibit large loop distortion during large deformation. This chapter aims to further study in a micro-scale the fibre strains in composite when it is subjected to various axial composite strains. It is demonstrated by studying the fibre loop made of ultra-high molecular weight polyethylene (UHMWPE) fibres embedded in low density polyethylene (LDPE) matrix composites under tensile loading. Raman microscopy is used to obtain the Raman band shift from which the localized fibre strains are mapped at different stages of large deformation. Although there may have the overlap of the Raman bands contributed by the embedded fibre through the LDPE matrix, due to different structure and crystallinity in the fibres and matrix, it is still possible to identify the Raman band shifts due to fibre stretching. Structural characterization of both the fibre and matrix are obtained by WAXS. Tensile testing is carried out on the fibre, matrix and knitted composites in the wale direction. Accordingly, a simple model describing the deformation of a plain knitted loop is developed to predict the overall fibre strains when the composite specimen is stretched in the wale direction. The predicted fibre strain will be compared with the measured strain mapped by Raman microscopy.

6.2 Sample Preparation and Experimental Details

6.2.1 Materials

Single fibre embedded dog bone composite and knitted composites were fabricated using ultra-high molecular weight polyethylene fibres as continuous filament yarn (1760denier) provided by (Dyneema SK75) DSM and the commercial available low density polyethylene LDPE matrix films with a thickness of 0.06mm. For the preparation of single UHMWPE fibre/LDPE dog bone composite, several number of single UHMWPE fibre were aligned parallel on the matrix films, which were cut to fit the size of a square mold frame (20cmx20cm). The fibres were stuck with tapes on both ends on the second top of the film laminates in order to ensure the fibre axis was kept straight during fabrication. The fibres were then covered with one film underneath so that the fibres were placed 60μm underneath the matrix surface. The film laminates were then placed inside a square mold for compression molding by using a hydraulic press (Model TMP) with a maximum temperature of 135°C and a maximum pressure of 10MPa for 40 minutes. As the LDPE matrix is ductile, the cured plastic sheets of approximately 1 mm were cut into dog-bone shaped specimens using a punch die and the continuous embedded UHMWPE fibres were aligned straight in the centre of the specimens. Pure LDPE matrix specimens were also prepared in dog-bone shape. The 1-mm thick knitted composite with rib 1x1 structure was produced by laminating the knitted fabric in between the LDPE matrix films and followed the same compression molding process. The knitted composite specimens were cut into a dimension of 2cmx10cm from the molded composite sheets.

6.2.2 Structural Characterization

Wide-angle X-ray scattering (WAXS) patterns of both of the free standing fibres from a bundle of parallel fibres and the LDPE matrix cut from a compression molded flat sheet matrix were recorded using a (Bruker Model:APEX) Single Crystal X-ray Diffractometer. This X-ray diffraction method is particularly useful to assess the crystallite and orientation of both fibre and matrix.

6.2.3 Mechanical Testing

Tensile tests of the UHMWPE fibre, yarns (1760 denier), LDPE matrix and the knitted composites were performed using an Instron mechanical testing machine (model 4466) with a10 N-load cell at 20±1°C and a relative humidity of 65 %. The tensile properties of the fibres were examined by following the ASTM standard D2256-97. Each individual UHMWPE fibre specimen was mounted on a card with a gauge length of 25 mm and was loaded at a crosshead speed of 2 m m/min. The diameters of each fibre specimen were measured using an optical microscope at three points along the fibre length and the average values were used to calculate the cross-sectional area for individual fibres. Tensile test of the yarn in a gauge length of 250 mm were performed by using a cross-head speed of 2mm/min. and a 5 KN-load cell. Tensile testing of the as-produced pure matrix and knitted composites were performed using a load cell of 500 N capacity with a crosshead speed of 100 mm/min. The specimens were cut into narrow strips with dimensions of 20mmx150mm and approximately 1 mm thick. The gauge length was 80 mm.

6.2.4 Raman Microscopy

A Ranishaw Raman microscopy (System 3000) was employed to record Raman spectra of single UHMWPE fibre and the composite samples at room temperature. Raman spectra were obtained by focusing the 514.5 nm green line of a 5 mW Argon laser to a spot of about 2 μm in diameter on the fibre surface with the objective lens of 50x. A grating system and a high sensitive CCD detector were used to obtain and record the Raman spectra. Only 7 scans were recorded in order to make the time interval between two consecutive measurements as short as possible to minimize the effect of stress relaxation. Data analysis was conducted by first selecting the spectrum ranging between 900-1500 cm^{-1} and subsequently subtracting the background from the spectrum. After the background subtraction, the Raman bands at 1060 cm^{-1} and 1130 cm^{-1} were curve fitted to two Gaussian functions to obtain the values of peak positions from the fibre.

6.2.5 Deformation of Single Fibre and Composites

As the UHMWPE fibre is very tough, careful preparation is needed to stretch it on a straining rig. The fibre was first mounted on a cardboard square frame using the Cyanoacrylate adhesive and covered by aluminum foil tabs. The card was then placed in the clamps of the straining rig fitting directly on the microscope stage, as illustrated in Fig. 6.1. The gauge length was 20 mm. The fibre should be clamped carefully and tightly without fibre slippage. The card edges were then cut and the single fibre was stretched manually by displacing the fibre using the micrometer attachment. Raman spectra were taken from the fibre surface at the specimen centre for each strain increment. The micrometer allowed precise reading of displacement to ±5μm.

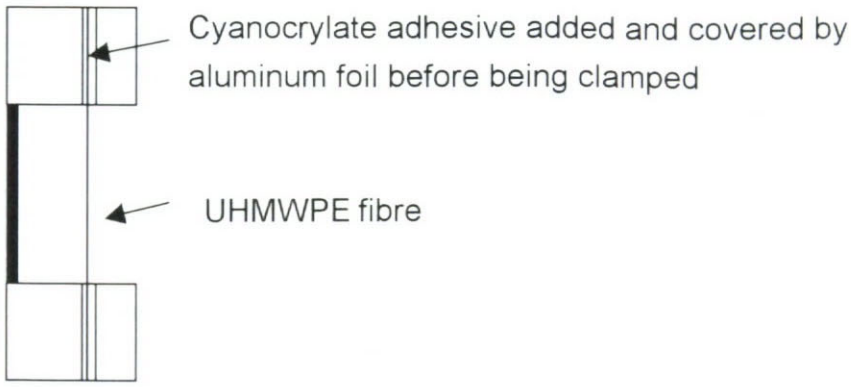

(a)

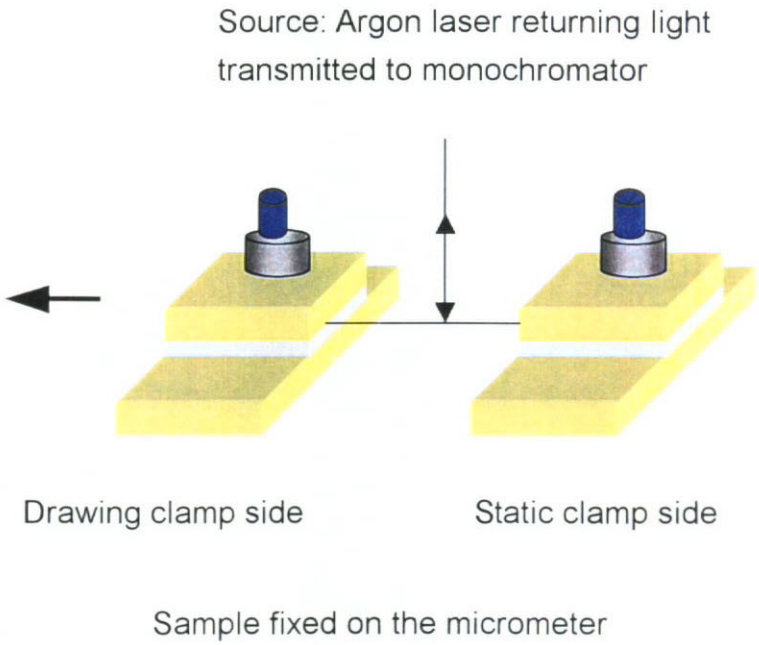

(b)

Figure 6.1 Sample preparation of (a) UHMWPE fibre wound on the plastic frame (b) which is further clamped on the strain rig for fibre extension under Raman microscopy

Before the Raman mapping on fibre loops, a preliminary test was taken by stretching dog-bone shaped single fibre embedded model composites and pure LDPE matrix on the tensile rig manually. The point of laser incidence was located at the centre of the dog-bone shaped specimen at each step of strain increment where necking may happen. Dimension of the dog-bone shaped samples is illustrated in Fig. 6.2.

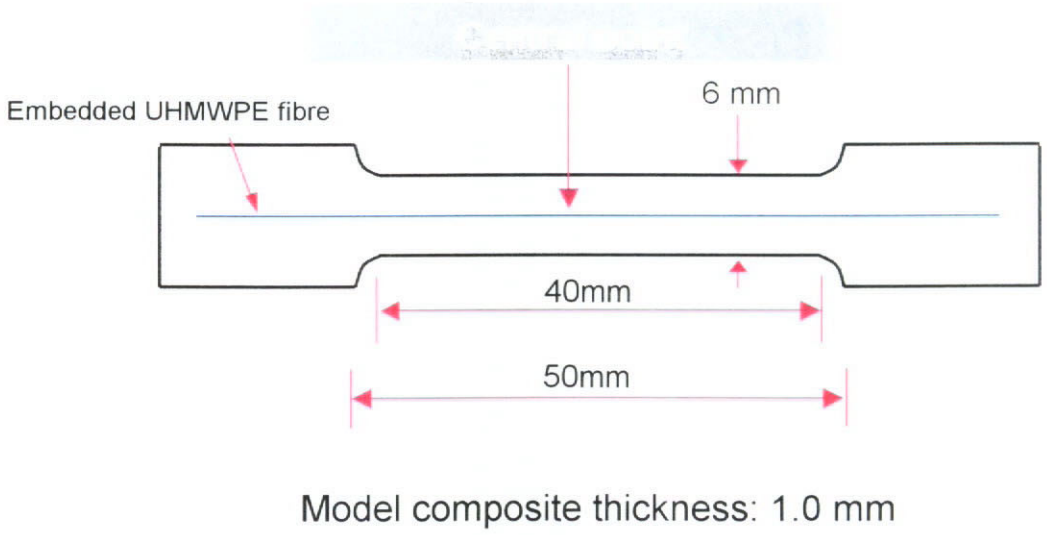

Figure 6.2 Schematic diagram of a model composite specimen in dog-bone shape

6.2.6 Fibre Strain Mapping in Knitted Loop

The fibre strains in an embedded loop during composite stretching in the wale direction at 0 %, 20 %, and 30 % composite strains were determined by the Raman mapping. The fibre loop being selected for strain mapping was located in the middle of the composite specimen. The optical micrograph of the knitted composites consisted of UHMWPE fibres in knitted loops embedded in LDPE matrix at an

un-stretched state and at a stretched state of 30 % extension are shown in Fig. 6.3 (a) and (b), respectively. A quarter of a single loop having part of two fibre bundles at the cross-over region was selected for Raman mapping as illustrated in Fig. 6.4. The mapping was done by focusing the laser beam on the fibre surface just underneath the matrix. The mapping started at fibre 'bundle 1' on the left to 'bundle 2' on the right of the repeat unit, from point to point of 50 μm intervals along each yarn cross-section and at a step of 500 μm apart from each cross-section in the repeat unit. The outline of the fibre bundles was produced by marking the coordinates of the localized points during mapping. However, the mapping at the cross-over region of the knitted loop where fibre bundles underneath the matrix was restricted. Besides, as there was the variation of fibre depth underneath the matrix along the two fibre bundles during composite stretching; the focus of laser beam on to the fibre surface through the transparent matrix had to be adjusted manually from point to point. As there were large mapping points to be taken at each stretched level, limited stretching levels were available on each composite specimen.

In order to study the effect of fibre stress relaxation during composite stretching, the Raman spectra were obtained over a period of time from the single fibre model composites, which were stretched at 3 %, 5.6 % and 8.3 %, respectively. Once the specimen was stretched, it was placed under the microscope and the Raman spectra were obtained in the middle of the embedded fibre.

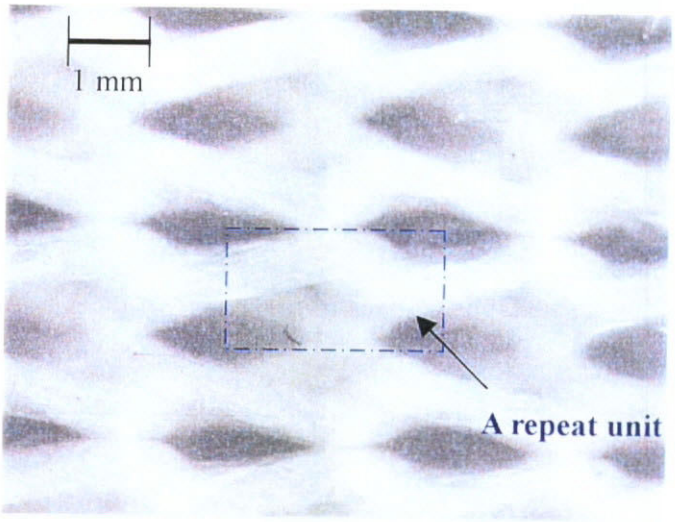

(a)

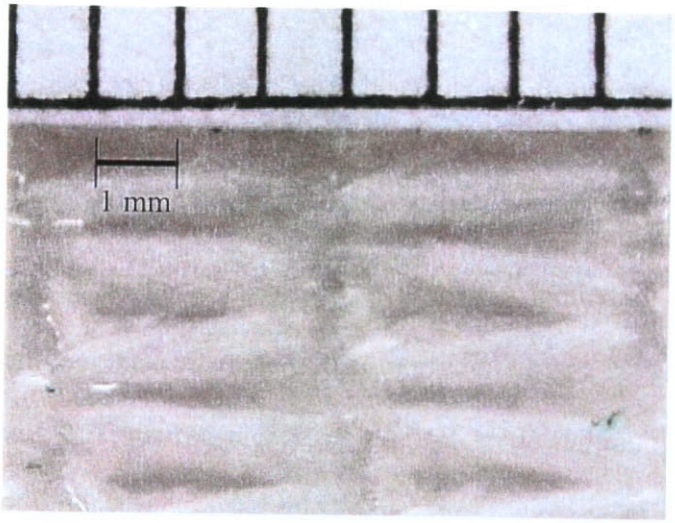

(b)

Figure 6.3 Optical micrographs of the UHMWPE fibre loop in LDPE matrix knitted composite (a) undeformed, (b) after extended 30% walewise

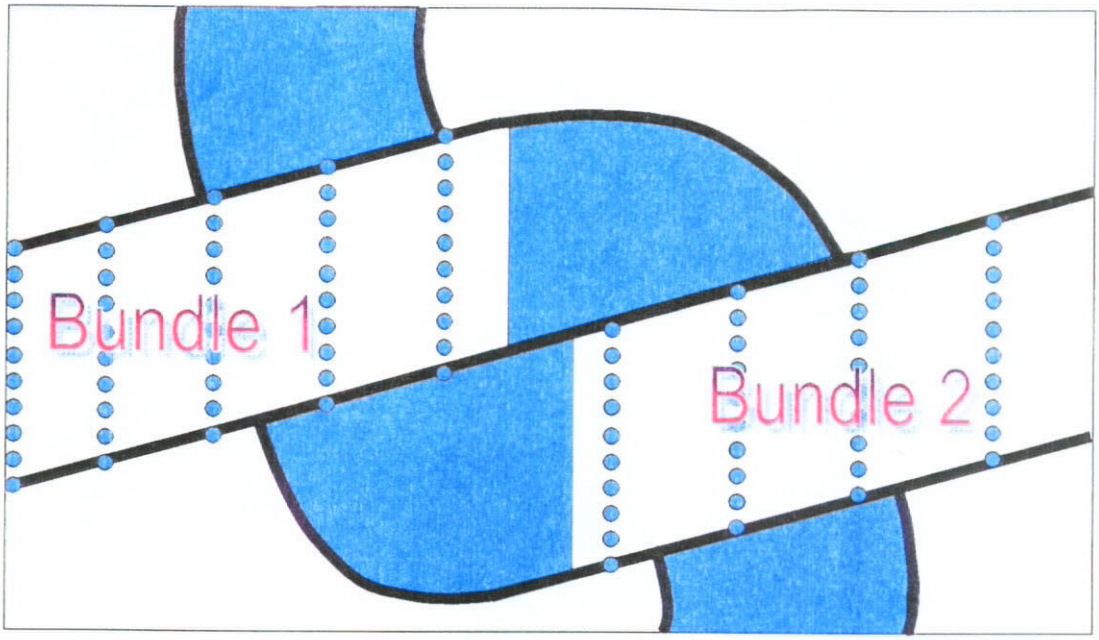

Figure 6.4 Fibre loop mapping procedure and the scope of mapping

6.3 Micro-Mechanics of UHMWPE/LDPE Knitted Composites

6.3.1 Molecular Orientation by XRD

WAXS patterns for the UHMWPE fibres and LDPE matrix are shown in Fig. 6.5. It is revealed that the fibres have sharp equatorial peaks indicating a good structural order in the crystalline phase whereas LDPE matrix exhibits a broad and diffuse ring contributed by the LDPE matrix, indicating no preferred orientation. Their structural difference is mainly due to the different production processing of the materials. The ultra high molecular weight polyethylene fibres are produced by the process of gel spinning followed by drawing at high temperature to very high draw ratios that leads to fully extended and aligned chain configuration along the axial direction. In the case of the flat sheet of thermoplastic LDPE matrix, it is produced by compression molding. The matrix may contain both amorphous and crystalline phase, but it does not have molecular orientation during the molding process and consolidation.

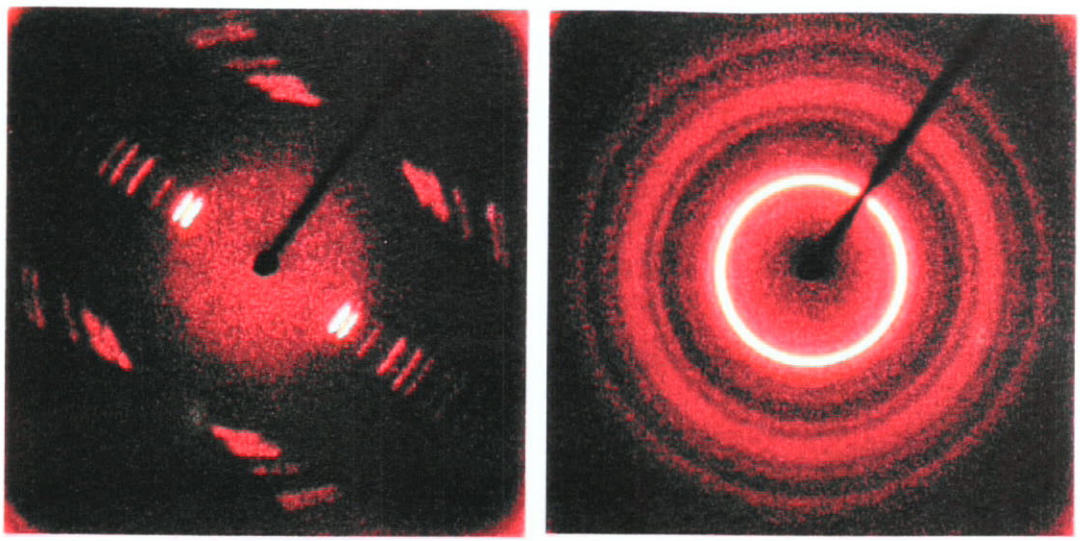

(a) (b)

Figure 6.5 X-ray diffraction (WAXS) patterns of (a) the UHMWPE fibres (*Dyneema*) (b) the LDPE matrix

6.3.2 Mechanical Properties

The tensile curves of the UHMWPE fibre, LDPE matrix and the resultant knitted composite are shown in Figs. 6.6 to 6.8. The material properties such as Young's modulus, strength and fracture strain of the individual UHMWPE fibre, matrix and composites are given in Table 6.1 and 6.2, respectively. The fibre is tough, with a high stiffness and little extension available (>5%), whereas LDPE is ductile and its extension can reach 800 %. When the fibres are oriented as knitted loops, the knitted composite exhibits a higher load level than soft matrix and has an extensibility of 74 %.

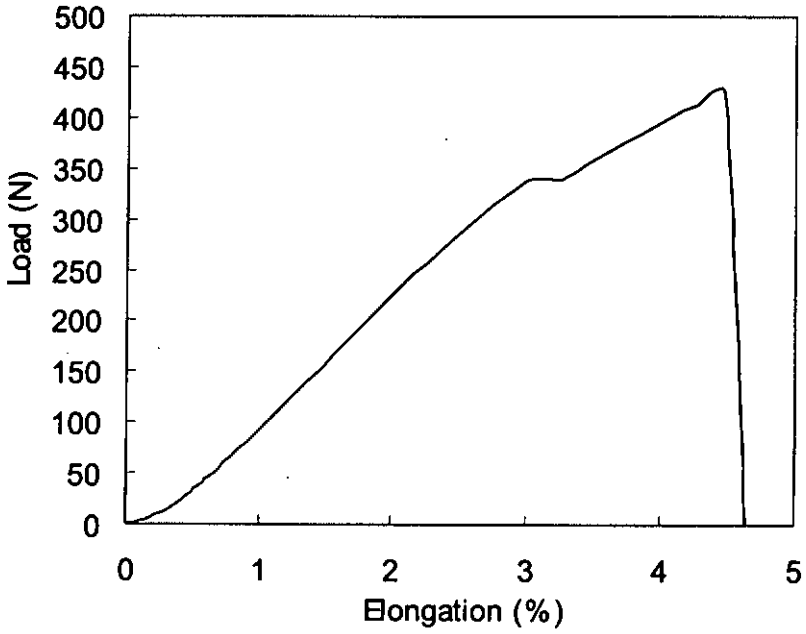

Figure 6.6 The tensile curve of the UHMWPE yarn (1760 denier)

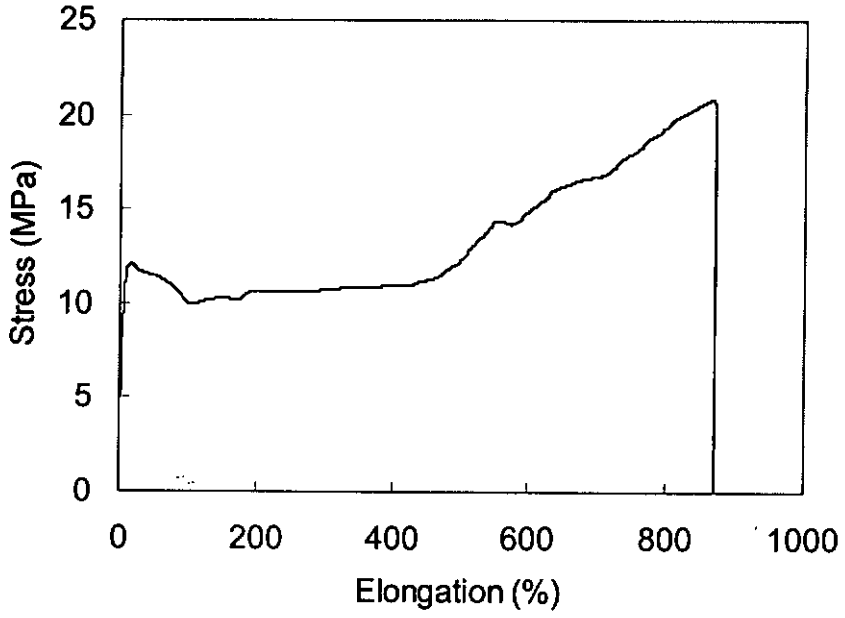

Figure 6.7 The tensile curve of the LDPE matrix

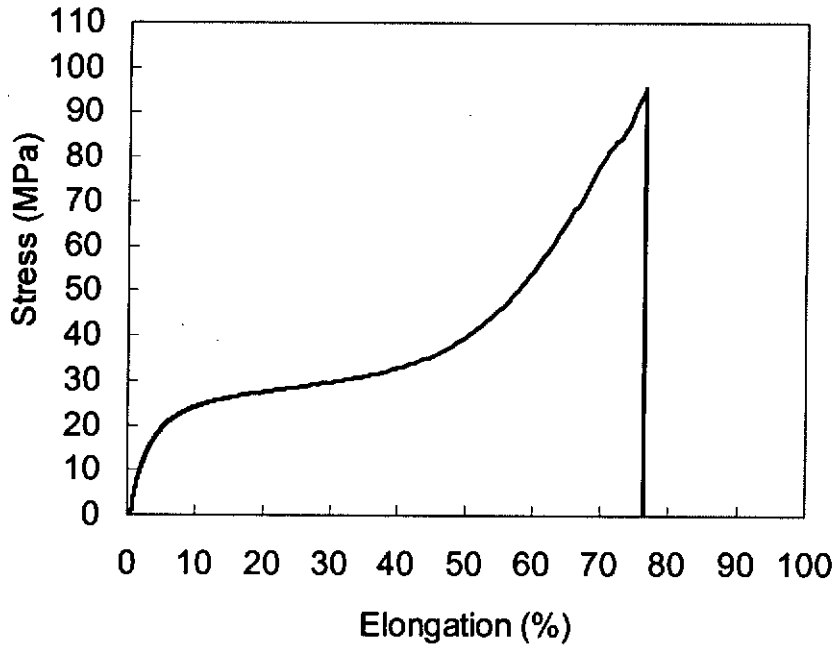

Figure 6.8 The tensile curve of the UHMWPE/LDPE composite

Table 6.1 Material properties of the UHMWPE fibre

	Young's modulus (GPa)	Tenacity (GPa)	Ultimate strain (%)
ISO2062 (DSM)	113.0	3.5	3.6
ASTM D2256-97 (measured)	103.64±54.81	3.05±1.11	5.68±1.78

Table 6.2 Material properties of the UHMWPE/LDPE knitted composite and the LDPE matrix

	Young's modulus (MPa)	Yield stress (MPa)	Yield strain	Ultimate strength (MPa)	Elongation (%)
Composite (walewise)	634.39±38.38	23.70±2.00	0.074±0.01	97.53±7.48	73.70±1.06
LDPE	300.98±60.92	11.27±0.86	0.095±0.01	20.51±2.50	878.06±61.14

6.3.3 Single Fibre Sensitivity

There are several well-defined Raman bands in the Raman spectrum obtained from both the UHMWPE fibre and the LDPE matrix, as shown in Figs. 6.9 (a-b). It is observed that the Raman bands obtained from the highly oriented polyethylene fibre are sharp and intense, whereas the LDPE has a weaker signal.

Figures 6.10 (a-b) show the Raman spectra in a region of 950-1200 cm^{-1} for a UHMWPE fibre before and after deformation in air. It can be seen that both 1060 cm^{-1} (assigned as C-C asymmetric stretching mode) and 1130 cm^{-1} (symmetric stretching mode) Raman bands split, upon stretching, into two components, which shift to lower wavenumbers at a different rate (Kip et al., 1991; Grubb and Li, 1992; Moonen et al., 1992; Wong and Young, 1994). It is possible to fit both of the bands to one broad Gaussian and one narrow Gaussian curves. It is also able to fit the Raman bands to two peaks before fibre deformation. The two Gaussian functions is the most suitable and best fit to deal with band asymmetry (Prasad and Grubb, 1989)

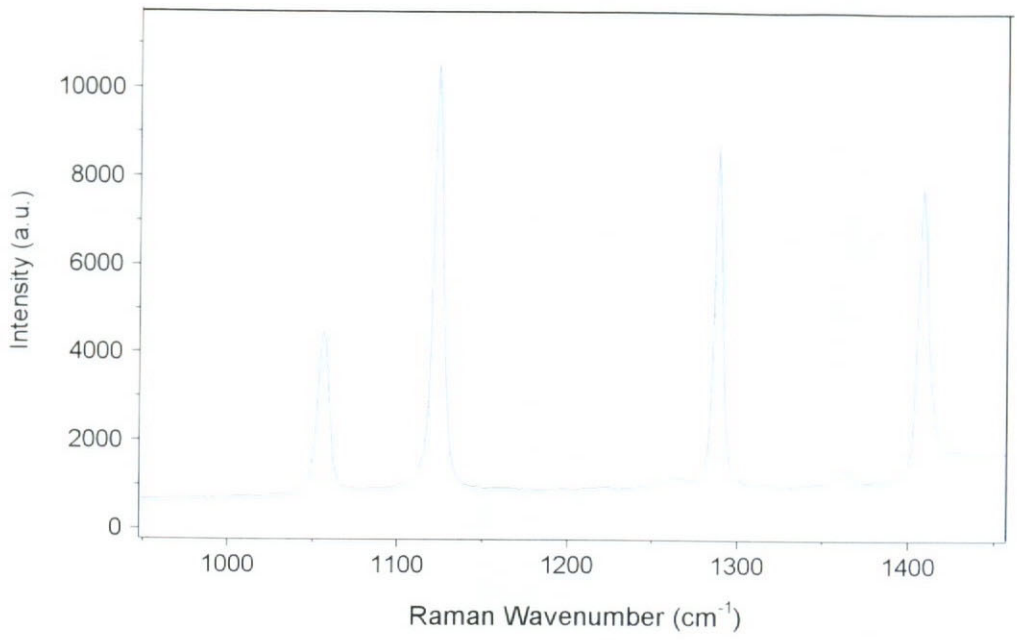

(a)

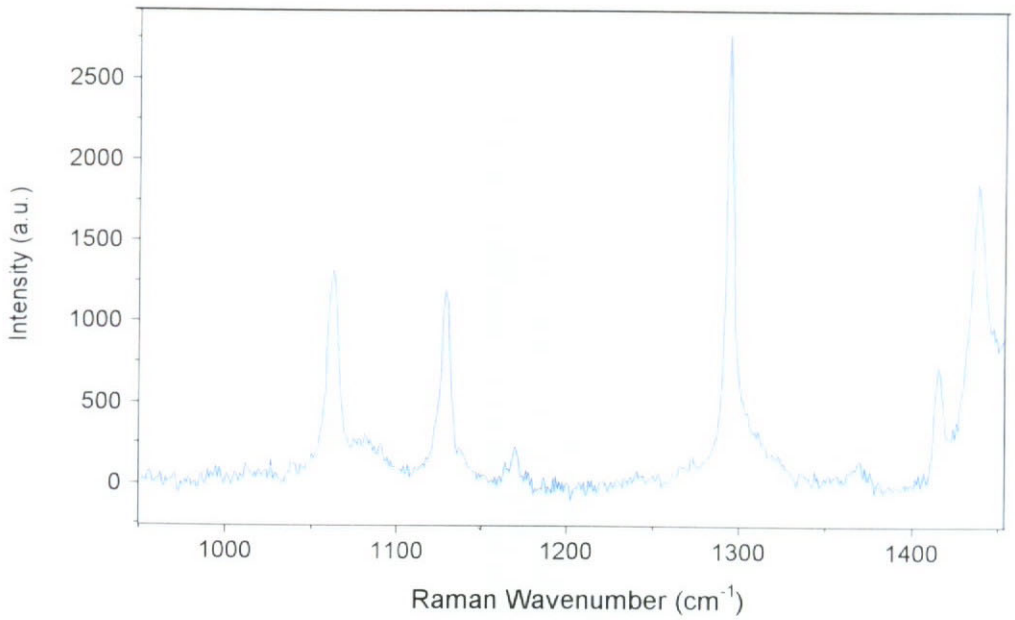

(b)

Figure 6.9 Raman spectrum of (a) a single filament of the Dyneema SK75 polyethylene fibre (b) a molded commercial graded LDPE matrix, in the region of 950-1450 cm^{-1}

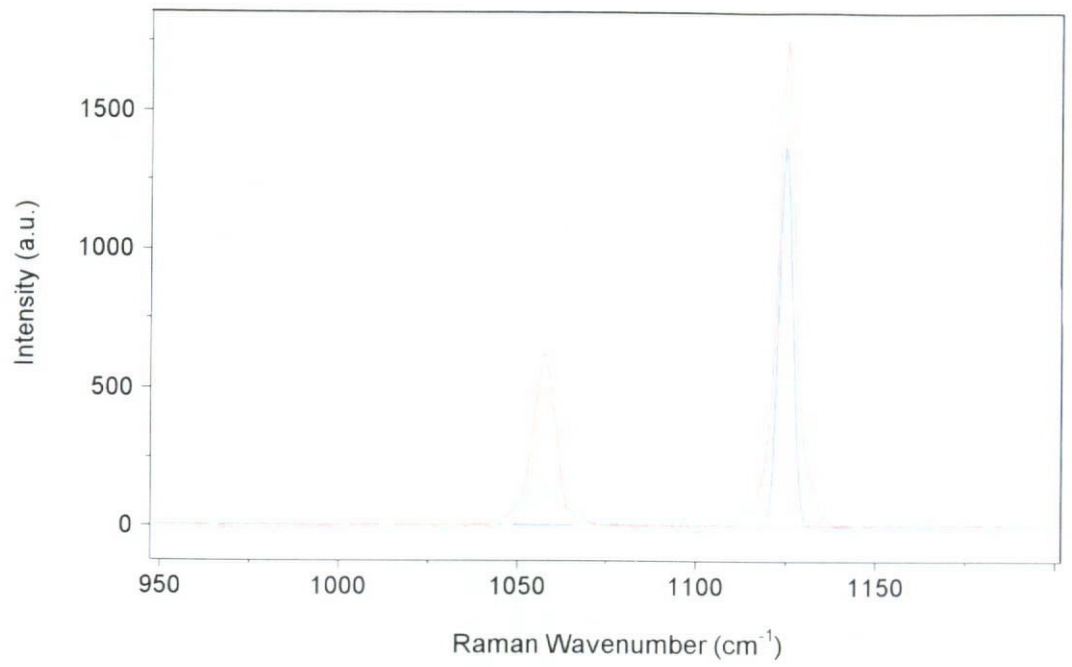

(a)

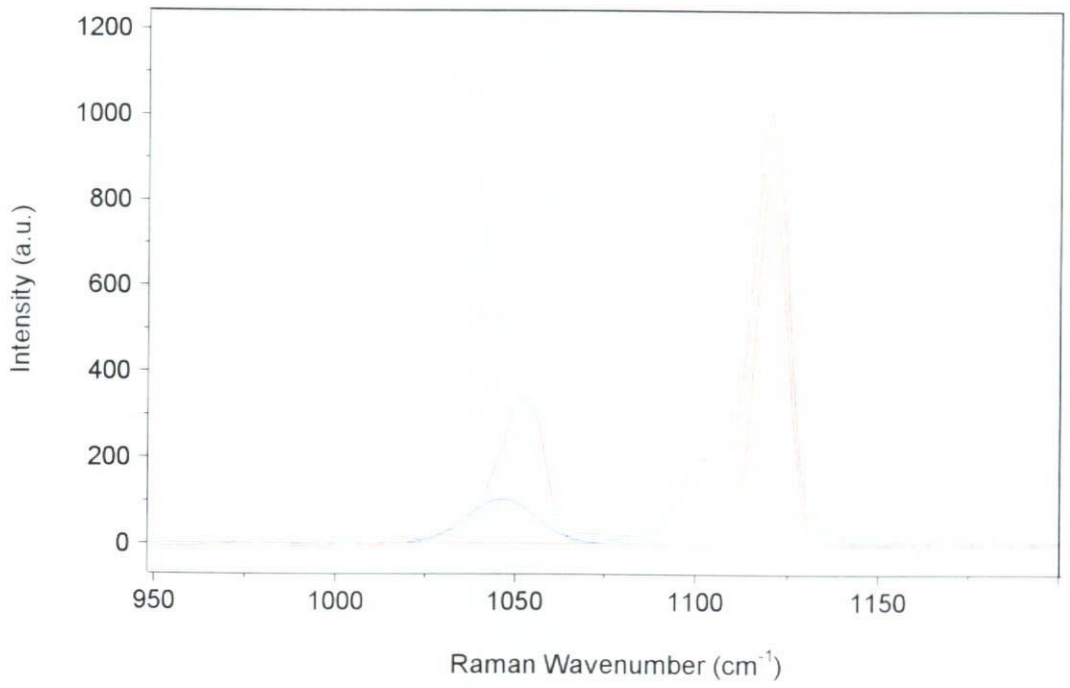

(b)

Figure 6.10 Curve fitting by two Gaussian functions to both of the Raman bands at 1060 cm^{-1} and 1130 cm^{-1} of the UHMWPE fibre stretched in air at (a) 0% strain (b) 2.8% strain

This type of behaviour for the UHMWPE fibre has been interpreted due to the presence of two populations of molecules in the microstructure in gel-spun polyethylene. During deformation, they experience different levels of stress. Kip et al (1991) described the molecular deformation of this fibre by Raman microscopy and found that both asymmetric and symmetric C-C stretching modes demonstrated well-defined band splitting and a bi-modal load distribution, with low-load (narrow peak) and high-load bearing (broad peak) C-C bonds. It is found that the size of the rapidly moving broad peak scales with the Young's modulus of the fibre and hence it appears that it is related to the presence of microstructural features which give rise to the impressive mechanical properties of the fibres.

There are the variations of the two fitted peak position with strain for both Raman bands at 1060 cm^{-1} and 1130 cm^{-1}. For the fitted narrow peak in Raman band at 1060 cm^{-1} as shown in Fig. 6.11 (a), there is a linearly decrease in the wavenumber shift to 2 % strain and then a plateau. As for the fitted broad peak, after a linear decrease of the shift up to approximately 2 % strain, the wavenumber shift is further decreased but becomes more scatter between 2 – 4 % strains. After 4 % strain, the wavenumber shift increases with strain up to fibre fracture. It is observed in Fig. 6.11 (b) that both the fitted peaks shift of the Raman band at 1130 cm^{-1} display similar patterns. The linear region of all of the broad and narrow peaks of the two Raman bands can be fitted with a linear function by the least-squares-fitting method, each has a slope of -4.8cm^{-1}/%strain and -3.12cm^{-1}/%strain for the broad and narrow peaks of 1060cm^{-1} Raman band, and -5.1cm^{-1}/%strain and -2.38cm^{-1}/%strain for the broad and narrow peaks of 1130 cm^{-1} Raman band, as shown in Figs. 6.12 (a-d). It is noted that the broad peak at 1130 cm^{-1} has a higher sensitivity to the axial strain, which is more

appropriate to be selected for monitoring the fibre deformation by the micro-Raman measurement.

The Raman wavenumber shifts with fibre strain for 1060 cm^{-1} and 1130 cm^{-1} Raman bands are similar as reported by Galiotis (1998). He explained that beyond the linear region and the formation of a plateau of the Raman band indicated the presence of a yield point of the fibre, that thought to be associated with the plastic flow of the amorphous part and the applied stress is transferred to the polymer crystal. His proposed structural model suggested that the crystal is thought to be linked in series with highly oriented amorphous chains.

Galiotis (1998) reported a real-time Raman measurement of the fibre deformation by taking the Raman spectra of the fibre, being extending at a specified strain rate on a mechanical tester with a short exposure time of 2 seconds at 7 mW laser power. In this study, however, the fibre was extended by a single-step stretching on the straining rig during Raman microscopy measurement. It may be the reason that led to the mismatch of the fracture strain obtained from the fibre tensile test (about 3 – 4 %) and deformation by Raman microscopy (up to 12 %). It may be the effect of stress relaxation of the fibre due to its viscoelastic behaviour. Nevertheless, the fibre strain is found to be within the linear region below 2 % in the micromechanics study of the knitted composites under large deformation up to 50 %.

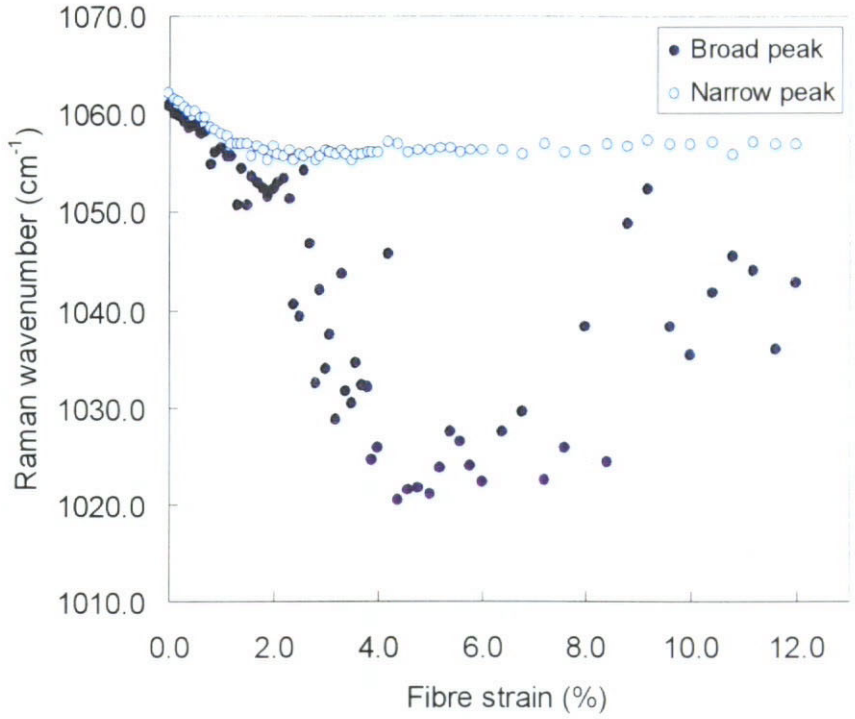

(a)

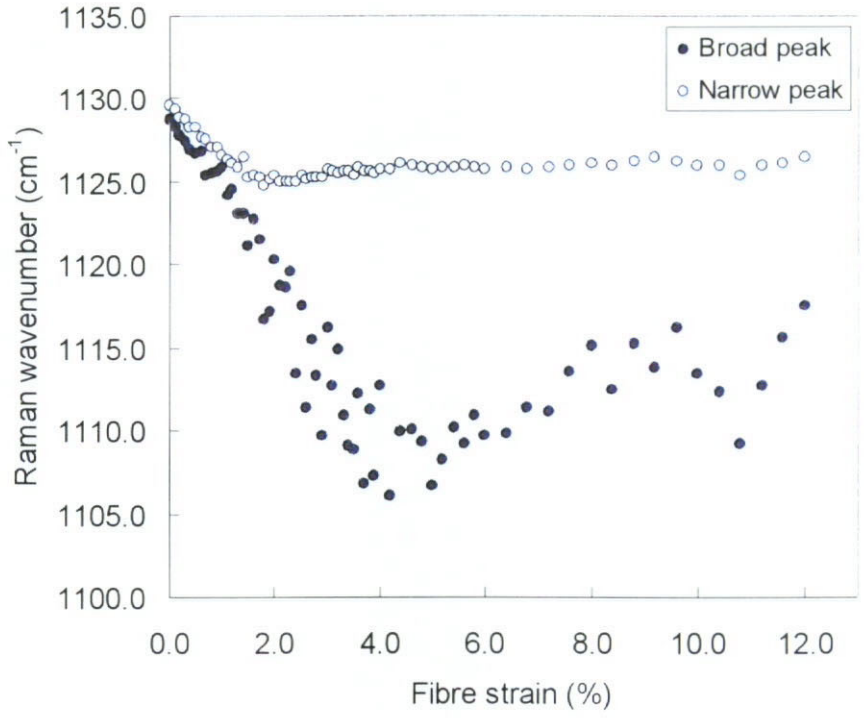

(b)

Figure 6.11 The shift of peak position of the two peaks in the (a) 1060 cm^{-1} and (b) 1130 cm^{-1} Raman bands of the UHMWPE fibre plotted against with fibre strain

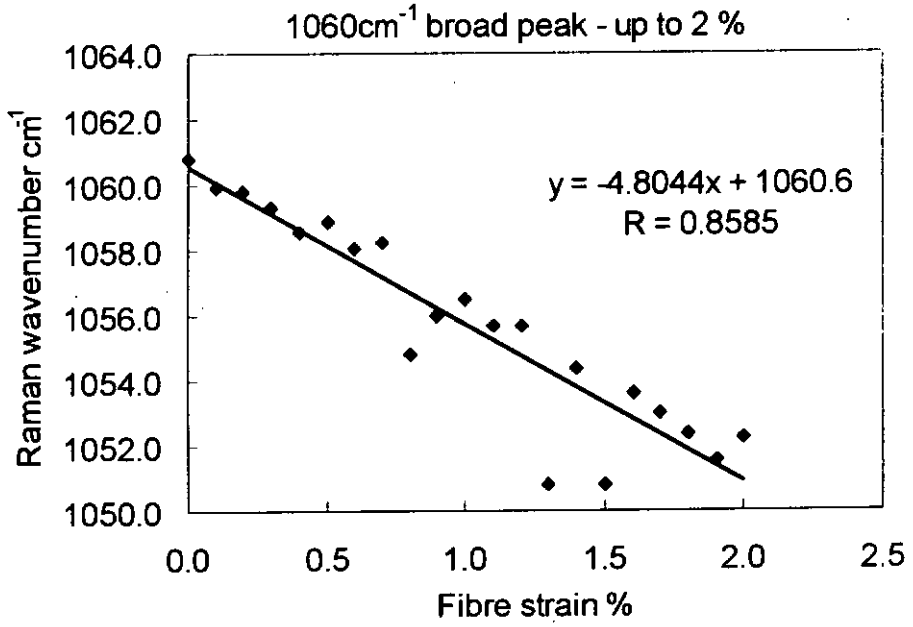
1060cm-1 broad peak - up to 2 %
Raman wavenumber cm-1
1064.0
1062.0
1060.0
1058.0
1056.0
1054.0
1052.0
1050.0
y = -4.8044x + 1060.6
R = 0.8585
0.0
0.5
1.0
1.5
2.0
2.5
Fibre strain %

(a)

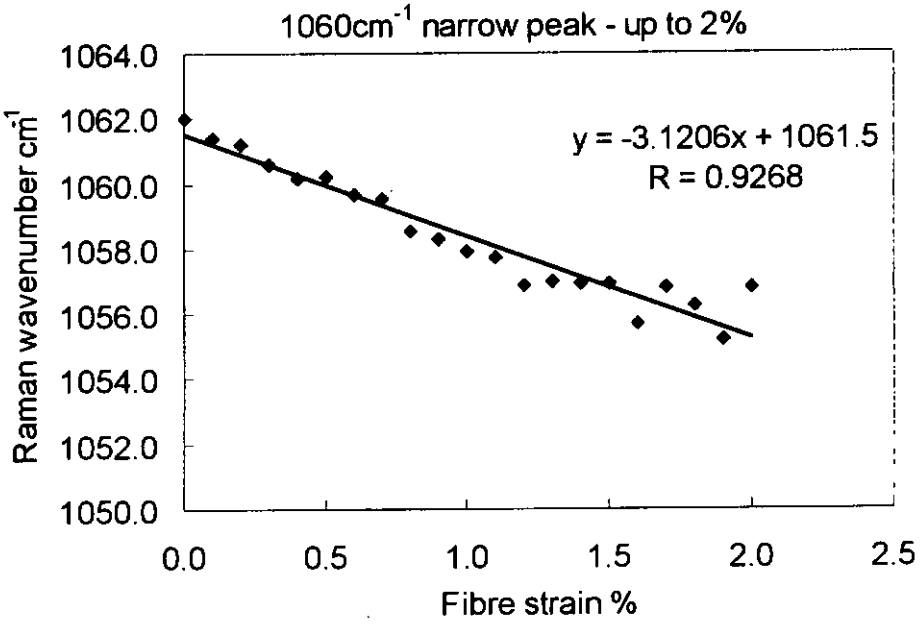
1060cm-1 narrow peak - up to 2%
Raman wavenumber cm-1
1064.0
1062.0
1060.0
1058.0
1056.0
1054.0
1052.0
1050.0
y = -3.1206x + 1061.5
R = 0.9268
0.0
0.5
1.0
1.5
2.0
2.5
Fibre strain %

(b)

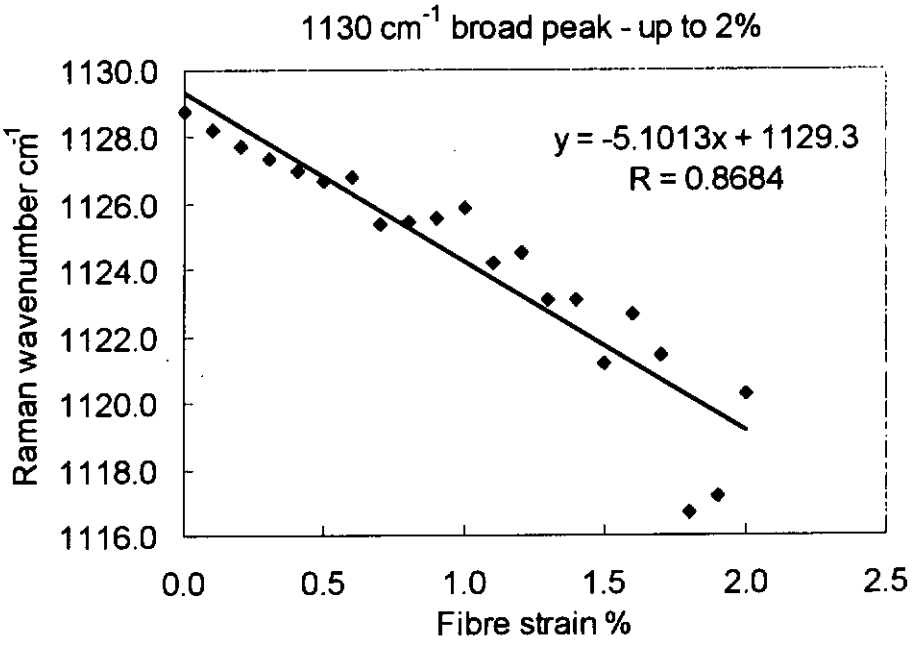

(c)

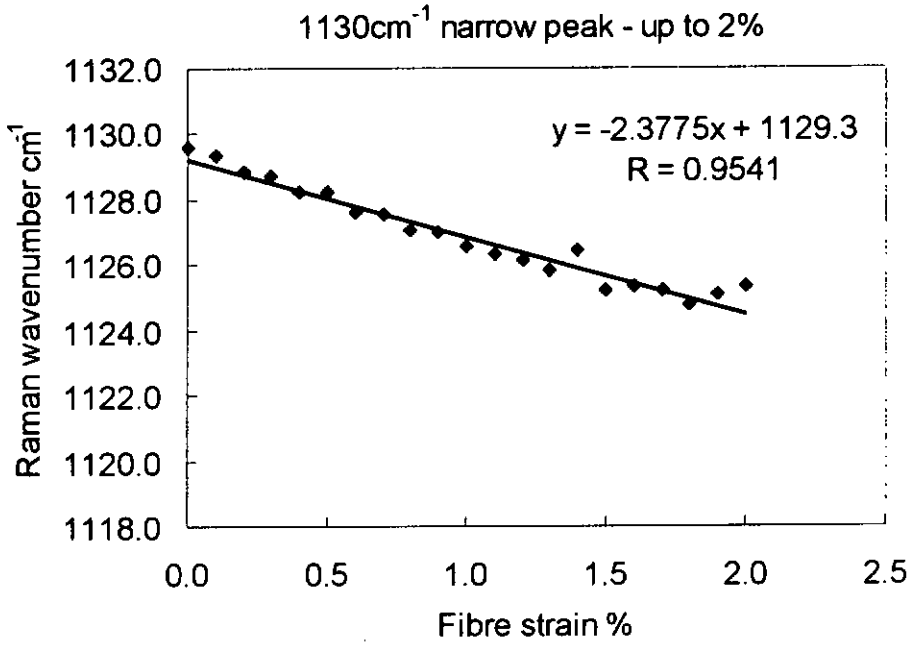

(d)

Figure 6.12 The Raman shift of the1060 cm^{-1} peak with fibre strain of UHMWPE fibre up to 2 % for the (a) broad band and (b) narrow band, and that of the1130 cm^{-1} peak with fibre strain for UHMWPE fibre up to 2 % for the (c) broad band and (d) narrow band

6.3.4 Raman Band Shift of Embedded Fibre and LDPE Matrix Upon Deformation

As the constituents of the composite fabricated for fibre strain measurement is of the same nature, the Raman spectra obtained from the embedded fibre surface through the transparent matrix may contain signals from LDPE. It is, thus, important to observe if there is the Raman band shift of the matrix under tension, which may adversely affect the accurate peak shift for the fibre strain measurement. Figure 6.13 shows the plot of Raman wavenumber shift against the applied strain of the embedded single UHMWPE fibre and pure LDPE matrix dog-bone specimens. The broad band of 1130 cm^{-1} Raman band shifts to lower wavenumbers and then increases gradually with the applied strain of the single fibre embedded in dog-bone specimen, which is similar to the shift pattern during stretching free standing fibre, while no significant shift is observed for the LDPE under stretching. Due to the significant difference of the strain induced Raman band shifts between the highly oriented UHMWPE fibre and the disoriented LDPE matrix, the Raman band shift obtained during the mapping is contributed by the embedded fibres.

It has been demonstrated in the last section that the highly oriented polymer chains in UHMWPE fibre would allow the effective transfer of the applied stress/strain to their backbone during stretching in the fibre direction, and lead to significant band shifts. In contrast, due to the disorientation of the compression molded LDPE matrix, which is also observed in the WAXD pattern of LDPE, there should be less transfer of load in the chain direction during the uniaxial drawing of the low modulus isotropic LDPE as most of the deformation on the molecular level is taken place by bond rotation and molecular uncoiling. At the necking region observed in the dog-bone specimen, the LDPE matrix may start the orientation of the polymer chains, but still

not as high as that of the highly oriented fibres to cause the Raman band shift.

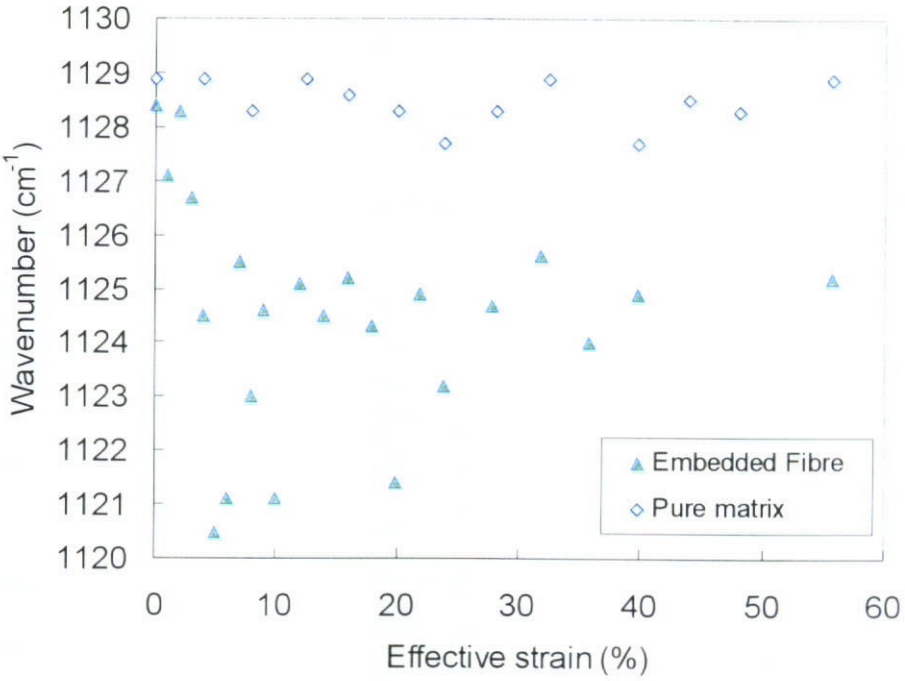

Figure 6.13 Wavenumber shift of the broad peak of 1130 cm^{-1} Raman band with the applied strain for the (▲) embedded UHMWPE fibre and (◇) pure matrix during deformation process of the dog-bone specimen

6.3.5 Fibre Loop Mapping in Composites

The fibre strain distributions of the knitted loop extended at (a) 0 %, (b) 20 % and (c) 30 %, along the wale direction are plotted in Fig. 6.14. The Raman band positions obtained from the unstretched fibre loop do not have obvious change, which implies that the residual stress induced by fabrication is very low. When the composite was extended to 20 % or 30 %, the fibre strains on the repeated unit of the mapped loop was unevenly distributed along the two bundles, with a maximum measured value of 0.5 % and 0.9 %, respectively.

In order to obtain a more obvious fibre strain distribution, the composite specimens were pre-notched on both edges at the specimen centre. The notches were made by cutting a 2-mm crack, as indicated in Fig. 6.15. When the specimen was stretched by the stretching frame, stress may concentrate on the wale loops at the specimen centre. Figure 6.16 shows the plots of fibre strain distribution at 20 % and 30 % composite stretching. The localized fibre strains reach a maximum value of 0.8 % and 1.8 %, respectively.

The fibre strains determined for the composite specimens are low, even the composites are pre-stretched. As the LDPE matrix is soft and ductile, assuming the fibres forming the loop bundle do not imply any twist, the loop shape change by rotating the loop legs and sliding of the fibre bundles are easy and dominate the early part of the large deformation. It can be observed that the mapped loop at the undeformed state is thick and round in shape. From the SEM micrograph in Fig. 6.17, the cross-section of the loop fibre bundles becomes elliptical resulted from compression molding. When it was extended, the mapped fibre bundles became

thinner and straightened, which are consistent to the fibre loops in the micrograph in Fig. 6.3. Significant loop shape changes during composite deformation have been discussed in details in literatures (Lam et al., 2003).

The fibre strains determined on the right side of the fibre bundle were generally higher than those on the lower side. It may be due to the stress transfer from left to right side of the specimen as it was stretched from the left and fixed at the other end, which leads to a subsequent loading of the fibre loops during the large deformation. Off-axis of fibre orientation along the fibre loop to the composite deformation direction may be another reason that affects the fibre strain measurement. Thus, the fibre legs which were more parallel to the stretching direction would have a higher load level that can be observed in Fig. 6.14 (b) and (c) and Fig. 6.16 (b) and (c).

The different fibre strain levels in these two fibre bundles may be caused by stress relaxation of the fibre upon stretching. As the mapping was done from point-to-point and from left to right of the repeated unit, fibre stress relaxation may occur during the mapping process. Figure 6.18 shows the effect of stress relaxation of the UHMWPE fibre embedded in the dog bone composite when it was held at different strain levels (3.0 %, 5.6 % and 8.3 %, respectively). The fibre strains measured were less than the effective strain of the composite. The reduction of fibre strains was more serious for the first 15 minutes. Then the embedded fibres tended to shift to the original stress/strain level. The fibre stress relaxation would be a critical problem during the mapping of the embedded knitted loop, which was held at different strain levels. From this observation, it would be better to start the mapping after 15-minutes just after the composite is being stretched, which allow the fibre strains to become

steady.

There are limitations on the focal depth of the laser beam through the matrix onto the embedded fibres using Raman microscopic technique. The signals were very weak and scattered at the cross-over region of the two fibre bundles, therefore, the fibre strain distributed can be determined on the fibre legs only. In addition, the fibre loop can be only mapped on the very surface underneath the transparent matrix. The fibre bundles are oriented in a three dimensional form, and have different depth underneath the matrix. The motor stepper can ensure the running from point to point in a plan, however, the laser beam has to be focused manually on the fibre surface. It cannot be a real-time process of the fibre strain measurement and is time consuming to focus the laser beam on the fibre surface that may lead to experimental error due to the fibre stress relax.

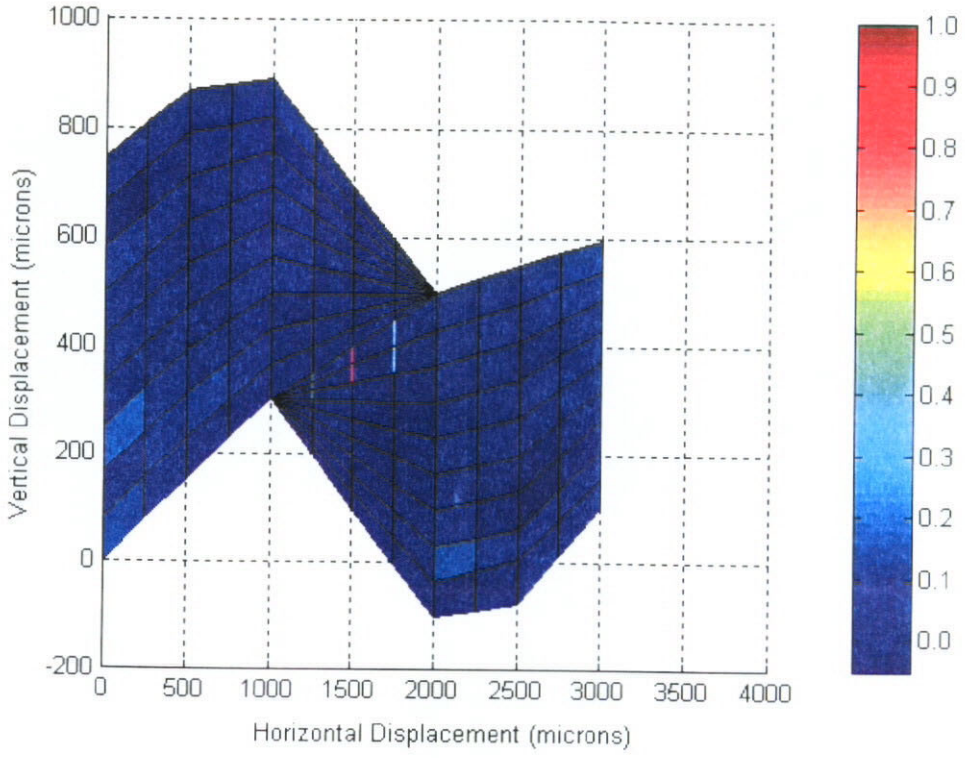
Vertical Displacement (microns)
1000
800
600
400
200
0
-200
0
500
1000
1500
2000
2500
3000
3500
4000
Horizontal Displacement (microns)
1.0
0.9
0.8
0.7
0.6
0.5
0.4
0.3
0.2
0.1
0.0

(a)

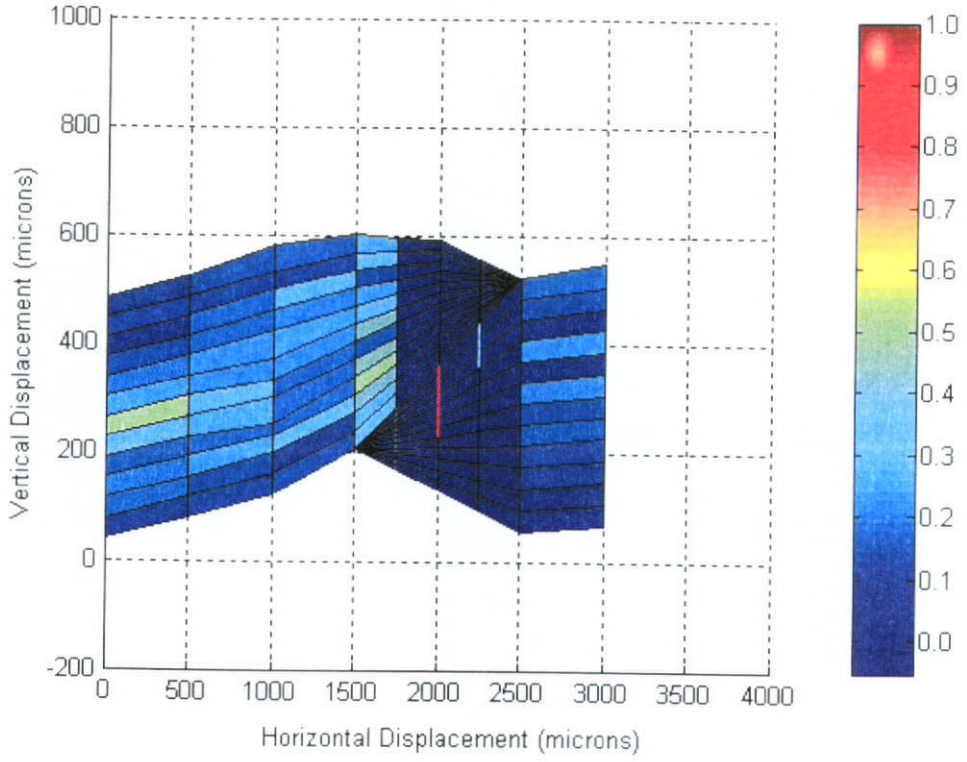
Vertical Displacement (microns)
1000
800
600
400
200
0
-200
0
500
1000
1500
2000
2500
3000
3500
4000
Horizontal Displacement (microns)
1.0
0.9
0.8
0.7
0.6
0.5
0.4
0.3
0.2
0.1
0.0

(b)

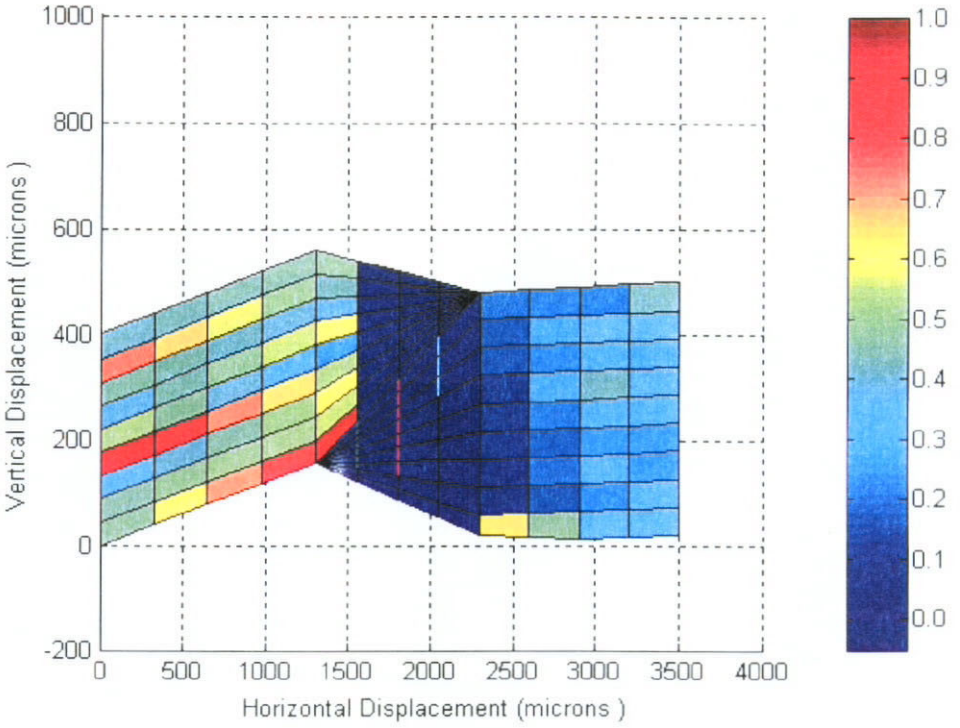

(c)

Figure 6.14 The fibre strain distribution of a knitted loop in the composite at different stretching levels (a) 0 %, (b) 20 % and (c) 30 %

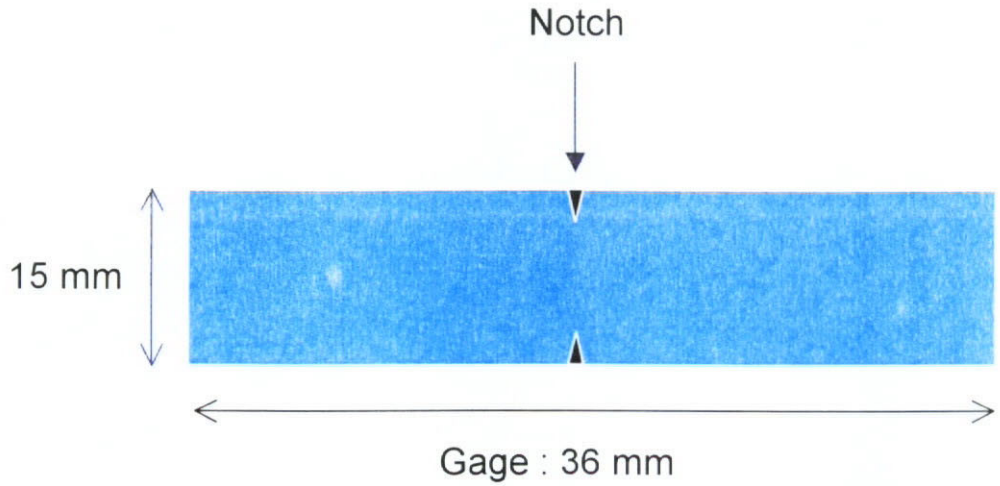

Figure 6.15 Schematic diagram of the flat knitted composites with notching before extending on the stretching frame

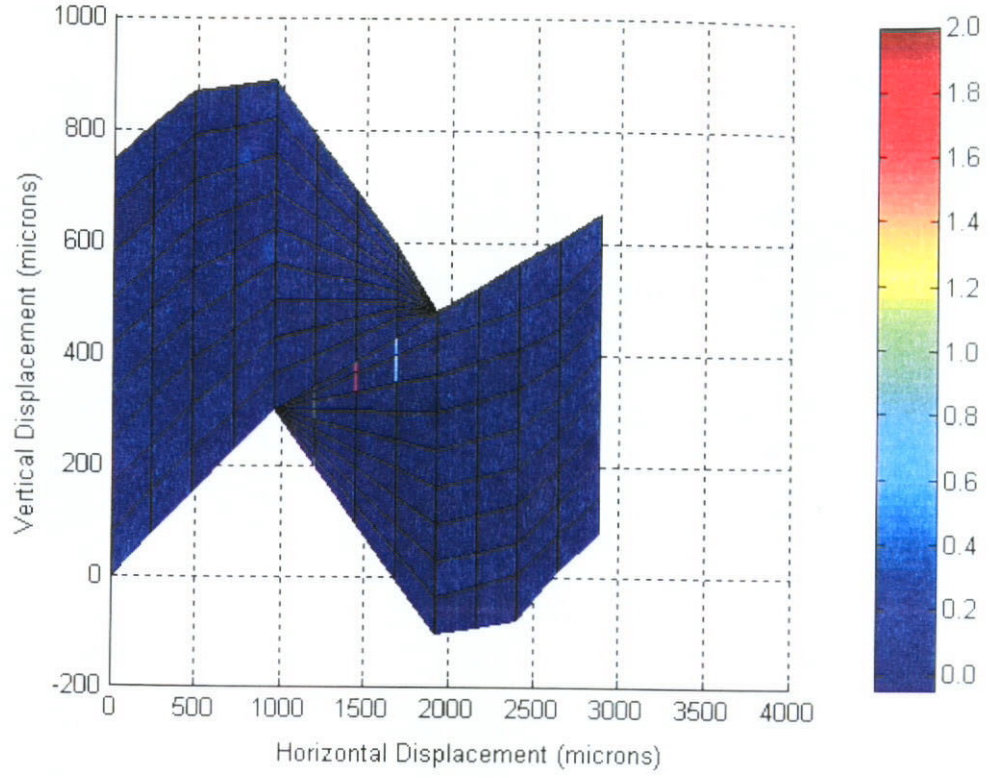
Vertical Displacement (microns)
1000
800
600
400
200
0
-200
0
500
1000
1500
2000
2500
3000
3500
4000
Horizontal Displacement (microns)
2.0
1.8
1.6
1.4
1.2
1.0
0.8
0.6
0.4
0.2
0.0

(a)

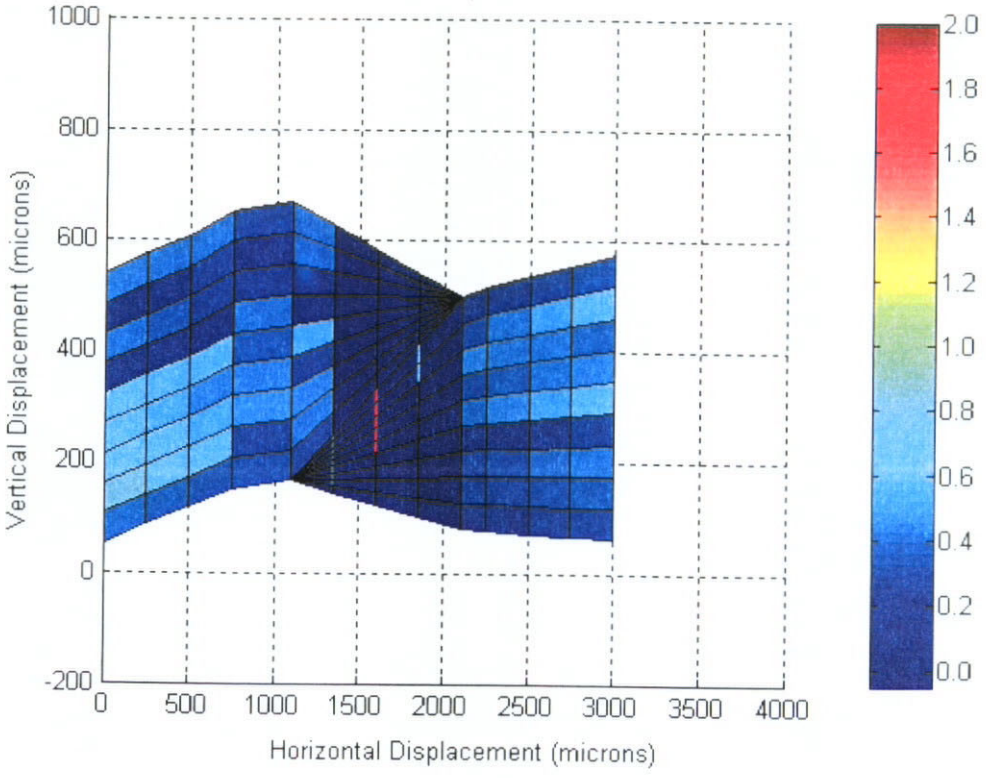
Vertical Displacement (microns)
1000
800
600
400
200
0
-200
0
500
1000
1500
2000
2500
3000
3500
4000
Horizontal Displacement (microns)
2.0
1.8
1.6
1.4
1.2
1.0
0.8
0.6
0.4
0.2
0.0

(b)

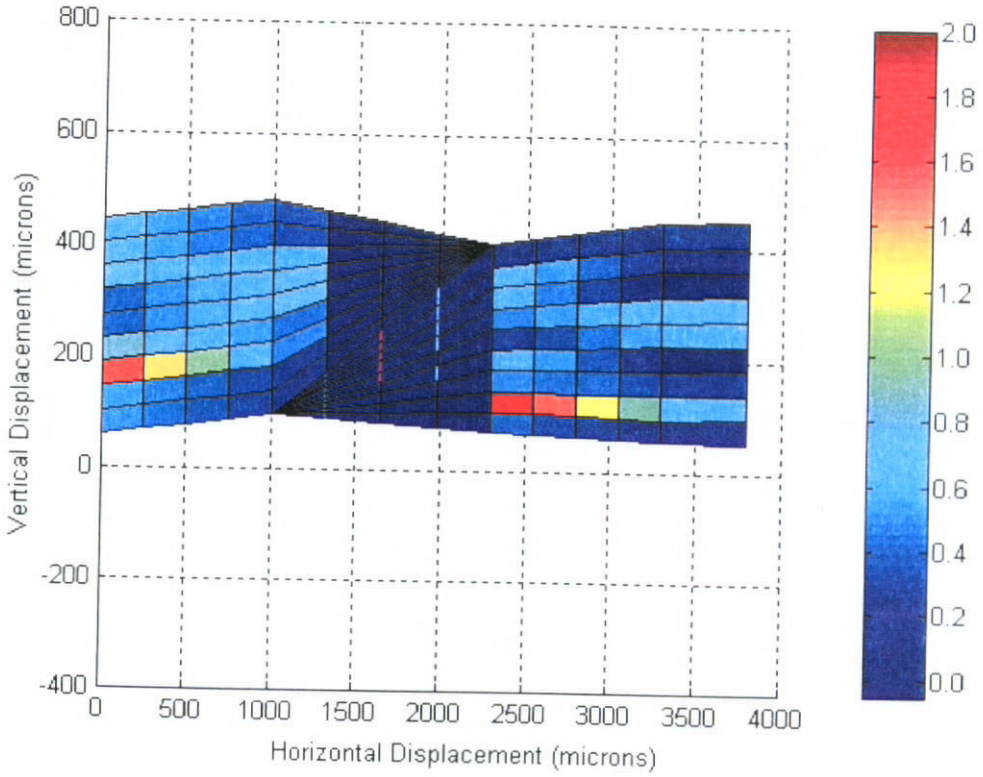

(c)

Figure 6.16 The fibre strain distribution of a knitted loop in the notched composite at different stretching levels (a) 0 %, (b) 20 % and (c) 30 %

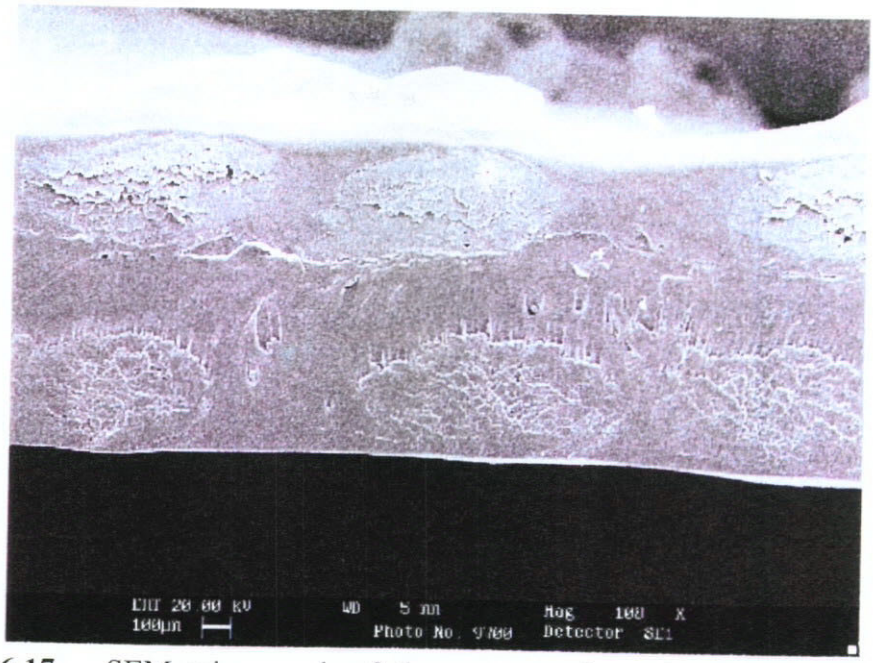

Figure 6.17 SEM micrograph of the cross section of the UHMWPE/LDPE knitted composite showing the elliptical shape of the fibre loops

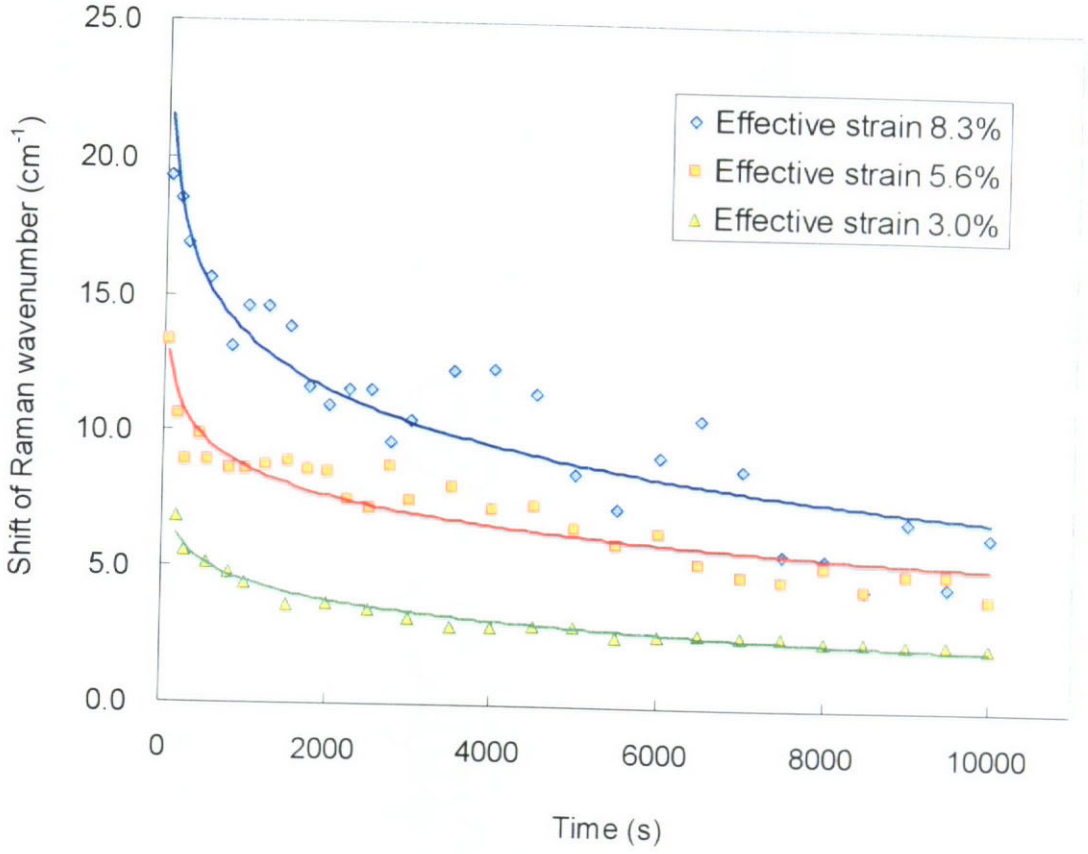

Figure 6.18 Stress relaxation process of an embedded fibre in dog-bone shaped composite

6.4 Fibre Strain Predication of Weft-Knitted Composites

The fibre strain in the knitted composites can be obtained experimentally during different levels of fibre stretching by Raman mapping. A simple model is proposed to predict the average fibre strain in the knitted composite being stretched in the wale direction. The UHMWPE/LDPE Rib1x1 knitted composite can be regarded as a plain knitted structure on one of its faces. A simple geometry is depicted as a projected dimension of the repeatable fibre loop, and further divided into one-forth of a single loop, as a unit cell of the fibre loop. The unit cell contains parts of two fibre bundles crossing over each other, as shown in Fig. 6.19. The two fibre bundles follow a straight path with a yarn length x and a thickness t, align with an angle θ to the loading direction, except at the cross-over region, which extend to form a half of hemi-spherical loop head. The inner line of the loop head has a radius r from the centre O located in the matrix to the mid-point of line AA'. In developing the model the following assumptions have been made:

1. The structural change of fibre loop is considered to be two-dimensional;
2. The fibre slippage in the fibre bundles is negligible;
3. The composite is free of voids;
4. The thickness or yarn width t is constant during tensile loading;
5. The total loop length in the repeat unit is constant during displacement;
6. From the diagram, the inner lines of both fibre bundles contact each other on the line AA' and the centre line of both fibre bundles at line MN parallel the length of the repeated unit.

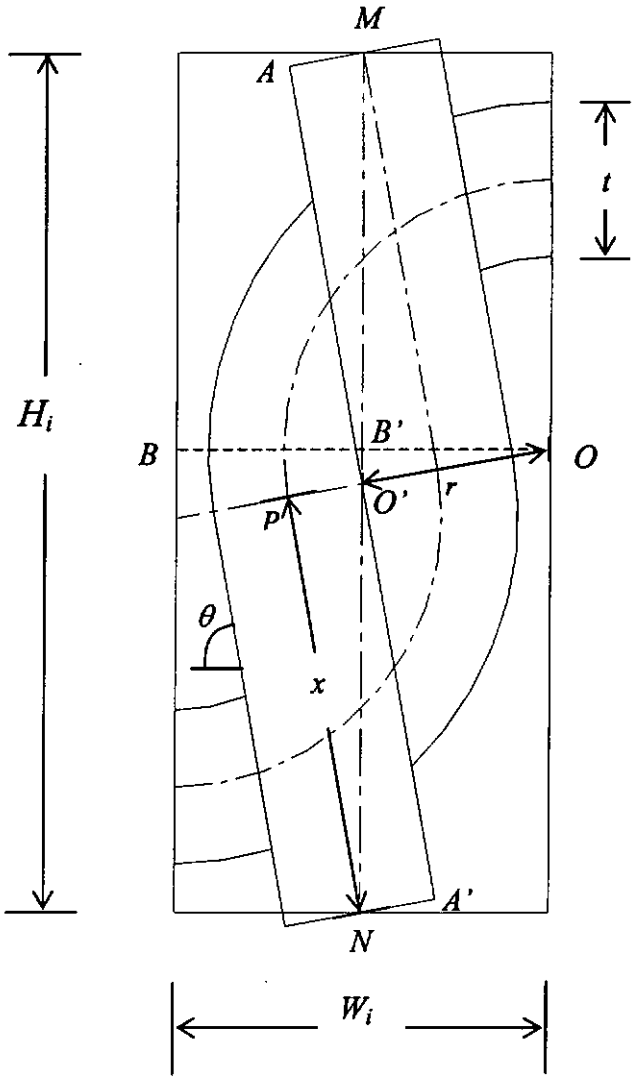

Figure 6.19 Unit cell geometry of the fibre loop

Then, the dimensions of the unit cell are given by

$$H_i = 2x\sin\theta + t\cos\theta \tag{6.1}$$

and $$W_i = 2r\sin\theta \tag{6.2}$$

where H_i and W_i are the length and width of the unit cell, respectively.

To solve the relationship between the angle and the cell dimensions, by considering the triangle $O'A'N$, x can be expressed as

$$x = \frac{H_i}{2}\sin\theta \tag{6.3}$$

substituting Eq.6.3 into Eq.6.1 gives

$$H_i = 2(\frac{H_i}{2}\sin\theta)\sin\theta + t\cos\theta$$

$$H_i = H_i \sin^2\theta + t\cos\theta$$
$$H_i(1-\sin^2\theta) = t\cos\theta$$
$$H_i\cos^2\theta = t\cos\theta$$
$$\cos\theta = \frac{t}{H_i}$$

Then, the angle of the fibre legs can be determined by H_i directly assuming the yarn thickness is constant and the sliding of fibres during loop distortion can be negligible.

$$\theta = \cos^{-1}(\frac{t}{H_i}) \tag{6.4}$$

where $0 < \theta < 90°$

Considering a loading force F is applied on the knitted composite specimen, most of the load bearing is supposed being taken up by the fibres, which exhibit a three order of the stiffness to that of the LDPE matrix. Therefore, the fibre tension T on each fibre bundle can be determined by considering n fibre bundles or knitted loop legs on cross-sections of the composite which aligned an angle θ to the loading direction with an applied force F:

$$\mathrm{T} = \frac{F}{n\sin\theta} \tag{6.5}$$

where the angle θ can be easily obtained with the change of H_i.

Accordingly, the fibre strain in the loop legs in composites at a particular stage of composite displacement Δ under a tensile force T with a cross-sectional area A can be expressed as:

$$\varepsilon_f = \frac{\mathrm{T}}{E_f A} \tag{6.6}$$

where E_f is the Young's modulus of the fibres.

Other than the relationship of between θ and the displacement of composite loop to be determined from the expression, the shape change ratio of the embedded loop in the coursewise direction during tension in the walewise direction can also be estimated. The length a of each fibre bundle in the unit cell and is given by

$$\begin{aligned} a &= x + (r + \frac{t}{2})(\frac{\pi}{2} + \frac{\pi}{2} - \theta) \\ &= x + (r + \frac{t}{2})(\pi - \theta) \end{aligned} \tag{6.7}$$

As $x = \frac{H_i}{2}\sin\theta$, sub it into Eq.(6.7),

$$a = (\frac{H_i}{2}\sin\theta) + (r + \frac{t}{2})(\pi - \theta)$$

Then, $$r = \frac{a - \frac{H_i}{2}\sin\theta}{(\pi - \theta)} - \frac{t}{2} \tag{6.8}$$

As shape change ratio $v = -\frac{\partial W_i}{\partial H_i} = \frac{\partial W_i}{\partial \theta} / \frac{\partial H_i}{\partial \theta}$

$$\frac{\partial H_i}{\partial \theta} = \frac{\cos\theta(0) - t(-\sin\theta)}{\cos^2\theta} = \frac{t\sin\theta}{\cos^2\theta} \tag{6.9}$$

substituting Eq.(6.8) into $W_i = 2r\sin\theta$

$$\begin{aligned} W_i &= 2[\frac{a - \frac{H_i}{2}\sin\theta}{(\pi - \theta)} - \frac{t}{2}]\sin\theta \\ &= [\frac{2a - H_i\sin\theta}{(\pi - \theta)}]\sin\theta - t\sin\theta \end{aligned}$$

substituting $H_i = \frac{t}{\cos\theta}$ into the above expression,

$$W_i = [\frac{2a - \frac{t}{\cos\theta}\sin\theta}{(\pi - \theta)}]\sin\theta - t\sin\theta$$

$$= [\frac{2a - t\cdot\tan\theta}{(\pi - \theta)}]\sin\theta - t\sin\theta$$

Then,

$$\frac{\partial W_i}{\partial\theta} = [\frac{2a - t\cdot\tan\theta}{(\pi - \theta)}]\cos\theta + [\frac{(\pi - \theta)(0 - t\cdot\sec^2\theta) - (2a - t\cdot\tan\theta)(0 - 1)}{(\pi - \theta)^2}]\sin\theta - t\cos\theta$$

$$= [\frac{2a - t\cdot\tan\theta}{(\pi - \theta)}]\cos\theta + [\frac{(2a - t\cdot\tan\theta) - t(\pi - \theta)\cdot\sec^2\theta}{(\pi - \theta)^2}]\sin\theta - t\cos\theta \qquad (6.10)$$

As $\frac{\partial\theta}{\partial H_i} = \frac{\cos^2\theta}{t\sin\theta}$ from (6.9)

Thus, $$\frac{\partial W_i}{\partial H_i} = [\frac{2a - t\cdot\tan\theta}{(\pi - \theta)}]\frac{\cos^3\theta}{t\sin\theta} + [\frac{(2a - t\cdot\tan\theta) - t(\pi - \theta)\cdot\sec^2\theta}{t(\pi - \theta)^2}]\cos^2\theta - \frac{\cos^3\theta}{\sin\theta}$$

$$= \frac{(2a - t\cdot\tan\theta)\cos^3\theta}{t\sin\theta(\pi - \theta)} + \frac{(2a - t\cdot\tan\theta)\cos^2\theta - t(\pi - \theta)}{t(\pi - \theta)^2}\frac{\cos^3\theta}{\sin\theta} \qquad (6.11)$$

As t and a are assumed to be a constant value, the shape change ratio is depended on angle θ. Due to the fact that there is a lack of experimental measurement of the dimension changes during the composite stretching, the expression of the shape change ratio is an optional product for the geometrical model.

Table 6.3 shows the details of the input parameters to predict the fibre strains of the UHMWPE knitted/LDPE composite. Figure 6.20 plots the relationship of the fibre strain in composite loop corresponding to the composite elongation up to 30 %. The measured fibre strains at 0 %, 20 % and 30 %, respectively, were obtained by averaging the mapped strains in fibre bundles during Raman mapping. Without

stretching, there has no or very little internal strain being measured by Raman mapping. When the composite is stretched to 20 %, the average values of the measured fibre strains are close to the predicted ones. At 30 % composite stretching, the deviations of the measured and the predicted strains become large as shown from the large standard deviations.

Strain mapping on a knitted loop is located at the specimen centre, where stress may concentrate there. However, the model provides an overall fibre strain prediction in the composite specimen. Thus, the predicted values are less than the measured ones. At low composite stretching, both fibres and matrix may have contribution on load bearing. At high composite stretching, most of the load should be taken by the fibres, the measured values, in contrast, deviated much more than the predicted ones. Limited experimental mapped fibre strains obtained for further observing such deviation is also a restriction to the comparison with the prediction.

Table 6.3 Input parameter to the model and model predictions for UHMWPE knitted/LDPE composites

Yarn Thickness, t		=0.6 mm
Loop height in unit cell, H_l	At composite elongation :	
	0%	=3.0mm
	10%	=3.1mm
	20%	=3.2mm
	30%	=3.5mm
No. of loop legs on cross-section of the composite specimen		=32
Estimated yarn cross-sectional area, A	(mm^2)	=0.2827mm^2

Parameters measured from experiment

			Measured fibre strain, ε_f (%)					
	Load, L (N)	Yarn Tension, T (N)	Loop 1		Loop 2		Loop 3 (Pre-notched)	
At composite elongation :			Bundle 1	Bundle 2	Bundle 1	Bundle 2	Bundle 1	Bundle 2
0%	0	0	0.056	0.057	-	-	-	-
10%	483.60	15.42	-	-	-	-	-	-
20%	547.89	17.43	0.180	0.175	0.227	0.136	0.411	0.383
30%	594.60	18.86	0.249	0.209	0.519	0.272	0.585	0.470

Parameters deduced from the model

	Angle, θ (deg)	Fibre strain ε_f (%)
At composite elongation :		
0%	78.46	0.000
10%	78.84	0.130
20%	79.19	0.150
30%	80.13	0.160

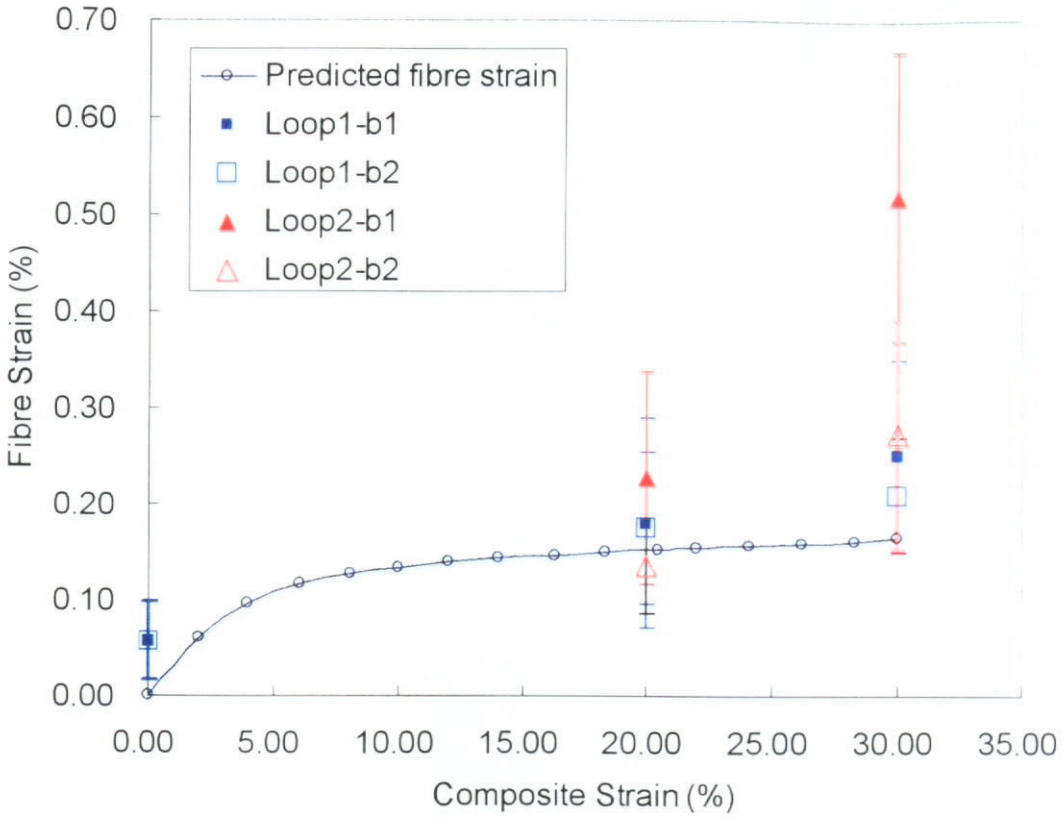

Figure 6.20 Predicted and experimental values of fibre strains at various levels of composite strain

6.5 Concluding Remarks

In this chapter, the fibre strains distributed in knitted composite were determined experimentally and theoretically during large deformation. Material characterizations have shown the unique properties of the UHMWPE fibres due to its high modulus and flexibility being bent into fabric loops. Raman microscopy was employed to

study the deformation of the UHMWPE fibre, which acts as an optical strain sensor that is able to determine the local fibre strains in the UHMWPE/LDPE knitted composite. The broad symmetric C-C stretching peak at Raman band 1130 cm^{-1}, which is the most sensitive to the applied strain, has a linearly shift to lower wavenumbers accounted for -5.1cm^{-1}/%strain up to about 2 % fibre strain. It is possible to map the gradual increase in fibre strains in the mapped loops during the increment of composite strains and depict the significant loop shape changes under large deformation.

Due to the loop shape changes by fibre rotation and sliding during large deformation, the fibre strain was low at the maximum order of 1 to 1.8 % even on notched composite. In particular, off-axis orientation and stress relaxation of the fibre material due to time delay during manually operation on laser beam focusing onto the fibre surface during mapping have attributed to the difficulty to achieve an accurate and time effective Raman mapping.

A geometrical model of a fibre loop was proposed to predict the fibre strains during composite stretching in the wale direction. The fibre strain prediction is managed to compare with the average values of the measured fibre strains except at high strain levels where there is a large deviation of the measured fibre strains, from the predicted ones.

CHAPTER 7

CONCLUSIONS AND FUTURE WORK

7.1 Conclusions

The multi-scales study of mechanical properties of thermoplastic cellular textile composites has achieved the objectives as outlined in Chapter 1 of this thesis. It has demonstrated that the use of light-weight and highly conformable non-woven fabrics provides a better fabrication process of thermoplastic cellular composites with a better material system for energy absorption purposes.

In this study, the large membrane stretching and bending of the composite materials while keeping the structure integrity of the cellular composites, have formed a primary mechanism of energy absorption of the cellular textile composites. Detailed findings are summarized as follows.

Characterization of Composites with Different Reinforcements

The energy-absorption behaviours of various thermoplastic cellular textile composites reinforced with both knitted and non-woven fabrics have been characterized under quasi-static compression and dynamic impact conditions. In knitted cellular composites, equivalent cell wall thickness has a predominant effect on governing the energy absorption capacity of the cellular structure where large amount of voids are present in the structure. While under the same thickness, the fibre volume fraction in non-woven cellular composites has demonstrated a positive effect on the reduction of high peak load and allowed a prolonged stroke. In response

to dynamic condition, as long as the fibre material is sufficiently strong, ductile and flexible to be bent to form knitted loops, strength of reinforcing fibres has little effect on the performance of the knitted cellular composites.

The non-woven composites exhibit a better performance on energy absorption than the knitted composites. The high conformability and cheap material cost of the non-woven fabric is believed to bring more advantages on cost reduction.

Mechanism of Energy absorption of Non-woven Cellular Composites

Detailed investigation on the performance PET/PP non-woven cellular composites under impact conditions has been carried out. The fracture mode of the non-woven composites varies with increasing fibre volume fraction. Increase in the fibre volume fraction in non-woven composites improves the shear strength and composite toughness under impact and thus, facilitates a full densification of the cell without premature failure. The non-woven composites exhibit high specific energy absorption capacity and retain the same level during multiple impacts.

A theoretical model has been proposed for such isotropic material reinforced cell which enables to predict the mean peak load and energy absorption capacity of a cell during plastic collapse. The theoretical predictions for pure material or non-woven reinforced composite are in good agreement with the experimental results, so it can guide an effective design of the similar material systems.

Characterization of the In-plane Properties of Knitted Composites and its Individual Components

Due to the anisotropy of PET/PP knitted composites, in-plane mechanical properties of various weft-knitted fabrics and their thermoplastic composites as well as the energy absorption mechanisms have been investigated. The knitted composites display superior tensile properties in the wale direction to in the diagonal and course directions. Both the matrix and fibres contribute to the load-carrying capacity in the elastic stage. The knitted composite has the most excellent combination of properties than its individual components in terms of energy absorption capacity. Increase in the fibre volume fraction of the composite structure leads to a positive effect on its mechanical properties. Surface modification by plasma treatments on PET fibre improves the interface adhesion, leading to a smooth load-deformation curve. Due to the stretchability of the knitted fabric reinforcement, the mechanical properties of the composites can be tailored by pre-stretching of the knitted reinforcement prior to the composite fabrication.

Deformation Mechanisms of Knitted Textile Composites

The in-plane deformation mechanism of PET/PP knitted composites has been identified: (1) both matrix and fibres contribute to the load-carrying capacity in the elastic stage. (2) Critical points including brittle matrix crack initiation from imperfect composite surfaces, fibre/matrix debonding, serious loop distortion along the loading directions and fibre straining during the large deformation until composite fracture have contributions on energy absorption of the composite during the large deformation process. (3) Localized compression and extension of the matrix, crack propagation of matrix, debonding of the fibre/matrix interface, deformation of

loop structure and extension of reinforcing fibres occur subsequently in the large composite deformation.

Micromechanics Study of the Unidirectional Single Short PET Fibre/PP Matrix Model Composite

Raman microscopic measurements have been conducted on single Poly(ethylene terephthalate) fibres in air and embedded in polypropylene matrix model composites. Well defined Raman spectra have been obtained from the PET fibres in air and in the PP matrix. The band of 1616cm^{-1} shifts due to tensile strain to low wavenumbers and broadens with a wavenumber related linear strain sensitivity –0.21cm^{-1}/%. It has been found that the whole length of the embedded fibre is under axial compression strain of –2.0%, which is caused by the different volume shrinkages of the fibre and matrix on cooling from high temperature fabrication. The fibre strain increment is consistent with the effective composite strain when the fibre is under the compression. The fibre strain becomes smaller than the composite strain where interfacial failure possibly happens. Micro-Raman measurement is also able to identify the delayed massive occurrence of interfacial failure at a relatively higher matrix strain on the plasma treated PET fibres, implying some improvement on the interfacial adhesion. However, considering the limitation of the Raman microscopy for the micromechanics study on those conventional fibre materials, alternative UHMWPE fibre is suggested for the fibre strain measurement in knitted composites by Raman microscopy.

Determination of Fibre Strain in Knitted Composite and Theoretical Prediction

High modulus UHMWPE fibres have a strain sensitivity as high as -5.1cm^{-1}/%strain

up to about 2% fibre strain for the symmetric C-C stretching peak at Raman band 1130cm^{-1}. It is successful to employ micro-Raman technique for mapping fibre strains on a knitted loop during composite deformation. The fibre strains in the embedded fabric loops have been determined at the maximum order of 1 to 1.8 % even on notched composite for the increment of effective composite strains up to 30%. The low fibre strains may be due to (1) significant loop shape change by fibres rotation and sliding during the large deformation, (2) off-axis orientation and (3) stress relaxation of the fibre material during mapping. A theoretical model of a single fibre loop in knitted textile composites have been developed to predict the fibre strains under different levels of composite stretching in the wale direction. The fibre strain prediction agrees with the average values of the measured fibre strains except at high strain levels where there is a large deviation of the measured fibre strains.

7.2 Potential Applications of Cellular Textile Composites

The primary purpose of this study is to develop cellular textile composites as energy absorption liner or protection devices in order to promote the crashworthiness of vehicles and the safety of people involved. The cellular textile composites made of fabric reinforcement and matrix material can be tailored with desired mechanical properties such as stiffness and toughness. With the light-in-weight properties, it can be designed to possess high specific energy absorption capacity. The material used in this study, especially the non-woven fabric structure made of conventional PET fibres and the PP matrix allows low material and manufacturing cost. They are not toxic thermoplastic polymeric material and the textile network can provide good ventilation by designed porous structure during forming the cells, thus enable to be

used for human protection.

The application of the thermoplastic cellular textile composites from knitted and non-woven reinforcement can be designed to achieve high specific energy absorption capacity in safety helmet similar to the developed thermoset cellular composite in the previous invention (US Patent 6,536,052) at medium and low velocities. The non-woven cellular textile composites developed in this study have been patented which is capable of retaining similar energy level under multi-impacts.

However, it should not be limited to the use of helmets. Other potential applications of using this textile fibre networks with grid dome cellular geometry are heat insulating textile material, protective packaging for delicate items, cushion or padding for semi-rigid support in medical cast and orthopedic devices, mattresses or shoe midsole for athletics shoes, seat cushions in automobile seats, etc.

7.3 Suggestions for Future Work

The major objectives of this thesis have been achieved. However, further work should be considered to develop a more comprehensive study for design and development of the cellular textile composite material as energy absorption devices in the following aspects:

Study of Cell Deformation Mode

In this study, the non-woven cellular composites have a controlled thickness of 1.0mm. However, cell wall thickness may affect the deformation modes. Thin wall

may lead to multi-folds under large deformation while thick wall increases the structural rigidity that may hinder the propagation of cell deformation. As concluded in chapter 2, the equivalent cell wall thickness governs the energy absorption capacity of the cellular composite, due to the negligible void volume during fabrication of the non-woven composites, at a given fibre volume fraction, thinner cell wall of the non-woven composites may help to reduce the stiffness and allow large deformation of the cell structure.

Fabrication of the Curved Composite Panel

In this study, the energy absorption behavior of the flat cellular textile composite panels has been characterized. More worthwhile investigation would be put on the curved specimens where performance of the energy absorbing liner in helmet can be characterized. In order to further maximize the energy absorption capacity, double-layer panels in different arrangement, such as overlapping or interlocking by gluing two cellular composite panels together, are worthy for the investigation. In the stage of prototype design, a compression mold for molding the constituent materials into a whole helmet form should be made to fabricate the three-dimensional headform shape for the whole helmet testing.

Testing on Curved Cellular Panel

The current study is confined to the impact performance of the flat cellular panels by using a flat square head/anvil. Depending on the application, it is interesting to further investigate the energy absorption capacity of cellular panels under various impact conditions. Considering the cellular composites to be applied as energy absorbing liner at low to medium velocities, such as bicycle helmets, there are

several US standards for the testing on such helmets, in which the US Customer Product Safety Commission (CPSC) Bicycle Helmet Standard or ASTM standard are widely adopted. Several kinds of anvil may be used for simulate the impact conditions, such as a hemispherical anvil and a sharp curbstone anvil. Thus, a more systematic impact testing plan on all flat, curved and whole headform shaped liner specimens may be carried out by using different shapes of load head.

Further Micromechanics Study by Employing Raman Technique

Raman technique is an effective tool on characterizing deformation properties of fibre or composites. Due to the limitation of installment of the Raman microscopic accessories, real-time Raman stress/strain measurement is restricted in this study. In the further investigation by equipping a small mechanical tester called minimat loading frame that fibres or composite specimens to be mount firmly, which is possible to conduct in-situ/real-time measurement or mapping the stress/strain during deforming high performance fibres/composites. Thus, the induced Raman band shift as a function of fibre stress or strain can be obtained and compared.

Further improvement on the fibre stress relaxation may be achieved by cooling the fibre/composite from room temperature to low temperature by exposing the specimen in a coolant bath containing ice or liquid nitrogen as coolants in the hot/cold stage of a sample cell. Van Eijk et al (1990) studied the stress relaxation in DSM high modulus polyethylene fibre. Cooling the fibre to 240 K caused the reduction of the effect of stress relaxation, although the relaxation cannot be removed completely. Later, Grubb (1992) reported that better Raman spectra were obtained on the cooled *Spectra* UHMWPE fibre to 273 and 77 K by simple set up of the coolant

bath for the stressed filament. The cooling on this polymeric fibre/composite reduced the effect of relaxation and even completely suppressed the stress relaxation at 77 K. The Raman band shifted linearly and best curve fitting were obtained. Thus, more reliable data can be obtained during single fibre deformation. Yet there is still the consideration on the set up of the cooling system when it is necessary to hold the stretched composite specimen with the comparatively large stretching frame at the controlled temperature environment. In addition, the effect of off-axis orientation of the fibres of knitted loop inside the composite loop should be studied because of the large deformation of loop shape during composite deformation. Therefore, a simple experiment can be conducted by tensile loading of a model composite in which the effect of the orientation angle of single fibre embedded in the model composite to the loading direction can be revealed by the Raman shifts obtained with the changing orientation angle.

Fibre Strain Prediction of Weft-Knitted Composites

Although assumption made on the thickness of fibre bundle is constant during tensile loading, the fibre bundle subject a reduction on thickness and a more variation in thickness in the interlocking region of the fibre loop during tensile loading. The effect of fibre and yarn diameter may be incorporated in the modeling of fibre strain inside a single loop during composite deformation. Referred to section 6.4, the thickness t in the present model is derived from the thickness in the interlocking region. An empirical method can be conducted experimentally to identify the relation between the changes in loop thickness and the external tensile force and consequently to apply this relation in Eq. (6.1) and (6.4).

Appendix 2.1 (a) Top mold of the 25-domes compression mold for fabricating thermoplastic cellular composites

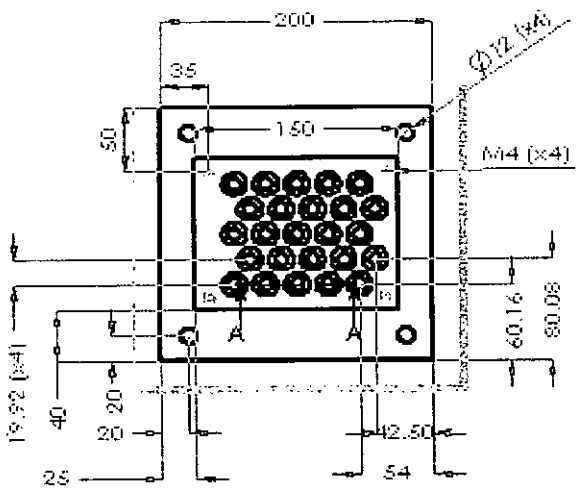

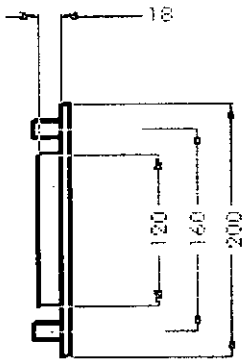

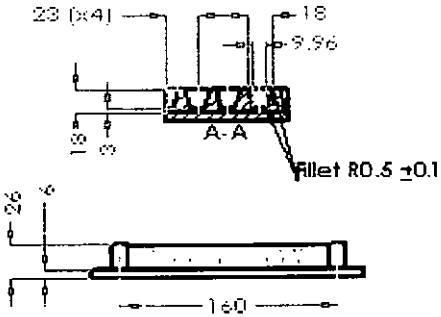

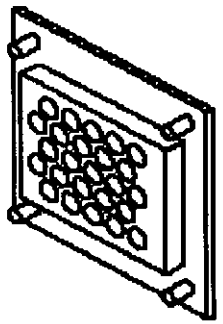

The istance between each hole is 22mm fixed

Top Mold
Quantity: 1

Appendix 2.1 (b) Bottom mold of the 25-domes compression mold for fabricating thermoplastic cellular composites

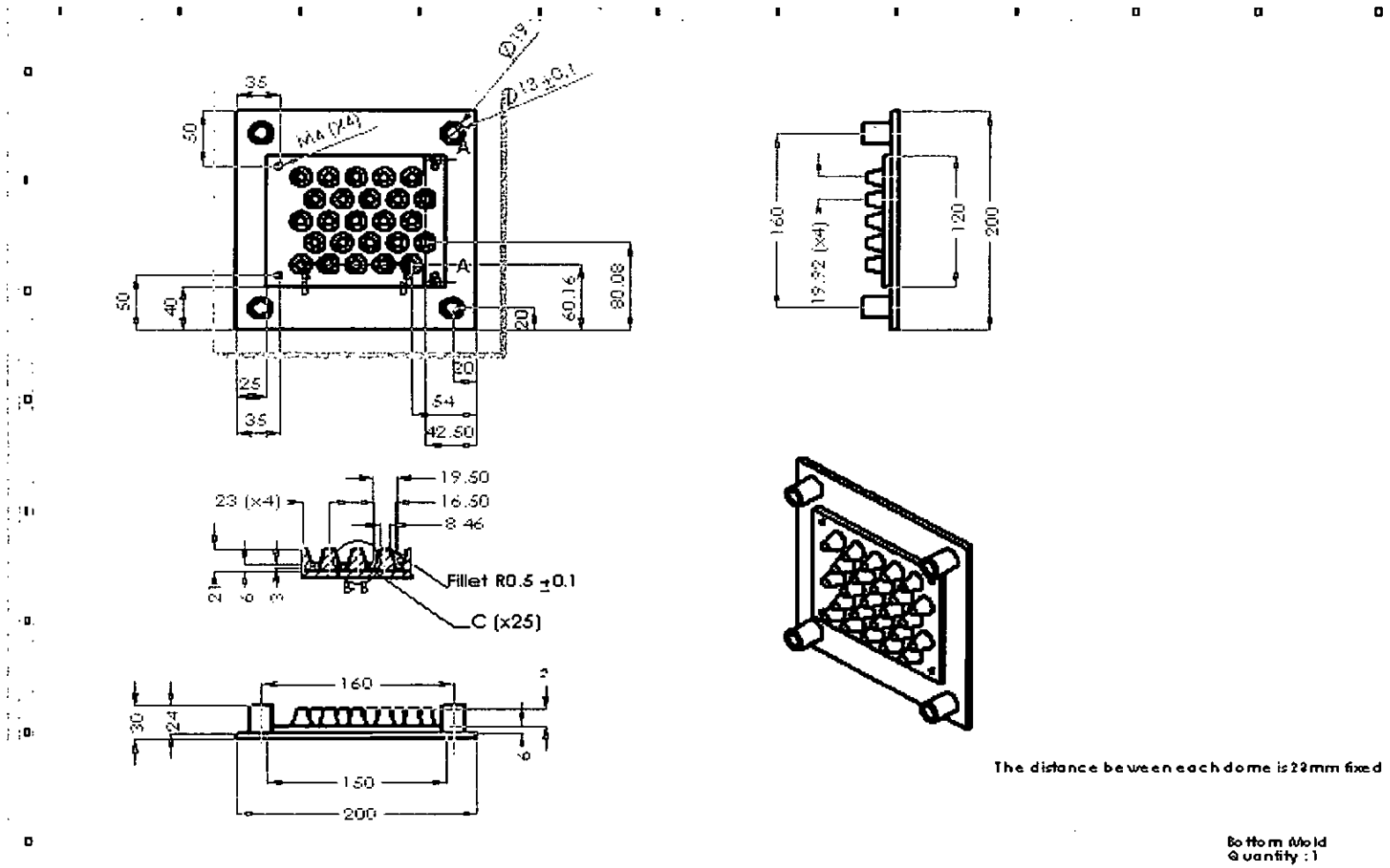

Appendix 3.1 Dimensions of the punch-type shear testing device (ASTM standard D732)

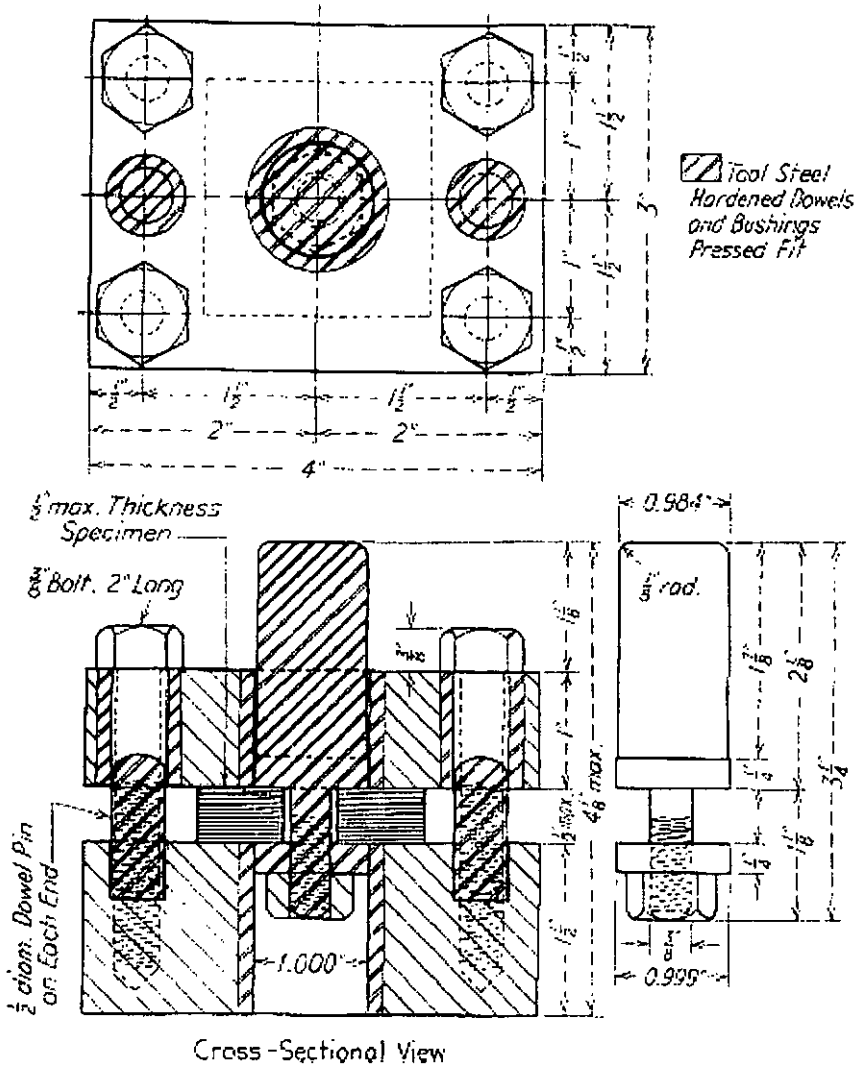

Appendix 6.1 Curve Fitting Process of the Raman Spectra

The curve-fitting procedures on analyzing the Raman bands at 1060 cm^{-1} and 1130 $cm^{-1}$of the UHMWPE fibre and LDPE matrix were done by fitting the bands with one 'broad' and one 'narrow' Gaussian curves after background subtraction to the obtained Raman spectra.

Equation below represents the Gaussian function and schematic diagram as shown in Fig. A1:

$$y = y_0 + Ae^{-\frac{(x-x_c)^2}{2w^2}}$$

where

x_c: the position in the band

w_1: Full width at half maximum intensity (FWHM) = $2w\sqrt{ln(4)}$ =2.355w

A: Intensity of Raman scattering

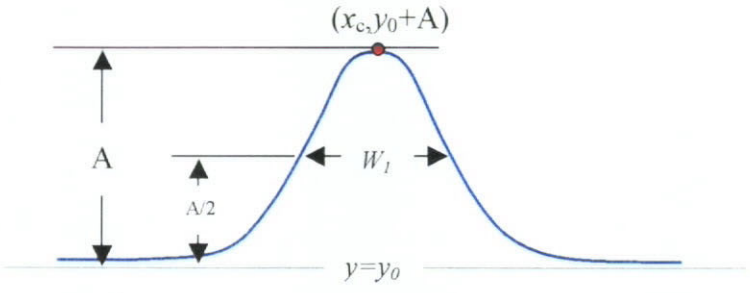

Figure A1. Schematic expression of the Gaussian function for the curve fitting to the Raman bands

Appendix 6.1(con't) Curve Fitting Process of the Raman Spectra

The 'goodness of fit' is measured by a chi-squared parameter χ^2, a measure of the difference between the fitted curve and the Raman band, given by

$$x^2 = \frac{\sum (A_R - A)^2}{n}$$

where

A_R : the intensity of the Raman data

n: the number of data points

During the curve-fitting procedure, the program continuously adjusts the fitting parameters in order to minimize the chi-squared value.

REFERENCES

Adams, D.F., 1974, Elastoplastic behavior of composites, Mechanics of Composite Materials, New York, Academic Press.

Akovali, G., 2001, Handbook of composite fabrication, Shawbury : Rapra.

Albrecht, W., Fuchs, H. and Kittelmann, W., 2003, Nonwoven fabrics. Weinheim : Wiley-VCH.

Andrews, M.C., Bannister, D.J. and Young, R.J., 1996, The interfacial properties of aramid/epoxy model composites, Journal of material Sciences, 31: 3893-3913.

Araujo, M., 1996, Production of shaped 3D reinforcing fabrics by knitting to shapes, Melliand Textilberichte 5, English version: 66-67.

Araujo, M.d., Hong, H. and Fangueiro, R., 2003, The use of finite element analysis to simulate the deformation behaviour of weft-knitted fabrics, European Conference on Simulation 2003.

ASTM D3039, Standard Test Method for Tensile Properties of Polymer Matrix Composite Materials.

Bao, R.H., Yu, T.X., Tao, X.M., Numerical simulation of large deformation of flat-topped conical cells made of textile composites. (in press).

Chao, T.Y., Gao, S. and Mu, Q., 1993, Effect of low-temperature-plasma surface treatment on the adhesion of ultra-high-molecular-weight-polyethylene fibres, Journal of Materials Science and Technology, 28(18): 4883-4891.

Chou, S., Chen, H.C. and Lai, C.C., 1992, The fatigue properties of weft knitted fabric reinforced epoxy resin composites, Composites Science and Technology, 45(4): 283-291.

Corbman, B.P., 1983, Ch.7, Felted and Nonwoven fabric formation, Textiles: fiber to fabric, New York : Gregg Division, 6th Edition, McGraw-Hill: 135-143.

Cox, B.N. and Davis, J.B., 2001, Knitted composites for energy absorption under tensile loading, Composites Part A: Applied Science and Manufacturing, 32A(1): 91- 105.

Day, R.J., Robinson, I.M., Zakikhani, M. and Young, R.J., 1987, Raman spectroscopy of stressed high modulus poly(p-phenylene benzobisthiazole) fibres, Polymer, 28(11): 1833-1840.

Delhaye, M. and Dhamelincourt, P., 1975, Raman microprobe and microscope with laser excitation, Journal of Raman Spectroscopy, 3(1): 33-43.

Disselbeck, D., Gebauer, E., 1994, Manufacture of a three-dimensionally shaped textile material and use thereof, issued 15 Nov 1994, (US5364686).

Disselbeck, D. and Stahl, D., 1986, Sheet-like sandwich molding, issued 23 Dec 1986, (US4631221).

Droste, R., 1986, Bullet-proof Vest or the Like, issued 22 Apr 1986, (US4584228).

DSM Product data sheet, 2001, Dyneema SK75 440dTex, issued 23 Jan.

Du, W.C., Tao, X.M., Tam, H.Y. and Choy, C.L., 1998, Fundamentals and applications of optical fibre Bragg grating sensors to textile structural composites, Composite Structures, 42(3): 217-229.

Epstein, M. and Nurmi, S., 1991, Near net shape knitting of fibre glass and carbon for composites, 36th International SAMPE Symposium: 102-113.

Feast, W.J., Munro, H.S. and Richards, R.W., 1993, Polymer surfaces and interfaces II, P.131-159. Chichester ; New York : Wiley & Sons.

Galiotis, C., Melanitis, N., Batchelder, D.N., Robinson, I.M. and Peacock, J.A., 1988, Residual strain mapping in carbon fibre/PEEK composites, Composites, 19(4): 321-324.

Galiotis, C., Robinson, I.M., Young, R.J., Smith, B.J.E. and Batchelder, D.N., 1985, Strain dependence of the Raman frequencies of a Kevlar 49 fibre, Polymer Communications, 26(12): 354-355.

Gelin, J.C., Cherouat, A., Boisse, P. and Sabhi, H., 1996, Manufacture of thin composite structures by the RTM process: numerical simulation of the shaping operation, Composites Science and Technology, 56(7): 711-718.

Gibson, L.J. and Ashby, M.F., 1997, Cellular solids: structure and properties. Cambridge, UK, Cambridge University Press.

Gioello D.A., 1982, Understanding fabrics: from fiber to finished cloth, Publisher New York : Fairchild Publications.

Grubb, D.T. and Li, Z.F., 1992, Molecular stress distribution and creep of high-modulus polyethylene fibres, Polymer, 33(12): 2587-2597.

Gupta, N.K. and Easwara, P.G.L., 1999, Quasi-static and dynamic axial compression of glass/polyester composite hemi-spherical shells, International Journal of Impact Engineering, 22: 757-774.

Gupta, N.K. and Velmurugan, R., 2002, Experiments and analysis of collapse behavior of composite domes under axial compression, Journal of Composite Materials, 36(8): 899-914.

Hansson, W., 1998, Textile preforming holds the key to increased industrial use of structural composites, Technical Textile International: 25-27.

Hoechst, A.S., 1991, Formable textile material and the shape of the mould obtained, (EP469558A1).

Hua, Y.L. and Yu, T.X., 1991, Mechanical behaviour of cellular solid, Advances in Mechanics, 21(4): 457-469.

Huang, Z.M., 2000, A unified micromechanical model for the mechanical properties of two constituent composite materials. Part I: Elastic Behavior, Journal of Thermoplastic Composites Materials, 13, 252-271.

Huang, Z.M., 2000, A unified micromechanical model for the mechanical properties of two constituent composite materials. Part II: Plastic Behavior, Journal of Thermoplastic Composites Materials, 13, 344-362.

Huang, Z.M. and Ramakrishna, S., 2000, Micromechanical modeling approaches for the stiffness and strength of knitted fabric composites: a review and comparative study, Composites Part A (Applied Science and Manufacturing), 31A(5): 479-501.

Ja, D.R. and Hodge, P.G., 1963, Crushing of a tube between rigid plates, Journal of Applied Mechanics, ASME, 30: 391.

Johnson, W. and Reid, S.R., 1977, Metallic energy dissipating systems, Applied Mechanics Review. ASME: 277-288.

Kamiya, R., Cheeseman, B.A., Popper, P. and Chou, T.W., 2000, Some recent advances in the fabrication and design of three-dimensional textile performs: A review, Composites Science and Technology, 60(1): 33-47.

Kelay, M.S., Bader, D.L. and Reed, P.E., 1997, Mechanical deformation mechanisms in knitted fabric composites, Journal of Thermoplastic Composite Materials, 10(1): 76-84.

Kim, D.W., Bessey, W.E., Nagel, J., Clark, G.M., Haas, J.S.W. and Oakley, E.O., 1999b, Medical casts and other orthopedic devices comprising thermoplastic three-dimensional fibre networks, issued 16 Mar 1999, (US5882322).

Kim, D.W., Bessey, W.E., Nagel, J., Clark, G.M., Haas, J.S.W. and Oakley, E.O., 1999c, Shoes comprising three-dimensional formed fiber product, issued 27 Apr 1999, (US5896680).

Kim, D.W., Haas, J.S.W. and Bessey, W.E., 1999a, Thermoplastic three-dimensional fibre network, issued 28 Dec 1999, (US6007898).

Kip, B.J., Eijk, M.C.P.V. and Meier, R.J., 1991, Molecular deformation of high-modulus polyethylene fibers studied by micro-Raman spectroscopy, Journal of Polymer Science: Part B: Polymer Physics, 29: 99-108.

Klecka, M., 1992, Web-like boundary layer connection and method to make same, issued 13 May 1992, (EP386387B1).

Ko, F.K. and Du, G.W., 1997, Processing of textile preforms, In: Gutowski T.G, Advanced Composites Manufacturing, Ch.5. New York, John Wiley & Sons.

Koenig, J.L., 1999, Spectroscopy of polymers, Amsterdam: Elsevier, 2nd ed.

Lam, S.W., 1999, Mechanical properties of textile composites for cushioning layer in helmet, B Sc(Hons) Thesis, Institute of Textiles and Clothing, The Hong Kong Polytechnic University.

Lam, S.W., Xue, P., Tao, X.M. and Yu, T.X., 2003, Multi-scale study of tensile properties and large deformation mechanisms of polyethylene terephthalate/polypropylene knitted composites, Composites Science and Technology, 63(10): 1337-1348.

Leaf, G.A.V., Glaskin, A., 1955, The geometry of a plain knitted loop, Journal of Textile Institute, 45: 587-605.

Leclerc, A., 1993, Embossed fabric, process for preparing the same and devices therefore, issued 15 Sept 1993, (EP559969A1).

Leong, K.H., Ramakrishna, S., Huang, Z.M. and Bibo, G.A., 2000, The potential of knitting for engineering composites-a review, Composites: Part A, 31: 197-220.

Lou, A.Y., 1991, Continuous fibre thermoplastic composites, Composite Material Series, 7: 167-204.

Lu, G.X. and Yu, T.X., in press, Energy absorption of structures and materials, Ch.4. Woodhead UK.

Mamalis, A.G, Manolakos, D.E., Saigal, S., Viegelahn, G and Johnson, W., 1986, Extensible plastic collapse of thin-wall frusta as energy absorbers, International Journal of Mechanical Science, 28(4): 219-229.

Mamalis, A.G, Manolakos, D.E., Viegelahn, G.L. and Johnson, W., 1988, The modelling of the progressive extensible plastic collapse of thin-wall shells, International Journal of Mechanical Science, 30(3/4): 249-261.

Marais, C. and Feillard, P., 1992, Manufacturing and mechanical characterization of unidirectional polyethylene-fibre/polyethylene-matrix composite, Composites Science and Technology, 45(3): 247-255.

Mazumdar, S.K., 2002, Composites manufacturing: materials, product, and process engineering. Boca Raton, FLA: CRC Press, c2002.

Moonen, J.A.H.M., Roovers, W.A.C., Meier, R.J. and Kip, B.J., 1992, Crystal and molecular deformation in strained high-performance polyethylene fibers studied by wide-angle X-ray scattering and Raman spectroscopy, Journal of Polymer Science, Part B (Polymer Physics), 30(4): 361-372.

Morton, W.E. and Hearle, J.W.S., 1993, Physical properties of textile fibres. Manchester, U.K., Textile Institute.

Mosleh, M., Suh, N.P. and Arinez, J., 1988, Manufacture and properties of a polyethylene homocomposite, Composites Part A: Applied Science and Manufacturing, 29(5-6): 611-617.

Mosleh, M., Suh, N.P. and Arinez, J., 1998, Manufacture and properties of a polyethylene homocomposite, Composites Part A, 29(A): 611-617.

Nairn, J.A. and Zoller, P., 1985, Matrix solidification and the resulting residual thermal stresses in composites, Journal of material Sciences, 20: 355-367.

Nardin, M. and Ward, I.M., 1987, Influence of surface treatment on adhesion of polyethylene fibres, Journal of Materials Science and Technology, 3(10): 814-826.

Prasad, K. and Grubb, D.T., 1989, Direct observation of taut tie molecules in high-strength polyethylene fibers by Raman spectroscopy, Journal of Polymer Sciences, Part B: Polymer Physics, 27(2): 381-403.

Ramakrishna, S., 1997, Characterization and modeling of the tensile properties of plain weft-knit fabric-reinforced composites, Composites Science Technology, 57: 1-22.

Ramakrishna, S., Hamada, H., Cuong, N.K. and Maekawa, Z., 1995, Mechanical properties of knitted fabric reinforced thermoplastic composites, Proc. of the 10th International Conference on Composite Material (ICCM-10), 245-252.

Ramakrishna, S., Huang, Z.M., Yew, H.M., 1999, Development of a novel flexible composite material, Journal of materials processing, 89-90: 473-477.

Ramakrishna, S., Maekawa, Z., Cuong, N.K. and Inoda, M., 1996, Mechanical properties of knitted fabric reinforced thermoplastic composites, Textile Composites in Building Construction 96, 279-286.

Romano, J.J., Soltani, S. and Bolden, M.V., 2001, Mattress or cushion structure, issued 7 Aug 2001, (US6269504 B1).

Roysancour, O.S.d., 1965, Heat insulating textile material and method of making same, issued 23Nov 1965, (US3219514).

Rudd C.D., Owen M.J. and Middleton V., 1990, Mechanical properties of weft knit glass fiber/polyester laminates, Composites Science and Technology, 39: 261-277.

Siesler, H.W. and Holland, M., 1980, Infrared and Raman spectroscopy of polymers, New York : M. Dekker.

Spencer, D.J., 2001, Knitting technology : a comprehensive handbook and practical guide, Cambridge : Woodhead Pub.

Svensson, N., 1998, Textile structures for load-carrying composites, Textile Magazine: 6-13.

Tao, X.M., Tang, L.Q., Du, W.C. and Choy, C.L., 2000, Internal strain measurement by fibre Bragg grating sensors in textile composites, Composites Science and Technology, 60(5): 657-669.

Tao, X.M., Yu, T.X., Ngan, K.M. and Ko, F.K., 1997, Energy absorption of cellular textile composite under quasi-static compression, Proc. ICCE/4, Hawaii, USA, 981-982.

Tao, X.M., Yu, T.X. and Xue, P., 2003, Safety helmets with cellular textile composite structure as energy absorber, (US6536052).

Tarantili, P.A., Andreopoulous, A.G. and Galiotis, C., 1998, Real-time micro-Raman measurements on stressed polyethylene fibres 1. Strain rate effects and molecular stress redistribution, Macromolecules, 31: 6964-6976.

Teishev, A., Incardona, S., Migliaresi, C. and Marom, G., 1993, Polyethylene fibres-Polyethylene matrix composites: Preparation and physical properties, Journal of Applied Polymer Science, 50: 503-512.

Tung, S. and Jayaraman, S., 1991, Three-dimensional multilayer woven preforms for composites, High-Tech Fibrous Materials: Composites, Biomedical Materials, Protective Clothing, and Geotextiles: 53-79.

Van Eijk, M.C.P., Leblans, P.R., Meier, R.J. and Kip, B.J., 1990, Raman spectroscopic determination of the number of high-stress bearing C-C bonds within high modulus polyethylene fibres during stress relaxation, Journal of Materials Science Letters, 9(11): 1263-1265.

Verpoest, I. and Dendauw, J., 1992, Mechanical properties of knitted glass fibre/epoxy resin laminates, 37th Int. SAMPE Symp., Anaheim, CA, USA, 369-377.

Verpoest, I. and Dendauw, J., 1993, Mechanical properties of knitted glass fibre/epoxy resin laminates, ECCM-6, Bordeaus, France, 20-24 Sept 1993, ed., Woodhead Publishing Ltd, Cambridge, 927-932.

Verpoest, I., Gommers, B., Huysmans, G, Ivens, J., Luo, Y., Panditu, S. and Philips, D., 1997, The potential of knitted fabrics as a reinforcement for composites, Proc. Of ICCM-11, Gold Coast, Australia: 109-132.

Wilde, D. and Ziegmann, 1997, Knitted fibre reinforced thermoplastics: Properties and applications, Asian Textile Journal: 90-95.

Willard, H.H., 1988, Instrumental methods of analysis, Belmont, Calif.: Wadsworth Pub. Co., 7th ed.

Wong, W.F. and Young, R.J., 1994, Analysis of the deformation of gel-spun polyethylene fibres using Raman spectroscopy, Journal of Materials Science, 29(2): 510-519.

Wu, W.L., Hamada, H., Kotaki, M. and Maskawa, Z., 1995, Design of knitted fabric reinforced composites, Journal of Reinforced Plastics Composites, 14(10): 1032-1042.

Xue, P., 2000, Cellular textile composites: Large deformation mechanisms and energy absorption behavior, PhD Thesis, The Hong Kong University of Sciences and Technology.

Xue, P., Yu, T.X. and Tao, X.M., 2000, Effect of cell geometry on the energy-absorbing capacity of grid-domed textile composites, Composites: Part A, 31: 861-868.

Xue, P., Yu, T.X. and Tao, X.M., 2001, Flat-topped conical shell under axial compression, International Journal of Mechanical Science, 43(9): 2125-2145.

Xue, P., Yu, T.X. and Tao, X.M., 2002, Tensile properties and meso-scale mechanism of weft knitted textile composites, Composites: Part A, Applied Science and Manufacturing, 33(1): 113-123.

Yang, X. and Young, R.J., 1995, Determination of residual strains in ceramic-fibre reinforced composites using fluorescence spectroscopy, Acta Metallurgica et Materialia, 43(6): 2407-2416.

Yeh, W.Y. and Young, R.J., 1998, Deformation processes in poly(ethylene terephthalate) fibers, Journal of Macromolecular Science Physics, B37: 83-118.

Young, R.J., Andrews, M.C., Rallis, N., 1996, Deformation micromechanics in high volume-fraction aramid/epoxy composites, Composites Part A, 27: 889-89.

Young, R.J., Day, R.J. and Zakikhani, M., 1990, The structure and deformation behaviour of poly(p-phenylene benzobisoxazole) fibres, Journal of Materials Science, 25(1A): 127-136.

Young, R.J., Day, R.J., Zakikhani, M. and Robinson, I.M., 1989, Fibre deformation and residual thermal stresses in carbon fibre reinforced PEEK, Composites Science and Technology, 34(3): 243-258.

Young, R.J., Lu, D. and Day, R.J., 1991, Raman spectroscopy of kevlar fibres during deformation-caveat emptor, Polymer International, 24(2): 71-76.

Young, R.J. and Yeh, W.Y., 1994, Chain stretching in a poly(ethylene terephthalate) fibers, Polymer, 35(18): 3844-3847.

Yu, T.X., 1986, Energy-absorbing devices utilizing plastic deformation of metals, Advances in Mechanics, 16(1): 28-39.

Yu, T.X., Tao, X.M. and Xue, P., 2000, The energy-absorbing capacity of grid-domed textile composites, Composites Science and Technology, 60: 785-800.

Zarandi, M.A. and Youssef, T., 1990, Energy absorption system for vehicle door and method of making, (US4890877).

Zhang, X.X. and Tao, X.M., 2001, Smart textiles (1): Passive smart, Textile Asia, 6: 45-48.

Zwagg, S., Northolt, M.G, Young, R.J., Robinson, I.M., Galiotis, C. and Batchelder, D.N., 1987, Chain stretching in aramid fibres, Polymer Communications, 28: 276-277.